Design of a Stable Nanocrystalline Alloy

By

Heather A. Murdoch

B.S. Materials Science and Engineering
Purdue University, 2008

SUBMITTED TO THE DEPARTMENT OF MATERIALS SCIENCE AND ENGINEERING
IN PARTIAL FULLFILLMENT OF THE REQUIREMENTS FOR THE DEGREE OF

DOCTOR OF PHILOSOPHY IN MATERIALS SCIENCE AND ENGINEERING
AT THE
MASSACHUSETTS INSTITUTE OF TECHNOLOGY

June 2013

© Massachusetts Institute of Technology. All rights reserved

ARCHIVES
MASSACHUSETTS INSTITUTE OF TECHNOLOGY
JUN 0 5 2013
LIBRARIES

Signature of Author:_____

Department of Materials Science and Engineering
February 21, 2013

Certified by:_____

Christopher A. Schuh
Department Head, Danae and Vasilis Salapatas Professor of Metallurgy

Accepted by:_____

Gerbrand Ceder
Chair, Departmental Committee on Graduate Students

Design of a Stable Nanocrystalline Alloy

By Heather A. Murdoch

Submitted to the Department of Materials Science and Engineering on February 21, 2013, in partial fulfillment of the requirements for the degree of Doctor of Philosophy in Materials Science and Engineering

ABSTRACT

Nanocrystalline materials are inherently unstable due to their high material fraction of grain boundaries, preventing their improved properties from being used in application. To stabilize the nanoscale grain size against rampant growth, past literature has proposed lowering the grain boundary energy through solute segregation to the boundaries. This approach has seen varied experimental success, using a metric of segregation strength to select an alloying element. In those alloys were some measure of stabilization is gained through alloying, precipitation of a second phase disrupts the necessary segregation state and triggers grain growth. This work considers the total stability of a nanocrystalline alloy – both stability against grain growth and stability against second phase precipitation – by examining the changes in free energy associated with segregation and nanostructuring. It is discovered that the relationship of segregation *and* mixing enthalpies for a particular system dictates the nanocrystalline stability of the alloy. Nanocrystalline stability maps are constructed for several conditions that can be used to predict an alloy's ability to support a nanostructure. Also revealed by the generation of stability maps are new types of stable nanocrystalline phases – in addition to the expected nano-phase stabilized by solute decoration of the grain boundary, a solute-rich nanocrystalline phase is expected to be stable under some conditions, as is an amorphous phase. To connect material systems to the results predicted by this work, a new model for the enthalpy of segregation was derived.

Thesis supervisor: Christopher A. Schuh
Title: Department Head, Danae and Vasilis Salapatas Professor of Metallurgy

Acknowledgements

Thanks, first and foremost to my advisor, Chris Schuh, who in addition to improving my skills as a researcher, contributed greatly to my growth as a presenter and writer. Thanks to my committee, Professor Ceder and Professor Tuller for good advice and challenging questions. Thanks to the members of the Schuh research group for both serious and fun office discussions and support. Thanks to my boyfriend, Matthew D. Haberland, for unwavering support and encouragement. Thanks to all my friends who have enriched my life greatly while at MIT including my tea and gym partner Sophie, my yoga host Liz, my pen-pal Cynthia, my roommates and baking partners Caroline and Sarah, my companion in running and other adventures Charlotte, and my wings buddy Mike. And lastly thanks to the steadfast love and support from my family.

Table of Contents

ABSTRACT 2

Acknowledgements 3

List of Abbreviations and Symbols 6

List of Figures 7

List of Tables 11

1. Introduction 12

1.1 Grain growth in pure nanocrystalline materials 12

1.2 Possible Stabilization 16

1.3 Thermodynamic approach to stabilization 17

1.3.1 Atomistic modeling 19

1.3.2 Experimental application of this approach 22

1.3.3 Observations based on existing experimental and modeled systems 41

1.4 Research problem 46

2. Regular Nanocrystalline Solution Model 47

2.1 Construction of Free Energy function 47

2.2 The Free Energy Surface 51

2.3 Comparison of Nanocrystalline Free Energies 53

2.4 Complete Free Energy Picture 57

2.5 Conclusions of this Chapter 60

3. Conditions for Complete Nanocrystalline Stability 61

3.1 Positive Enthalpy Systems 61

3.1.1 Symmetric systems (Equal $\Omega\gamma/t$) 61

3.1.2 Recasting of axes 63

3.1.3 Delineations of Stability Regions 65

3.1.4 Temperature 66

3.1.5 Non-symmetric (Unequal $\Omega\gamma/t$) 68

3.2 Negative Enthalpy of Mixing 70

3.3 Types of Stable Nanostructures Predicted 74

3.3.1 "Classical" Stable Nanocrystalline 74

3.3.2 Amorphous Limit 78

3.3.3 Dual-phase Nanocrystalline 79

3.3.4 Amorphous and Dual-phase 82
3.3.5 Discussion of stability 83
3.4 Metastable structures 88
3.4.1 Metastability when $\Delta H_{mix}>0$ 88
3.4.2 Locally metastable 90
3.4.3 Locally dual-phase metastable 90
3.5 Conclusions of this chapter 91
4. Placement of Alloys on Maps: Enthalpy Calculations 92
4.1 Enthalpy of Mixing 93
4.2 Enthalpy of Segregation 98
4.2.1 Critical examination of existing segregation models 98
4.2.2 New model for grain boundary segregation enthalpy 101
4.3 Comparison to existing segregation data and models 107
4.4 Populating nanocrystalline stability maps 109
4.6 Conclusions of this Chapter 111
5. Connections to Materials Systems 112
5.1` Previous experimental binary alloys 112
5.2 Tungsten based alloys 117
5.2.1 Tungsten alloy nanocrystalline stability map 118
5.2.2 Dual-phase analysis 120
5.3 Conclusions of this Chapter 124
6. Conclusions 125
6.1 Summary 125
6.2 Contributions 127
6.3 Future Directions 127
References 129
Appendix A 139
Appendix B 200

List of Abbreviations and Symbols

APFIM	Atom probe field ion microscopy
BCC	Body centered cubic
DSC	Differential scanning calorimetry
ECAE	Equal channel angular extrusion
EDS	Energy-dispersive X-ray spectroscopy
EELS	Electron energy loss spectroscopy
FCC	Face centered cubic
GB	Grain boundary
GFR	Glass forming range
HCP	Hexagonal closest packed
MA	Mechanical alloying
NC	Nanocrystalline
NM	Nanometer
RNS	Regular nanocrystalline solution
TEM	Transmission electron microscopy
XRD	X-ray diffraction
f_{gb}	Fraction of grain boundary region
γ	Grain boundary energy
γ^S	Surface energy
k	Boltzmann's constant
Ω	Atomic volume
R	Gas constant
T	Temperature
T_{cr}	Critical temperature – apex of miscibility gap
T_m	Melting temperature
t	Grain boundary thickness
ν	Transitional bond fraction
ω_c	Grain interior/crystal interaction parameter
ω_{gb}	Grain boundary interaction parameter
X	Global solute composition
X_c	Solute composition in the grain interior, or crystal
X_{gb}	Solute composition in the grain boundary
z	Coordination number

List of Figures

Figure 1.1 Grain growth for pure nc-metals Ni [11], Cu [13], Fe [14], Pd [15], Cr [16].

Figure 1.2 Rampant grain growth in electrodeposited nanocrystalline nickel – significant grain growth after only 10 minutes of annealing at 0.2Tm and out of the nanocrystalline regime by 30 minutes (not pictured).

Figure 1.3 Differences in grain growth due to processing methods in nc-Cu (A) and nc-Fe (B). Dashed lines were electrodeposited [17] [19], solid lines were mechanically alloyed [13] [14]. Points indicated by "C" were cryo-milled [26].

Figure 1.4 Illustration of thermodynamic approach to grain size stabilization, with the red curve showing the increase in free energy due to increased GB area (decrease in grain size). The blue curve shows the potential of solute segregation to lower the free energy, creating a local minimum stable with respect to variations in grain size.

Figure 1.5 MD simulations of nanocrystalline copper without dopants (A) and subject to an annealing process resulting in grain growth (B). The addition of dopants – red atoms in (C) results in no appreciable grain growth after the same anneal. From [33]. (D) Molecular Dynamics simulations of varied concentrations of dopants (black atoms) in copper after the same annealing treatment. Image adapted from [32].

Figure 1.6 Grain growth curves for experimentally studied iron-based nanocrystalline alloys. Data is taken from Fe-Al [26], Fe-Zr [49], Fe-Ta [49], Fe-Cu [50], Fe-Ni: electrodeposited[51] MA [52], Fe-Ag[53], Fe-Cr [54].

Figure 1.7 Grain growth curves for Fe-based systems re-plotted to show grain growth relative to initial grain size of the particular system. The data sources are the same as Fig. 1.6.

Figure 1.8 Grain growth in experimental copper-based nanocrystalline alloys. Data is from: Cu-Zr [48], Cu-Fe [50], Cu-W [60], Cu-Ag [61], Cu-Nb [62], Cu-Bi electrodeposited [63] and gas-deposited [18].

Figure 1.9 Grain growth in nc-nickel-based alloys. Data is presented from: Ni-Co [69], Ni-W [70], Ni-Fe – 20% [71], 45% [72], Ni-Mn [73], Ni-Cu [12], Ni-P [74], pure Ni [11].

Figure 1.10 Grain growth in Pd alloys: pure nc-Pd [15], Pd-Fe [87], Pd-Y [84], Pd-Zr [47].

Figure 1.11 Second phase precipitation connected directly to grain growth in two example nc-Ni systems; (B) Appearance of short range order in Ni-W heralding rapid grain growth. Figure from [78] (C) Appearance of Ni_3P phase triggering rapid grain growth, figure from [79]

Figure 2.1 Schematic of two nanocrystalline grains with GB segregation, viewed equivalently as an array of atoms (left) or as a continuum (right). On the left, solvent atoms are in gray; solute, red. GB thickness, t, and characteristic size, d, are depicted on the left, as are the interaction parameters associated with the various bonds. Figure from [112].

Figure 2.2 (A) A schematic of the increase in free energy caused by a decrease in grain size, followed at right by a free energy surface reflecting the same; the free energy surface has a trivial minimum that falls back to the free energy of a regular solution (blue arrow), showing that segregation is not effective at lowering GB energy or total energy in this case. (B) Segregation can mitigate the effect of grain size on free energy via the schematic on the left, blue curve. This creates a minimum in the free energy surface, as seen at right, at a particular grain size and segregation distribution where the GB energy is zero.

Figure 2.3 Minima in the free energy surface for two global solute concentrations, $X+$ (magenta curve) and $X-$ (black curve). Arrow A (blue) describes the rapid increase in free energy from holding the minimum $X_{gb}+$ and $d+$ values constant, while decreasing global composition $X+ \rightarrow X-$. In the other direction, arrow B (green) shows the decrease in free energy from holding $X_{gb}-$ and $d-$ constant while increasing global composition $X- \rightarrow X+$; however, the free energy can be reduced further (arrow C) by falling to the $(X_{gb}+,d+)$ minimum. Figure from [112].

Figure 2.4 (A) The minimum (X_{gb}, d) points from the two compositions presented in Fig. 2.3 are presented by black $(X-)$ and magenta $(X+)$ points; minima of other compositions are presented by blue points. The variation in free energy with respect to changes in composition while maintaining (X_{gb}, d) of the minima are plotted as a black, dashed curve for $X-$ and magenta curve for $X+$. The GB energy as a function of this variation is shown in (B).The GB energy is zero at the minimum (X_{gb}, d) pair. Figure from [112].

Figure 2.5 The free energy of the nanocrystalline phases, as represented by their minimum point and the U-shaped curve, can be stable (green), metastable (yellow), or not stable (red) compared to the free energy of the bulk phase. In this case, that of a system with a miscibility gap, the stable phases are denoted by the common tangent (dashed black line) of the regular solid solution (solid black line).

Figure 2.6 The free energy of the nanocrystalline phases, as represented by their minimum point and the U-shaped curve, can be stable (green), metastable (yellow), or not stable (red) compared to the free energy of the bulk phase. In the case of a system with an ordered compound (denoted A_3B, and by a solid black point), the stable phases are those whose free energy falls below the common tangent (dashed black line) of the regular solid solution (solid black line) and the line compound.

Figure 3.1 Example map of parameter combinations in the (ωc , ωgb) space – each point represents the full composition range for that parameter set, an example shown on the far right for each of three possibilities – not stable (red) , metastable (yellow), and stable (green). Each blue point is the minimum for that composition's free energy surface, shown to the left of the free energy – composition plot. For metastable cases, the minimum falls above the common tangent of the regular solution (represented by black dashed line); stable, below it.

Figure 3.2 Design map for the fraction 0.35 of critical temperature (absolute temperature shown across top) with enthalpic axes. Regions of stability are denoted by color (green: stable, yellow: metastable, red: not stable) and label.

Figure 3.3 Nanocrystalline stability maps and their accompanying figure of merits for five fractions of the critical temperature.

Figure 3.4 Free energy function of regular solution at different temperatures showing diminishing region of metastability.

Figure 3.5 Stability map for 1000K, $\Delta H^{mix}>0$.

Figure 3.6 Stability maps for $\Omega_A\gamma_A \neq \Omega_B\gamma_B$. (A) the GB energy – atomic volume constant for the solvent is lower than that of the solute (B) the GB energy – atomic volume constant for the solute is lower

Figure 3.7 Comparison of free energy for stability conditions in a compound forming system. Both plots have a A_3B compound in the system in addition to a solid solution (thick black curve), but in the schematic (A), the compound has a free energy of -30 kJ/mol, as compared to -50 kJ/mol in (B). A NC phase that is stable in (A), as depicted by green dot, is no longer stable in (B) due to the lower free energy of the A_3B compound.

Figure 3.8 Stability map for Negative mixing enthalpy systems at 1000K. The region of metastability is defined by the free energy of the A_3B intermetallic compound, listed on the right of the stability map.

Figure 3.9 "Classical" stability – the nanocrystalline phases in blue are lower in free energy than the common tangent of the regular solution (black curve). (A) presents the whole composition range, (B) the lower composition limit of stabilized nanostructures, starting at the solubility limit of the regular solution. (C) the upper limit of composition, characterized by the limit of X_{gb}-d space(see text). Image adapted from [112].

Figure 3.10 Grain size versus global composition for the stable "classical" nanocrystalline system shown in Figure 3.9. Image adapted from [112].

Figure 3.11 Free energy plot of a system in which the amorphous limit is the lowest energy phase. Amorphous Limit is depicted by the green dashed line, nanocrystalline compounds in blue, and bulk regular solution in black. Image from [112].

Figure 3.12 Dual-phase stable nanostructure: (A) free energy plot (B) free energy surface, showing two minima (C) schematic of the grain structure. Image adapted from [112].

Figure 3.13 Dual-phase (solvent-rich points in blue and solute-rich points in open red squares) and Amorphous (green dot-dashed line) stable. Thin black common tangent lines represent the equilibrium phase fields. Image from [112].

Figure 3.14 Nanocrystalline stability map for T=0.35Tcr; the stable nanocrystalline region is divided into subsections describing the various types of possible stable nanocorystallline structures. Image from [112].

Figure 3.15 Nanocrystalline stability map for 1000K for compound forming systems with A_3B compound. The stable region is subdivided into stable amorphous and stable dual-phase.

Figure 3.16 Metastability in $\Delta H^{mix}>0$ systems: (A) Free energy plot of nanocrystalline phases (blue points) with respect to the regular solution (black curve)and its equilibrium common

tangent (dashed purple line). (B) Grain size as a function of composition in this example system. (C) Free energy curves if the minimum values of (X_{gb}, d) and held constant for two different composition free energy surfaces. (D) GB energy as a function of composition for two compositions, holding their minimum values of X_{gb} and d constant. Minimum values have a GB energy of zero. Image adapted from [112].

Figure 3.17 Local Metastability in $\Delta H^{mix}<0$ systems: (A) an example free energy surface with a local minimum (B) The relationship of the local minimum to other phases.

Figure 4.1 Calculated enthalpies of mixing for a wide range of binary systems

Figure 4.2 Enthalpies calculated using Miedema model inputs to Eq. (4.9) and ΔH^{mix} Eq (4.1).

Figure 4.3 Segregation enthalpies for a wide range of binary alloys

Figure 4.4 A comparison of our segregation model, ΔH_M^{seg} , with the Hondros-Seah model (ΔH_{H-S}^{seg}) and elastic-only enthalpy (ΔH_{el}^{seg}).

Figure 4.5 Predictions of nanocrystalline stability for a wide range of binary alloys using the models for segregation and mixing enthalpy discussed in this chapter.

Figure 5.1 Tungsten alloy nanocrystalline stability map at 1100°C. Figure from [136].

Figure 5.2 Free energy surface and free energy plot for W-Ti at 400K

Figure 5.3 Free energy plot and common tangent construction for W-Ti at 1100°C

Figure 5.4 Phase diagram for W-Ti taking into account the nanocrystalline phases; the bulk two phase region is in hatched red/blue. Nanocrystalline two-phase region is delineated by black lines. (A) pure W after anneal (B)W-5%Ti after anneal (C) W-20%Ti after anneal. Micrographs courtesy Tongjai Chookajorn.

List of Tables

Table 1.1 Iron-based alloys ranked in order of experimentally observed thermal stability, from most delay in grain growth to least. Traditional metrics for predicting efficacy of solute for stabilization (elastic mismatch, radius difference, segregation strength via solubility) are shown for comparison to actual experimental stability. Thermal stability of alloys in italics are those not depicted on the grain size versus temperature curves.

Table 1.2 Copper-based alloys ranked in order of experimentally observed thermal stability, from most delay in grain growth to least. Traditional metrics for predicting efficacy of solute for stabilization (elastic mismatch, radius difference, segregation strength via solubility) are shown for comparison to actual experimental stability. Thermal stability of alloys in italics are those not depicted on the grain size versus temperature curves.

Table 1.3 Nickel-based alloys ranked in order of experimentally observed thermal stability, from most delay in grain growth to least. Traditional metrics for predicting efficacy of solute for stabilization (elastic mismatch, radius difference, segregation strength via solubility) are shown for comparison to actual experimental stability. Thermal stability of alloys in italics are those not depicted on the grain size versus temperature curves.

Table 2.1 Bonds in the RNS model

Table 3.1 Constants for the Stability Figure of Merit when $\Omega_A\gamma_A \neq \Omega_B\gamma_B$

Table 3.2 Example concentration distribution, grain size, and free energy for an example classical stable nanostructure with $\Delta H^{mix}>0$

Table 3.3 Example concentration distribution, grain size, and free energy for an example Dual-phase nanostructure: $\Delta H^{mix}>0$

Table 3.4 Example concentration distribution, grain size, and free energy for an example Dual-phase nanostructure: $\Delta H^{mix}<0$

Table 3.5 Example concentration distribution, grain size, and free energy for example classical nanostructure: $\Delta H^{mix}<0$ where the nanocrystalline structures are higher in free energy than the Amorphous Limit

Table 4.1 Miedema Model Enthalpy of Mixing Terms

Table 4.2 Quantitative Literature Segregation Enthalpy Values

Table 5.1 Experimental Nanocrystalline Alloys ($\Delta H^{mix}>0$)

Table 5.2 Experimental Nanocrystalline Alloys ($\Delta H^{mix}<0$)

Table 5.3 Summary of values for W-Ti calculations, including the enthalpy of segregation range. Table adapted from [136].

1. Introduction

1.1 Grain growth in pure nanocrystalline materials

Nanocrystalline (nc) metals promise unique and improved properties, such as high wear strength [1, 2], corrosion resistance[3, 4], and enhanced thermoelectric performance [5]. These gains are unfortunately mitigated by their inherent instability which is due to the excess energy associated with their high volume fraction of grain boundaries (GBs). There is, therefore, a significant driving force for grain growth, even at relatively low temperatures. Nanocrystalline copper [6-8], silver [8], palladium [9], and aluminum [10] have all presented grain growth out of the nanoscale regime while at ambient conditions; this room-temperature growth was observed despite differences in processing methods. For example, nc-copper prepared by gas-condensation showed an increase of 20nm in grain size over a period of two weeks, and micron sized grains were observed (amidst nanocrystalline regions) after one month in all nc-Cu samples regardless of processing conditions [6]. A second study of nc-Cu using the gas-condensation method also observed abnormal grain growth leading to several micron-sized grains after a few days at room temperature [7]. Additionally, electrodeposited copper with differing initial grain sizes (~10 or ~40nm) both grew to exceed 100nm in size after 30 hours at room temperature [8]. In this same study, electrodeposited nc-Ag also exhibited grain growth past 100nm from an initial grain size of ~25nm after a day at room temperature [8]. Gas-condensed nc-Pd doubled in grain size after 12 hours at ambient conditions, and many micron-sized grains were observed after 2 months [9]. The grain size of nc-Al produced by chemical synthesis also doubled at room temperature, and after only 1 hour [10].

Moving beyond problematic room temperature performance, the behavior of several pure nanocrystalline metals with respect to annealing treatments of approximately one hour

(represented as a fraction of material melting temperature) is shown in Fig. 1.1. By a homologous temperature of $0.2T_m$ (if not earlier), only one hour of heat treatment leads to a sharp increase in grain size. While room temperature grain growth is observed in [8] for Al and Cu, a similar electrodeposited nickel film was found to be stable under ambient conditions. In another study, electrodeposited nc-Ni was found to be stable at room temperature for over one year, and at 370K ($0.07T_m$) for over one week [11] . However, at higher temperatures, grains showed significant growth; the response of the deposited nc-Ni to one hour anneals at several temperatures is shown in Fig. 1.1. A similar trend of rapid growth is observed after three hour anneals in another electrodeposited study [12].

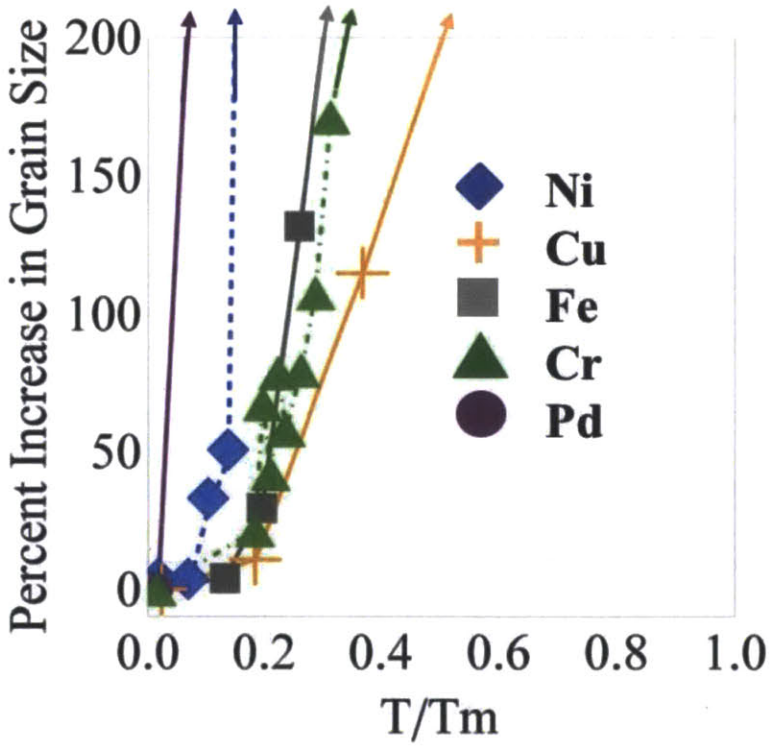

Figure 1.1 ***Grain growth for pure nc-metals Ni [11], Cu [13], Fe [14], Pd [15], Cr [16].***

In the case of pure copper, a mechanically alloyed (MA) sample is annealed for one hour [13], with a slightly better response than nc-Ni (Fig. 1.1), but still a very poor response. Ramped DSC anneals in electrodeposited nc-Cu [17] (shown in Fig. 1.3) and four hour anneals in gas-deposited nc-Cu [18] also show poor resistance to grain growth. Mechanically alloyed nc-Fe doubles in grain size after an eighty minute anneal at just ~20% of the melting temperature (300°C) [14]. Electrodeposited iron [19] (annealed for 150 minutes) and other mechanical alloying studies [20] annealed for varying times do not demonstrate any improvement in stability. Exhibiting very poor nanocrystalline stability is electrodeposited palladium [15] which had been annealed for one hour. The growth of nc-Cr produced via electrodeposition and annealed for one hour [16] is in line with instability in other pure metals; a 30 min anneal in another deposition study [21], observed very similar growth.

For an alternative visual representation of this rampant grain growth, observe the microstructure of electrodeposited nanocrystalline nickel is presented in Fig. 1.2 – grain growth is clearly visible after only 10 minutes of annealing at $0.2T_m$ (300°C).

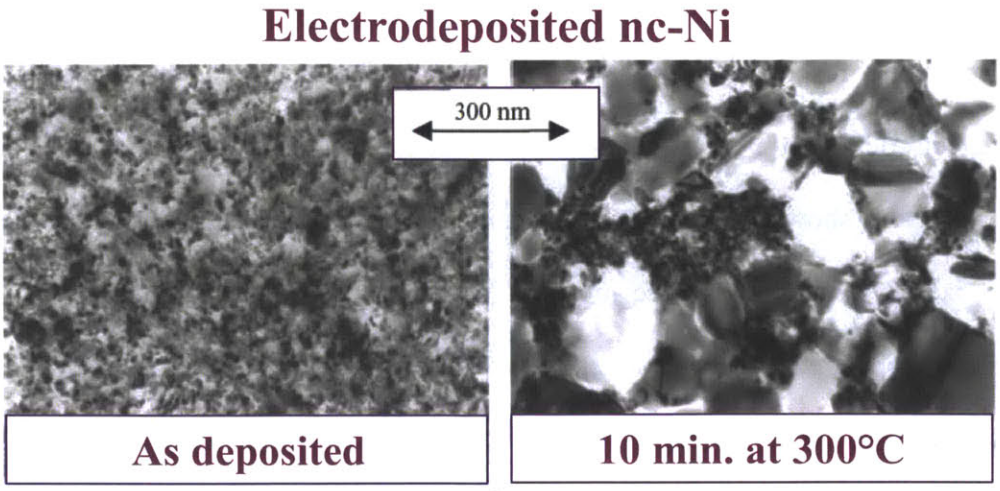

Figure 1.2 Rampant grain growth in electrodeposited nanocrystalline nickel – significant grain growth after only 10 minutes of annealing at $0.2T_m$ and out of the nanocrystalline regime by 30 minutes (not pictured).

In addition to the metals presented in Fig. 1.1, the thermal stability of pure nanocrystalline cobalt [22], aluminum [23], and gold [24] has been investigated. The grain growth in electrodeposited nc-Co [22] was examined thorough the maximum temperature of DSC peaks associated with the growth process. The effect of various parameters involved with the starting microstructure on this peak temperature was evaluated; the microstructural evolution after two minutes of annealing at 573K presented abnormal grain growth, with a few grains reaching micron-size. Mechanical alloying of aluminum resulted in a grain size of 96 nm after 25 hours of milling [23], difficult to compare with other nc-metals which are solidly in the nanocrystalline regime (<100nm); additionally, the lowest temperature at which heat treatments were performed was $0.68T_m$ (450°C). The grain size almost doubled after 30 minutes at this treatment. Nanocrystalline Au was prepared by gas deposition [24] and annealed for one hour, with the lowest temperature being ~$0.4T_m$ (425°C). The substrate was reported to have reached a

temperature of 400K ($0.12T_m$) during the deposition, and it is unclear how this would affect grain size and its evolution.

The instability exhibited in these studies of pure nanocrystalline metals would seem to disqualify them from useful application, despite promising properties conferred by the nanocrystalline grain size.

1.2 Possible Stabilization

In searching for possible solutions to stabilize this rampant grain growth, we first look at how the different processing routes for the same pure nanocrystalline metal affect the minor differences in thermal stability of pure nc-metals. In nc-Al [10], of two chemical synthesis processes, that which had less impurities grew more rapidly and was reported to be far more unstable than mechanically alloyed aluminum [23]. Fig. 1.3 presents the thermal stability of pure nc-Cu (Fig. 1.3A) and pure nc-Fe (Fig. 1.3B) with respect to processing methods. Mechanically alloyed metals show some improvement over electrodeposited in terms of the onset of rampant growth; there is a more marked difference in copper. Cryo-milling (MA below room temperature) is better still, in the case of iron [25], possibly attributable to the different impurities (and their compounds with iron) present in the different atmosphere used. These impurities may generate slight improvements, but only represent minor kinetic barriers to grain growth (via a pinning process). Additionally, the time scales over which these minor gains affect the onset of growth (Fig. 1.3) do not exceed two hours; examinations of isothermal grain size over longer annealing times show continued growth.

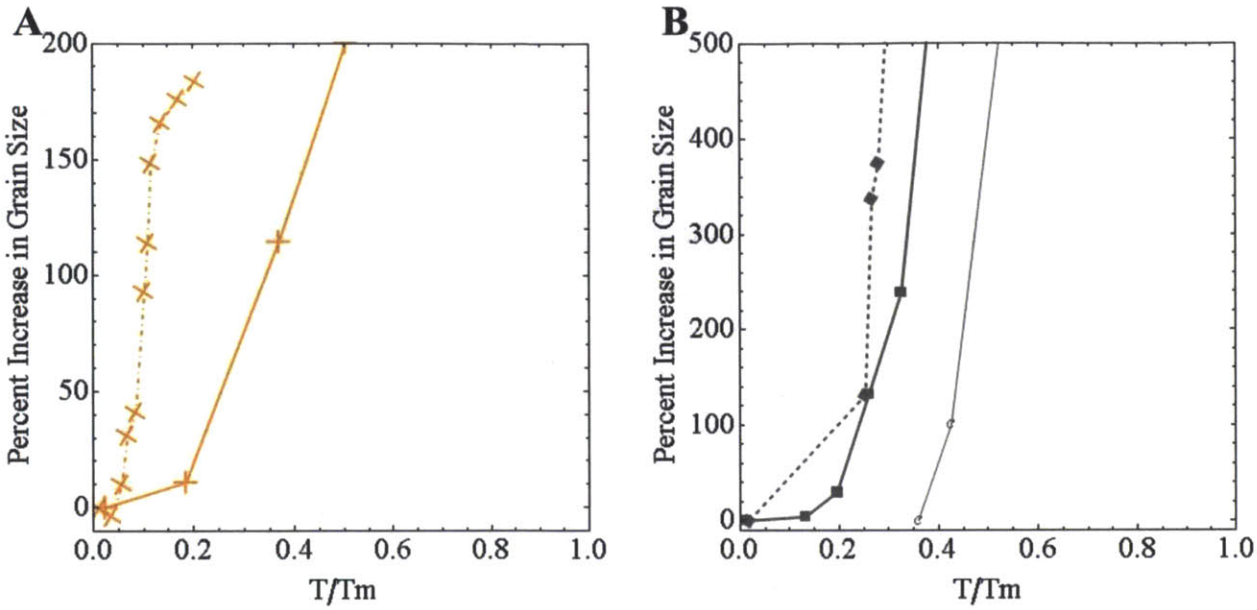

Figure 1.3 Differences in grain growth due to processing methods in nc-Cu (A) and nc-Fe (B). Dashed lines were electrodeposited [17] [19], solid lines were mechanically alloyed [13] [14]. Points indicated by "C" were cryo-milled [26].

Since the instability of nc-metals is an inherent property of the nanostructure, an approach to lower the energy associated with the large fraction of grain boundaries will be more useful.

1.3 Thermodynamic approach to stabilization

The free energy of a polycrystalline system is affected by the energy and area of its boundaries:

$$dG \propto \gamma dA \tag{1.1}$$

Starting from the Gibbs adsorption equation, Weissmuller [27, 28] noted that the segregation of solute atoms to the grain boundaries in a dilute system reduces the grain boundary energy, γ:

$$\gamma = \gamma_0 - \Gamma(\Delta H^{seg} + kT\ln X) \tag{1.2}$$

where the reduction in grain boundary energy from the unalloyed condition, γ_0, is a function of the enthalpy of segregation for the binary system (ΔH^{seg}) and the solute excess (Γ) at the grain boundary for a particular global solute concentration (X) and temperature (T), with k the Boltzmann constant. Weismuller proposed a metastable state, where $\gamma \rightarrow 0$ through appropriate solute segregation, and the grain size (or grain boundary area) would be stable with respect to variations. This approach was derived with the assumption of a strongly segregating system and in the dilute limit of solute. Kirchheim used a different starting point to derive the relation in Eq. (1.2) [29, 30], also assuming an ideal dilute solution.

The general approach of this method is illustrated in Fig. 1.4. The red curve represents the increase in free energy generated by the increasing fraction of grain boundaries and their attendant boundary energy, $dG \propto \gamma dA$. The blue curve demonstrates the effect on the free energy of adding solute to the grain boundaries. Ideally, the cusp represents a metastable state where the segregation state creates a local minimum in the free energy, and the system is insulated against variations in grain size.

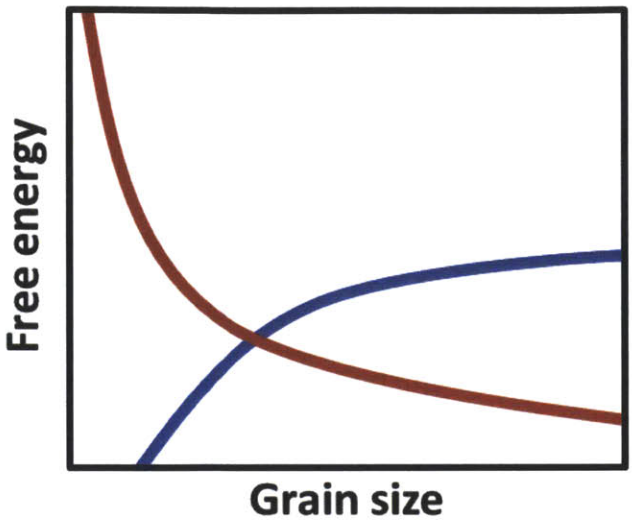

Figure 1.4 Illustration of thermodynamic approach to grain size stabilization, with the red curve showing the increase in free energy due to increased GB area (decrease in grain size). The blue curve shows the potential of solute segregation to lower the free energy, creating a local minimum stable with respect to variations in grain size.

1.3.1 Atomistic modeling

Several atomistic modeling studies have attempted to examine the possibilities and conditions of this thermodynamic approach. Using the general, adjustable Lennard-Jones potential, Millet and co-workers have used atomistic simulations to show that decorating grain boundaries with solute can reduce GB energy to zero and inhibit grain growth [31-33]. In particular, their simulations have revealed that the atomic size mismatch correlates with the magnitude of GB energy reduction through segregation [31], and a critical concentration is necessary to reduce the grain boundary energy to zero [32]. In a simulated polycrystalline system, grain growth was not observed following an annealing step when grain boundaries were appropriately saturated with solute [33].

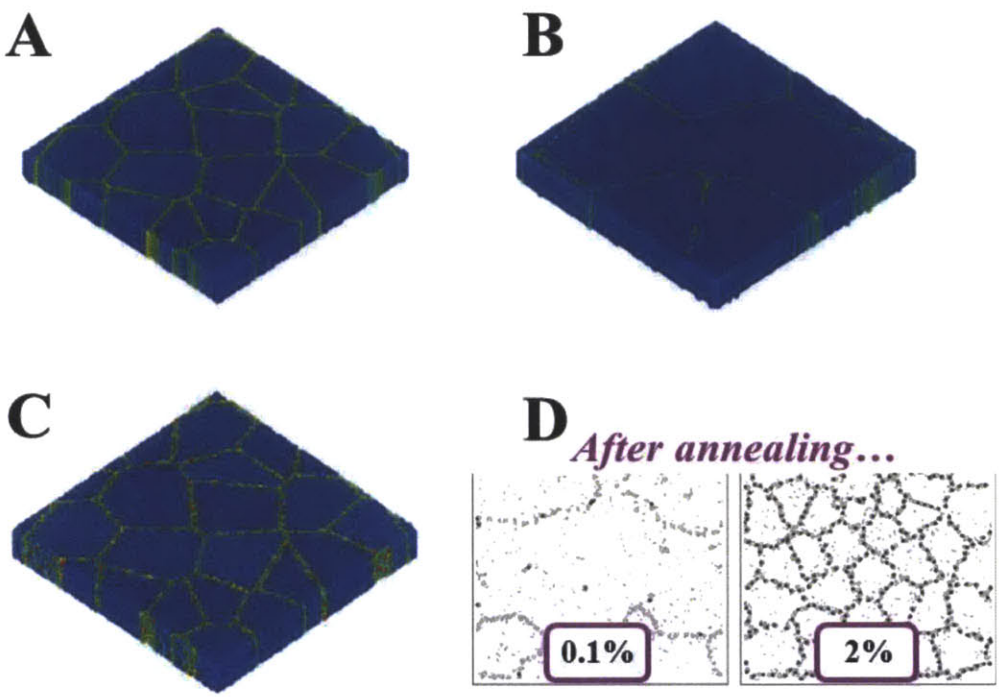

Figure 1.5 MD simulations of nanocrystalline copper without dopants (A) and subject to an annealing process resulting in grain growth (B). The addition of dopants – red atoms in (C) results in no appreciable grain growth after the same anneal. From [33]. (D) Molecular Dynamics simulations of varied concentrations of dopants (black atoms) in copper after the same annealing treatment. Image adapted from [32].

In studies in which realistic potentials for specific alloy systems are used, grain boundary behavior is more varied and nuanced:

In simulated copper, bismuth [34, 35] lowered the enthalpy at the grain boundaries when it was placed on some specific sites (even reaching negative local enthalpy), but the overall grain boundary energy remained positive. It was concluded that these locally negative regions of grain boundaries could retard the overall growth of grains. In this same study, silver solute in copper was found to be insufficient for grain boundary stabilization [34, 35]. Additionally in [36, 37], Cu-Ag was found to have a minor effect on the grain boundary energy; similarly Fe in copper had a negligible effect. However, Nb solutes at a global concentration of 1.9%Nb were found to

bring the GB energy to zero [36, 37]. This correlates to a grain boundary composition of 8.3%Nb [38].

In the case of tantalum in copper, tantalum segregation had a stabilizing effect, but agglomerated at higher temperatures [39]. Antimony atoms placed randomly at copper grain boundaries lowered their energy, with a stronger effect seen at higher concentrations [40, 41] to a level at which grain size no longer increased after an annealing treatment. (The effect of the dopants on deformation was also studied). Modeling of lead solute in aluminum showed that segregation on some sites can lead to locally negative grain boundary enthalpies at 300 K ($0.04T_m$) [42-44].

In the above discussed specific alloy simulations, only in some of the cases [39] [40, 41] was the thermal response evaluated. Additionally, in many atomistic simulations on this topic, the segregation state is achieved via manual decoration of solute atoms, which likely represent artificial segregation states. There have been fewer simulations where the segregation is thermodynamic. For example, in [45] a nanocrystalline system of nickel with tungsten solute was equilibrated by a Monte Carlo method, and found that while addition of tungsten reduced the grain boundary energy, there was not an equilibrium solute segregation configuration that brought the grain boundary energy to zero; the GB energy was reduced by 60%.

This molecular scale modeling has focused on adding varying concentrations of a solute atom dopant to a nanocrystalline matrix whose grain size is initially set. For the limited number of systems studied via molecular dynamics simulations, the use of dopants to stabilize nanocrystalline grain size has been shown to have varying levels of success, but there is not enough information to be able to extrapolate the utility of other alloying elements in additional system.

In an alternative, and more generalizable modeling approach, Trelewicz [46] derived a free energy function that encapsulates the thermodynamic stabilization of Eq. (1.2) and Fig. 1.4. However, it improves upon the ideas of Weismuller and Kirchheim by accessing the whole composition range (not just the dilute limit) and explicitly defining the total energy of a segregated system as opposed to simply the energy of the grain boundary. Differences in the grain sizes and composition ranges of stabilized states with respect to general materials parameters were studied in [46] and will be discussed in more detail in Chapter 2.

Through the findings of these theoretical and atomistic model approaches, alloying has emerged as a critical component for the development and deployment of nanocrystalline materials, although our basic understanding of thermodynamic stability in nanocrystalline alloys remains incomplete.

1.3.2 Experimental application of this approach

While many more nanocrystalline alloys have been experimentally studied than atomistically modeled, the great variety in approach also precludes generalizable conclusions about the efficacy of the thermodynamic approach. For example, annealing times range from seconds to days, with most on the shorter end of that scale. Temperature ranges for annealing treatments are often selected with an eye to service temperatures, so even the lowest temperatures tested show immediate grain growth. Additionally, most grain size measurements are taken from XRD; however, concurrent TEM observations often indicate large discrepancies either in average grain size [47-49] or grain size distribution, revealing the appearance of a few abnormally large grains. And, as mentioned above, different processing methods lead to varying degrees and sources of contamination (impurities).

Nonetheless, as will be detailed in the following section, alloyed nanocrystalline materials are more stable than their pure counterparts. (While scores of alloys have been produced with a nanocrystalline structure, we focus only on those whose thermal stability has been evaluated.)

1.3.2.1 Iron-based nanocrystalline alloys

The grain growth as a function of annealing temperature for iron-based alloys in presented in Fig. 1.6. As starting grain sizes differed between alloys and within alloys with differing compositions, we re-plot the experimental data as a percentage increase in grain size relative to the initial size (Fig. 1.7), rather than absolute dimensions to allow for comparison across alloys. Grain growth in pure iron [14, 26] is also represented for comparison.

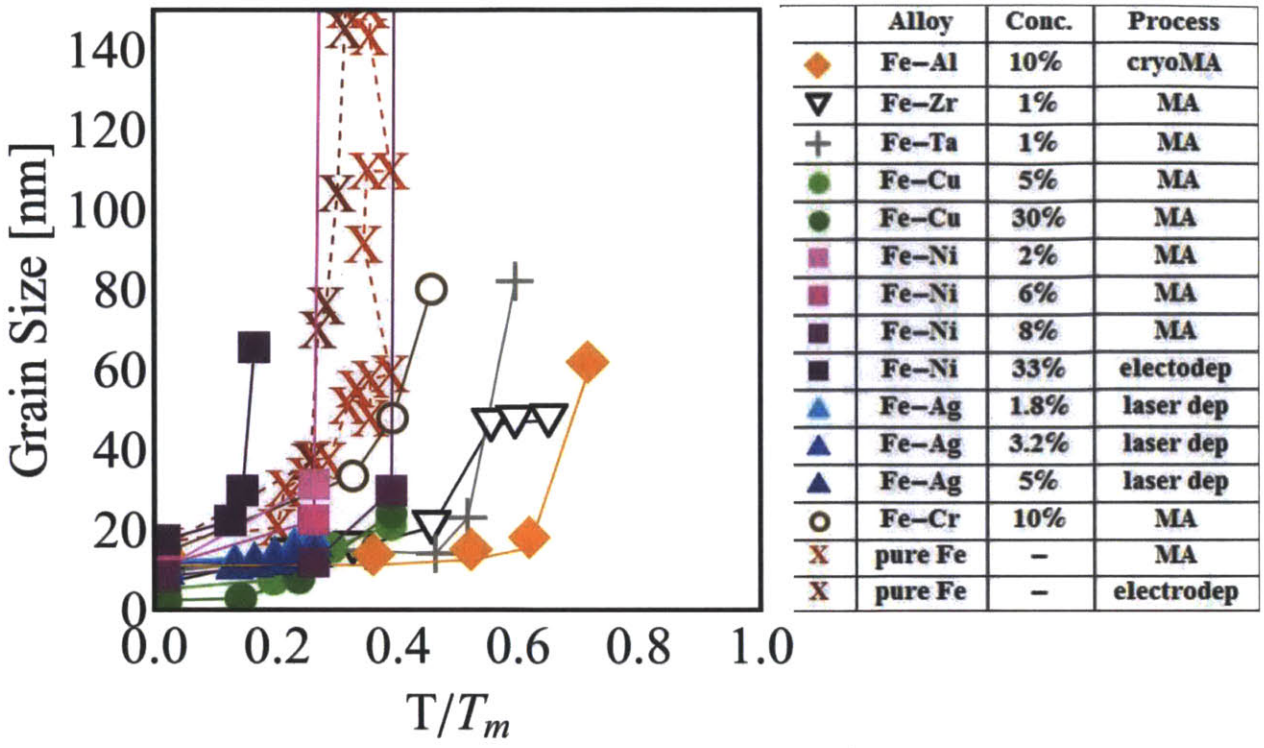

Figure 1.6 Grain growth curves for experimentally studied iron-based nanocrystalline alloys. Data is taken from Fe-Al [26], Fe-Zr [50], Fe-Ta [50], Fe-Cu [51], Fe-Ni: electrodeposited[52] MA [53], Fe-Ag[54], Fe-Cr [55].

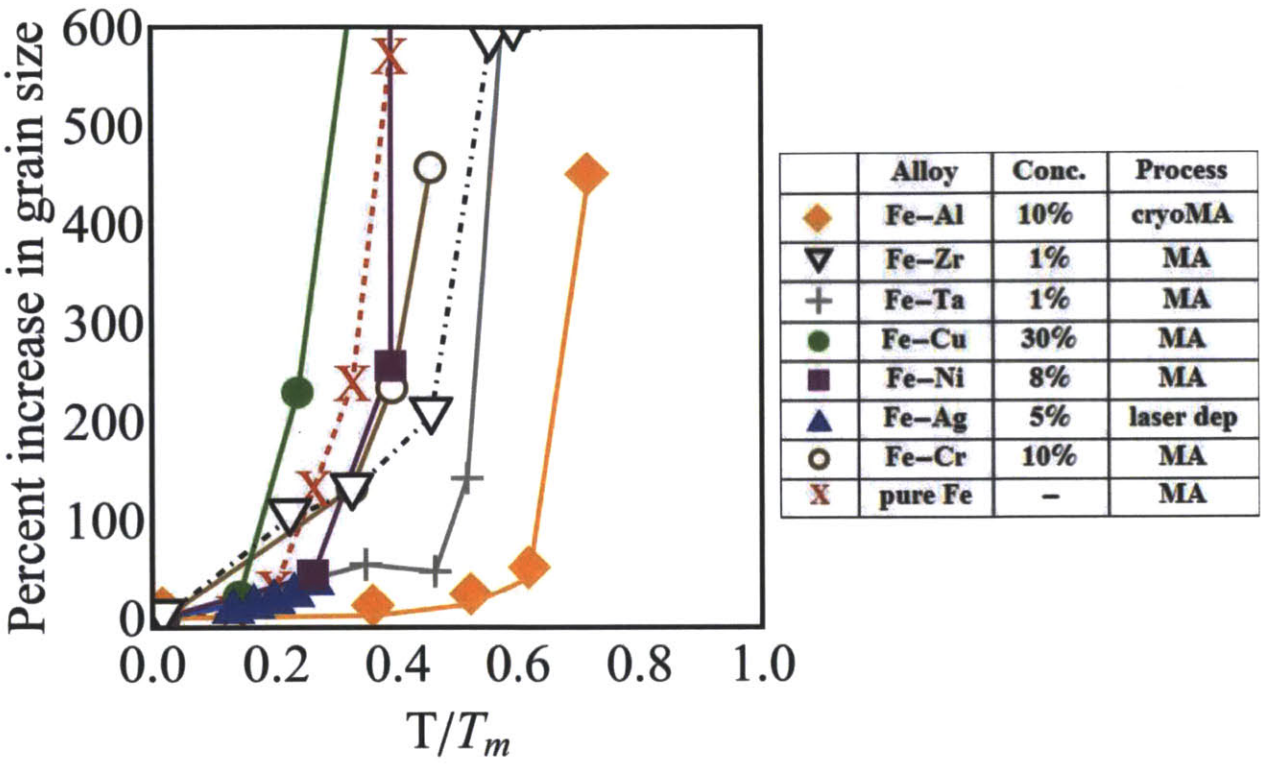

Figure 1.7 Grain growth curves for Fe-based systems re-plotted to show grain growth relative to initial grain size of the particular system. The data sources are the same as Fig. 1.6.

The majority of nanocrystalline iron-based alloys are created via mechanical alloying; it is noted in many of these studies that additional impurities are present that may also contribute to the stabilization of the nanocrystalline microstructure through either kinetic pinning or segregation stabilization, as for the case of pure nc-Fe produced via MA. It can be noted, for example, that the electrodeposited Fe-Ni alloy [52] has more rapid grain growth than the mechanically alloyed Fe-Ni alloys [53] in the same anneal period (one hour), despite having a higher concentration of nickel available for solute segregation (from the MA study, increasing composition delayed onset of grain growth [53]). Both studies exceed the solubility limit of nickel in iron (~3.5% for processing temperature, as reported in [53]), but there is no explicit evidence presented for grain boundary segregation of nickel. The grain size represented in Figs. 1.6 and 1.7 for each of these

studies is measured by XRD, but additional TEM observations observe a bimodal grain size distribution with several large (>100nm) abnormally grown grains [52]. This abnormal grain growth was also observed after one year of room temperature aging, in addition to phase separation [52]. Neither the electrodeposited or mechanically alloyed Fe-Ni alloys show significant improvement over pure nanocrystalline alloys (produced by mechanical alloying) (See Fig. 1.7).

Also showing little improvement with respect to pure iron was the Fe-Ag alloy system, produced via laser deposition [54, 56]. Alloys of three compositions, 1.8, 3.2, and 5% Ag, were annealed for one hour at temperatures up to 673 K [54], after which the silver-rich solid solution precipitates [56]. In fact, the iron solid solution phase separates at room temperature after four weeks.

The highly immiscible Fe-Cu system was mechanically alloyed at compositions of 5% and 30% copper [51]; the 30%Cu alloy remained entirely two phase despite the highly energetic ball-milling. The lower concentration alloy exhibits some grain growth at 570 K ($0.19T_m$), and at 720K ($0.29T_m$) significant grain growth has occurred; additionally, there is evidence of phase separation. At 870K ($0.39T_m$), the precipitating FCC phase is distinct. This study cites the difference in cohesive energies of iron and copper and some previous microcrystalline observations as expectations for solute segregation to the grain boundaries. In a more recent work [57], EDS profiles of microcrystalline Fe-4%Cu show clear and extensive grain boundary segregation (up to 60%Cu).

Mechanically alloyed Fe-10% Cr showed grain growth after thirty minutes of annealing at 500, 600, and 700°C (0.33, 0.39 ,and $0.46T_m$) [55], but the material remains nanocrystalline, a

helpful result for the end goal of a nc-product after a powder compaction process. Most of the grain growth occurred within the first 15 minutes at 500°C, and then plateaued; growth continued with time for annealing at 600°C and 700°C, with the grain size appearing to be >100nm after an hour of annealing at 700°C [55].

The relationship of solute concentration to grain growth was evaluated in the Fe-Zr system [20, 58]: a mechanically-alloyed system with 1/3% Zr exhibited grain growth resulting in a bimodal distribution of micron- and nano-sized grains at 700°C ($0.46T_m$) for one hour, whereas this result was not observed until 870°C ($0.57T_m$) for 4% Zr. The microstructure of the 4%Zr system was composed of micron-sized grains after an hour anneal at 1173°C ($0.76T_m$) with some large nano-precipitates (~400nm) of 42%Zr (the micron grains were 3% Zr). Increasing the solute content to 10% resulted in precipitation of Fe_2Zr at 700°C [58]. Surface EDS of the milled particles shows strong segregation of Zr to the particle surface and an examination of lattice behavior via XRD shows Zr leaving the lattice after a short anneal, both supporting the hypothesis of solute segregation to the grain boundary [20].

Iron alloyed with either titanium or molybdenum retained nanoscale grains until ~900°C ($0.59T_m$), where the transition of $\alpha \rightarrow \gamma$ iron coincides with a loss of thermal stability [59]. An FCC (γ-Fe) peak appeared in Fe-2%Ti samples heated at 911°C ($0.59T_m$) for less than 15 minutes, and continued to grow, exhibiting peak widths too narrow to be nano-scaled. The grain size of the initial BCC-Fe(Ti) doubled in an hour. The 2%Ti concentration falls in the Fe(Ti) region of the phase diagram which does not predict the $\alpha \rightarrow \gamma$ phase transition; however, XRD lattice analysis showed that the composition of Ti in the grain lattice is much lower (~0.23%, within the region of $\alpha \rightarrow \gamma$) potentially as a result of grain boundary segregation and some titanium oxide formation. The increase of titanium concentration to 5% maintained enough

titanium in the lattice to bypass the region in which the $\alpha \rightarrow \gamma$ transition would occur (at ~900°C), and an anneal at 930°C ($0.6T_m$) for 30 minutes maintained a nanostructure in the 5% alloy whereas the 2%Ti alloy produced the bimodal large-grained FCC-Fe and growing nano-BCC-Fe [59]. Similar results were indicated for Fe-Mo alloys, but not described [59].

Fe-10% Al alloys were produced via cryo-milling; hour anneals at 1073 and 1223K (0.52 and $0.62T_m$) resulted in minute increases in grain size (within error of the measurement method). Significant grain growth occurred after annealing at 1373K ($0.72T_m$) [26]. APFIM studies showed an inhomogeneous distribution of Al in Fe-Al (this time a 5% Al alloy) with segregation of aluminum, oxygen, nitrogen and the compounds AlN and Al_2O_3 at the grain boundaries [25]. Cryo-milling in argon versus nitrogen atmosphere shows lower stability (growth at 1273K vis a vis 1373K), which showed that the AlN grain boundary precipitates (which are only present when milled in nitrogen) are important in thermal stability [60].

1.3.2.2 Copper-based nanocrystalline alloys

Relative grain growth in experimentally produced copper alloys is presented in Fig. 1.8. Pure copper grain growth is represented for two processing methods, electrodeposited nc-Cu [17] by red "X"s, and gas-deposited [18] by dark red "X"s .

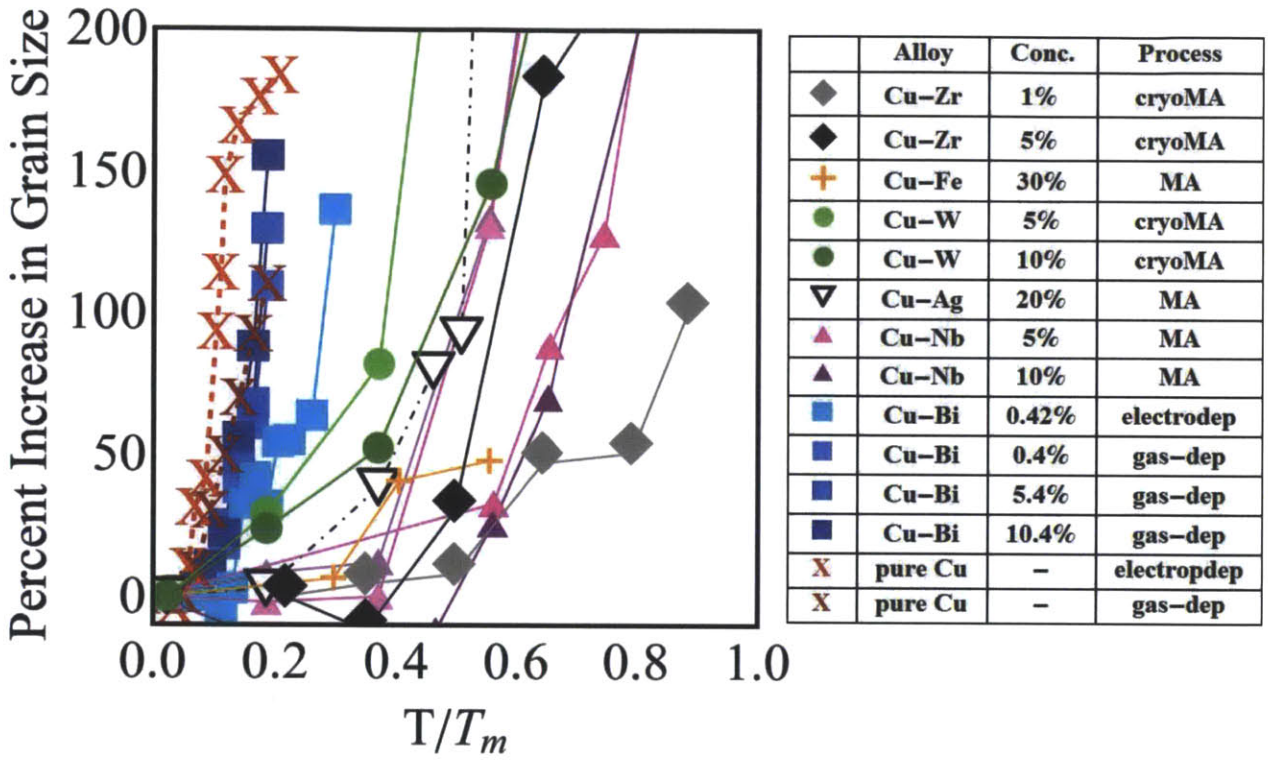

Figure 1.8 Grain growth in experimental copper-based nanocrystalline alloys. Data is from: Cu-Zr [48], Cu-Fe [51], Cu-W [61], Cu-Ag [62], Cu-Nb [63], Cu-Bi electrodeposited [49] and gas-deposited [18].

Mechanically alloyed Cu-Zr showed high thermal stability up to ~$0.5T_m$ according to grain size measurements derived from XRD [48] [64]; however, TEM observations of the nanostructure revealed higher grain sizes (and therefore higher growth) than the XRD measurements (about 20nm higher). Additionally, precipitates of ZrO_2 and Cu_5Zr were observed only through microscopy due to their small size (<5nm). Thermal stability at high temperatures

(900°C, $0.83T_m$) was therefore attributed to Zener pinning based on stabilization requirements – only a volume fraction of 2.4% is needed for a 2nd phase to stabilize the 30nm grain size is only 2.4% (if particles are assumed to be 3.5nm, which is reasonable based on the experimental observations). Modeled contributions of 2nd phase particles to hardness also agree well with experimental measurements. Zirconium is proposed to lower the grain boundary energy only at lower temperatures due to assumptions made in the segregation model [48].

Atomistic modeling found that 1.9%Nb in copper was capable of reducing the grain boundary energy to zero [36]; all experimentally assessed alloys have larger concentrations of Nb, but do exhibit good stability. For several compositions of Cu-Nb alloy prepared through MA [13], it was found that >5%Nb content was necessary for stability up to 400°C ($0.37T_m$) (one hour anneal). The appearance of Nb-rich phase peaks in the XRD for Cu-7.5%Nb at 600°C ($0.55T_m$) coincides with the start of significant grain growth. In both this study [13], and another [63, 65], the thermal stability of Cu-10%Nb is evaluated. The lowest temperature at which the 10%Nb alloy is annealed in [63] is 500°C ($0.46T_m$), and at this temperature, the nanostructure is observed to be composed of nc-Cu (50nm, grown from an initial size of 6nm) and a Nb phase (of size <5nm) which comprises ~14% of the material. Impurity phases are also observed: NbO, Cu_2O, and Fe_7Nb_6 [65].

The precipitation of an iron-rich phase observed via XRD at 720K ($0.41T_m$) coincides with a jump in grain growth in mechanically alloyed Cu-30%Fe [51]; grain boundary segregation of iron is not anticipated due to differences in cohesive energies. Indeed, atomistic modeling shows a very shallow decrease in grain boundary energy with addition of iron to the grain boundaries [36].

Additionally, in Cu-20%Ag, the formation of an Ag-rich second phase was concurrent with significant grain growth; shifts in the copper XRD peaks at 473K ($0.18T_m$) indicated silver leaving the matrix, and visible Ag peaks were observed at 673K ($0.37T_m$). Both the Cu and Ag phases exhibit growth upon further annealing [62].

Copper-bismuth alloys have been both gas-deposited [18] and electrodeposited [49], with the electrodeposited alloy of the same composition (~0.4%Bi) showing better stability. However, after only 10 minutes annealing at 200°C ($0.18T_m$), several large grains (>100nm) were observed via TEM. Regarding the gas-deposited samples, the bismuth alloy showed improvement over pure copper produced in the same method for the three compositions tested (0.4, 5.4, 10.4% Bi) [18]. The 10.4%Bi alloys showed second phase precipitation via XRD, but little difference in the grain growth pattern from the solid solution samples.

The stability of Cu-0.2% and 0.5%Sb alloys produced via ECAE was evaluated based on microhardness measurements, assuming the correlation of microhardness with grain size [40]. The microhardness dropped after annealing at ~200°C ($0.18T_m$) for pure Cu, compared to ~400°C ($0.37T_m$) for Cu-0.2% and -0.5%Sb, after which the hardness returned to bulk (micro-crystalline) values. Microscopy observed an initial grain size of 350nm; after one hour at 250°C ($0.23T_m$), the grain size grew to two microns.

1.3.2.2.1 Two-phase nanocrystalline copper alloys

During the course of evaluating thermal stability for several copper alloys, it was observed that the nanostructures likely initially consisted of two phases, not simply the expected solid solution. In mechanically alloyed Cu-36%Pb [66], the onset of grain growth was delayed with respect to pure nc-Cu (starting at 100°C, $0.09T_m$), but a full solid solution was not achieved after milling.

An initial structure of nc-Cu and nc-Ta grains of size <10nm in an MA Cu-10%Ta alloy evolved to a copper grain size of 111nm and bimodal distribution of Ta consisting of ~49nm grains and ~7nm clusters at copper grain boundaries after a four hour annealing treatment at 1173K ($0.83T_m$) [39].

Cryo-milling in the immiscible Cu-W system did not achieve complete nano-scaling of tungsten [61] – at 1%W, nano-W particles dispersed in ~40nm grains of copper stabilized this grain size up to one hour at 400°C ($0.37T_m$); however, some tungsten phase regions were found to be >1 micron in size. In the 10%W alloy, the grain size of copper was stabilized up to an annealing temperature of 600°C ($0.55T_m$); again, the W was present as both ~10nm and >1μm precipitates. Upon further annealing, the grain size of the copper matrix grew while the nanoscale W phases remained approximately the same size. Conversely, in magnetron sputtered Cu-10%W, a tungsten phase was not observed until 550°C ($0.51T_m$), a temperature consistent with diffusion calculations in this alloy [67]. In this study, both Cu10%Mo and Cu-10%W saw second phase precipitation (400°C for Mo) and the stability of this second phase was evaluated with respect to both heat treatments and irradiation.

In mechanically alloyed Cu-5%Y [68], a heat treatment at 500°C ($0.46T_m$) for 2 hours produced grain growth from 46 to 59 nm, observed via TEM. Diffraction patterns revealed either Cu_5Y or Cu_4Y present before and after the heat treatment.

1.3.2.5 Nickel-based nanocrystalline alloys

Electrodeposition is the processing method of choice for nanocrystalline nickel-based alloys. The response of several alloys and their varying compositions to annealing treatments is

shown with respect to annealing temperature in Fig. 1.9; pure electrodeposited nickel is presented in red for reference.

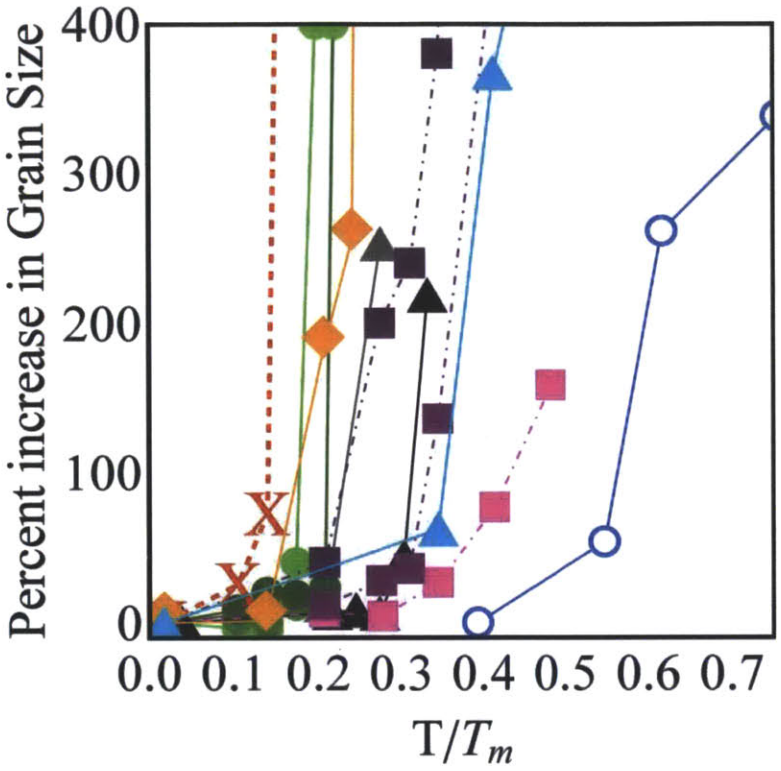

	Alloy	Conc.	Process
○	Ni–Co	20%	electrodep
■	Ni–W	6%	electrodep
■	Ni–W	13%	electrodep
■	Ni–W	21%	electrodep
▲	Ni–Fe	20%	electrodep
▲	Ni–Fe	45%	electrodep
▲	Ni–Mn	0.43%	electrodep
●	Ni–Cu	12%	electrodep
●	Ni–Cu	30%	electrodep
●	Ni–Cu	40%	electrodep
◆	Ni–P	1.2%	electrodep
X	pure Ni	–	electrodep

Figure 1.9 Grain growth in nc-nickel-based alloys. Data is presented from: Ni-Co [69], Ni-W [70], Ni-Fe – 20% [71], 45% [72], Ni-Mn [73], Ni-Cu [12], Ni-P [74], pure Ni [11].

An electrodeposited Ni-20%Co alloy showed good thermal stability as reported in [69]; however, the annealing time at temperature is not reported – annealing was performed via DSC, but neither the heating rate nor hold time was reported. Conversely, in another study of Ni-37%Co [75], abnormal grain growth was observed after only 10 seconds at 573K ($0.2T_m$), while the nc-matrix was entirely consumed after 120 seconds (the grain size grew from 15nm → 400nm).

A Ni-21%Fe electrodeposited alloy showed no change in grain size up to 373K ($0.07T_m$) for a 90 minute anneal [76, 77] and good stability up to 573K ($0.2T_m$), after which the grain size increased rapidly. Alloys of compositions 15%Fe [76] and 20%Fe [71] showed similar results, while a 45%Fe electrodeposited alloy [72] showed α-phase precipitation at 573K after 20 hours or 673K ($0.28T_m$) after 0.5 hr. Grain growth began at a lower temperature than in the lower iron content alloys where second phase precipitation was not observed.

Ni-W alloys of three compositions (6, 13, 21%W) showed good thermal stability to ~500°C ($0.34T_m$) for 24 hour anneals [70]. Around this temperature, short range ordering began to be observed, culminating in precipitation of the Ni_4W phase at 700°C ($0.48T_m$). In support of the stabilization of grain size via boundary solute segregation, atom probe observations quantify tungsten segregation to the grain boundaries [78]. Additionally, atomistic modeling showed that tungsten segregation can reduce the grain boundary energy by ~60% in a system with a starting grain size corresponding to that of the experimental 21%W sample [45].

Evidence of segregation was also quantified in electrodeposited Ni-Cu using EELS (electron energy loss spectroscopy) [12]; in a 44%Cu deposit, the grain boundary concentration of Cu was measured as high as 82%. For alloy compositions of 30 and 44%Cu, the grain size was stable to 573K ($0.2T_m$) after a three hour anneal; for 12%Cu, only 473K ($0.14T_m$). A Cu-rich phase precipitated when annealing temperatures exceeded 525K ($0.17T_m$) – in the Ni-30%Cu alloy, 15% of the material was Cu phase at 573K and 25% Cu phase at 625K ($0.24T_m$).

Segregation of phosphorous to grain boundaries in nickel was observed via atom probe in Ni-3.6%P (11%P in GB) and Ni-1%P [79]. The 1%P alloy was mostly stable to 250°C ($0.17T_m$), and substantial grain growth immediately preceded the observation of Ni_3P precipitation in grain

boundaries at 450°C ($0.31T_m$). Similarly, in a Ni-1.2%P alloy [74], the average grain size doubled from 10nm at 300°C ($0.21T_m$), with more extensive grain growth occurring after 360°C ($0.25T_m$), when Ni_3P precipitation is first observed. At 480°C ($0.33T_m$), the average grain size had surpassed 100nm. The annealing in this study was performed in the DSC in steps of 20°C with 10 minute holds to 'allow the microstructure to stabilize'.

Ni-Mn alloys were prepared by both direct current (0.12%Mn) and pulsed current (0.43%Mn) electrodeposition [73]. Following anneals of 1 hour, substantial grain growth was reported to start at 500°C ($0.34T_m$). At 600°C ($0.41T_m$) precipitation of tiny Mn clusters was observed using both atom probe and TEM. Atom probe studies found evidence of Mn, O, and C segregation to grain boundaries at annealing temperatures of 600 and 700°C ($0.48T_m$).

In contrast to the stability gained by many of the above alloying elements in nickel, grain growth was observed in electrodeposited Ni-45%Zn by 'simply exposing the sample to the electron beam' for 5 minutes [80].

1.3.2.6 Cobalt-based nanocrystalline alloys

In electrodeposited Co-1.1%P [81], the allotropic hcp→fcc Co phase transformation was observed between 673-733K ($0.27\text{-}0.31T_m$),followed by abnormal grain growth. Precipitates of Co_2P and CoP appeared between 733-753K ($0.31\text{-}0.32T_m$). Grain boundary segregation of P was confirmed via atom probe. In a second study [82], rapid grain growth began at 733K for 1.1%P and 713K for 3.2%P. Growth occurred earlier for the 3.2%P alloy due to earlier precipitation of Co_2P in the grain boundaries – the as deposited alloy contained 25%P in the GB as measured by atom probe; Co_2P and CoP precipitated in the GB of the lower P content alloy at 753K.

The cobalt phase transition (HCP→FCC) also triggered grain growth in an electrodeposited Co-5.5%Ni alloy [69], from an initial grain size of 20nm to 50nm. The 20nm initial grain size was observed to be stable up to 623K ($0.23T_m$). The allotropic transition occurred at 701K ($0.29T_m$), which agrees with the bulk phase diagram (695K). For much higher concentrations of nickel (47%)[75] the alloy was initially FCC, and abnormal grain growth was observed starting at 573K ($0.2T_m$); the nanocrystalline matrix was consumed after 6000s at that temperature. A two-phase (FCC and HCP) Co-26%Ni alloy also produced abnormal growth. Only the HCP-Co-Ni alloy [69] exhibited stability.

No cobalt transition was observed in electrodeposited Co-W alloys [83], but Co_3W appeared at 400°C ($0.27T_m$) for a 24.5%W alloy and 600°C ($0.4T_m$) for a 34.4%W alloy. However, difficulty in differentiating Co(W) solid solution and Co_3W XRD peaks cannot rule out its presence in the as deposited specimens. Grain growth observations (as measured by XRD peak broadening) were erratic, perhaps due to the aforementioned XRD resolution challenges.

1.3.2.7 Palladium-based nanocrystalline alloys

All three palladium alloys and their attendant compositions show marked improvement in thermal stability when compared to pure nc-Pd (Fig. 1.10).

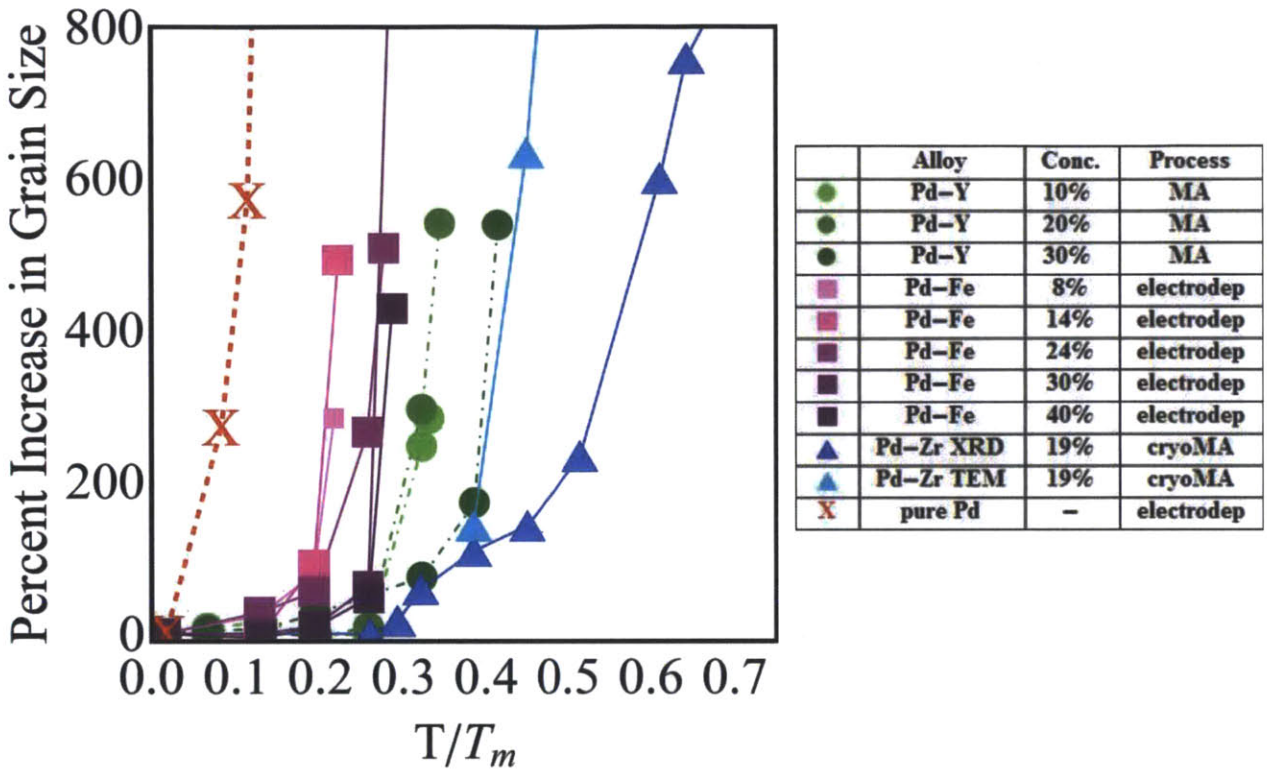

	Alloy	Conc.	Process
●	Pd–Y	10%	MA
●	Pd–Y	20%	MA
●	Pd–Y	30%	MA
■	Pd–Fe	8%	electrodep
■	Pd–Fe	14%	electrodep
■	Pd–Fe	24%	electrodep
■	Pd–Fe	30%	electrodep
■	Pd–Fe	40%	electrodep
▲	Pd–Zr XRD	19%	cryoMA
▲	Pd–Zr TEM	19%	cryoMA
X	pure Pd	–	electrodep

Figure 1.10 Grain growth in Pd alloys: pure nc-Pd** [15], **Pd-Fe [84, 85], Pd-Y [86], Pd-Zr [47].

Pd-Zr was mechanically alloyed [87] to produce several compositions, 10, 15, 19, and 20%Zr – thermal stability increased with zirconium composition. For the 20%Zr alloy, the grain size was maintained to 800°C ($0.51T_m$). Assuming some geometrical assumptions about the grain boundaries, a segregation enthalpy equal to elastic mismatch, and GB concentrations related to the lattice parameters, the authors showed a decrease in GB energy due to assumed Zr segregation. To test other reasons for stability, the authors deliberately increased the impurity contents (by increasing the sample's exposure to oxygen), creating observable ZrO_2 phase.

However, these extra impurities that would contribute to kinetic stabilization did not improve the stability – they actually decreased the stability, perhaps by disrupting the necessary segregation state. Kirchheim also found a reduction in GB energy in an analysis of nc-Pd-Zr data, concluding that GB stabilization via solute is at work, but that it did not render the material completely stable [88]. However, a reexamination of grain growth [47] in a Pd-19%Zr alloy indicated that, at higher temperatures (≥600°C, ~$0.3T_m$), XRD measurements of grain size were unreliable. Measurements using TEM are shown in Fig. 1.10 in cyan, in comparison to the XRD measurements in blue. Regardless of measurement technique, the alloy showed good stability up to $0.3T_m$.

Electrodeposited Pd-Fe [84, 85] of varying composition (8, 14, 24, 30, 40%Fe) was annealed for six hours, and the resulting grain growth is shown in Fig. 1.10. Iron was observed to leave the Pd lattice during annealing, and pre-annealing measurements exhibit slightly lower in-grain Fe content based on XRD measurements, supporting the idea of iron segregation to the grain boundaries. However, Fe_2O_3 was observed after annealing for the alloys with the highest stability (30%Fe and 40%Fe), possibly contributing to stability via kinetic pinning.

Mechanically alloyed Pd-Y alloys [86] exhibited phase separation at 400°C ($0.26T_m$) for 10%Y and 300°C ($0.19T_m$) for 20%Y, just prior to rampant grain growth. For an alloy of 30%Y, Pd_3Y is the predicted dominant equilibrium phase – it is visible after annealing at 200°C ($0.13T_m$); according to the phase diagram, it is likely the as-milled alloy was Pd_3Y as well, but without long range order.

1.3.2.8 Aluminum-based nanocrystalline alloys

It is difficult to evaluate the stability of aluminum-based alloys due to the lack of comparable pure nc-Al grain growth data. Nonetheless, we examine the reported thermal stability of several nc-Al binary alloys:

Al-Pb remained two-phase after extensive mechanical alloying [89] [90], and both aluminum-phase and lead-phase grain growth occurred. Atomistic modeling of Al-Pb alloys showed definite Pb segregation to grain boundaries, but also Pb clustering, depending on the concentration of lead [42-44]; no thermal treatments were applied to the model.

Cyro-milled Al-7.6Mg [91] showed steady grain growth (but remained nanoscale average grain sizes) for anneals at temperatures of 150-370°C (0.23-0.56T_m) for both times of both 2 and 60 minutes. Further examination of the microstructure revealed large, several-hundred nanometer-size, grains. In a lower magnesium content alloy, 4.8%, the thermal stability was evaluated with three hour anneals from 250-400°C (0.38-0.61T_m) [92]. At the lowest temperature anneal, the grain size had almost tripled (via XRD measurements).

Steady grain growth in mechanically-alloyed Al-25%W was followed by precipitation of Al_4W when the sample was annealed at 900°C [93].

Al-4.5%Cu was synthesized via mechanical alloying; the Al_2Cu phase precipitated at 160°C (0.24T_m) [94].

1.3.2.9 Other nanocrystalline alloys

An Ag-Cu alloy was examined as a companion to the Cu-Ag system described earlier [62]: the presented measurements are of Cu-phase size vs. annealing time, with temperatures beginning at 673K (0.54T_m). At this temperature, the Cu-Ag alloy had already phase separated –

therefore we assume that the Ag-20%Cu sample was also two phase. A gas-condensed alloy of Ag-5%Au was reported to have "basically the same" grain growth and activation energy as pure silver [7].

In a nanocrystalline Au-Ni alloy [95], phase separation began at 200°C ($0.19T_m$); at 400°C ($0.38T_m$) after a 1 hour anneal definite phase separation was observed. Nanocrystalline Au-Cu [96] was electrodeposited in concentrations of 4, 12, 14, and 18%Cu; 18%Cu had Au_3Cu phase visible via XRD at 483K ($0.36T_m$), and dissolved back to solid solution at 683K ($0.51T_m$), which follows the phases presented on the bulk phase diagram. All compositions showed grain growth at 483K, which was the lowest temperature tested [97].

In Y-Fe [98] for iron contents of less than 30%, the majority of iron was segregated to the GB – lattice measurements of Y showed the Fe was not in the matrix; the as prepared and annealed grain size decreased with increasing Fe content, culminating in amorphous alloys for Fe>45%. Precipitation of YFe_2 occurred around 350°C ($0.23T_m$); grain growth was not reported in this study after this precipitation.

Nanocrystalline Cr-Ni [99] was created via magnetron sputtering in argon in concentrations of 2% and 6%Ni. The Ni-rich phase precipitates at 773K ($0.36T_m$) in 6% after annealing 2 hours, and after 1000s at 973K ($0.46T_m$). Nanostructure stability was evaluated on the basis of microhardness analysis, not grain size measurement.

In a study on electrodeposited nanocrystalline Zn-Ni [80, 100], XRD scans were presented for annealing at 200°C ($0.11T_m$) for up to 24hrs, but the grain size was not measured or presented; the scans also show the precipitation of the $Zn_{11}Ni_2$ phase.

Nb-Cu was mechanically alloyed [101]: for compositions of less than 20%Cu, the material was one phase; at 25&30%Cu the study observed the copper-rich phase via XRD. The authors posit a metastable equilibrium between a saturated Cu GB and Nb grain, one that maintains a nanocrystalline grain size until copper-rich FCC phase precipitates from the grain boundary; for the 10%Cu alloy, significant growth occurred at 550°C ($0.22T_m$).

In mechanically alloyed W-30%Cu [66], the Cu-rich phase is visible in XRD after 1 hour annealing at 300°C ($0.09T_m$) – the Cu rich phase forms on the surface of the MA particles, supportive of segregation. After annealing at 400°C ($0.12T_m$) for 1 hour the grain size was was stable; rampant grain growth occurred after 600°C ($0.18T_m$).

1.3.3 Observations based on existing experimental and modeled systems

Reviewing the experimental studies, we find that the addition of an alloying elements generally lead to gains in stability. Examining Figs. 1.7-1.10 we see that the temperatures at which rampant grain growth begins in an alloy generally increases compared to the pure nanocrystalline material, in some instances by a significant fraction of the melting temperature. It is difficult to definitively attribute this improvement to thermodynamic stabilization as few studies managed a direct analysis of grain boundary segregation ([78, 102] [79, 103] [73] [81, 82] [25] [12, 57, 98]); however, additional support for a thermodynamic contribution to stability is found in the oft observed connection between grain size and solute content [12, 18, 29, 53, 82, 96, 98, 103-105], which indicates a system's preference for existing grain boundary sites for solute.

1.3.3.1 Solute selection: in theory vs. in practice

We attempt to connect experimental observations of stability to the expected effect of the alloying element on grain boundary energy via Eq. (1.2). Tables 1.1-1.3 rank the stability of

alloy systems in terms of their success in delaying the onset of rapid grain growth. Most authors' reading of Eq. (1.2) works under the assumption that a strongly segregating solute element (large ΔH^{seg}) will be effective at decreasing the grain boundary energy to zero. Since GB segregation science is incomplete, especially at the nanoscale, the alloy selection process has usually been based on qualitative ideas about the strength of grain boundary segregation ($\sim\Delta H^{seg}$) – atomic size mismatch [49, 98] or elastic enthalpy [58, 64, 87], solubility [48, 49, 58, 61, 73, 81, 106], or cohesive energy difference [12, 54, 101] . As seen in Tables 1.1-1.3, this approach has not been entirely successful – some alloys show exceptional stability despite low segregation [45, 70] or low expectations of segregation [26, 51, 62, 72, 75], while others with high expected segregation due to low solubility [54, 56] or high elastic enthalpy [53] do not show significant improvement in stability. In the nickel-based systems, all alloys have very low elastic mismatch enthalpies, but show some good improvement in stability

Table 1.1 Iron-based alloys ranked in order of experimentally observed thermal stability, from most delay in grain growth to least. Traditional metrics for predicting efficacy of solute for stabilization (elastic mismatch, radius difference, segregation strength via solubility) are shown for comparison to actual experimental stability. Thermal stability of alloys in italics are those not depicted on the grain size versus temperature curves.

Alloy	$\sim\Delta H^{seg}$		Δr [%]
	elastic	solubility	
Fe-Al	19	13	13.5
Fe-Ta	56	Large[1]	18.3
Fe-Ti	36	35	16.7
Fe-Mo	19	39	10.3
Fe-Zr	89	Large[1]	27
Fe-Ni	0.1	24	-0.8
Fe-Ag	26	Large[1]	14.2
Fe-Cr	1.6	25	3.2
Fe-Cu	0.3	32	1.6

[1] *Solubility is essential zero, so the* $Log[X_{sol}] \sim \Delta H^{seg}$ *is extremely large*

Table 1.2 ***Copper-based alloys ranked in order of experimentally observed thermal stability, from most delay in grain growth to least. Traditional metrics for predicting efficacy of solute for stabilization (elastic mismatch, radius difference, segregation strength via solubility) are shown for comparison to actual experimental stability. Thermal stability of alloys in italics are those not depicted on the grain size versus temperature curves.***

Alloy	$\sim\Delta H^{seg}$		Δr [%]
	elastic	solubility	
Cu-Zr	57	Large[1]	25.0
Cu-Nb	24	58	14.8
Cu-Pb	95	79	36.7
Cu-Fe	0.3	62	-1.6
Cu-Ag	15	41	12.5
Cu-Bi	63	88	32.8
Cu-Ta	31	65	16.4
Cu-Sb	37	37	24.2

[1] *Solubility is essential zero, so the* $Log[X_{sol}] \sim \Delta H^{seg}$ *is extremely large*

Table 1.3 ***Nickel-based alloys ranked in order of experimentally observed thermal stability, from most delay in grain growth to least. Traditional metrics for predicting efficacy of solute for stabilization (elastic mismatch, radius difference, segregation strength via solubility) are shown for comparison to actual experimental stability. Thermal stability of alloys in italics are those not depicted on the grain size versus temperature curves.***

Alloy	$\sim\Delta H^{seg}$		Δr [%]
	elastic	solubility	
Ni-Co	0	11	0
Ni-W	29	16	12
Ni-Fe	0.9	14	0.8
Ni-Mn	0.2	15	1.6
Ni-Cu	0.7	15	2.4
Ni-P	0.2	Large[1]	2.4
Ni-Zn	8	13	9.6

[1] *Solubility is essential zero, so the* $Log[X_{sol}] \sim \Delta H^{seg}$ *is extremely large*

1.3.3.2 Second phase precipitation problem

In an additional complication, the onset of rapid grain growth has been observed in many cases to coincide with observations of precipitated second phases [59, 66, 70, 75, 79, 81, 82, 90, 103, 107]. This suggests that a segregation state existed that provided a metastable nc-phase, one that was only stable with respect to changes in grain growth. However, this nanocrystalline state was not stable against phase separation; in some cases GB segregation aids second phase precipitation by providing high local concentrations of solute in the grain boundaries [81, 82, 103, 106, 108]. In these systems, the second phase precipitation disturbs the segregation state and can trigger rapid grain growth.

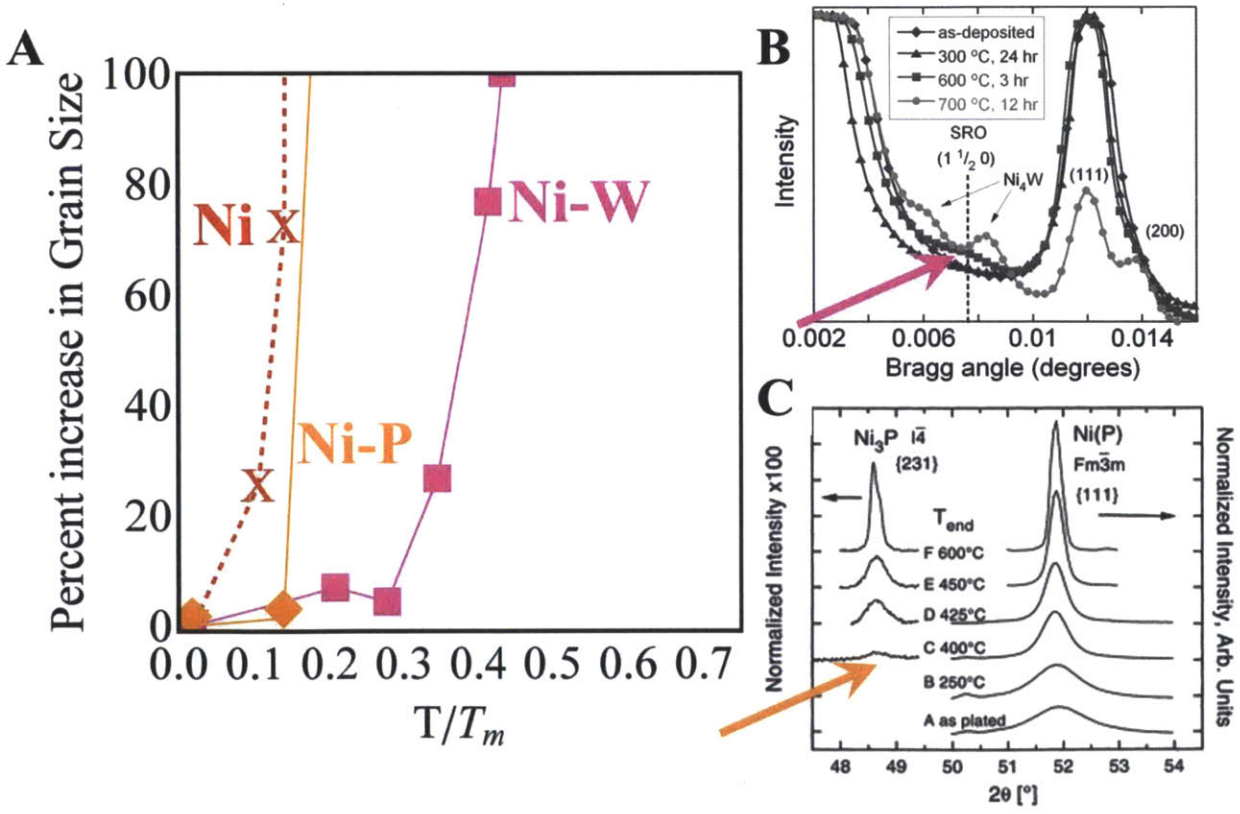

Figure 1.11 (A) Second phase precipitation connected directly to grain growth in two example nc-Ni systems; (B) Appearance of short range order in Ni-W heralding rapid grain growth. Figure from [78] (C)Appearance of Ni_3P phase triggering rapid grain growth, figure from [79]

Fig. 1.11 shows two such examples in the nc-nickel based systems: as previously mentioned, the appearance of short range order signifying the formation of Ni_4W coincides with the onset of rapid grain growth ~$0.3T_m$ (Fig. 1.11B). Similarly in Ni-P, the Ni_3P phase precipitation triggers rapid grain growth (Fig. 1.11C).

1.4 Research problem

The above studies using experiment and simulation have achieved varying levels of success on specific individual alloy systems; it is clear that alloying is a valuable direction for stabilizing nanocrystalline structures in metals. However, the total number of alloy systems studied is small, and there is not enough information to be able to extrapolate to other alloying elements in unexplored systems: this leads to the design challenge of this thesis, which centers on two questions:

(1) Stability against grain growth: are there combinations of solvent and solute where the segregation to the grain boundaries can lower the energy of the boundary to zero?

(2) Stability against phase precipitation: are there segregated configurations that lower the total free energy of the system below that of the expected bulk (coarse-grain) phases?

The first question is the one that has been most often discussed in literature, with researchers approaching alloy design with this question (and not question two) in mind. The second question addresses the larger, and more fundamental, issue of thermodynamic stability. As seen in this introduction, success in alloy stabilization via question one can be mitigated by phase separation. This thesis will examine the potential for segregated nanocrystalline alloys to be thermodynamically stable – not simply stable against grain growth, but also against phase precipitation.

2. Regular Nanocrystalline Solution Model

As detailed in the preceding chapter, the problem of grain growth in nanocrystalline metals has been approached through alloying – more specifically the idea that solute segregation to the grain boundaries can lower their interfacial energy [27-29, 109]. This approach centers on solute segregation strength and GB coverage, and aims to reduce grain boundary energy to zero, thus eliminating the propensity for grain growth. This reduction of GB energy has been the only examined consideration for nanocrystalline stability; however, in numerous experimental studies, precipitation of the thermodynamically favored non-nc-phase occurred and disrupted the segregation stability. These results show that the total energy (and not just GB energy) of the nanocrystalline system must be considered for complete stability of a nanocrystalline state. To this end, we look at the model developed by Trelewicz and Schuh [46] which was first used to examine the relationship between solute content and grain sizes stable against growth for some general systems. It is a statistical thermodynamic model that describes the effect of solute segregation and grain size on the free energy of a regular solution, hereafter referred to as the Regular Nanocrystalline Solution, or RNS model.

2.1 Construction of Free Energy function

At the nano-scale, the fraction of material that exists as grain boundary is increasingly significant; it can be represented by the following relation:

$$f_{gb} = 1 - \left(\frac{d-t}{d}\right)^D \qquad \textbf{(2.1)}$$

The GB fraction, f_{gb}, is a function of the grain size, d, the grain boundary thickness, t, and the dimensionality, D. The thickness is on the order of 0.5-1 nm [110] and the value of 0.5 nm will be used in this work (in accordance with [46]) unless otherwise indicated. Following this

relation, if the grain size of a nanocrystalline metal of interest is 10nm, the fraction of GB region is 14%. Accordingly, the RNS model defines both a traditional "crystal" region (c) which describes the crystal lattice in the grain interiors, and a GB region (gb) to describe the non-trivial fraction of material that is grain boundary; for an illustration, see Fig. 2.1. Solute can be apportioned between these two regions, satisfying the balance [111]:

$$X = f_{gb}X_{gb} + (1 - f_{gb})X_c \tag{2.2}$$

The global solute content, X, is distributed either in the grain interior (or crystal), denoted as X_c, or the grain boundary, X_{gb}.

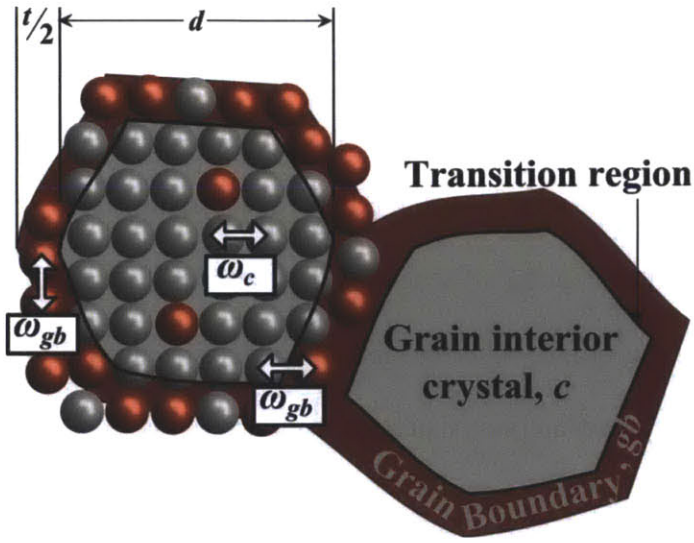

Figure 2.1 ***Schematic of two nanocrystalline grains with GB segregation, viewed equivalently as an array of atoms (left) or as a continuum (right). On the left, solvent atoms are in gray; solute, red. GB thickness, t, and characteristic size, d, are depicted on the left, as are the interaction parameters associated with the various bonds. Figure from [112].***

Table 2.1 ***Bonds in the RNS model***

Region	Number	Bond Energy	Probability	Bonds per region
Crystal (c)	N_c^{AA}	E_c^{AA}	$(1-X_c)^2$	$z/2(1-f_{ig})N_0$
	N_c^{BB}	E_c^{BB}	X_c^2	
	N_c^{AB}	E_c^{AB}	$2X_c(1-X_c)^2$	
Grain Boundary (gb)	N_{gb}^{AA}	E_{gb}^{AA}	$(1-X_{gb})^2$	$(z/2f_{ig} - zvf_{ig})N_0$
	N_{gb}^{BB}	E_{gb}^{BB}	X_{gb}^2	
	N_{gb}^{AB}	E_{gb}^{AB}	$2X_{gb}(1-X_{gb})^2$	
Transition	N_t^{AA}	E_{gb}^{AA}	$(1-X_c)(1-X_{gb})$	$zvf_{ig}N_0$
	N_t^{BB}	E_{gb}^{BB}	X_cX_{gb}	
	N_t^{AB}	E_{gb}^{AB}	$X_c(1-X_{gb})+X_{gb}(1-X_c)$	

The number, energy, and probability of atomistic bonds in the grain and grain boundary are quantified separately; additionally, bonds exist between the atoms in the grain and those in the grain boundary – these are termed transition bonds. These quantities are presented in Table 2.1, and illustrated in the left of Fig. 2.1. The spatial distribution of atomic bonds between the three regions (grain, GB, transition), the energies associated with creating grain boundaries, and region-weighted entropic considerations are encapsulated in the final free energy function derived from the model:

$$\Delta G^{mix} = (1 - f_{gb})\Delta G_c^{mix} + f_{gb}\Delta G_{gb}^{mix} + zvf_{gb}(X_{gb} - X_c)\left[(2X_{gb} - 1)\omega_{gb} - \frac{1}{zt}(\Omega^B\gamma^B - \Omega^A\gamma^A)\right] \quad (2.3)$$

The bond energetics are described by two interaction parameters: ω_c for the crystalline region and ω_{gb} for the boundary and transition region bonds. This parameter is defined by the following relationship of bond energies:

$$\omega = E^{AB} - \frac{E^{AA}+E^{BB}}{2} \tag{2.4}$$

The interaction parameter describing the GB region may or may not differ from that of the crystal, and its significance will be discussed further in later sections. Eq. (2.3) also includes a coordination number, z, grain boundary energy of the pure material, γ, atomic volume, Ω, (where subscripts A and B denote solvent and solute species respectively), and a transitional bond fraction ,v , which describes the fractional coordination of atoms which contribute bonds to the transitional bonding region.

The leading terms, ΔG_c^{mix} and ΔG_{gb}^{mix}, represent the bounds of the systems, defined by two regular solutions – if the material moves to the limit of infinite grain size ($d \rightarrow \infty, f_{gb} \rightarrow 0$), the material is entirely composed of grain interior, or crystal region:

$$\Delta G_c^{mix} = z\omega_c X_c(1 - X_c) + kT[X_c lnX_c + (1 - X_c)ln(1 - X_c)] \tag{2.5}$$

and the full free energy function reduces to a classical regular solution. In the opposite direction, that of the lower limit of grain size ($d \rightarrow t$), a *grain boundary* regular solution emerges which has a dependence on the energetics of pure grain boundaries in addition to standard regular solution terms:

$$\Delta G_{gb}^{mix} = z\omega_{gb}X_{gb}(1 - X_{gb}) + \frac{\Omega^A\gamma^A}{t}(1 - X_{gb}) + \frac{\Omega^B\gamma^B}{t}X_{gb} + kT[X_{gb}lnX_{gb} + (1 - X_{gb})ln(1 - X_{gb})] \tag{2.6}$$

This describes the free energy of a material which is entirely composed of "grain boundary". These two regular solutions are weighted by their respective volume fractions; the terms in Eq. (2.3) following the weighted regular solutions describe the transition region.

Minimization of the RNS free energy, Eq. (2.3), with respect to GB solute content, X_{gb}, and grain size at constant global solute, X, defines an equilibrium state wherein grain boundary energy is reduced to zero through solute segregation. A parametric study [46] showed some of the effects of the input parameters on the stable grain size resulting from segregation.

2.2 *The Free Energy Surface*

The best way to represent the equilibrium condition is as a free energy surface of the kind illustrated in Fig. 2.2. A surface exists for each global composition, X, and the free energy is plotted as a function of grain size (d) and GB concentration (X_{gb}). This surface is presented alongside the illustrations of the theoretical basis for GB-segregation stabilization depicted earlier in Fig. 1.4. A minimum in the free energy surface (Fig. 2.2B) represents a nanocrystalline structure at a particular pair value (X_{gb}, d) that is stabilized against grain growth – the alloy grain boundary energy is zero and the GB is ideally saturated with solute. The existence and location of this minimum in a given free energy surface depend upon the input parameters (interaction parameters, temperature, coordination, pure GB energy, global concentration). In many cases, the minimum is at infinite grain size (Fig. 2.2A), i.e., the lowest energy of the system falls back to that of a conventional regular solution (Eq. (2.5)), a trivial minimum. In the cases where a nanocrystalline minimum exists, the free energy surface also returns to the value of a regular solution at large grain sizes (as shown in the flattened free energy surface of Fig. 2.2B, replotted in Fig 2.2C to a longer length scale).

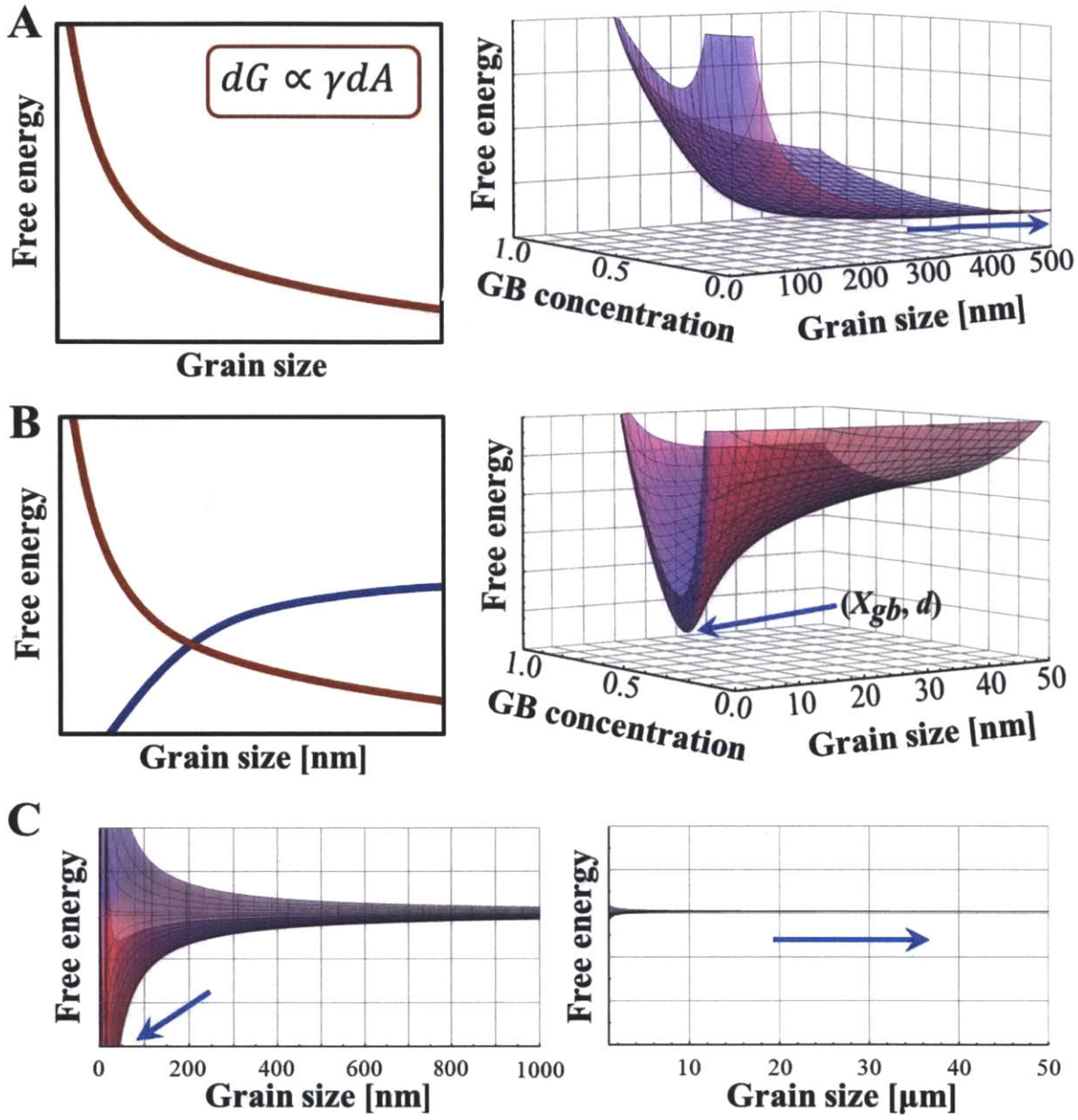

Figure 2.2 *(A) A schematic of the increase in free energy caused by a decrease in grain size, followed at right by a free energy surface reflecting the same; the free energy surface has a trivial minimum that falls back to the free energy of a regular solution (blue arrow), showing that segregation is not effective at lowering GB energy or total energy in this case. (B) Segregation can mitigate the effect of grain size on free energy via the schematic on the left, blue curve. This creates a minimum in the free energy surface, as seen at right, at a particular grain size and segregation distribution where the GB energy is zero. (C) In cases where there is a nanocrystalline minimum, the free energy at large grain sizes also falls back to the free energy of the regular solution, as shown in the flattened side view for the free energy surface in (B).*

2.3 *Comparison of Nanocrystalline Free Energies*

The nontrivial minimum in the free energy surface (Fig. 2.2B) represents the preferred grain size and solute distribution at a given composition, and a grain boundary energy of zero. This satisfies the first necessary stability condition, that of stability against grain growth, by eliminating the driving force for growth. The second condition, that of stability against phase precipitation, must be addressed by an analysis of the free energies of other possible phases and configurations. It is noted in the previous section (2.2) that, in the case of a trivial minimum (preferred grain size is infinite), the free energy returns to the value of a regular solution. Of interest and importance is the question of the free energy for cases in which a stable nanocrystalline minimum exists.

A comparison of the free energy surfaces for two compositions X- and X+ within the same system (i.e. all other model input parameters are the same) is made in Fig. 2.3. Each composition has its own preferred grain size and segregation state (X_{gb}-,d-) and (X_{gb}+,d+) respectively. If the grain size and GB solute content satisfying the equilibrium condition for one composition are maintained while the global composition, X, is varied, the free energy will necessarily change. In the case of decreasing composition from X+ to X- while maintaining X_{gb}+ and d+, the free energy increases rapidly, as indicated by the blue arrow A on Fig. 2.3. It is noted that this sharp increase in free energy in response to a small change in composition is similar to the behavior of a stoichiometric line compound. In the reverse direction, that of increasing composition from X- to X+ and maintaining X_{gb}- and d-, the free energy is lowered; however, the free energy can be lowered still by heading to the X+ minimum values of X_{gb}+ and d+ (green arrow B on Fig. 2.3).

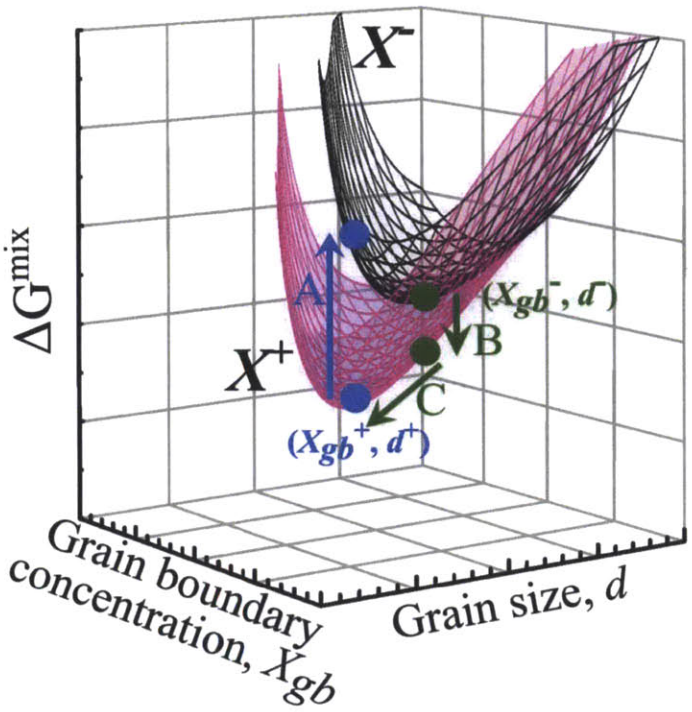

Figure 2.3 ***Minima in the free energy surface for two global solute concentrations, X+ (magenta curve) and X- (black curve). Arrow A (blue) describes the rapid increase in free energy from holding the minimum X_{gb}+ and d+ values constant, while decreasing global composition X+ → X-. In the other direction, arrow B (green) shows the decrease in free energy from holding X_{gb}- and d- constant while increasing global composition X- → X+; however, the free energy can be reduced further (arrow C) by falling to the (X_{gb}+,d+) minimum. Figure from [112].***

A perhaps more intuitive visualization is to plot the variation of free energy with respect to only global solute concentration while holding constant values of X_{gb} and d for a given minimum. In Figure 2.4, the minima of the X+ and X- composition surfaces are denoted by the points on the solid magenta and dashed black curve respectively; the solid magenta line illustrates the free energy variation with composition for the minimum (X_{gb}+,d+) pair, while the dashed black line depicts the same for the (X_{gb}-,d-) minimum. Minima from additional composition surfaces are signified by blue points. As in the free energy surface depiction in Fig. 2.3, lowering the composition while maintaining (X_{gb}+ , d+) leads to a rapid increase in free energy. In the opposite direction, the free energy of a different ($X_{gb,}$ d) minimum pair is lower,

and favorable. In Fig. 2.4B, it is shown that the GB energy of the material is zero at the minimum pair values for the respective compositions. In support of the propensity to decrease from grain size from *d*- to *d*+ concurrent with an increase in global composition (*X*- to *X*+), the grain boundary energy is negative in this situation, which would indicate a driving force for grain shrinkage. The blue line connecting the minima is a common tangent to all the nanocrystalline minima – ergo, the chemical potential is the same in all possible nanocrystalline states.

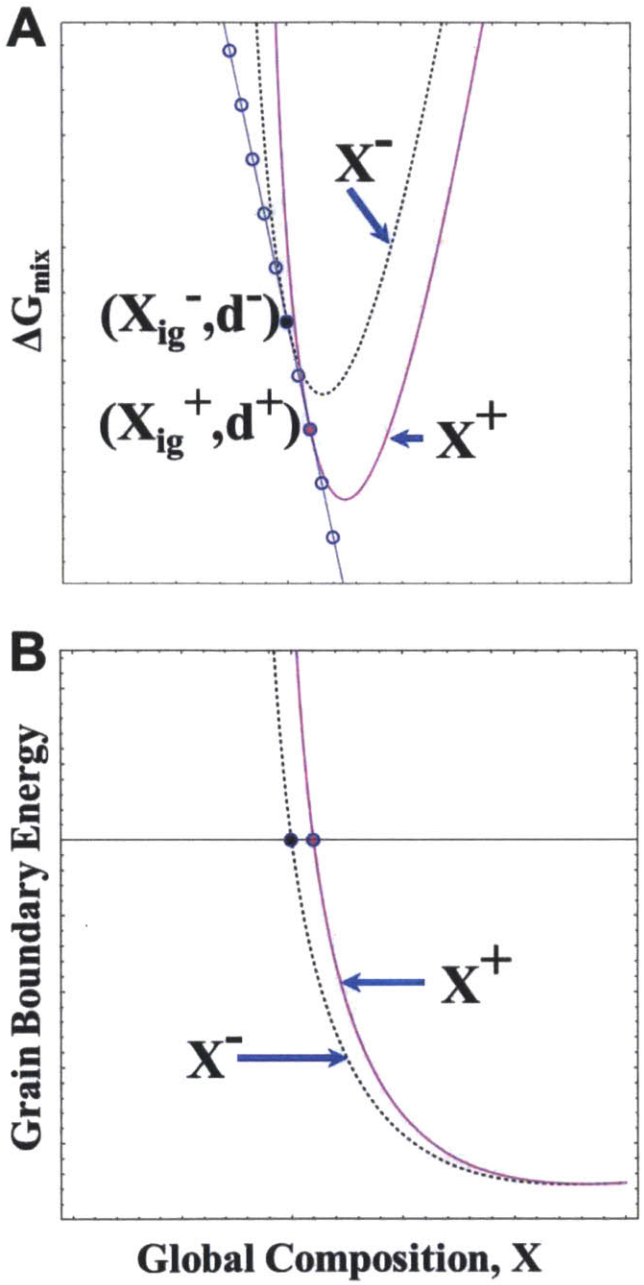

Figure 2.4 (A) The minimum (X_{gb}, d) points from the two compositions presented in Fig. 2.3 are presented by black (X-) and magenta (X+) points; minima of other compositions are presented by blue points. The variation in free energy with respect to changes in composition while maintaining (X_{gb}, d) of the minima are plotted as a black, dashed curve for X- and magenta curve for X+. The GB energy as a function of this variation is shown in (B).The GB energy is zero at the minimum (X_{gb}, d) pair. Figure from [112].

2.4 *Complete Free Energy Picture*

Now that the nanocrystalline phase can be represented as a "stoichiometric" line compound as developed above, it can be compared to other possible nanocrystalline and most importantly to non-nanocrystalline (expected) bulk phases. First, and simplest, is the comparison with a classical, symmetric regular solution with positive enthalpy of mixing – one that defines a miscibility gap between solvent-rich and solute-rich solid solutions. A representative free energy curve for this type of bulk system is shown in Fig. 2.5 as a solid black curve. At the temperature represented by this plot, a miscibility gap exists, and its two-phase region is defined between the tangent points of the dashed black common tangent line. This common tangent defines the lowest energy phases in the bulk system; the addition of possible nanocrystalline phases (shown by their minimum points on the narrow U-shaped free energy curves as in Fig. 2.5) necessitates a re-examination of this two-phase boundary. If no nanocrystalline minimum exists at the given composition, the system free energy falls back to that of the bulk solid solution, indicated by the red nanocrystalline "not stable" point. When a minimum does exist, its free energy could fall into two categories: "metastable" – stable against grain growth (segregation brings GB energy to zero) but not against second phase precipitation, as its free energy is higher than the bulk equilibrium common tangent, or, the nanocrystalline phase could be "stable" – a complete stability, against both grain growth and the expected bulk phase separation.

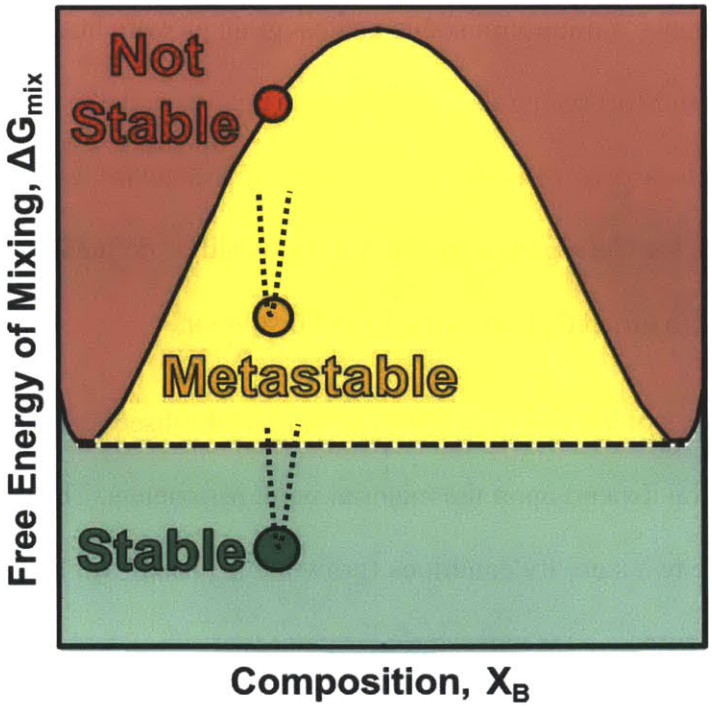

Figure 2.5 ***The free energy of the nanocrystalline phases, as represented by their minimum point and the U-shaped curve, can be stable (green), metastable (yellow), or not stable (red) compared to the free energy of the bulk phase. In this case, that of a system with a miscibility gap, the stable phases are denoted by the common tangent (dashed black line) of the regular solid solution (solid black line).***

In the case of a miscibility gap, or positive ΔH^{mix} system, the free energy of the nanocrystalline phase(s) must be evaluated only against the common tangent of the solid solution. In these systems, as depicted by the schematic in Fig 2.5, the NC-phase is metastable when its free energy is above that of the common tangent, and stable when below. The case of a negative ΔH^{mix}, or compound forming system is more complex. Pictured in Fig. 2.6 is an example schematic of a free energy plot for a simple compound-forming system, with only one intermetallic. The solid solution is again depicted as a solid black curve, and the introduced ordered bulk phase, here A_3B, is drawn as a line compound. The region of metastability is then redefined by the common tangent between two distinct, separate phases – the solid solution and the compound A_3B. Additionally, a region of "local metastability" is expected wherein the free

energy surface contains a minimum stable against grain growth, but its free energy is above that of the solid solution. Most materials systems with negative enthalpy of mixing have more than one intermetallic phase; the methodology for stability and metastability would follow the same scheme as Fig. 2.6, but the region of metastability would be defined by the common tangents between the multiple ordered phases and the solid solution.

The existence of a nanocrystalline minimum and subsequently its position vis-a-vis the bulk regular solution depend upon the material input parameters. The relationship between these parameters and the two stability condtions (growth and phase) will be discussed in the next chapter.

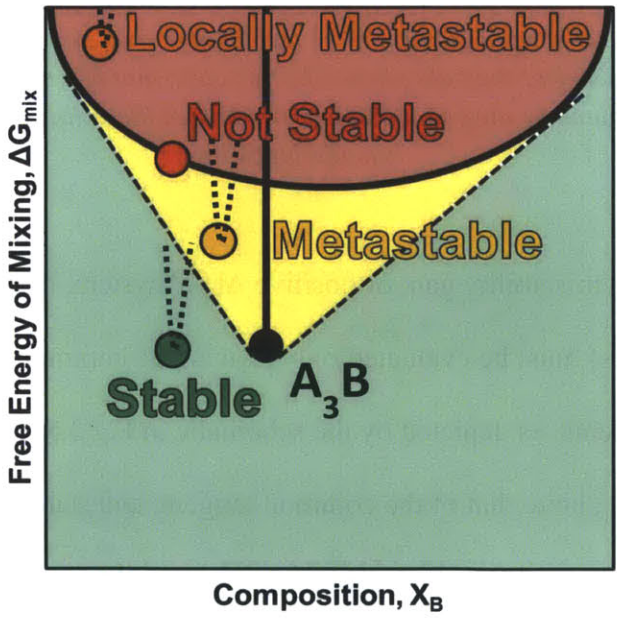

Figure 2.6 ***The free energy of the nanocrystalline phases, as represented by their minimum point and the U-shaped curve, can be stable (green), metastable (yellow), or not stable (red) compared to the free energy of the bulk phase. In the case of a system with an ordered compound (denoted A_3B, and by a solid black point), the stable phases are those whose free energy falls below the common tangent (dashed black line) of the regular solid solution (solid black line) and the line compound.***

2.5 *Conclusions of this Chapter*

A derived free energy of a segregated nanocrystalline solution [46] was previously used only for examination of stability against grain growth ($\gamma \rightarrow 0$). The formalism required for using the RNS model for the second nanocrystalline stability condition, that of stability against second phase precipitation, is developed. If an appropriate segregation state exists, the free energy surface for a given composition can present a minimum in the nanocrystalline regime; this minimum represents stability against grain growth, its free energy in comparison with other expected phases via the methodology presented here describes stability vis a vis phase precipitation/separation.

3. Conditions for Complete Nanocrystalline Stability

Both the existence of a minimum in the nanocrystalline space of a free energy surface and its location depend upon the input parameters to the RNS model, namely: the two interaction parameters ω_c and ω_{gb}, coordination number, pure grain boundary energies and atomic volumes, transitional fraction ν, temperature, and composition. An alloy's stability against grain growth (free energy surface minimum) and stability against phase separation (free energy of the NC minimum relative to other phases) are evaluated with respect to these parameters

3.1 Positive Enthalpy Systems

3.1.1 Symmetric systems (Equal Ωγ/t)

For simplicity, in the first systematic study the combination of atomic volume and grain boundary energy, divided by the grain boundary thickness, $\Omega\gamma/t$, (which always appear as a unit in the RNS equation) of solute and solvent will be set equal; the terms in the free energy equation containing this quantity are generally on the order of a tenth the magnitude with respect to other terms, and less when they appear together as a difference [112]. The value of this quantity will be set as 8.25 kJ/mol for both species (values for some common metals are, aluminum: 6.5, gold 7.7, copper 8.9, iron: 10.6, and nickel: 11.5), which corresponds, as an example, to a GB energy of 0.5 J/m^2, an atomic volume of 8.25 cm^3/mol, and a GB thickness of 0.5 nm.

Additionally, the first study will be of phase separating systems, which limits the possible precipitating non-nanocrystalline phases to two – the A-rich and B-rich solid solutions. These systems have a positive enthalpy of mixing, which correlates directly to the bulk, or crystal, interaction parameter ω_c. The grain boundary interaction parameter, ω_{gb}, describes the character of atomic interactions in the GB and transition regions, and in general will be different than that of the bulk crystal, as it describes the driving force for segregation [46]. A characteristic

temperature of positive ΔH^{mix} systems is that of the apex of the miscibility map, or T_{cr}. This critical temperature is a direct relation to ω_c ($T_{cr}=z\omega_c/2R$, when the system is described by a regular solution model); as this temperature can be related to other parameters, it simplifies the design space.

The predominant metrics, ω_c and ω_{gb}, are then varied. For each pair of (ω_c, ω_{gb}), a free energy surface is calculated for 100 global solute compositions across the full range (X= 0 to 1, in increments of 0.01), and the minimum found, if it exists. The existing minima are plotted with respect to each other and the solid solution of the same ω_c for ΔG vs. global composition, X. The comparison of Fig. 2.4 is made for the (ω_c, ω_{gb}) system and classified as either "stable nanocrystalline" (green), "metastable nanocrystalline" (yellow), "or "nanocrystalline not supported" (red). Figure 3.1 illustrates the result of this series of calculations for an example (ω_c, ω_{gb}) space.

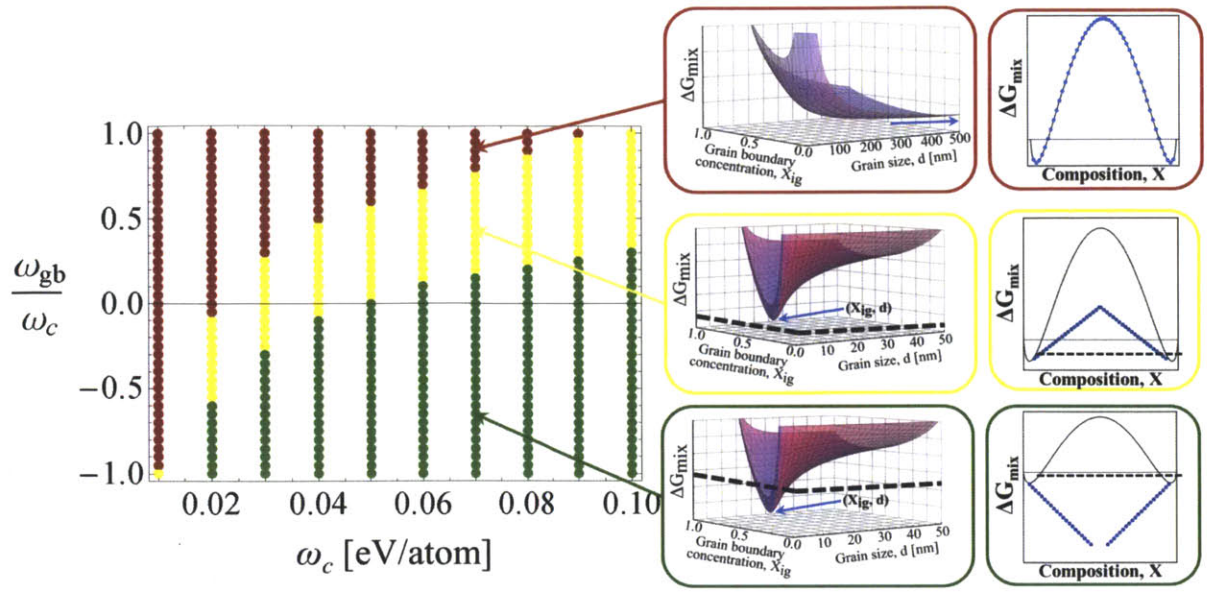

Figure 3.1 Example map of parameter combinations in the (ω_c , ω_{gb}) space – each point represents the full composition range for that parameter set, an example shown on the far right for each of three possibilities – not stable (red) , metastable (yellow), and stable (green). Each blue point is the minimum for that composition's free energy surface, shown to the left of the free energy – composition plot. For metastable cases, the minimum falls above the common tangent of the regular solution (represented by black dashed line); stable, below it.

Through the thousands of individual calculations conducted to create a map as in Fig. 3.1, the conditions for a stable nanocrystalline alloy can be discerned; however, while the parameter ω_c is a familiar one (common to regular solution models), ω_{gb} is an unknown metric and requires more discussion.

3.1.2 Recasting of axes

As mentioned previously, many of the inputs are observable materials quantities (i.e. z, γ, Ω) or can be directly related to known quantities; for example ω_c to the enthalpy of mixing in a regular solution:

$$\Delta H^{mix} = z\omega_c X_A X_B \tag{3.1}$$

However, the GB interaction parameter, ω_{gb}, must be interpreted; it is similar in concept to a Fowler-Guggenheim [113, 114] type parameter, which accounts for the effect of solute-solute GB interactions on segregation, but the F-G parameter is quantified by fitting experimental data.

In the RNS model, the segregation enthalpy is expressed as:

$$\Delta H^{seg} = z\left[\omega_c - \omega_{gb}\left(1 - \frac{\nu}{1-f_{gb}}\right) - \frac{1}{zt}(\Omega^B\gamma^B - \Omega^A\gamma^A)\left(1 - \frac{\nu}{1-f_{gb}}\right)\right] + 2zX_{gb}\omega_{gb}\left(1 - \frac{\nu}{1-f_{gb}}\right) - 2z[X_c\omega_c + \nu(X_{gb} - X_c)\omega_{gb}] \quad (3.2)$$

defined by recasting the stability condition dG/dX_{gb} in a segregation isotherm:

$$\frac{X_{gb}}{1-X_{gb}} = \frac{X_c}{1-X_c} exp\left[\frac{\Delta H^{seg}}{kT}\right] \quad (3.3)$$

Simplifying the relation of Eq. (3.2) to the dilute limit, we distil the enthalpy to its essential characteristic parameters:

$$\Delta H_0^{seg} = z\left(\omega_c - \frac{\omega_{gb}}{2} - \frac{(\Omega^B\gamma^B - \Omega^A\gamma^A)}{2zt}\right) \quad (3.4)$$

Although the enthalpies of mixing, Eq. (3.1) and grain boundary segregation, Eq. (3.4) share terms associated with the bulk interaction parameter, the grain boundary interaction parameter is considered an independent quantity here, and only contributes to the heat of grain boundary segregation; the two parameters thus can be cast as the new axes of the design space, as shown in Fig. 3.2. While in general the mixing parameters ω_c and ω_{gb} are more fundamental to the RNS model, these enthalpy axes are more physically familiar, and therefore likely more useful in placing specific binary alloy systems on the stability map landscape.

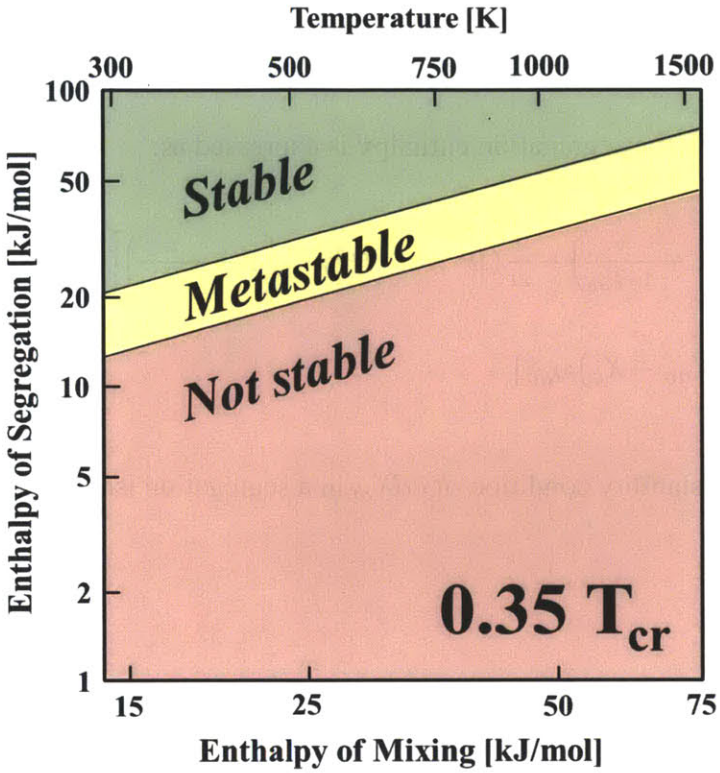

Figure 3.2 ***Design map for the fraction 0.35 of critical temperature (absolute temperature shown across top) with enthalpic axes. Regions of stability are denoted by color (green: stable, yellow: metastable, red: not stable) and label.***

3.1.3 Delineations of Stability Regions

The regions separating stability, metastability, or non-stability of a nanostructured alloy system are demarcated by straight lines in the double-logarithmic space of Fig. 3.2, empirically captured by the following relationship:

$$\frac{\Delta H^{seg}}{\left(\Delta H^{mix}\right)^{a}} = c \qquad (3.5)$$

where ***a*** is the power-law slope, and ***c*** reflects the intercepts. Both of these are in general a function of temperature; for the map presented in Fig. 3.2, T = 0.35 T_{cr}; for other temperatures

investigated thus far (see Fig. 3.3), the map has the same basic form, but with shifted boundaries reflected in the different fitted values of ***a*** and ***c***.

The relationship of Eq. (3.5) can be used as a figure of merit for nanostructral stability in positive mixing enthalpy systems and it, along with the stability maps, show that the interplay between grain boundary and bulk segregation as controlling the ability to stabilize a nanocrystalline phase.

3.1.4 Temperature

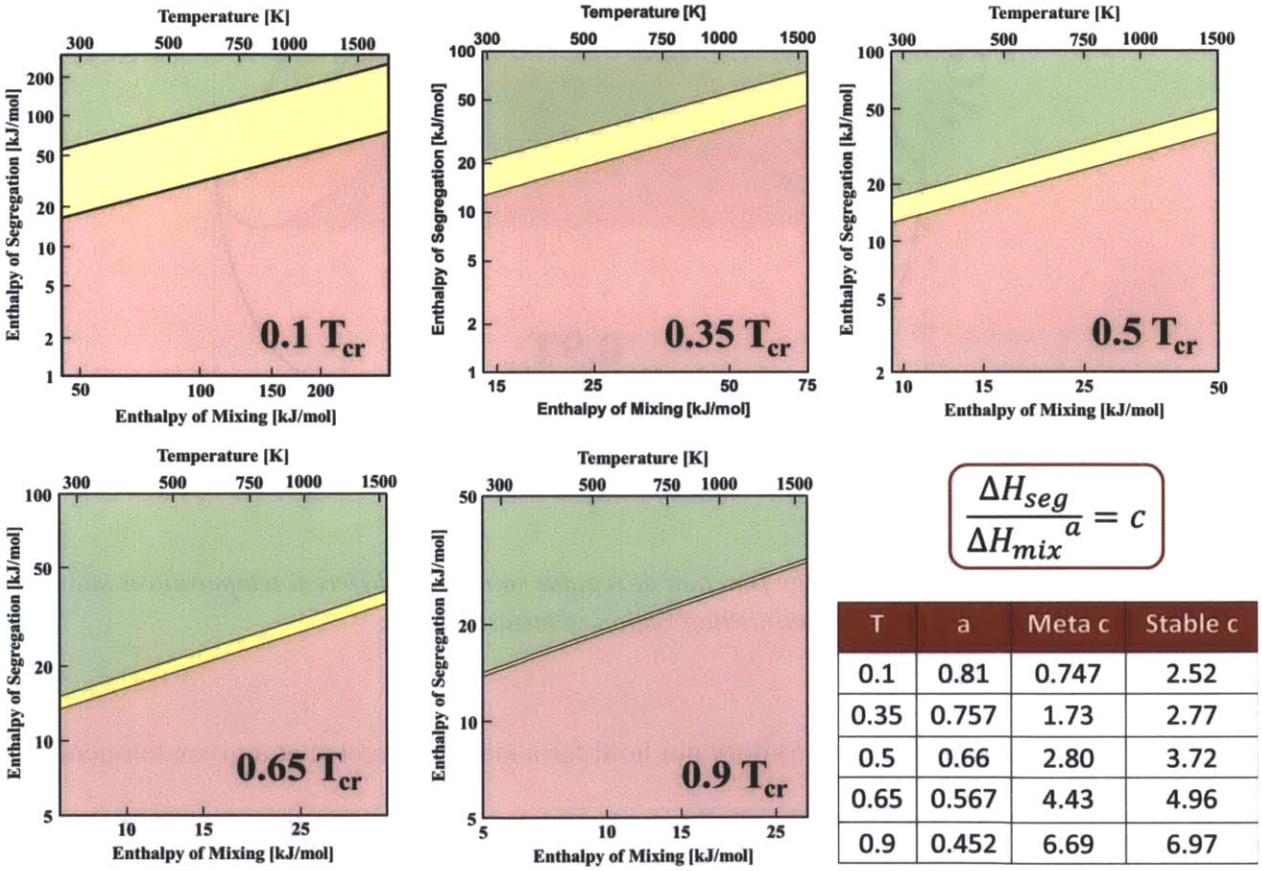

T	a	Meta c	Stable c
0.1	0.81	0.747	2.52
0.35	0.757	1.73	2.77
0.5	0.66	2.80	3.72
0.65	0.567	4.43	4.96
0.9	0.452	6.69	6.97

Figure 3.3 ***Nanocrystalline stability maps and their accompanying figure of merits for five fractions of the critical temperature.***

Higher fractions of the critical temperature signify a smaller two-phase region in the miscibility gap; this in turn decreases the potential free energy space for metastable nanocrystalline alloys (Fig. 3.4).

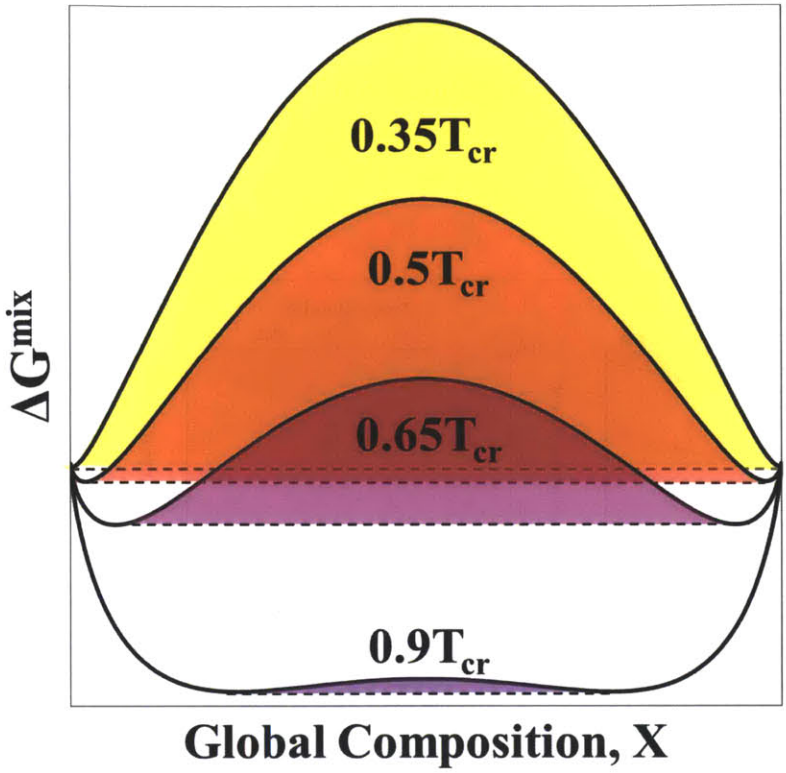

Figure 3.4 ***Free energy function of regular solution at different temperatures showing diminishing region of metastability.***

The relationship of Eq. (3.5) does not hold for a map constructed at a given temperature, here 1000K (Fig. 3.5). A linear ratio of enthalpies still defines the existence of a NC minimum (not stable vs. meta- or complete stability). The decreasing region of metastability (a la Fig. 3.4) is also reflected in this absolute temperature map.

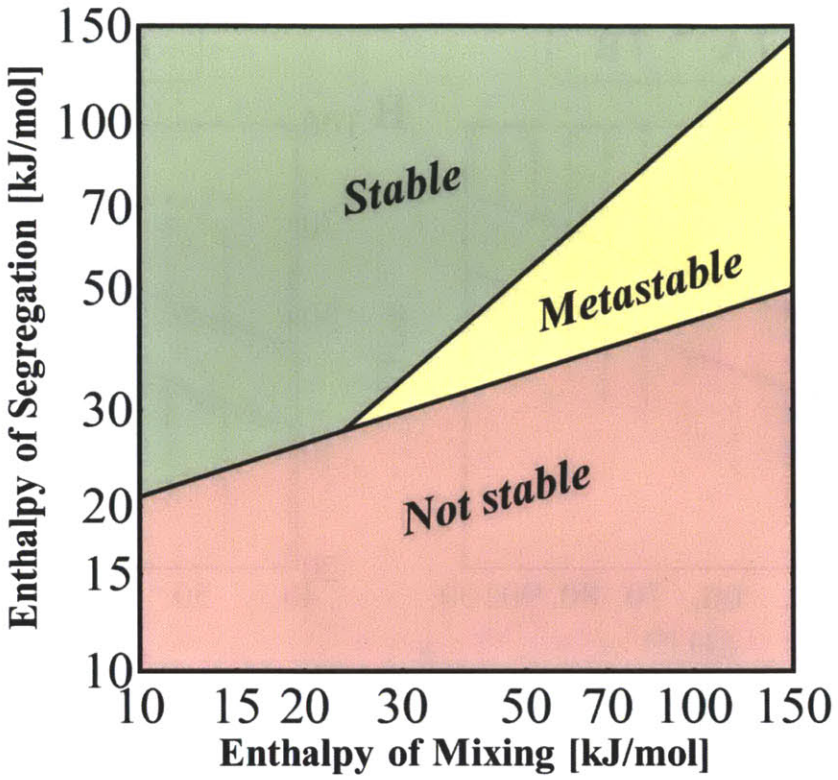

Figure 3.5 Stability map for 1000K, $\Delta H^{mix}>0$.

3.1.5 Non-symmetric (Unequal Ωγ/t)

The above results were for the condition $\Omega_A\gamma_A = \Omega_B\gamma_B$, that is, that the combination of atomic volume and GB energy for the solvent and solute species were equal. Figure 3.6 depicts two maps for the temperature $0.5T_{cr}$ where this equality is not assumed. The dashed black lines indicated the figure of merit demarcations from the case of $\Omega_A\gamma_A = \Omega_B\gamma_B$, shown in Fig. 3.3. For the case of the solvent having a lower combination of GB energy and atomic volume, these lines are also a reasonable fit for the regions of stability, metastability and no stability; a better fit is shown in purple, and the comparison of constants ***a*** and ***c*** are shown in Table 3.1

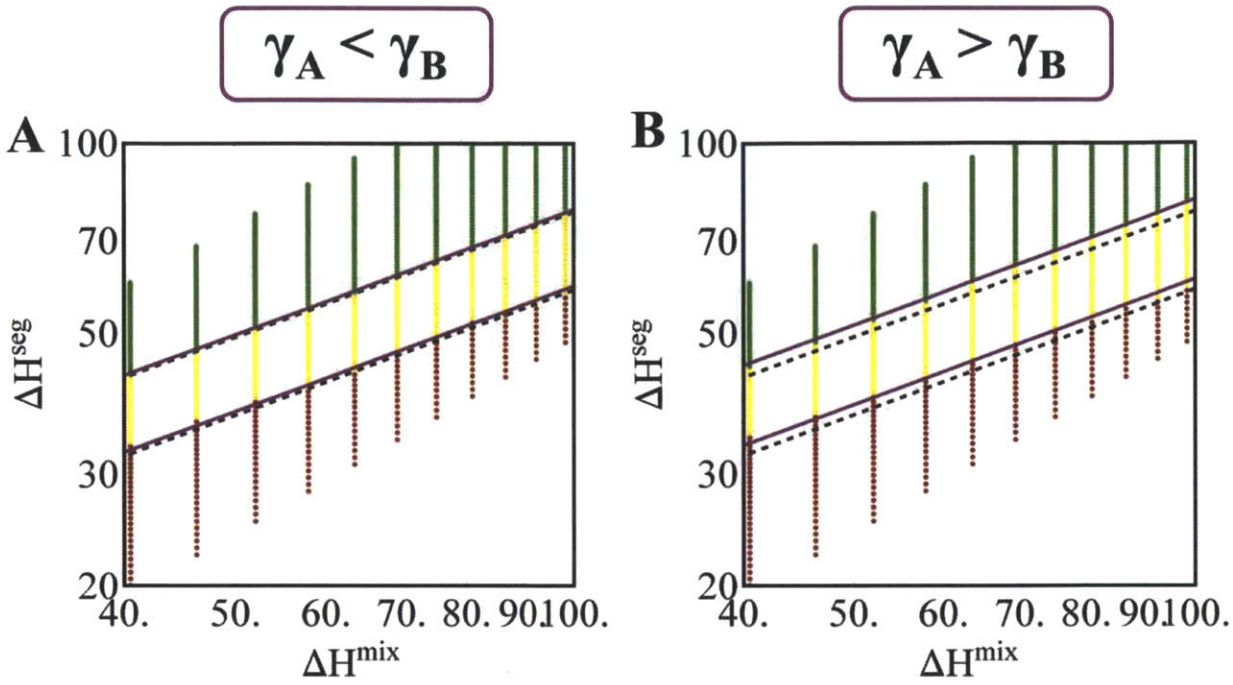

Figure 3.6 ***Stability maps for $\Omega_A\gamma_A \neq \Omega_B\gamma_B$. (A) the GB energy – atomic volume constant for the solvent is lower than that of the solute (B) the GB energy – atomic volume constant for the solute is lower.***

Table 3.1 ***Constants for the Stability Figure of Merit when $\Omega_A\gamma_A \neq \Omega_B\gamma_B$***

	a	*c* not stable	*c* stable
$\Omega_A\gamma_A = \Omega_B\gamma_B = 0.085$	0.66	2.80	3.72
$\Omega_A\gamma_A = 0.085 < \Omega_B\gamma_B = 0.1$	0.66	2.84	3.75
$\Omega_A\gamma_A = 0.1 > \Omega_B\gamma_B = 0.085$	0.66	2.91	3.89

The GB energy of the solvent is more important to the condition of total stability than that of the solvent (Fig. 3.6A), not surprisingly, as it is the quantity that needs to be lowered to zero for the first stability criteria. Increasing the GB energy of the solvent relative to that of the solute raises the threshold for meta- and complete stability (Fig. 3.6B). The slope, ***a***, or the power to which the enthalpy of mixing is raised, remains constant across the $\Omega\gamma$ inequality conditions as the

difference in GB energies only affects the segregation strength, not the conditions of bulk mixing.

3.2 *Negative Enthalpy of Mixing*

As in positive enthalpy of mixing maps, the (ω_c, ω_{gb}) pairs are the predominant variation, and stability for full composition ranges for each set of parameters is cast in terms of the enthalpies of mixing and segregation via Equations (3.1) and (3.4). However, in the case of compound forming systems, there is no characteristic temperature that can be related to the other RNS model inputs as in the case of the miscibility apex. A negative enthalpy of mixing map will then be constructed only for an absolute temperature.

The most challenging aspect of evaluating the stability conditions in $\Delta H^{mix} < 0$ systems is the comparison of the free energy of the nanocrystalline phase with the bulk ordered compound(s). In positive mixing enthalpy systems, the competing phases were described by solid solution model which depends directly on ω_c, which is also an input to the RNS model. This made phase comparison a relatively simple process, as all the phases could be generated with the same parameter inputs for a given system. Conversely, the intermetallics in compound-forming systems cannot be described by the same input parameters. For example, the common $L1_0$ compound must be defined in terms of both ω_c, which is a collection of the energies of A-A, B-B, and A-B bonds, *and* the energies of the pure A-A and B-B bonds (Ex: [115]). There is no analogous parameter in the RNS model for only bulk E_{AA} and E_{BB} bonds, separate of E_{AB} (in ω_c) or grain boundary bonds ($\gamma \propto E_{bulk}^{AA} - E_{gb}^{AA}$). Unfortunately, this means that the compounds cannot be naturally integrated into the existing axes of the stability map, as produced for a simple solid solution in positive mixing enthalpy systems.

The comparison will instead be made to an absolute value of free energy for a compound phase, divorced from specific structural considerations; this has the advantage of allowing representation of numerous types of intermetallic compounds at the same composition by the same stability metric, regardless of their specific crystal structure. For example, an intermetallic of energy -30 kJ/mol of stoichiometry A_3B could be of any type structure, depending upon binary alloy system, but all represented by the same metric on a stability map (Fig. 3.7A). Depending on the free energy of the compound, a nanocrystalline state that is stable with respect to a solid solution of the same parameters (z, ω_c) will be completely or meta- stable (Fig. 3.7). A NC phase that is stable against a solid solution (thick black line) may be completely stable in an alloy system that has a A_3B compound with a free energy of -30 kJ/mol (Fig. 3.7A), but in a system with a compound energy of -50 kJ/mol, this same phase would be metastable (Fig. 3.7B).

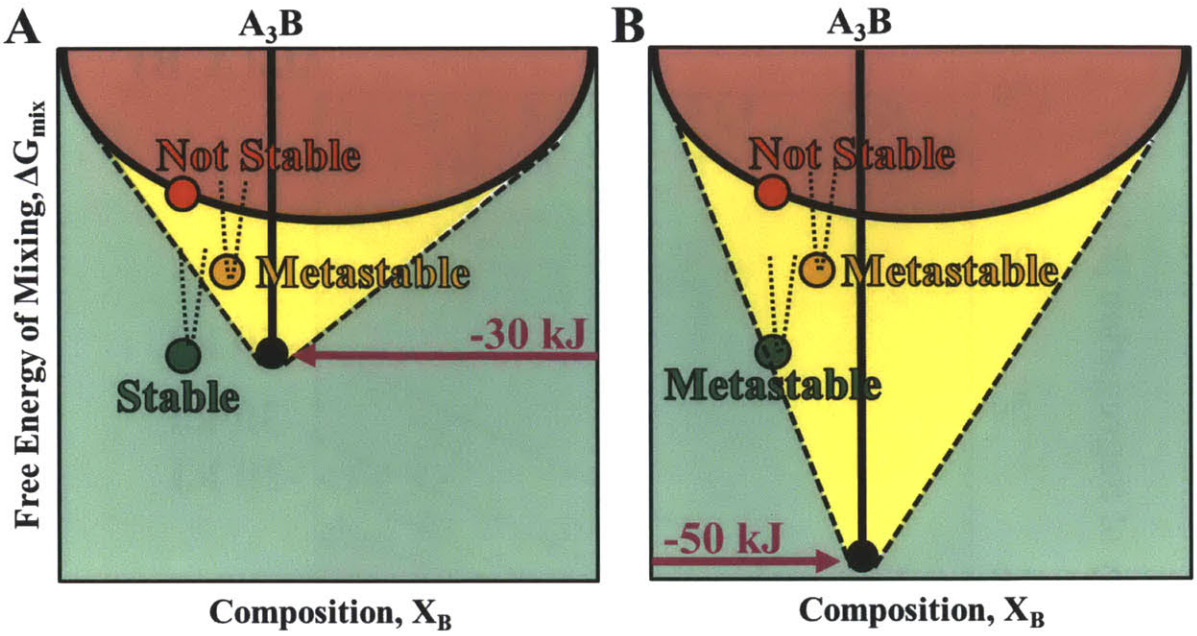

Figure 3.7 ***Comparison of free energy for stability conditions in a compound forming system. Both plots have a A_3B compound in the system in addition to a solid solution (thick black curve), but in the schematic (A), the compound has a free energy of -30 kJ/mol, as compared to -50 kJ/mol in (B). A NC phase that is stable in (A), as depicted by green dot, is no longer stable in (B) due to the lower free energy of the A_3B compound.***

The comparison of Fig. 3.7 is made for a variety of parameters and tabulated in a nanocrystalline stability map in Fig. 3.8. The region of nanocrystalline metastability grows as the free energy of the compound lowers.

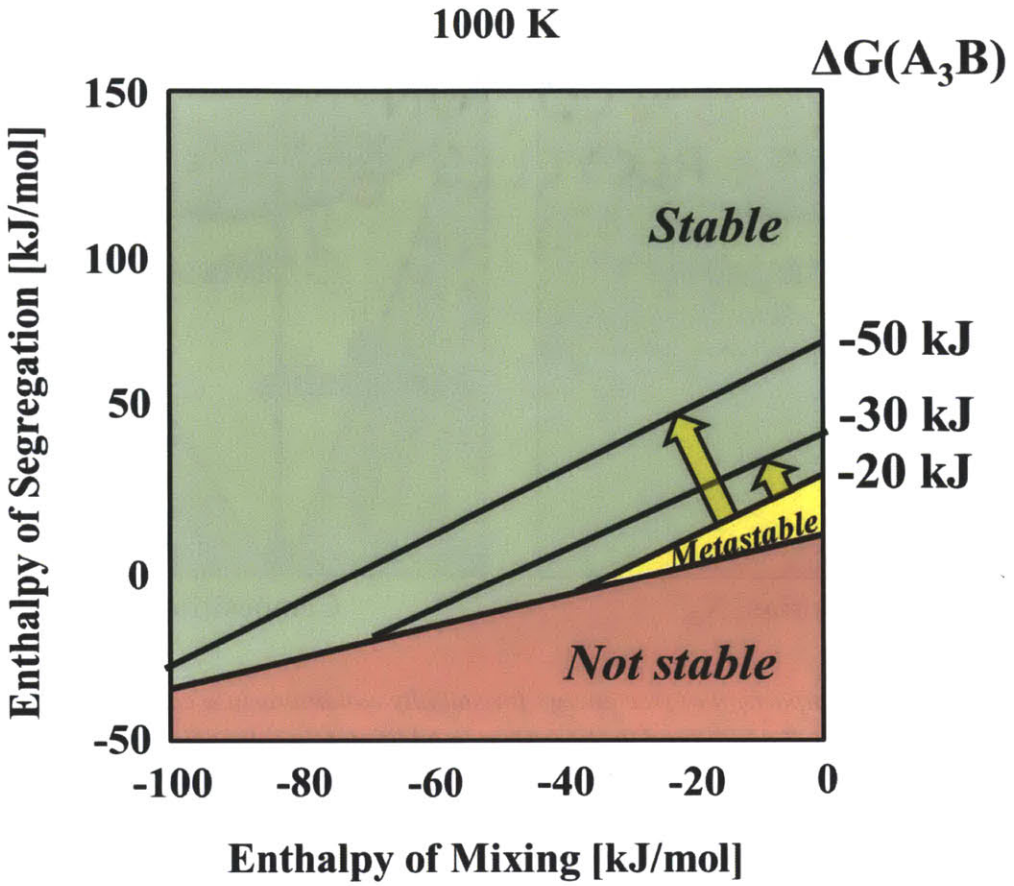

Figure 3.8 Stability map for Negative mixing enthalpy systems at 1000K. The region of metastability is defined by the free energy of the A_3B intermetallic compound, listed on the right of the stability map.

3.3 Types of Stable Nanostructures Predicted

Since the desired outcome of this work is to predict stable nanocrystalline alloys, the region of stability is examined in more detail. Notably, the expected grain boundary-segregated single nanocrystalline phases state only represents a small sliver of the design space; several new types of stable nanostructures are identified through this look at nanocrystalline segregation and free energy, and they are discussed in this chapter.

3.3.1 "Classical" Stable Nanocrystalline

The type of segregation-stabilized nanostructure envisioned by Weissmuller [27, 28] and Kirchheim [29, 109], and discussed in literature is that of a solvent-rich grain with the GB decorated by solute in an appropriate quantity (Recall Fig. 2.1). This type of nanostructure is only observed for the combinations of high positive enthalpies of both mixing and segregation, such that the GB interaction parameter approaches ideal behavior, ω_{gb}~0; a very small swath of the stable nanocrystalline region, as will be shown later in Fig. 3.14. This stability behavior will be named "classical" stability, and the free energy plot of a representative parameter set is shown in Fig. 3.9. The blue points are the nanocrystalline "compounds" and their free energy, like their grain size (Fig. 3.10), decreases as solute composition increases.

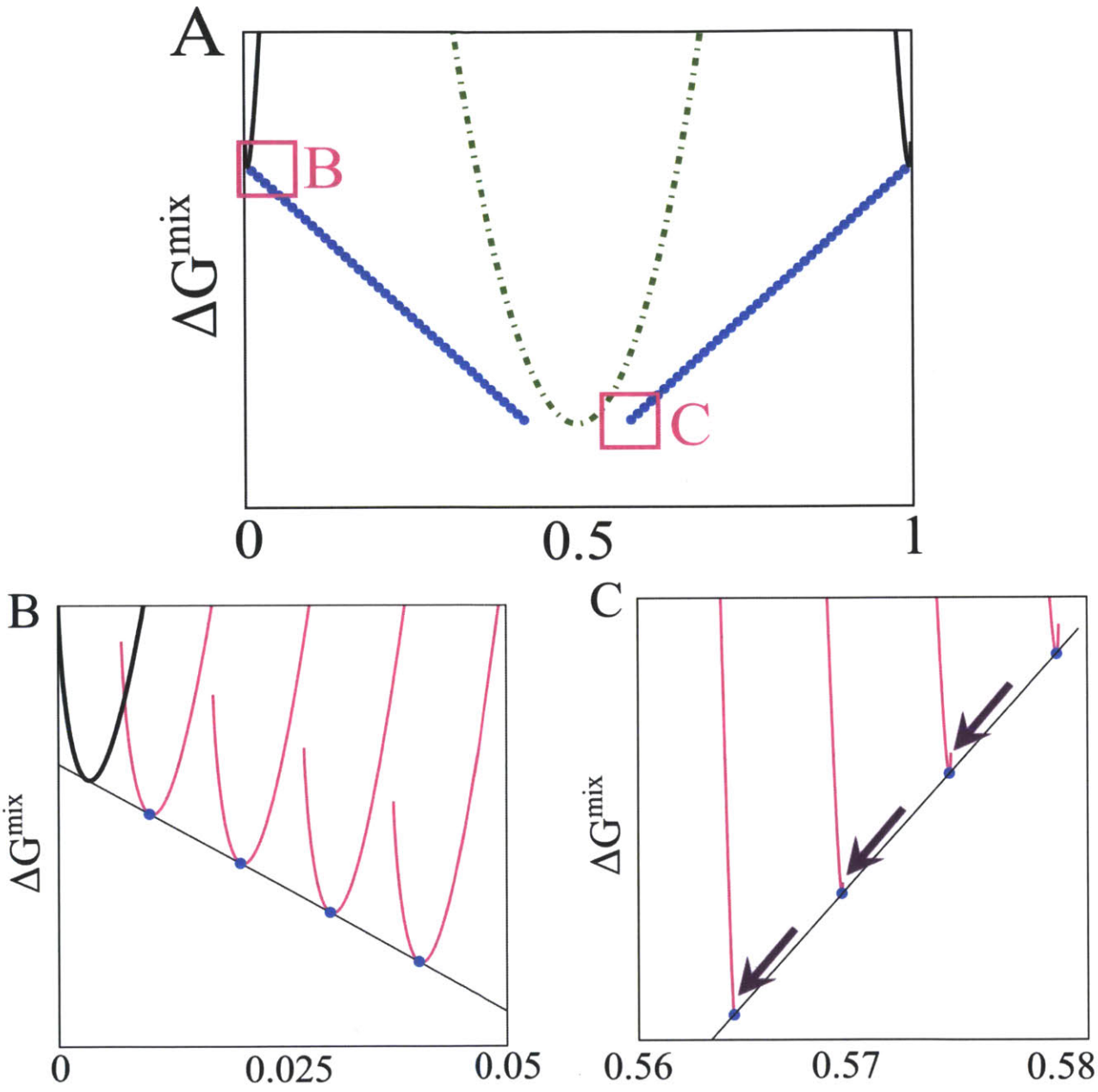

Figure 3.9 ***"Classical" stability – the nanocrystalline phases in blue are lower in free energy than the common tangent of the regular solution (black curve). (A) presents the whole composition range, (B) the lower composition limit of stabilized nanostructures, starting at the solubility limit of the regular solution. (C) the upper limit of composition, characterized by the limit of X_{gb}-d space(see text). Image adapted from [112].***

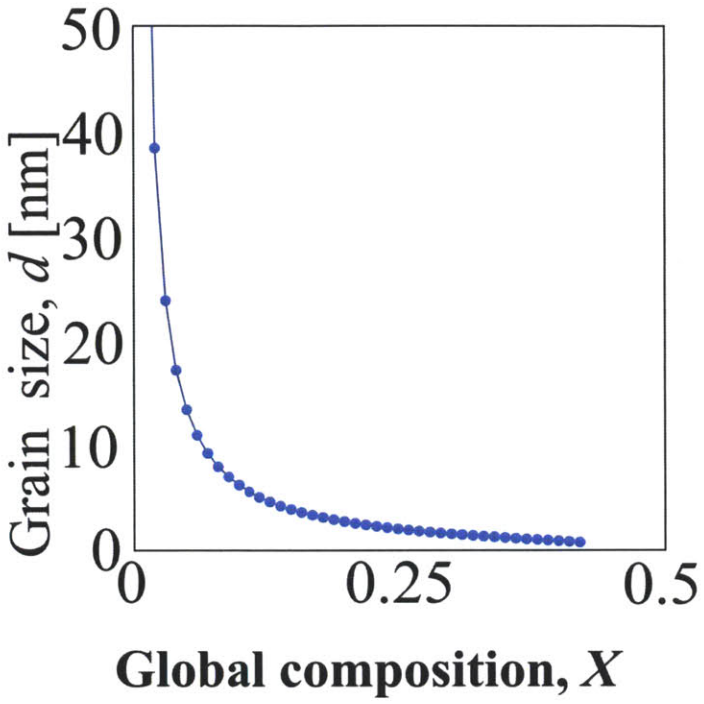

Figure 3.10 ***Grain size versus global composition for the stable "classical" nanocrystalline system shown in Figure 3.9. Image adapted from [112].***

The composition bounds of the system are clearly defined – the solubility limit of the bulk regular solution (black curve, Fig. 3.9B) distinguishes the lower limit, below which no stable NC states exist; the upper bound (Fig. 3.9C) is limited by the required solute concentration in the GB for stability, X_{gb}, of the free energy surface minimum. The predominant factor in the numerical value of X_{gb} at the minimum (that is required for GB energy to be zero) is temperature; at a particular set of parameters, X_{gb} necessary for stability is essentially constant, regardless of global composition. Recalling the distribution of solute between the grain interiors and boundaries, $X=X_c(1-f_{gb})+X_{gb}f_{gb}$, the lowest global composition which supports a nanocrystalline minimum is that in which all solute is in the GB; the relation $X= X_{gb}f_{gb}$ then restricts the smallest grain size and largest global solute composition at which a nanocrystalline phase is possible.

This limitation creates boundaries on the free energy surface, beyond which no surface exists; this can be seen in, e.g. Fig. 3.1 (on the left-hand side where the smallest grain sizes cannot be accessed on the free energy surface). This truncation of the free energy curves can also be seen in the magnified view in Fig. 3.9C, which shows the points for the nanocrystalline states close to the limiting composition, as well as their individual free energy curves; note that these are all truncated on the right-hand side (highlighted by arrows), at the limits achievable by $X = X_{gb} f_{gb}$. The truncation becomes more and more severe as the concentration rises, and the last nanocrystalline compound—that with the largest possible solute content—is the last that has a minimum in the free energy surface contained within the available range of grain size and solute distribution (Fig. 3.9C).

This last nanocrystalline "compound" or "terminal" nanocrystalline structure has the lowest free energy of the system. A common tangent drawn between the terminal NC structure and the regular solution shows that all the NC phases lie along this tangent; the points shown are simply the example concentrations calculated systematically in this study – an infinite number of stabilized NC grain sizes are achievable between the two composition bounds. These nanocrystalline compounds are symmetric, due to our assumption of equal $\Omega\gamma/t$ for solvent and solute.

A third phase appears in Fig. 3.9, denoted by a green dashed line; it is the grain boundary regular solution (Eq. 2.6) which describes the limit of the RNS free energy as grain size approaches the GB width, t. This regular solution can also be considered the "amorphous limit" as the system is comprised entirely of GB material, the system is no longer orderly crystal. In Fig. 3.9, the amorphous limit has a free energy lower than that of the bulk crystal regular solution, but higher than the NC compounds. However, as seen in the following section, the

amorphous limit can be the lowest energy phase of the system. This is not the first work to predict the existence of a thermodynamically stable amorphous phase (see, for example, [116]), but it constitutes an entirely different approach to its stability.

3.3.2 Amorphous Limit

The amorphous limit is characterized by a preference for grain boundary region over crystalline; in other words, ω_{gb} is strongly negative and very different from the the crystal interaction parameter (i.e. in $\Delta H^{mix}>0$ systems, ω_c is strongly positive; in $\Delta H^{mix}<0$ systems, ω_c and ω_{gb} are both negative, but $\omega_{gb}<<\omega_c$). An example system is shown in Figure 3.11. Despite the existence of nanocrystalline compounds stable with respect to grain growth and lower in free energy than the bulk miscibility gap common tangent line, the resulting stable state in these systems is an equilibrium between the bulk regular solution and the amorphous/grain boundary regular solution.

This may be able to be related to a common metric for assessing binary amorphous systems: the Glass Forming Range, or GFR. There are a number of approaches to estimate the GFR (i.e. size/structure difference, eutectic shape, and enthalpy models[116]), and the present RNS model offers a new approach, one based on GB segregation behavior.

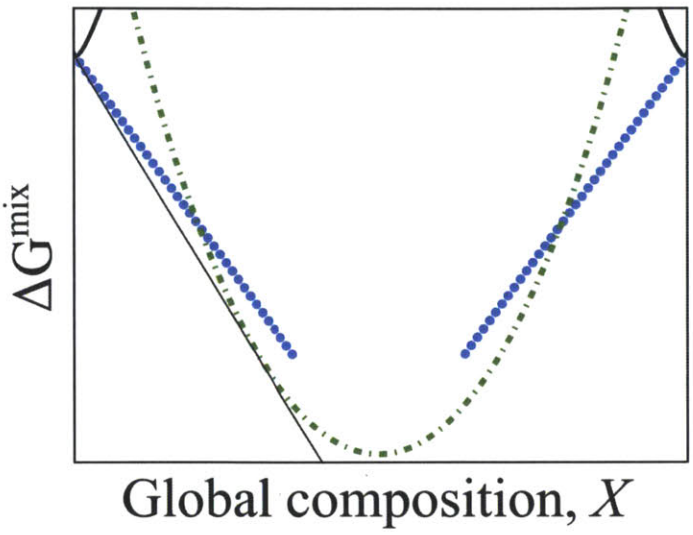

Figure 3.11 Free energy plot of a system in which the amorphous limit is the lowest energy phase. Amorphous Limit is depicted by the green dashed line, nanocrystalline compounds in blue, and bulk regular solution in black. Image from [112].

3.3.3 Dual-phase Nanocrystalline

In cases where the enthalpy of segregation is larger than the enthalpy of mixing, such that ω_{gb} is negative, but not sufficient to drive the system to the amorphous limit, the free energy surface at a given composition (Fig. 3.12B) supports two minima where the grain boundary energy is zero; hence the designation "dual-phase nanocrystalline". One of these minima is the "classic" grain boundary segregation-stabilized state – the solute is strongly segregated to the grain boundaries (Fig. 3.12C, left), and the stabilized grain size continues to decrease with an increase in composition along the nanocrystalline common tangent line; the second minimum has solute-rich grains with the solvent segregated to the grain boundary (Fig. 3.12C, right). Because ω_{gb} also describes the cross-interactions between the crystalline and grain boundary regions, a mildly negative value of this parameter leads the system to maximize unlike bonds crossing between these regions (whereas a strongly negative ω_{gb} pushes the system to all GB, or amorphous). This in turn promotes a finer grain size, and in order to support the increased grain

boundary volume, the grain boundary region must be occupied by the majority element (the solvent). Thus, the roles of solute and solvent are exchanged and the preferred system is a "solute nanocrystalline phase". The composition range of such solute nanocrystalline phases is limited by the same (X_{gb}, d)-space constraints as the "classical" solvent nanocrystalline phases, discussed in 3.3.1. The solute nanocrystalline phases also follow a composition-grain size relationship; however, as the solute concentration decreases from the equiatomic concentration, the grain size decreases.

While we describe this case as "dual-phase nanocrystalline" due to the existence of two nanocrystalline phases stable against grain growth at a single composition, the solute nanocrystalline phase is lower in free energy. Constructing common tangents on Fig. 3.12A leads to the conclusion that over a broad range of compositions the solute nanocrystalline phase is in equilibrium with the bulk regular solution; on the solvent rich side of the phase diagram, the stable states are a solvent rich solid solution and a solute rich nanocrystalline phase with grain boundary segregation. In the middle of the diagram, the equilibrium is between two solute nanocrystalline phases, which should be an interesting dual-phase nanocomposite that would in general be a true stable bimodal structure.

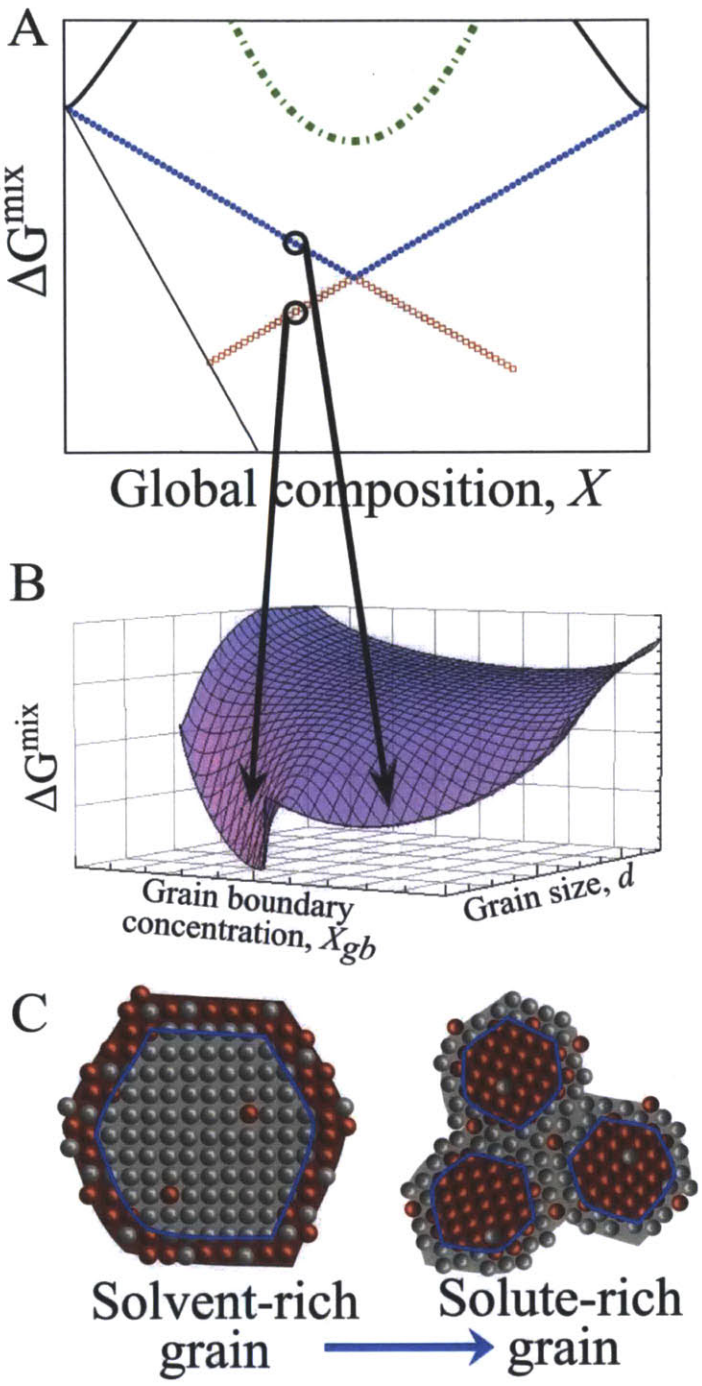

Figure 3.12 Dual-phase stable nanostructure: (A) free energy plot (B) free energy surface, showing two minima (C) schematic of the grain structure. Image adapted from [112].

3.3.4 Amorphous and Dual-phase

In the previous two sections we have seen cases where the nanocrystalline points compete with an amorphous phase, or with one another (solute nanocrystalline phase). These cases correspond to a relatively higher and lower magnitude of negative ω_{gb}, respectively. Between these two extremes lies a condition in which both the grain boundary free energy curve (amorphous limit) and the terminal compositions of the nanocrystalline free energy lines are stable. An example of this situation is shown in Fig. 3.13, where the low energy of the grain boundary regions places it in equilibrium with the bulk regular solution at low solute levels. At higher concentrations, the amorphous limit is in equilibrium with the solute nanocrystalline phase defined by the terminal structures of the nanocrystal free energy lines. The two solute nanocrystalline phases are in equilibrium around the equiatomic composition.

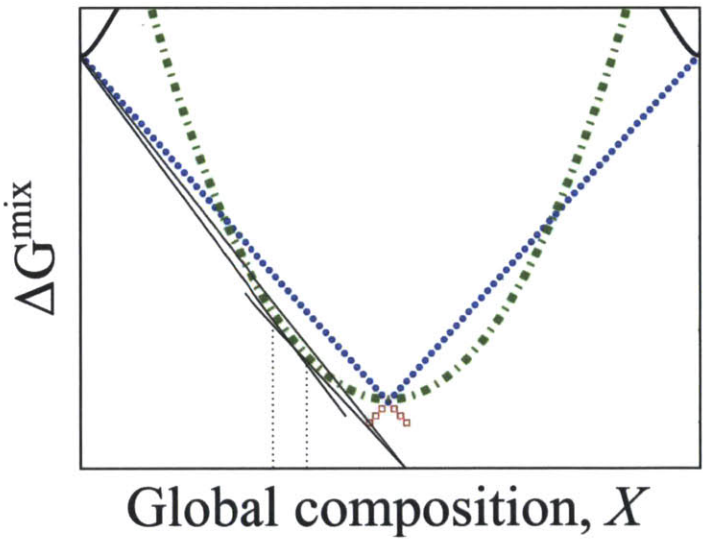

Figure 3.13 Dual-phase (solvent-rich points in blue and solute-rich points in open red squares) and Amorphous (green dot-dashed line) stable. Thin black common tangent lines represent the equilibrium phase fields. Image from [112].

3.3.5 Discussion of stability

Each of the above types of stability populate a subregion of the stable nanocrystalline design space. As mentioned in their discussion, "classical" nanostructures in the positive enthalpy of mixing alloys fill the space around ideal GB behavior (ω_{gb}~0) which is the upper right of the stable region (Fig. 3.14). In the $\Delta H^{mix}<0$ map (Fig. 3.15), the stable design space has no classical region, only stable dual-phase and amorphous. The design space for negative mixing enthalpy systems near which ω_{gb}~0 does not present minima in the free energy surface, as the crystal interaction parameter denotes a preference for ordering, the solute would prefer to sit in the crystal lattice (forming AB bonds) rather than in the grain boundaries. The stabilized nanostructures exist in the $\Delta H^{mix}<0$ systems only when the GB interaction parameter is more negative than that of the crystal.

Stable amorphous phases are found where ω_{gb} is strongly negative and ω_c is high in magnitude (strongly positive for $\Delta H^{mix}>0$, strongly negative for $\Delta H^{mix}<0$), dual-phase appears where ω_{gb} is slightly more negative than ω_c. The subregions that correspond to the various stable nanostructures are shown in Figures 3.14 and 3.15.

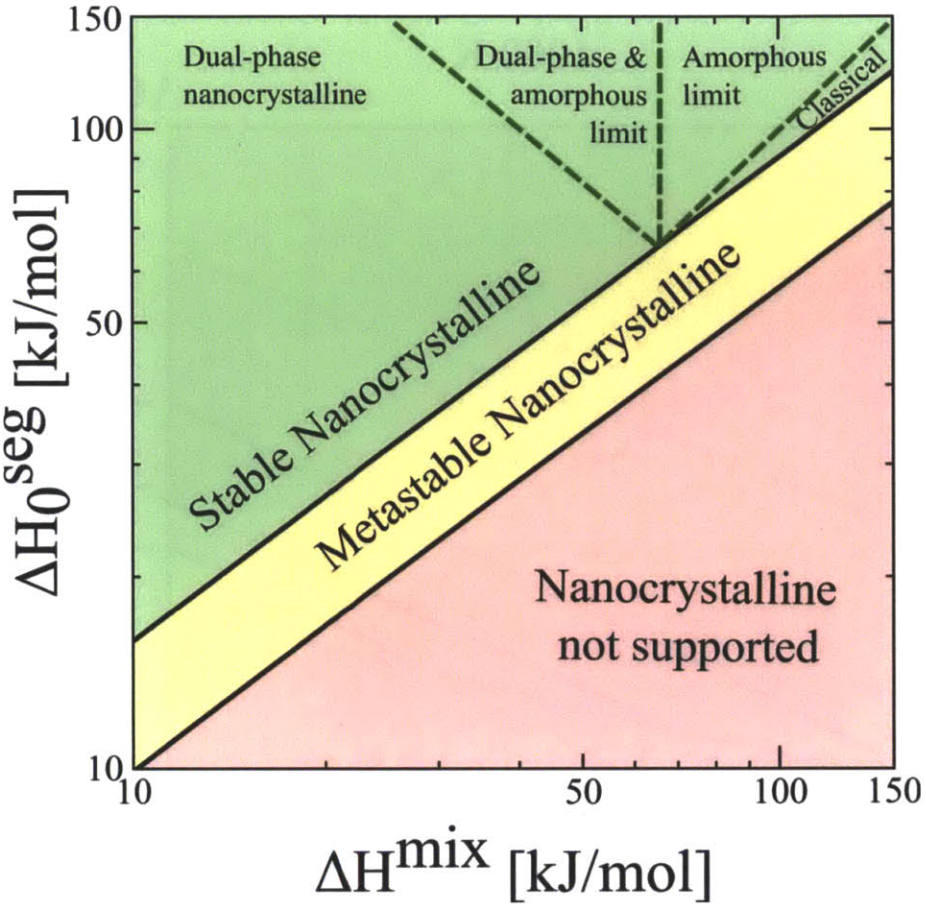

Figure 3.14 Nanocrystalline stability map for T=0.35Tcr; the stable nanocrystalline region is divided into subsections describing the various types of possible stable nanocorystallline structures. Image from [112].

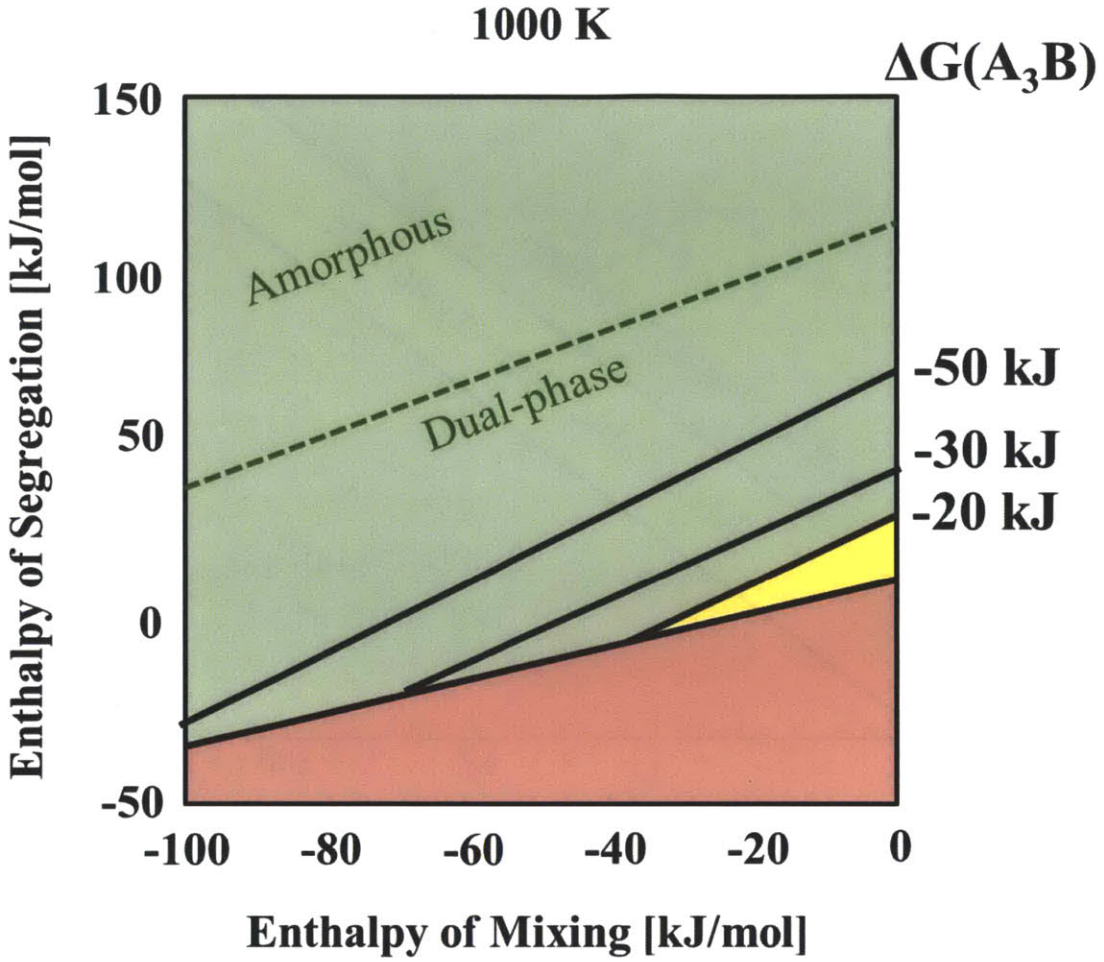

Figure 3.15 Nanocrystalline stability map for 1000K for compound forming systems with A_3B compound. The stable region is subdivided into stable amorphous and stable dual-phase.

Some example grain sizes, solute distributions, and free energies of stable nanostructures are in the following tables. All interaction parameters and free energies are in are in eV/atom. Across all types of stable nanostructures, the solute concentration inside the grains never exceeds the solubility limit, despite the global concentration being above this value. All solute in excess of the solubility limit is in the grain boundary.

Table 3.2 ***Example concentration distribution, grain size, and free energy for an example classical stable nanostructure with $\Delta H^{mix}>0$***

Classical	$\Omega\gamma_A/t$	$\Omega\gamma_B/t$	X_{gb}	X_c	d [nm]	ΔG_{mix}
X=0.1	0.085	0.085	0.44	0.0024	6.2	-0.00389
ω_c= 0.07	0.085	0.1	0.44	0.0024	6.2	-0.00316
ω_{gb}= 0.0	0.065	0.1	0.36	0.0009	4.9	-0.00709
T=0.35Tcr	0.1	0.085	0.495	0.0033	7.1	-0.0015
(1705K)	0.1	0.065	0.495	0.0033	7.1	-0.0025

Table 3.3 ***Example concentration distribution, grain size, and free energy for an example Dual-phase nanostructure: $\Delta H^{mix}>0$***

Dual-phase	$\Omega\gamma_A/t$	$\Omega\gamma_B/t$	X_{gb}	X_c	d [nm]	ΔG_{mix}
X=0.1	0.085	0.085	0.74	0.0022	10.8	-0.0025
ω_c= 0.03	0.085	0.1	0.74	0.0022	10.8	-0.0018
ω_{gb}= -0.015	0.065	0.1	0.64	0.0026	9.3	-0.0036
T=0.35Tcr	0.1	0.085	0.80	0.0020	11.7	-0.0013
(731K)	0.1	0.065	0.80	0.0020	11.7	-0.0023

Dual-phase	$\Omega\gamma_A/t$	$\Omega\gamma_B/t$	X_{gb}	$X_c B$	d [nm]	ΔG_{mix}
X=0.4	0.085	0.085	0.26	0.97	1.2	-0.0143
ω_c= 0.03	0.085	0.1	0.20	0.99	1.33	-0.0072
ω_{gb}= -0.015	0.065	0.1	0.20	0.99	1.33	-0.013
T=0.35Tcr	0.1	0.085	0.26	0.97	1.2	-0.0099
(731K)	0.1	0.065	0.36	0.96	0.84	-0.02

Table 3.4 ***Example concentration distribution, grain size, and free energy for an example Dual-phase nanostructure: $\Delta H^{mix}<0$***

Dual-phase	$\Omega\gamma_A/t$	$\Omega\gamma_B/t$	X_{gb}	$X_c B$	d [nm]	ΔG_{mix}
X=0.45	0.085	0.085	0.37	0.99	1.0	-0.2390
ω_c=-0.04	0.085	0.1	0.31	0.99	1.2	-0.2310
ω_{gb}=-0.08	0.065	0.1	0.31	0.99	1.2	-0.2365
T=1000K	0.1	0.085	0.37	0.99	1.0	-0.2352
	0.1	0.065	Not found			

The GB concentration required to bring the boundary energy to zero in classical nanosystems, not surprisingly, increases with increasing solvent GB energy; the solute GB energy has no effect. This trend continues for the classical type solvent-rich grains in a dual-phase nanostructure, Table 3.2. For the solute-rich nanograins, the GB energy of the solute becomes the determining factor in the GB coverage, X_{gb}, required.

Nanostructures that are lower in free energy than the bulk regular solution, but higher in free energy than the grain boundary regular solution are described in Table 3.5. The grain interior, X_c, concentration of these nanocrystalline compounds is essentially zero, as the GB interaction parameter is significantly larger in magnitude, and drives the solute to the GB environment. The amorphous phase, which represents the entire material being in a GB environment is the lowest energy configuration for this parameter system.

Table 3.5 Example concentration distribution, grain size, and free energy for example classical nanostructure: $\Delta H^{mix}<0$ where the nanocrystalline structures are higher in free energy than the Amorphous Limit

Amorphous	$\Omega\gamma_A/t$	$\Omega\gamma_B/t$	X_{gb}	X_c	d [nm]	ΔG_{mix}
X=0.1 ω_c= -0.04 ω_{gb} = -0.24 T=1000K	**0.085**	0.085	0.63	~0.00	8.9	-0.1395
	0.085	0.1	0.63	~0.00	8.9	-0.1388
	0.065	0.1	0.53	~0.00	7.4	-0.1412
	0.1	0.085	0.69	~0.00	9.8	-0.1380
	0.1	0.065	0.69	~0.00	9.8	-0.1390

3.4 Metastable structures

Metastable alloys, while susceptible to phase separation, are still stable against grain growth. The types of metastable nanostructures are discussed below.

3.4.1 Metastability when $\Delta H_{mix}>0$

Figure 3.16A shows a representative free energy plot for a metastable case in the positive enthalpy of mixing systems. The grain size decreases as composition increases (Fig. 3.16B), however the free energy increases. Indeed, the situation surrounding the free energy minima in the metastable case is not quite the same as seen in the earlier analysis using $X+$ and $X-$ for the case of a stable nanocrystalline structure (Section 2.3, Fig. 2.4). In that case, decreasing the composition at the set values of X_{gb} and d resulted in a sharp increase, and increasing the composition led to a lowering of the free energy through decreasing grain size.

In the metastable case, the same types of behavior are seen, but with opposite composition tendencies (Fig. 3.16C&D). For an increase in composition, the free energy increases rapidly; for a decrease in composition, the grain boundary energy is positive, and as a result the system favors grain growth. This pattern continues until the infinite grain size of the regular solution is obtained (Fig. 3.16B). At the nanocrystalline compound values of X_{gb} and d the grain boundary energy has been reduced to zero, eliminating the drive for grain growth (Fig 3.16D), but the free energy of a system with a larger grain size is always a lower free energy state. At the same time, the lower free-energy of the common-tangent bulk phases dictates that the structure phase separate, so the equilibrium structure is a coarse-grained, phase separated system.

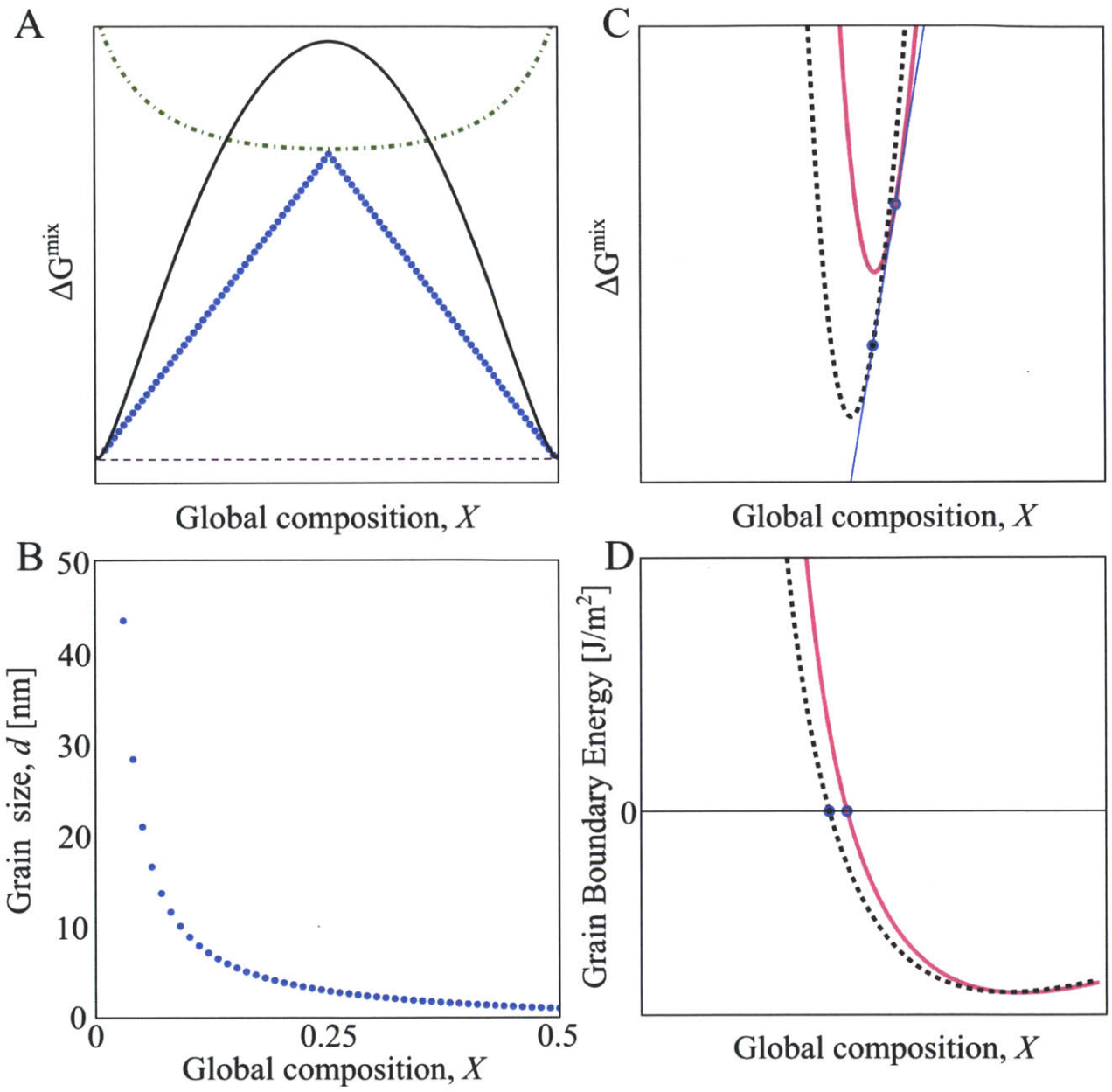

Figure 3.16 ***Metastability in $\Delta H^{mix}>0$ systems: (A) Free energy plot of nanocrystalline phases (blue points) with respect to the regular solution (black curve)and its equilibrium common tangent (dashed purple line). (B) Grain size as a function of composition in this example system. (C) Free energy curves if the minimum values of (X_{gb}, d) and held constant for two different composition free energy surfaces. (D) GB energy as a function of composition for two compositions, holding their minimum values of X_{gb} and d constant. Minimum values have a GB energy of zero. Image adapted from [112].***

3.4.2 Locally metastable

Local metastability exists in negative mixing enthalpy systems and is described by the free energy surface in Fig. 3.17A and location of the minimum point relative to other phases in Fig 3.17B. A minimum exists in the free energy surface where the GB energy is zero, but this is a *local* minimum, rather than a *global* one, and the lowest free energy at this composition is the bulk regular solution at infinite grain size.

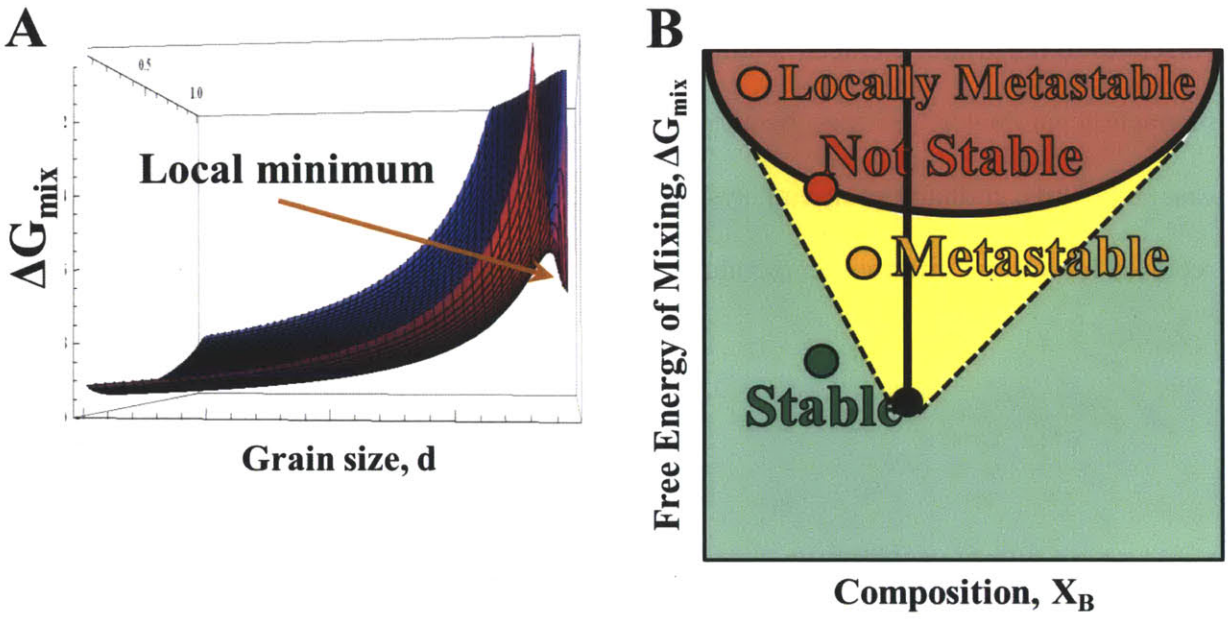

Figure 3.17 Local Metastability in $\Delta H^{mix}<0$ systems: (A) an example free energy surface with a local minimum (B) The relationship of the local minimum to other phases.

3.4.3 Locally dual-phase metastable

As metastability in negative enthalpy cases is conferred by the independent free energy of the ordered compound, nanostructures of the dual-phase type as discussed in Section 3.3.3 which are stable with respect to the bulk solid solution can be metastable with respect to compound phase precipitation

3.5 *Conclusions of this chapter*

In this chapter, the requirements for binary systems to support nanocrystalline phases stable against both grain growth and phase separation were examined. This work found several new types of stable nanostructures in addition to the expected, "classical", solute GB-decorated system. The stable nanostructures were represented on nanocrystalline stability maps, with useful materials quantities, the enthalpies of mixing and segregation, as defining axes. In both negative and positive mixing enthalpy of systems, the relationship of the enthalpies – mixing, which correlates to the grain, or crystal interaction parameter, and segregation, which includes the GB interaction parameter – defines the alloys which will be stable, metastable, or not stable. In the case of positive enthalpy of mixing systems, a figure of merit regarding these two enthalpies was reported for several different temperatures.

4. *Placement of Alloys on Maps: Enthalpy Calculations*

As shown in Chapter 3, it is the relationship of the enthalpy of segregation, ΔH^{seg}, to the enthalpy of mixing, ΔH^{mix}, that signifies nanocrystalline complete-, meta-, or non-stability; values for these two enthalpies must be found for a materials system in order to determine whether it can support a stable nanostructure. Enthalpies of mixing are relatively easy to attain – for example, through the prevalent Miedema model, CALPHAD-style models, or atomistic potentials.

However, enthalpies of grain boundary segregation are challenging – this quantity has been measured or calculated via simulation for only a few systems (which will be discussed in section 4.2), and these values can vary wildly even within one alloy system. For example, reported values for the copper-silver binary range from 25-63 kJ/mol, including experimental and atomistic modeling results [114, 117, 118]. Additionally, it is the *dilute* segregation enthalpy that constitutes the ordinate axis of the segregation maps presented in Chapter 3; an appropriate analogue to Eq. (3.4):

$$\Delta H_0^{seg} = z\left[\omega_c - \frac{\omega_{ig}}{2} - \frac{\Omega_B\gamma_B - \Omega_A\gamma_A}{2zt}\right] \tag{3.4}$$

is what is necessary for predicting stable nanocrystalline alloys. Furthermore, in order to screen a wide range of alloys, a segregation model with simple, generalizable parameters would be ideal. In the following chapter, previous predictive models of interfacial segregation enthalpy are examined, en route to the development of a new, simple analytical model for GB segregation.

As seen in Eq. (3.4) and mentioned in the last chapter, the segregation enthalpy necessarily includes a differentiation between the grain boundary environment, ω_{gb}, and the

crystal environment, ω_c, – thus the methods of description for the crystal interaction parameter, which is necessary for calculation of both enthalpies is discussed first.

4.1 Enthalpy of Mixing

The Miedema model is a commonly used semi-empirical model that is widely applied to calculations of mixing and formation enthalpies for solutions and compounds [119, 120]. The enthalpy of mixing of a concentrated solid solution is composed of three terms that describe the chemical, elastic, and structural enthalpy changes associated with a solid solution of two atomic species:

$$\Delta H_{S.S.}^{mix} = \Delta H_{S.S.}^{chemical} + \Delta H_{S.S.}^{elastic} + \Delta H_{S.S.}^{structural} \tag{4.1}$$

The structural term, $\Delta H_{S.S.}^{structural}$, was found by Miedema and others [119, 120] to be negligible (only existing if both species are transition metals, and on the order of ±1 kJ/mol, compared to magnitudes of total enthalpy ranging in general from 10-150 kJ/mol), therefore this term in omitted going forward. The contributions to the chemical and elastic terms are summarized in Table 4.1.

Table 4.1: Miedema Model Enthalpy of Mixing Terms

Model variables			
V_A, V_B	molar volume	ψ_A, ψ_B	work function for electron transfer
c_A, c_B	Concentration	n_{ws}^A, n_{ws}^B	electron density at boundary of Wigner-Seitz cell
c_A^s, c_B^s	surface fraction		
K	bulk modulus	P, Q	constants
G	shear modulus	W_A, W_B	spherical volume of an atom or hole

Model definitions	
$\Delta H_{s.s.}^{chemical} = c_A c_B (c_B^s \Delta H_{AinB}^{inter} + c_A^s \Delta H_{BinA}^{inter})$	
$\Delta H_{AinB}^{inter} = \frac{(V_A)^{2/3}}{\frac{1}{2}\left(\frac{1}{n_{ws}^{A\ 1/3}} + \frac{1}{n_{ws}^{B\ 1/3}}\right)}\{-P(\Delta\psi)^2 + Q(\Delta n_{ws}^{1/3})^2\}$	$\Delta H_{BinA}^{inter} = \frac{(V_B)^{2/3}}{\frac{1}{2}\left(\frac{1}{n_{ws}^{A\ 1/3}} + \frac{1}{n_{ws}^{B\ 1/3}}\right)}\{-P(\Delta\psi)^2 + Q(\Delta n_{ws}^{1/3})^2\}$
$c_A^s = \frac{c_A * V_A^{\ 2/3}}{c_A * V_A^{\ 2/3} + c_B * V_B^{\ 2/3}}$	$c_B^s = \frac{c_B * V_B^{\ 2/3}}{c_A * V_A^{\ 2/3} + c_B * V_B^{\ 2/3}}$
$\Delta H_{s.s.}^{elastic} = c_A c_B (c_B \Delta H_{AinB}^{elastic} + c_A \Delta H_{BinA}^{elastic})$	
$\Delta H_{AinB}^{elastic} = \frac{2 * K_A * G_B * (W_A - W_B)^2}{3 * K_A * W_B + 4 * G_B * W_A}$	$\Delta H_{BinA}^{elastic} = \frac{2 * K_B * G_A * (W_A - W_B)^2}{3 * K_B * W_A + 4 * G_A * W_B}$
$W_A = \left(V_A + \alpha * \frac{(\psi_A - \psi_B)}{n_{ws}^A}\right)$	$W_B = \left(V_B + \alpha * \frac{(\psi_A - \psi_B)}{n_{ws}^B}\right)$
$\alpha = 1.5 * \frac{(V_A)^{2/3}}{\frac{1}{n_{ws}^{A\ 1/3}} + \frac{1}{n_{ws}^{B\ 1/3}}}$	$\alpha = 1.5 * \frac{(V_B)^{2/3}}{\frac{1}{n_{ws}^{A\ 1/3}} + \frac{1}{n_{ws}^{B\ 1/3}}}$

Sources of Data			
ΔH_{AinB}^{inter} & ΔH_{BinA}^{inter}	*See Appendix A.1*	V_A&V_B	*Table A2 [119]*
$\psi_A, \psi_B, n_{ws}^A, n_{ws}^B$	*Table A1 [119]*	K,G	*Table A2 [119]*

The chemical contribution centers on ΔH_{AinB}^{inter}, which describes the chemical interaction of an A atom completely surrounded by B atoms, and the surface fraction, c_A^s, which describes the adjustment made to the interacting surface when the A atom has non-B neighbors. It is important to note that this chemical interaction does not describe bond coordination, but rather the available interacting surface between the atoms. The elastic term makes use of Eshelby's elastic

formalism and describes fitting an approximate sphere of one atom in a hole in the matrix of the other species. For full descriptions of these terms see [119, 120].

The Miedema model form is not that of a regular solution; in order to extract the regular solution interaction parameter, namely ω_c, $\Delta H_{S.S.}^{mix}$ was calculated across the full range of global composition, X, and fit to an equation of the regular solution form: $\Delta H^{mix} = z\omega_c X_A X_B$. The enthalpy of mixing was calculated for ~2500 binary systems; values for ΔH^{mix} are in Appendix A and are represented in Figure 4.1 by a solid color square, with red scale signifying positive ΔH^{mix} and increasing intensity of blue squares representing increasingly negative ΔH^{mix}. It is the symmetric regular solution enthalpy, i.e. $z\omega_c$, that is presented in these tables.

While the Miedema model makes a reasonable estimate for a wide range of binary alloys, it can sometimes result in non-physical predictions; for example, when the calculated formation enthalpy is negative (indicating an ordering system) while the phase diagram presents a phase-separating miscibility gap. Additionally, values for ΔH_{AinB}^{inter} were not calculated for a significant number of useful binary alloys (e.g. specifically many binary alloys containing the "noble" metals copper, gold, and silver).

The next source for a wide range of alloys is the CALPHAD method which aims to fit free energy models to experimentally determined phase diagrams. Most free energy functions fitted using this method utilize the Redlich-Kister-Muggiano equation for the excess free energy term (enthalpy of mixing):

$$G^{excess} = X_A X_B \sum_i (X_A - X_B)^i L_i(T) \text{ where } L_i(T) = A_i + B_i T \quad (4.2)$$

Again, the full form for the excess term is fit to the regular solution model. The calculated enthalpy of mixing for a binary system using the RKM model is represented on Fig. 4.1 by the same color scale as the Miedema model, but with the addition of a black dot in the colored square. When both Miedema and RKM data exists for a particular binary systems, its square is split diagonally, with the upper right representing the Miedema value and the lower left the RKM value. In some cases, the RKM model parameters for a system result in an extremely asymmetric enthalpy function; in these systems, extracting a regular-solution-type enthalpy is not reasonable, and the space in Fig. 4.1 is marked with an "x".

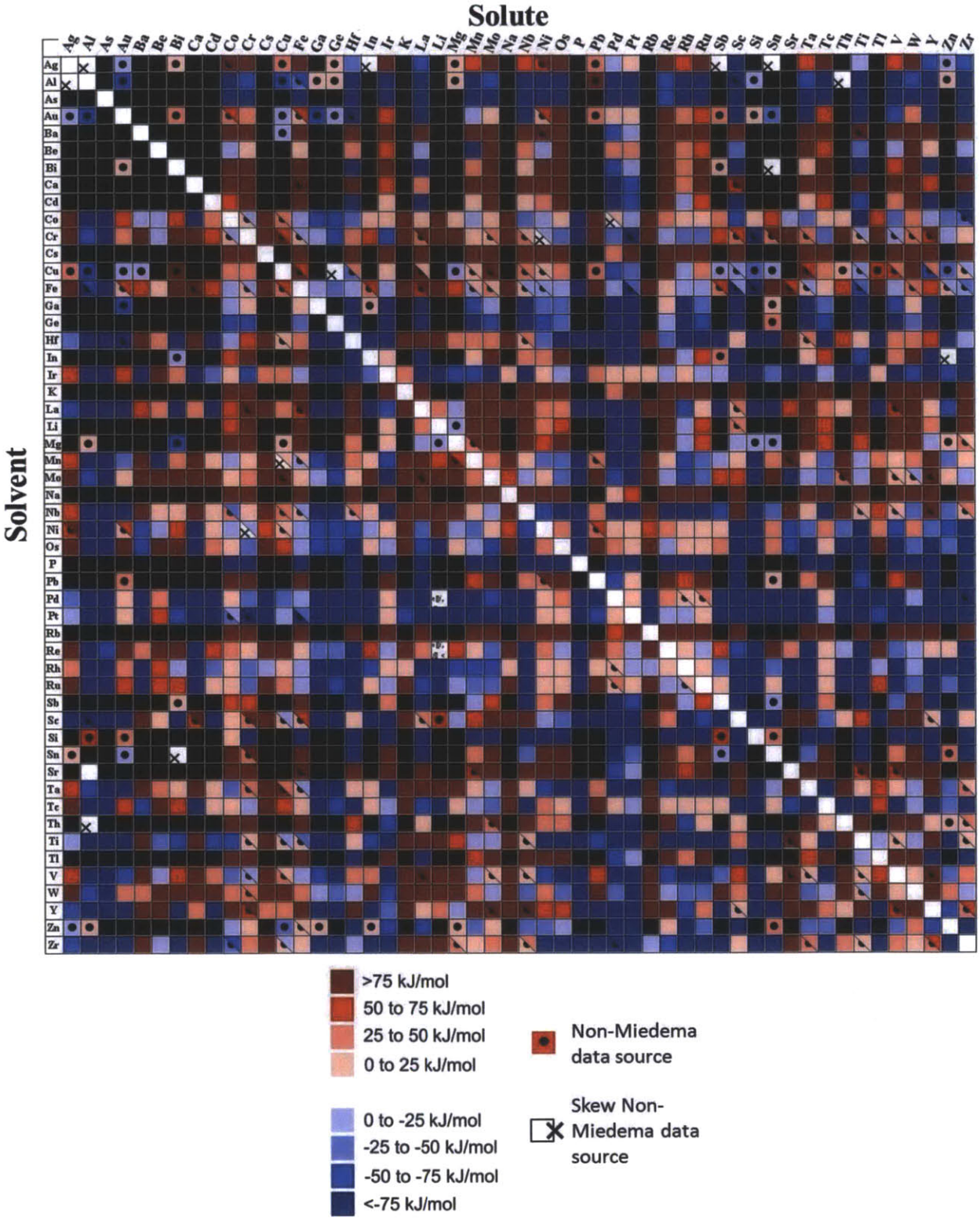

Figure 4.1 Calculated enthalpies of mixing for a wide range of binary systems

For RKM coefficients that are temperature dependent, the critical temperature, T_{cr}, which is necessary for the application of the predictive enthalpy relation, Eq. (3.5), must also be calculated. In a symmetric regular solution the top of the miscibility gap simply equals $\Delta H^{mix}/2R$; for RKM models, asymmetry and/or temperature dependencies in the coefficients require a more rigorous method to calculate T_{cr} through examining the evolution of the free energy with temperature.

These calculations are performed using the program presented in Appendix B.1. Values for ΔH_{AinB}^{inter} derived from RKM models are shown in Appendix A.

4.2 Enthalpy of Segregation

4.2.1 Critical examination of existing segregation models

Among all the possible binary metal pairs that may be of interest in designing nanostructured materials, very few experimental measurements or atomistic modeling predictions of segregation enthalpies exist. In fact, literature values of these quantities are presented in Table 4.2, and the systems represented comprise less than 1% of those that are possible. It should also be noted that most studied systems are those in which GB segregation occurs; a considerable number of alloys should be anti-segregating (or the GB is depleted in the solute species), as has been observed, mostly qualitatively in some systems [121, 122] and often observed in surface segregation [123, 124]. Therefore, a comprehensive predictive model is required; however, existing predictive models to date are less than ideal. General models to predict the propensity for grain boundary segregation include those of Hondros and Seah [125, 126], McLean [127], Wynblatt and Ku [128], and Darling et. al. [50]. These are briefly detailed in what follows.

Table 4.2 ***Quantitative Literature Segregation Enthalpy Values***

(Positive value denotes propensity for GB segregation)

Solvent	Solute	Reported [kJ/mol]	Data Type	Ref.
Ni	Cu	14	atomistic – MC EAM	[129]
Cu	Ni	-7	atomistic – MC EAM	[129]
Al	Pb	111	atomistic -	[43]
Ni	W	10	atomistic -	[45]
Cu	Ag	63	atomistic – MC	[117]
		30	model -	[118]
		25,40	experiment	via [114]
		40	experiment	via [118]
Cu	Au	10	experiment	via [114]
		~60 (1st layer)	atomistic – MC	[117]
Ag	Ni	40	experiment	via [114]
Fe	Si	3-17	experiment	via [114]
Fe	Al	12	experiment	via [114]
Fe	Cr	8	experiment	via [114]
Cu	Bi	53	experiment	via [114]
		60-88	experiment	[130]
Ni	Bi	117	experiment	[131]
Fe	Cu	50-58	model fit to exp.	[57]
Fe	Sn	13-23	experiment	via [114]
Ni	In	38	experiment	via [114]
Ni	Sb	4,63	experiment	via [114]
Co	Sb	5	experiment	via [114]
Zr	Cr	12	experiment	via [114]
Fe	Ag	60-100	model fit to exp.	[54]

Requiring the least materials system inputs is the empirical solubility-based model of Hondros and Seah which was obtained by fitting experimental segregation data predominantly for impurities in steel. The solute GB enrichment ratio was correlated to the bulk solute solubility, X_{sol}, of the alloy system:

$$\Delta H_{H-S}^{seg} = RTLog[X_{sol}] - 10 \pm 6kJ \qquad (4.4)$$

The range of alloys used for this correlation is very limited, and the physical validity of solubility as an indicator of segregation is questionable [132]. In addition to being strictly empirical, the model hinges on the bulk solubility, which derives from bulk phase equilibria considerations and does not speak to the energetics of grain boundaries – this segregation enthalpy essentially relies entirely on mixing enthalpy.

Moving in the opposite direction, McLean's segregation enthalpy model uses as its impetus only the release of strain energy associated with the movement of a solute from the grain matrix to the GB environment. He wrote the elastic strain energy change using an Eshelby-type continuum linear elastic formalism to describe the enthalpy change of substituting a solute atom for a solvent atom in the matrix [133] and further assumed this elastic enthalpy to be fully released by GB solute segregation:

$$\Delta H_{el}^{seg} = \Delta E_{el} = \frac{24\pi K_A G_B r_B r_A (r_B - r_A)^2}{3K_A r_A + 4G_B r_B} \tag{4.5}$$

Here, the solute is denoted by subscript B and solvent by subscript A; K is bulk modulus, G is shear modulus, r is the atomic radius; the subscript "*el*" denotes elastic. McLean's term is always positive, which means it will predict that a solute will segregate to the grain boundary in all cases, a non-physical result.

A more detailed model, the Wynblatt-Ku model for surface segregation [128] combines both the elastic mismatch with chemical and interfacial energy contributions; the difference in interfacial energies, γ^S, normalized by the area per mole of the interface, $\sigma = N_{avg} V_B^{2/3}$ is described by the first term of Eq. (4.6):

$$\Delta H_{W-K}^{seg} = (\gamma_B^S - \gamma_A^S)\sigma + 2\omega_c \left[z^l (x - x^s) + z^v \left(x - \frac{1}{2} \right) \right] - \Delta E_{el} \tag{4.6}$$

while the second term describes the chemical interactions, where ω_c is the bulk crystalline interatomic interaction parameter and z, the total coordination number of the system, is split into in-plane, z^l, and out of plane, z^v, coordination through the following relation: $z = z^l + 2z^v$.

It has been suggested that the elastic term needs no modification to be used in both surface and grain boundary segregation [134], provided that the original complete-relaxation assumption of McLean is deemed acceptable. However, Darling and coworkers suggested a modifying parameter, α, to the chemical and interfacial terms to account for the difference between free surfaces and grain boundaries. Specifically, α is the ratio between interfacial and surface strengths (taken as 5/6 by the model's authors), and their adaptation of Eq. (4.6) is written [50]:

$$\Delta H_D^{seg} = (\gamma_B^S - \gamma_A^S)(1-\alpha)\sigma - \frac{8\Delta H_{mix}}{z}\left[z^l(x^s - x) - z^v\left(x - \frac{1}{2}\right) + \alpha\left(x^s - \frac{1}{2}\right)\right] - \Delta E_{el} \quad (4.7)$$

Darling and coworkers showed that this approach is useful for comparing the segregation efficacy of possible solute choices at a fixed composition.

4.2.2 New model for grain boundary segregation enthalpy

While the solubility based ΔH_{H-S}^{seg} and the elastic enthalpy based ΔH_{el}^{seg} are capable of easily predicting segregation enthalpies for a wide range of binary alloys, they are not rigorous descriptions of GB segregation. The Wynblatt-Ku segregation model, and its adaptation ΔH_D^{seg}, encompass desired contributions to interfacial segregation; however, they do not give a segregation enthalpy independent of grain boundary solute content, nor can they be taken to the dilute limit to arrive at the necessary analogue to the ordinate axis of the nanocrystalline stability maps.

Motivated by the prior success of the Miedema model for rapidly and reasonably predicting bulk thermodynamics (as detailed in Section 4.1), the Miedema model for surface segregation will be adapted to the GB environment, in the same spirit to the adaption of the Wynblatt-Ku surface segregation [128].

Miedema's model for dilute surface segregation [135] includes both a chemical interaction enthalpy, ΔH_{BinA}^{int}, and interfacial energy terms describing the chemical and interfacial driving forces for segregation that are mirrored in the previously discussed models for segregation:

$$\Delta H^{seg} = 0.71 * \frac{1}{3} * [-\Delta H_{BinA}^{int} - c_0 \gamma_A^S V_A^{2/3} + c_0 \gamma_B^S V_B^{2/3}] \quad (4.8)$$

the term $c_0 \gamma^S V^{2/3}$, is the surface enthalpy of a pure metal as defined by Miedema, where c_0 = $4.5 \text{x} 10^8$ is a dimensionless semi-empirical constant, V is atomic volume, and γ^S is surface energy of the pure subscripted component. The coefficient $\frac{1}{3}$ describes the fraction of contact at an atom's interface (recall that the Miedema models use interacting surface rather than bond coordination); when the segregant B atom is at the surface rather than in the bulk, it has gone from being surrounded by A atoms to being only $\frac{2}{3}$rds in contact. With this fractional contact, $\frac{1}{3}$ of the interaction energy ($\frac{1}{3}\Delta H_{BinA}^{int}$) and one third of the surface ($\frac{1}{3} c_0 \gamma_A^S V_A^{2/3}$) is lost, but one third of the new surface is now B ($+\frac{1}{3} c_0 \gamma_B^S V_B^{2/3}$).The coefficient 0.71, calibrated by Miedema [135] describes the surface relaxation due to surface electron density distribution and surface geometry which reduces the exposed surface area.

As formulated by Trelewicz, the regular nanocrystalline solution model takes the fraction of interface atoms contributing to the effective coordination of transitional bonds, v, to be ½ [46].

Following the Miedema formulation, an atom in the grain boundary will therefore lose 1/3*ν, or $1/6^{th}$ of its contact with other atoms. We add the elastic term, Eq. (4.5), to account for the elastic strain effects that contribute to segregation, and arrive at the following model for the dilute grain boundary segregation enthalpy:

$$\Delta H_M^{seg} = -0.71 * \frac{1}{3} * \nu * \left[-\Delta H_{BinA}^{int} - c_0 \gamma_A^S V_A^{\frac{2}{3}} + c_0 \gamma_B^S V_B^{\frac{2}{3}} \right] + \Delta E_{el} \qquad (4.9)$$

Note that the sign convention in Eq. (4.9) is reversed from that of the original Miedema model in Eq. (4.8), in order to match the convention of the RNS model, where a positive value of segregation enthalpy denotes propensity for grain boundary segregation. Equation (4.9) requires no temperature and composition assumptions and contains readily available materials data.

The chemical interaction term, ΔH_{BinA}^{int}, appears in the Miedema models for both the enthalpy of mixing and segregation, as the interaction parameter, ω_c, figures in both the regular solution ΔH^{mix} and segregation enthalpy models, Eqs. (4.1) and (4.9). Figure 4.2 shows that, despite this shared term, the additional contributions to both enthalpies differentiate the total values substantially. We also see that a wide range of enthalpy pairs is possible.

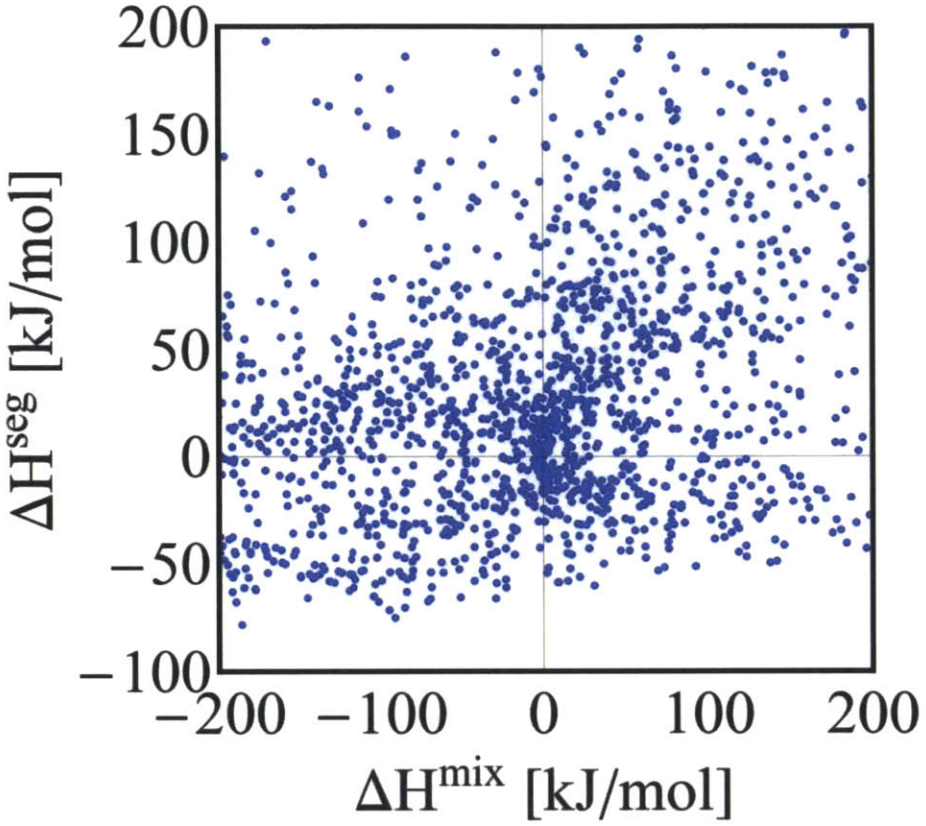

Figure 4.2 ***Enthalpies calculated using Miedema model inputs to Eq. (4.9) and ΔH^{mix} Eq (4.1).***

In the same manner as the calculations of the mixing enthalpies in Section 4.1, both Miedema values of ΔH_{BinA}^{int} and those derived from other sources are used when possible. Calculated values of ΔH^{seg} are in Appendix A using the program in Appendix B.1. The values are presented graphically in Fig. 4.3, as a solid color for Miedema based calculations– red for GB-segregating solutes and blue for anti-segregating, color-intensity scaled by strength. Calculations with non-Miedema sources are indicated in the figure by a dot. If both Miedema values and other sources were used to make the calculation, the square is bisected and the upper, solid quadrant represents Miedema values, while the additional sources color in the lower left

quadrant, again marked with a dot. A black square indicates no data was found to make the calculation, and an "X" indicated the RKM model was too skew to accurately extract a regular solution type parameter.

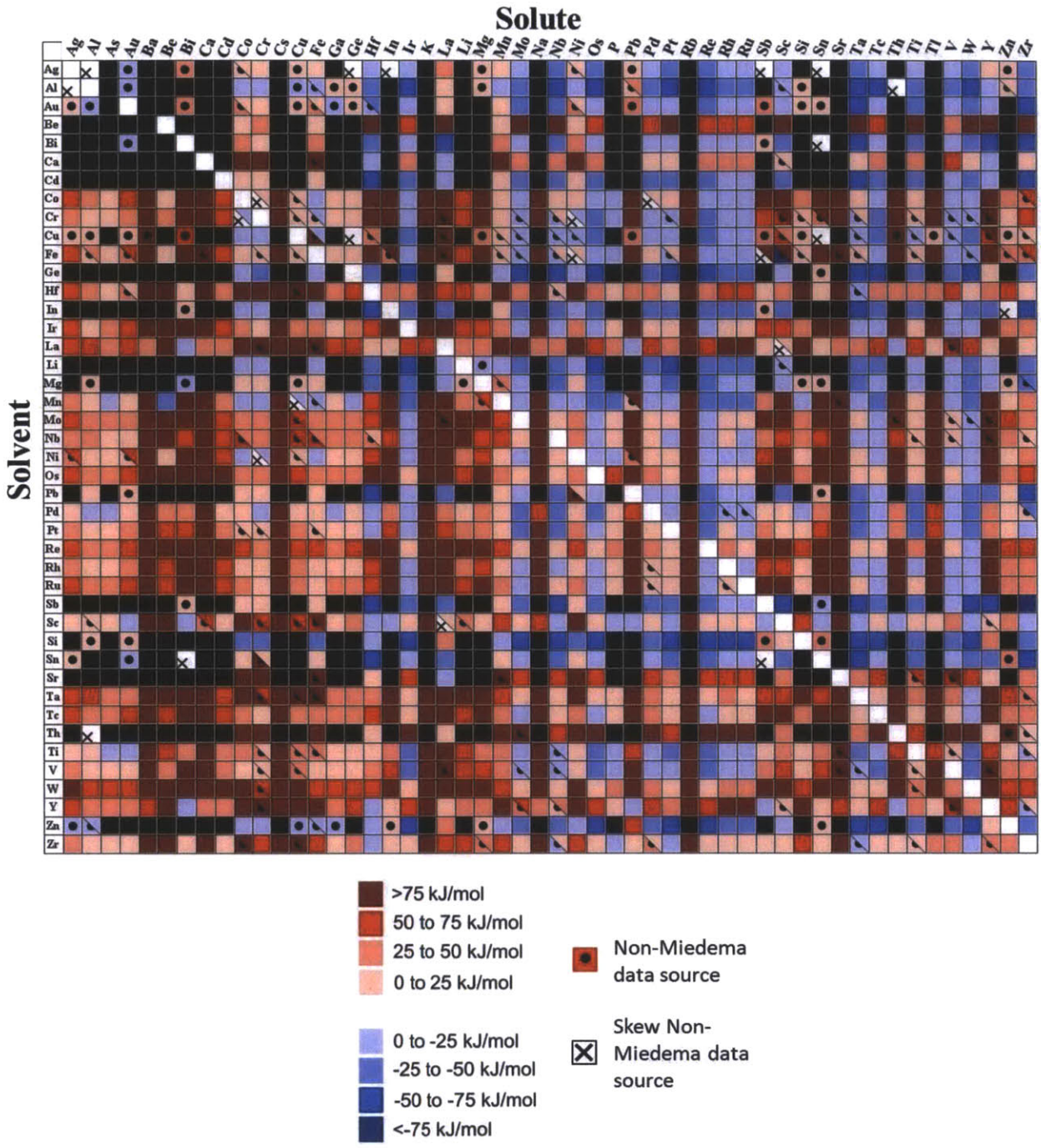

Figure 4.3 Segregation enthalpies for a wide range of binary alloys

4.3 *Comparison to existing segregation data and models*

Figure 4.4 compares our predicted values of segregation enthalpy to the enthalpies predicted by the Hondos-Seah equation (Eq. (4.4)) and the McLean elastic-only model (Eq. (4.5)). Direct comparisons are not possible to the Wynblatt-Ku and Darling models without making assumptions about GB concentration. In both cases, our model ΔH_M^{seg} predicts cases where an alloy would be anti-segregating where ΔH_{H-S}^{seg} and ΔH_{el}^{seg} cannot. For example, in the Cu-Ni system, atomistic modeling shows depletion of nickel at the GBs compared to the bulk [129] with a segregation energy of -7 kJ/mol. The elastic enthalpy prediction, ΔH_{el}^{seg}, is very low, but still positive, 0.6 kJ/mol; the Hondros-Seah equation predicts 21-33 kJ/mol at 300K, which would correlate to definite enrichment of nickel in the GB. However, our model, ΔH_M^{seg} predicts anti-segregation, with an enthalpy of -8 kJ/mol. However, it is difficult to make comparisons to many of the reported segregation values of Table 4.2 due to the dilute nature of ΔH_M^{seg} .

There is no correlation between our segregation enthalpy model and the solubility-based model of Hondros and Seah (Fig. 4.4). As the elastic enthalpy is a component of our model, there is a positive correlation between ΔH_M^{seg} and ΔH_{el}^{seg}, but the chemical and interfacial components are integral in quantifying grain boundary segregation. This comparison between segregation models will be revisited in the following chapter, when predictions of nanocrystalline stability with the existing segregation models are evaluated.

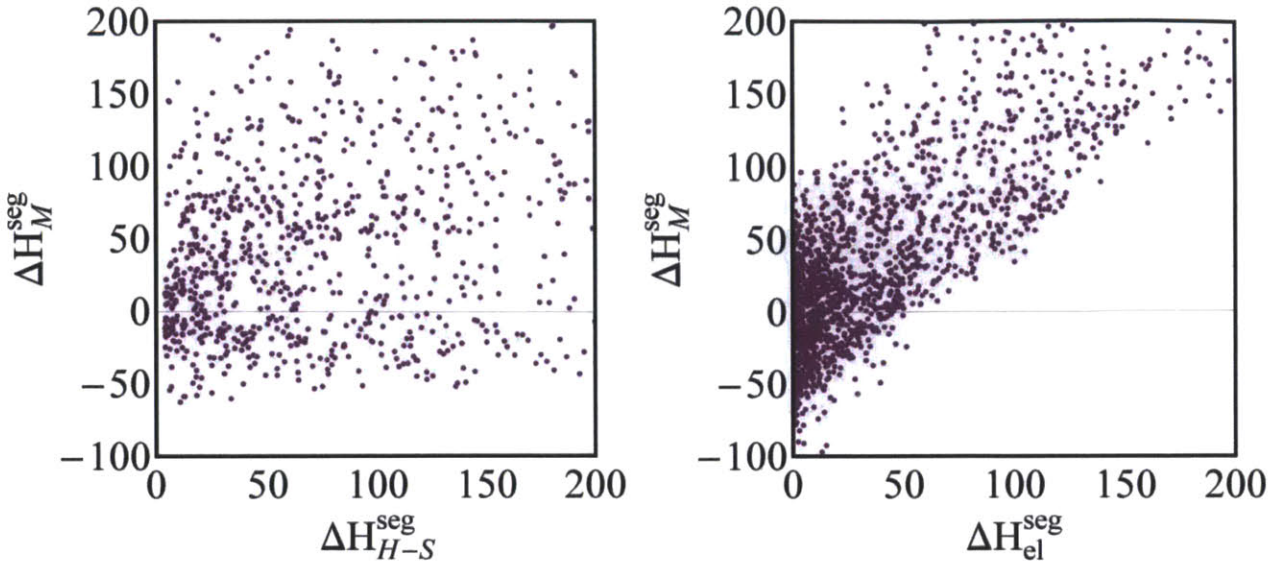

Figure 4.4 ***A comparison of our segregation model, ΔH_M^{seg} , with the Hondros-Seah model (ΔH_{H-S}^{seg}) and elastic-only enthalpy (ΔH_{el}^{seg}).***

4.4 Populating nanocrystalline stability maps

The goal in deriving our GB segregation model and calculating the segregation enthalpy is not to analyze the detailed environment of the grain boundary, but to make predictions about the ability of a binary alloy system to support a nanocrystalline state through solute stabilized GBs. Obviously, detailed atomistic models of specific systems would provide better results regarding the GB segregation behavior, but such atomistic methods do not have the throughput capability of a simple analytical expression of the type derived and presented here. The results of our segregation model combined with calculations of ΔH^{mix} are used to place binary alloys on nanocrystalline stability maps. Several example maps are presented in Fig. 4.5; for simplicity, only Miedema sources of chemical interaction data are presented in this figure with the exception of a handful of alloys which are highlighted to connect with experimental systems. These alloys are indicated on the maps in Fig. 4.5 by larger labels, and are both in italics and underlined if their calculation used sources alternate to Miedema's tables of ΔH_{BinA}^{int}. The connections between our predictions and existing experimental systems will be discussed in the next chapter.

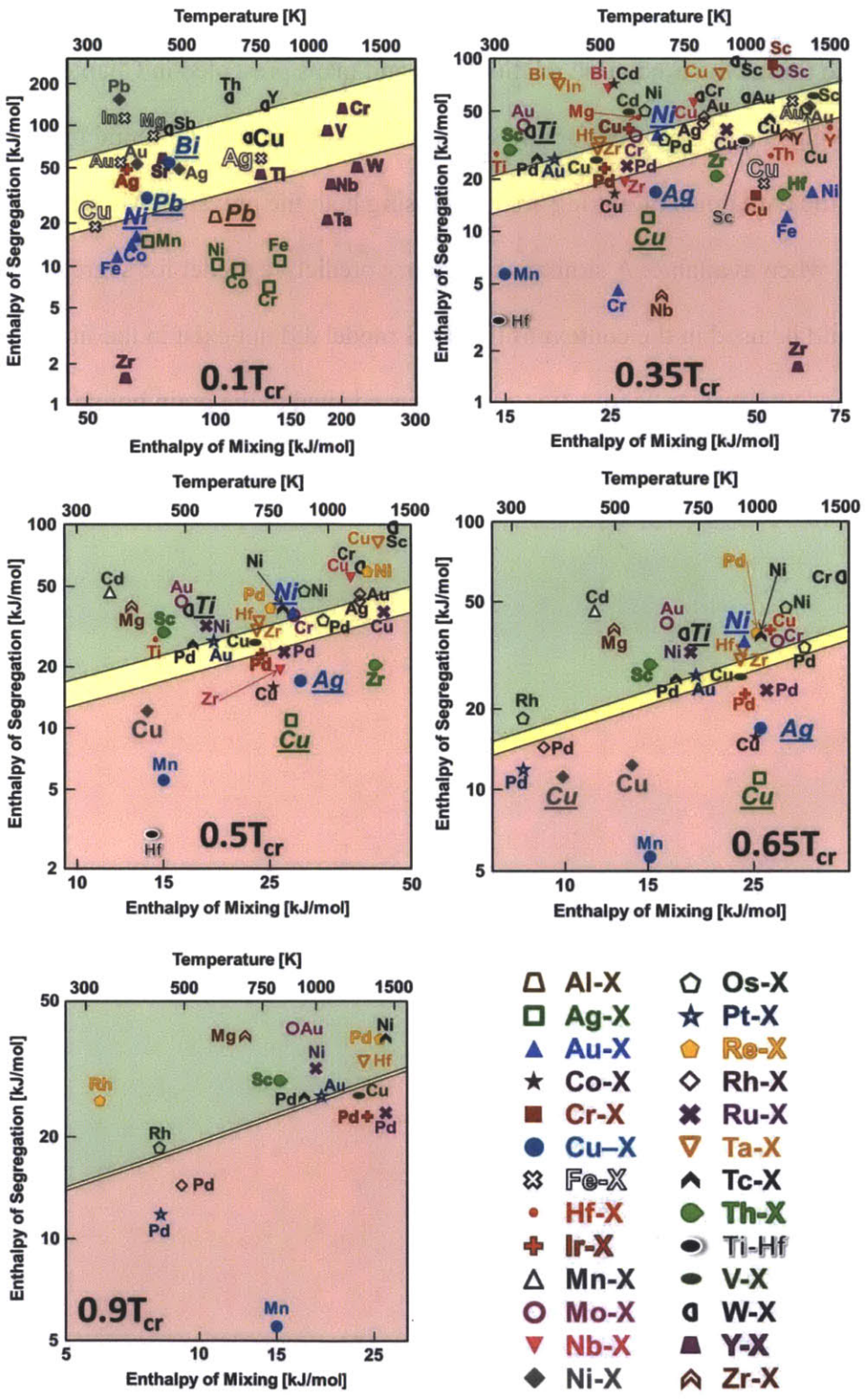

Figure 4.5 Predictions of nanocrystalline stability for a wide range of binary alloys using the models for segregation and mixing enthalpy discussed in this chapter.

4.6 *Conclusions of this Chapter*

In order to utilize the predictive relationships and maps presented in Chapter 3, the enthalpies of mixing and segregation for any given binary system must be found or predicted. Calculations for the enthalpies of mixing are made using both the prevalent Miedema model and the RKM model, when available. A similar satisfactory predictive model for segregation enthalpy that could be used in the context of the RNS model did not exist in the literature, therefore, the Miedema surface segregation model was adapted to the grain boundary environment. After calculating the enthalpies for ~2500 binary alloys, example predictive plots were presented.

5. Connections to Materials Systems

5.1` Previous experimental binary alloys

In the introduction, a variety of previously-produced nanocrystalline binary alloys were evaluated in terms of the available direct observations of their thermal stability. The variations of annealing temperatures and times, compositions, and most importantly observational techniques (i.e. discrepancies between TEM/XRD, lack of TEM observations, no strong evidence for segregation) make direct comparisons difficult. However, we will make an attempt to correlate model predictions with the existing experimental systems. Obviously the best validation of the model would be to make a prediction and then produce the system experimentally according to the predicted temperature and composition parameters; this will be addressed in a subsequent section.

Table 5.1 presents the existing phase-separating experimental systems, separated into predicted metastability (yellow fill) and non-stability (light red fill). The temperatures of prediction are limited to those for which stability maps were constructed, i.e. 0.1, 0.35, 0.5, 0.65, 0.9 T_{cr}; the fractional temperature closest to that of experimental observations was chosen to make the stability prediction based on the figure of merit, $\Delta H^{seg}/(\Delta H^{mix})^a$, using the calculated values of ΔH^{mix} and ΔH^{seg} from our model. Predictions using both the Miedema model source (left-hand column) and other sources (right-hand column) are shown wherever possible.

The columns ΔH_{H-S}^{seg} and ΔH_{el}^{seg} show the values for the enthalpy of segregation using the solubility-based and elastic-based segregation models (discussed in the previous chapter), and what the stability prediction would be if those models were used as the segregation input to the figure of merit (yellow fill: metastable; light red fill: not stable; green fill: predicted complete

stability). They are meant to show the necessity of our constructing the new, more comprehensive segregation model in the preceding chapter.

Table 5.1 Experimental Nanocrystalline Alloys ($\Delta H_{mix}>0$)

Alloy	Ref.	T [K] of prediction	ΔH^{mix} [kJ/mol] Mied.	Non-M.	ΔH_M^{seg} [kJ/mol] Mied.	Non-M.	ΔH_{H-S}^{seg} [kJ/mol]	ΔH_{el}^{seg} [kJ/mol]
W-Cu	[66]	726	121	-	82	-	131	20
Cu-Bi	[35, 49]	469	-	78	-	54	88	63
Cu-Pb	[66]	414	-	67	-	30	79	95
Fe-Ag	[54]	768	128	-	58	-	138	26
Fe-Cu	[51]	312 / 1089 800	52	37	19 / 19	17	61	0.3
Cu-Ag	[62]	652	-	27	-	17	41	15
Ag-Cu	[62]	631	-	30	-	12	40	12
Al-Pb	[42, 43, 90]	601	-	100	-	23	110	35
Au-Ni	[95]	390	65	-	16	-	75	22
Ni-Cu	[12]	548	14	10	12	12	23	0.7
Cu-Ta	[39]	1158	55	105	-14	-27	65	31
Cu-Nb	[63]	734	48	42	-9	-15	58	24
Cu-Fe	[51]	690	52	42	-6	-7	62	0.3
Cu-W	[61]		108	-	-28	-	Large[1]	13

[1] *Solubility is essential zero, so the Log[X_{sol}] ~ ΔH_{H-S}^{seg} is extremely large*

Our segregation model predicts a metastable nanocrystalline state for W-Cu, Fe-Ag, Fe-Cu, Cu-Bi, and Cu-Pb; and no stable nanostructured states for Cu-Ag, Ag-Cu, Al-Pb, Au-Ni, Ni-Cu, Cu-Ta, Cu-Nb, Cu-Fe, and Cu-W. In the metastable cases, the thermodynamically stable phase is the large-grained solid solution, but appropriate segregation negates the driving force for grain growth. For example, in the W-Cu system, the nanostructure is retained after annealing at 673K for one hour, but subsequent phase separation leads to rampant grain growth [66]. Phase separation occurred at 373K in Cu-Pb [66] and at 570K in Fe-Cu [51], triggering grain growth. Minimal grain growth occurred before phase separation in Fe-Ag [54].

Looking at the predicted unstable cases, phase separation and rampant grain growth was observed in the Cu-Ag system [62], and atomistic modeling concluded that silver was not

sufficient to significantly lower the energy of the GBs [35]. Similar conclusions were reached in the Al-Pb system [42, 43, 90], where Pb segregation was found in simulations to have the ability to lower the grain boundary energy of only some sites; experimentally, grain growth and phase separation are observed. It is, however, very difficult to determine true metastability or instability from the experimental studies, due to short anneal times or other factors.

Notable in Table 5.1 is that solubility (ΔH_{H-S}^{seg}) is not an effective measure for alloy element selection for the purposes of nanocrystalline stabilization – it routinely predicts large segregation enthalpies which in turn lead to predictions of complete stability via the figure of merit. It is clear that none of these alloys has shown complete nanocrystalline stability.

For the negative enthalpy of mixing systems, shown in Table 5.2, all comparisons are at 1000K, the only map constructed in this work for such systems. Additionally, the map only plotted stability with respect to an A_3B stoichiometry – only Pd-Fe, Pd-Zr, and Ni-P have their first intermetallic at this composition, and of these Pd-Zr and Ni-P have enthalpies of mixing that are higher in magnitude than the largest calculated parameter set for the negative enthalpy of mixing map (>100 kJ).

In Pd-Fe, which is predicted to be not stable, grain size is somewhat retained up to $0.2T_m$, but substantial growth has occurred in compositions between 8-40%Fe before 1000K, the prediction temperature. Additionally, Fe_2O_3 is observed in alloys with the best low-temperature stability, probably contributing to stability via kinetic pinning.

Table 5.2 Experimental Nanocrystalline Alloys (ΔH_{mix}<0)

Alloy	Ref.	1st intermetallic ΔG [kJ/mol]	ΔH^{mix} [kJ/mol]		ΔH_M^{seg} [kJ/mol]		ΔH_{H-S}^{seg} [kJ/mol]	ΔH_{el}^{seg} [kJ/mol]
			Mied.	Non-M	Mied.	Non-M		
Cu-Zr		Cu_5Zr: -17	-6	2	18	16	Large	57
Cu-Sb		Liquid phase	-	*-20*	-	*36*	*31*	*37*
Pd-Y		Pd_7Y: -2	*-286*	-	*31*	-	*22*	*73*
Pd-Fe		Pd_3Fe: -4	-6	-	5	-	18	9
Pd-Zr		Pd_3Zr: -92	*-338*	*-222*	*-28*	*17*	*20*	*33*
Al-Mg		Liquid @ T	-	*1.6*	*liquid*	*13*	*liquid*	*9*
Al-Cu		Liquid @ T	-	*-51*	*liquid*	*-8*	*liquid*	*10*
Y-Fe		Fe_2Y: -2	*158*	-	*141*	-	*Large*	*146*
Cr-Ni		POSITIVE	*-25*	*X*	*-0.2*	*X*	*42*	*138*
Ni-Co		S.S.	-1	-	-2	-	11	0
Ni-W		Ni_4W: -3	*41*	*X*	*9*	*X*	*16*	*29*
Ni-Fe		S.S.	-5	-	-3	-	14	0.1
Ni-Mn		NiMn: -11	-32	-	10	-	15	0.2
Ni-P		Ni_3P: -49	*-184*	-	*-3*	-	*large*	*0.2*
Ni-Zn		NiZn: -21	-57	-	23	-	13	8
Fe-Al		S.S.	-74	-84	29	22	13	19
Fe-Zr		Fe_2Zr: -30	-35	-19	61	37	large	89
Fe-Ta		Fe_2Ta: -19	-10	13	15	9	large	56
Fe-Ti		Fe_2Ti: -22	-43	-51	22	12	35	36
Fe-Mo		Fe_2Mo: -3	*19*	*28*	*-4*	*-1*	*39*	*19*
Fe-Ni		S.S.	-5	-2	2	X	24	0.1
Fe-Cr		FeCr: -2	-6	11	4	6	25	1.6

We can attempt to draw some conclusions about alloy systems with other stoichiometries. For example, it is reasonable to assume that if a nanocrystalline state is stable with respect to an intermetallic at X=0.25 and free energy of -10 kJ/mol, that it could also be stable against intermetallics at larger compositions but the same free energy. The first intermetallic in the Ni-Mn and Fe-Cr systems is that of an equiatomic composition; in Ni-Mn, a stable "dual-phase" nanocrystalline structures is predicted to exist – this predicts an equilibrium mixture of bulk (not nc) solvent-rich solid solution and very small nanocrystalline solute-rich grains. "Tiny" manganese clusters are observed via atom probe and TEM starting at 600°C (873K) in the Ni-

Mn system while substantial grain growth has occurred in the nickel matrix grains [73]; the bulk phase diagram is a complete solid solution (i.e. not a two-phase region between (Ni) and Ni_3Mn) at the temperature and composition of the experimental alloy.

As predicted, Fe-Cr is not stable at 1000K, showing rapid grain growth prior to this temperature [55]. Using an estimate of the segregation enthalpy based on solubility would predict stability at this temperature. In the predicted stable Fe-Al, no change in grain growth at 1073K (~1000K) was observed [26].

Fe-Ta is predicted to be metastable versus an A_3B intermetallic at the same free energy of the existing Fe_2Ta phase; in the experimental Fe-1%Ta, no Fe_2Ta was observed; however, at only 1%Ta, the expected phases upon decomposition would be >99% Fe(Ta), which is present at 5% in 700°C and 30% in 800°C with grain sizes of several microns. In less agreement is the Fe-Zr system, while predicted to be stable, exhibits Fe_2Zr precipitation at 700°C (1 hour anneal) [58], but again the map is for stability against a different intermetallic. Results for the Fe-Ti system (with Fe_2Ti intermetallic) are only presented at temperatures higher than 1000K, and only show that the alloy is still nanocrystalline, with no discussion of initial versus final grain size [59].

Some alloys have no intermetallics at the temperature presented by the map and composition produced experimentally, thereby allowing comparison via the solid solution line on the nanocrystalline stability map: Ni-Co, Ni-Fe and Fe-Ni. In Ni-37%Co [75], abnormal grain growth consumed the entirety of the nanocrystalline (initial grain size 15nm) material after 120s at 573K – while our prediction for no stability is at 1000K, nc-Ni-Co is clearly unstable. Similarly, Fe-Ni shows significant grain growth prior to 1000K [52, 53]; samples left at room

temperature for one year exhibited abnormal grain growth and phase separation [52]. Depending on the composition, Ni-Fe alloys show either phase separation [72] or significant grain growth [71, 76] prior to 1000K.

Many experimental alloys have problematic data: Y-Fe, Cr-Ni, Fe-Mo, and Ni-W are all compound forming systems that have predicted *positive* enthalpies of mixing based on Miedema model calculations; additionally, Ni-W and Cr-Ni have highly skew RKM models. The Cu-Sb system was produced via ECAE and had an initial grain size of >100nm; additionally, stability was measured in terms of hardness. Both the RKM model and the Miedema model predict positive enthalpies of mixing in the compound-forming Fe-Mo system. The aluminum systems are liquid at 1000K.

5.2 Tungsten based alloys

The preceding analysis of experimental stability in terms of our model serves to show the improved utility over earlier solute selection methods and some brief validation. The primary value of this work, however, is the ability to evaluate potential alloying candidates in terms of their potential to provide complete nanocrystalline stability. To illustrate this process, we choose tungsten as the solvent species, and use the method outlined in this thesis to select an appropriate solute.

While the maps in Chapter 3 were constructed using average values of atomic volume and GB energy, our focus in this case study is on tungsten-based alloys, so we use the specific materials parameters of tungsten (Table 5.3) for the solvent parameters γ_A and Ω_A; average values for the solute, γ_B and Ω_B, are still used, as the solute is an unknown quantity.

Table 5.3 ***Summary of values for W-Ti calculations, including the enthalpy of segregation range. Table adapted from [136].***

Property	Value		Source
ΔH^{mix}	15115.2+3.90656*T[K] J/mol		[137]
Molar Volume, V	W	9.53 cm^3	[138]
	Ti	10.64 cm^3	[139]
γ^s	W	3.675 J/m^2	[120]
	Ti	1.7 J/m^2	[140]
K (bulk W)	310 GPa		[138]
G (shear Ti)	175 GPa		[141]
ΔH^{seg}	47 kJ/mol		
ΔH^{seg} range (Fig. 5.1)	$X_{gb} \rightarrow 0$	39 kJ/mol	[50]
	$X_{gb} \rightarrow 1$	86 kJ/mol	

Experimentally, high energy ball milling is used to produce nanocrystalline tungsten. The powder particles generated via this method must then be consolidated through a sintering treatment into a bulk object. Due to the high melting point of tungsten, the temperature necessary for the appropriate sintering step is considerable, ~1100°C [136]. The nanostructure must be stable at this temperature in order for the compacted material to retain its desirable, as-milled, nanocrystalline grain size. Therefore, we construct a specific nanocrystalline stability map for tungsten-based binary alloys at the temperature 1100°C.

5.2.1 Tungsten alloy nanocrystalline stability map

Following the map construction method of Chapter 3, the stability map for phase-separating tungsten alloys is generated and shown in Fig. 5.1. We treat the metastable region as "bulk stable", in addition to the previously labeled "not stable" region, as in both cases the equilibrium structure is that of a phase-separated system. The alloy points are the Miedema values of ΔH^{mix} and ΔH^{seg} with the exception of W-Ti, whose Miedema model prediction did not correlate well enough with the experimental phase diagram.

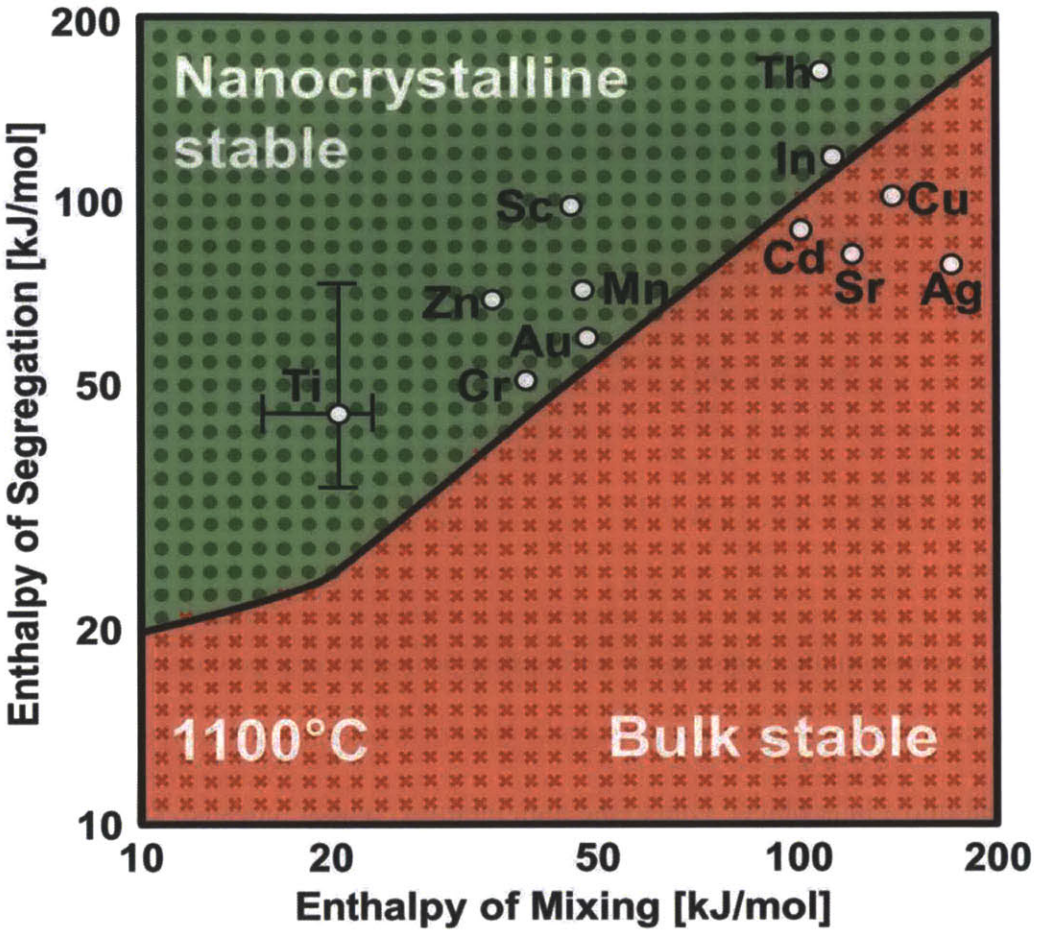

Figure 5.1 Tungsten alloy nanocrystalline stability map at 1100°C. Figure from [136].

The W-Ti point is also distinguished by "range bars", illustrating examples of the variance in available data and models for a particular binary alloy system. W-Ti, for example, has three sources of RKM-style enthalpy of mixing models [137] which creates the horizontal range bar. The bounds of the vertical range – that of the enthalpy of segregation – encompass the values for ΔH^{seg} using our model presented in Chapter 4 for the several values of ΔH_{BinA}^{int} obtained from the three W-Ti RKM ΔH^{mix}. It also includes predictions of the composition-dependent ΔH_D^{seg} model, spanning up to complete saturation of the GB by solute (see Table 5.3).

The W-Ti system has the advantage of being solidly in the stable nanocrystalline region, and being of the "dual-phase" nanostructure subset first predicted by this work [136]. Tungsten-titanium alloys were synthesized by Tongjai Chookajorn in the course of her thesis work (experimental details can be found in Ref. [136]) and her experimental results will be connected to our nanocrystalline stability model.

5.2.2 Dual-phase analysis

To begin, we examine the free energy landscape for W-Ti in greater detail. The free energy plot is shown in Figure 5.2B; the regular solution is in purple, the "classical" nc-tungsten grains in blue, and the nc-titanium-rich grains in red. An example free energy surface for a particular composition is shown in Figure 5.2A.

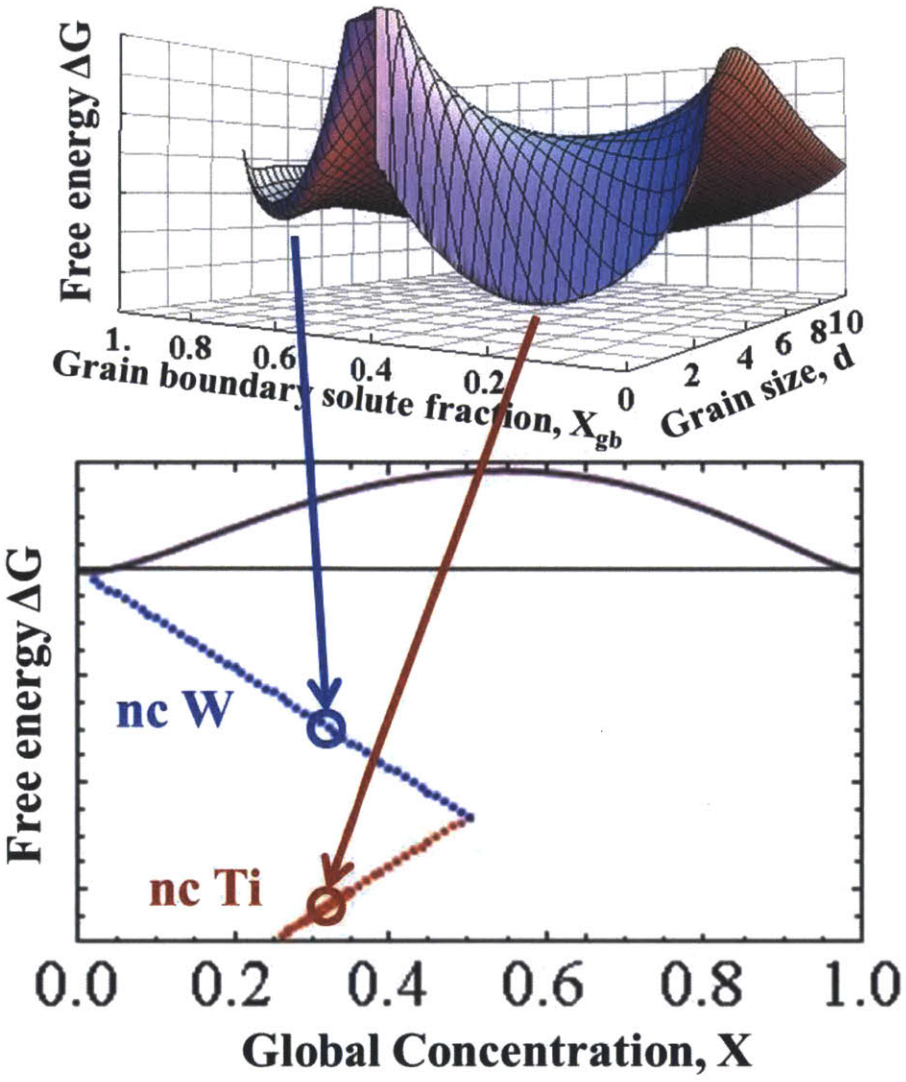

Figure 5.2 Free energy surface and free energy plot for W-Ti at 400K

The plot for 1100°C is shown in Fig 5.3, with the equilibrium phase regions indicated via the common tangent construction. A two phase region of bulk (not nc) tungsten and nc-Ti is expected, in contrast to the bulk expectation of a solid solution, (W) in that region. This difference between the expected equilibrium phases once possible nanocrystalline phases are taken into account, and those presented on the bulk diagram can be seen again in Fig 5.4, where a new phase diagram was constructed on the basis of the stable nc model.

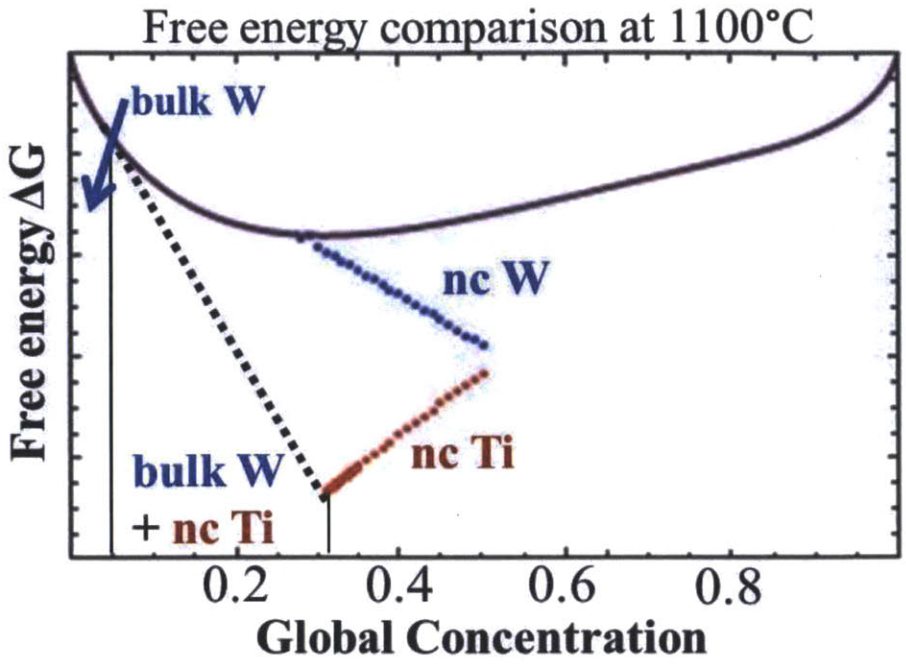

Figure 5.3 Free energy plot and common tangent construction for W-Ti at 1100°C

The thick black lines represent the boundaries of this new two phase region of bulk tungsten and nanocrystalline titanium; the two phase miscibility gap in the bulk diagram is represented by the red and blue hatched region. The grey scale surrounding the thick black lines represents the possible bounds of the two phase region if the enthalpies representing the upper and lower limits of the W-Ti data range lines (Fig 5.1) are used.

Starting with an initial grain size of ~25nm, pure tungsten, and W-Ti alloys of 5%Ti and 20%Ti were annealed at 1100°C for one week. Final microstructures are presented at the top of Fig 5.4 (A – pure W, B – 5%Ti, C – 20%Ti). The pure and 5%Ti samples show considerable grain growth, while the 20% alloy still has grains of ~25nm. A closer examination of the alloyed samples shows an inhomogeneous distribution of solute; in the 5% sample, the white regions (arrow) are titanium-rich.

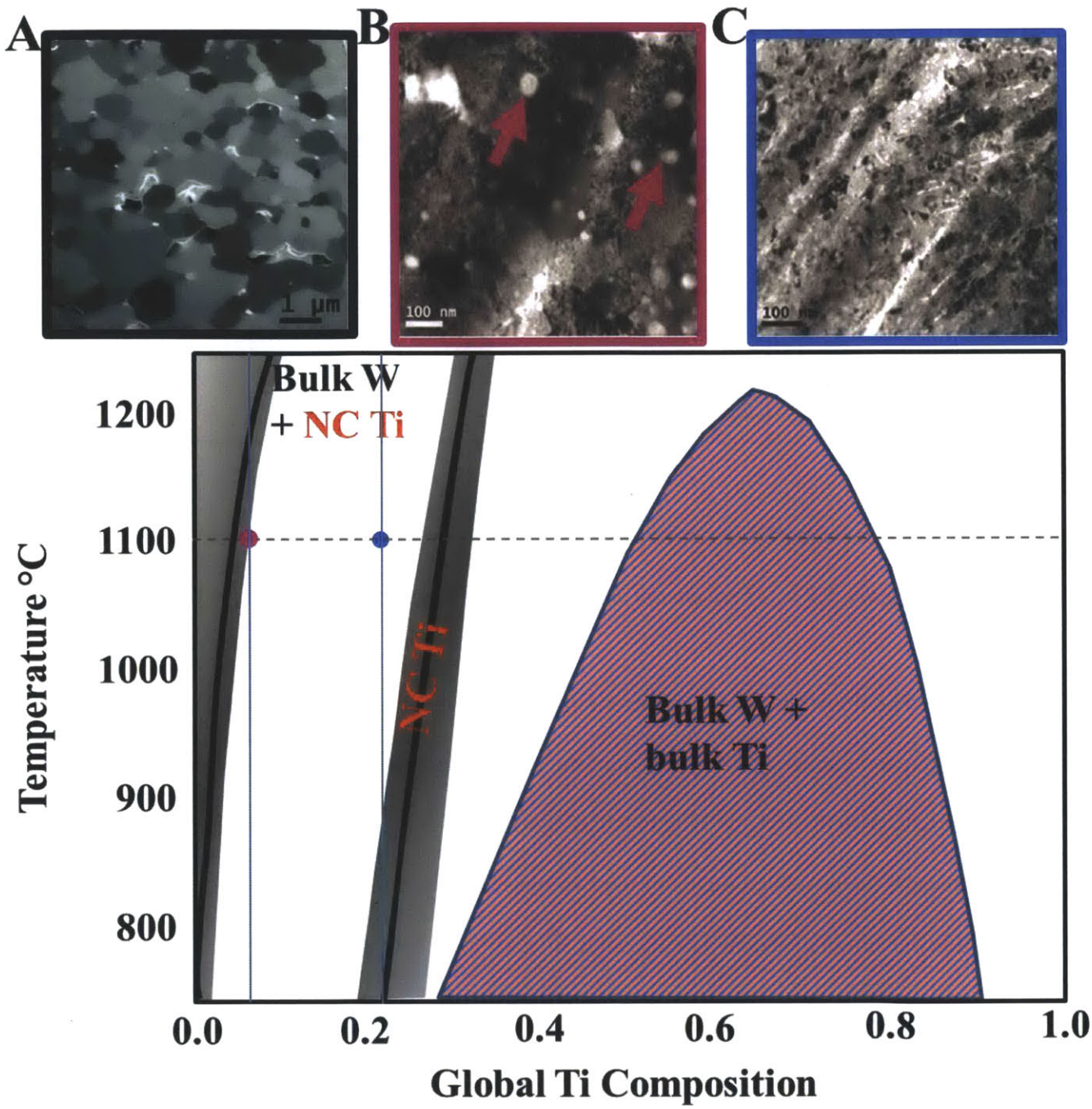

Figure 5.4 Phase diagram for W-Ti taking into account the nanocrystalline phases; the bulk two phase region is in hatched red/blue. Nanocrystalline two-phase region is delineated by black lines. (A) pure W after anneal (B)W-5%Ti after anneal (C) W-20%Ti after anneal. Micrographs courtesy Tongjai Chookajorn.

While the 5%Ti alloy shows the expected bulk (large) W and nanocrystalline titanium phase in small fraction, the 20%Ti alloy shows an entirely nanocrystalline structure. Elemental maps and compositional line scans reveal this structure to be inhomogeneous [136], with distinct W-rich and Ti-rich regions. If we assume the Ti-rich regions are the stable nc-Ti predicted, the nc-W regions require further explanation. At 1100°C and 20%Ti, there are no minima in the free energy surface representing complete lowering to zero of the GB energy of a classical nc-W grain stabilized by Ti GB segregation (Fig. 5.3); however, if we calculate the GB energy at W-20%Ti using the GB concentration of the minima at higher Ti concentrations (blue points in Fig. 5.3), it has been reduced by 94% - significantly lowering the driving force for grain growth. In contrast, in a 5%Ti alloy, the reduction in GB energy is only 22%.

5.3 Conclusions of this Chapter

In this chapter, existing experimental systems where the nanocrystalline stability was studied were compared with model predictions, with good agreement where comparisons were possible. The primary utility of the model, and its attendant stability maps, however, is to select alloys to produce based on stability predictions. One such alloy, W-Ti, is examined in further detail. A nanocrystalline phase diagram is constructed, with good agreement to experimental results.

6. Conclusions

6.1 Summary

The inherent instability of pure nanocrystalline metals disqualifies them from meaningful application; to address this instability, past literature has focused on choosing alloying elements to reduce the grain boundary energy through solute segregation. This approach has garnered some successes, but those alloys which were most successful at stabilizing grain size did *not* have the highest values of the metrics previously used to estimate their efficacy (i.e. ΔH^{seg}). Furthermore, this approach to stabilization only focused on resistance to grain growth; in alloys where a measure of stabilization was achieved through segregation, a second phase often precipitated that disrupted this necessary segregation state and triggered rampant grain growth. A second stability condition, that of the nanocrystalline state's stability against precipitation of other phases needed to be addressed.

To consider both stability conditions (grain growth and phase precipitation), this work extended the RNS model for the free energy of a segregated nanocrystalline solution to use in global free energy comparisons to multiple phases. Once this methodology was established, the design space for binary alloys could be assessed for the important parameters governing the complete stability, metastability, or non-stability of nanostructured phases. The relationship of the enthalpy of segregation to the enthalpy of mixing was found to be the key metric in determining nano-stability (as opposed to the previously presumed enthalpy of segregation alone).

Stability maps were created for a number of conditions (i.e. temperatures, and ranges of enthalpies). These maps have as their axes the two enthalpies (mixing and segregation) rather than the explicit inputs to the RNS model (i.e. interaction parameters) so that connections to

materials systems can be more easily made. However, while the enthalpy of mixing is a common parameter and can be simply estimated for a host of binary alloys, the enthalpy of segregation has long been approximated by either basic models (i.e. as correlating to solubility or to elastic mismatch) or complex, boundary-structure dependent models. Very few experimental or modeled values of the enthalpy of segregation exist, necessitating a new model for enthalpy of segregation that can easily make predictions for a range of alloys. A surface segregation model was adapted to the grain boundary environment in this work to provide the necessary detail for a segregation model to make predictions according to the nanocrystalline stability maps.

Enthalpies were calculated for over 2500 binary alloys, and this information was used to place these alloys on the stability maps generated in this thesis. When possible, connections were made between existing experimental nanocrystalline alloys and our predictions. However, the true value of this work lies in predicting as yet unexplored materials systems that have expectations of nanocrystalline stability. In this work, not only are predictions made about new alloy systems, but also about new types of stable nanostructures. The previously envisioned stable nanocrystalline state, that of solute decorating the grain boundary, is only stable in a narrow range of the enthalpic design space. More common is a dual-phase nanocrystalline state, in which a solute-rich nanostructure is the lowest energy phase. Also appearing is a stable grain boundary, or amorphous phase, for a region of the design space.

One of these new types of stable nanostructures was briefly explored through the creation of a stability map specifically for tungsten alloys at a temperature relevant for material processing. An alloy was selected that would exhibit this dual-phase nanostructure, and a colleague experimentally evaluated the stability with respect to specific phase predictions

through the nanocrystalline stability model. In good agreement, a nanocrystalline solute phase was found to remain nanoscale after one week at this elevated temperature.

6.2 Contributions

Direct contributions from this work to the field of nanocrystalline metals include: a methodology for comparing the free energy of nanocrystalline phases, the prediction of the existence of thermodynamically stable nanostructures, nanocrystalline stability maps enabling the evaluation of prospective binary alloys for nanostructuring, including a specific figure of merit for phase-separating systems, predictions of new types of stable nanocrystalline phases and new stable alloys, and a new model for GB segregation enthalpy. These contributions lead to several important avenues of future study, as described in the next section.

6.3 Future Directions

Some interesting future directions suggested by this work are discussed below:

For compound forming alloys (those with a negative enthalpy of mixing) many additional complications can arise that were not addressed in this work. Only maps for a system with one intermetallic (of a stoichiometry A_3B) were constructed, while the majority of systems have multiple intermetallics that would affect the metastable region of the stability map. Additionally, the free energy of an intermetallic was taken to be that of the bulk phase – however, nanostructuring the compound could cause changes in the free energy through contributions from the grain boundary volume changing the equilibrium phase [142, 143] or changes in the order parameter [45]. Furthermore, in some cases, GB segregation was found experimentally to stabilize intermetallic compounds [110, 144, 145], which may lower the free energy of the compound in the same method as the binary solutions shown in this work. No theory yet exists for segregation stabilization in ordered compounds.

This work presents a "coarse" prediction method for binary alloys, ie. the two enthalpy inputs are not usually a precise representation, with measured and predicted values falling within a range (see an example depiction of this range in Fig. 5.1). Using these inputs allow progress on the overall design problem of predicting stable nanocrystalline alloys, but more detailed methods, i.e. atomistic modeling, would give a more comprehensive picture of segregation in a particular alloy system. As such, those alloys which are predicted to be stable or metastable but near the stable boundary, would benefit from further modeling to assist in experimental production of specific, desired nanostructures.

Finally, this work briefly touched on a new way to model stability of amorphous metals; further examination of the grain boundary regular solution and its ability to predict in a new way the glass forming range of a binary system could provide some new insights as to the suitability of particular alloy systems to amorphization.

References

[1] Kumar KS, Van Swygenhoven H, Suresh S. Mechanical behavior of nanocrystalline metals and alloys. Acta Materialia 2003;51:5743.

[2] Li WL, Tao NR, Han Z, Lu K. Comparisons of dry sliding tribological behaviors between coarse-grained and nanocrystalline copper. Wear 2012;274–275:306.

[3] Gupta RK, Raman RKS, Koch CC. Electrochemical characteristics of nano and microcrystalline Fe-Cr alloys. Journal of Materials Science 2012;47.

[4] Ralston KD, Birbilis N. Effect of Grain Size on Corrosion: A Review. Corrosion 2010;66.

[5] Poudel B, Hao Q, Ma Y, Lan YC, Minnich A, Yu B, Yan XA, Wang DZ, Muto A, Vashaee D, Chen XY, Liu JM, Dresselhaus MS, Chen G, Ren ZF. High-thermoelectric performance of nanostructured bismuth antimony telluride bulk alloys. Science 2008;320:634.

[6] Gertsman VY, Birringer R. ON THE ROOM-TEMPERATURE GRAIN-GROWTH IN NANOCRYSTALLINE COPPER. Scripta Metallurgica Et Materialia 1994;30:577.

[7] Kumpmann A, Günther B, Kunze HD. Thermal stability of ultrafine-grained metals and alloys. Materials Science and Engineering: A 1993;168:165.

[8] Pantleon K, Somers MAJ. Interpretation of microstructure evolution during self-annealing and thermal annealing of nanocrystalline electrodeposits—A comparative study. Materials Science and Engineering: A 2010;528:65.

[9] Ames M, Markmann J, Karos R, Michels A, Tschöpe A, Birringer R. Unraveling the nature of room temperature grain growth in nanocrystalline materials. Acta Materialia 2008;56:4255.

[10] Haber JA, Buhro WE. Kinetic instability of nanocrystalline aluminum prepared by chemical synthesis; Facile room-temperature grain growth. Journal of the American Chemical Society 1998;120:10847.

[11] Natter H, Schmelzer M, Hempelmann R. Nanocrystalline nickel and nickel-copper alloys: Synthesis, characterization, and thermal stability. Journal of Materials Research 1998;13:1186.

[12] Pellicer E, Varea A, Sivaraman KM, Pane S, Surinach S, Dolors Baro M, Nogues J, Nelson BJ, Sort J. Grain Boundary Segregation and Interdiffusion Effects in Nickel-Copper Alloys: An Effective Means to Improve the Thermal Stability of Nanocrystalline Nickel. Acs Applied Materials & Interfaces 2011;3.

[13] Mula S, Bahmanpour H, Mal S, Kang PC, Atwater M, Jian W, Scattergood RO, Koch CC. Thermodynamic feasibility of solid solubility extension of Nb in Cu and their thermal stability. Materials Science and Engineering a-Structural Materials Properties Microstructure and Processing 2012;539.

[14] Moelle CH, Fecht HJ. Thermal stability of nanocrystalline iron prepared by mechanical attrition. Nanostructured Materials 1995;6:421.

[15] Würschum R, Gruß S, Gissibl B, Natter H, Hempelmann R, Schaefer HE. Free volumes and thermal stability of electro-deposited nanocrystalline Pd. Nanostructured Materials 1997;9:615.

[16] Chojnowski G, Przenioslo R, Sosnowska I, Bukowski M, Natter H, Hempelmann R. Microstructure evolution and grain growth kinetics in annealed nanocrystalline chromium. Journal of Physical Chemistry C 2007;111.

[17] Lu L, Tao NR, Wang LB, Ding BZ, Lu K. Grain growth and strain release in nanocrystalline copper. Journal of Applied Physics 2001;89:6408.

[18] Konrad H, Haubold T, Birringer R, Gleiter H. Nanostructured Cu-Bi alloys prepared by co-evaporation in a continuous gas flow. Nanostructured Materials 1996;7:605.

[19] Natter H, Schmelzer M, Loffler MS, Krill CE, Fitch A, Hempelmann R. Grain-growth kinetics of nanocrystalline iron studied in situ by synchrotron real-time X-ray diffraction. Journal of Physical Chemistry B 2000;104:2467.

[20] Darling KA, Chan RN, Wong PZ, Semones JE, Scattergood RO, Koch CC. Grain-size stabilization in nanocrystalline FeZr alloys. Scripta Materialia 2008;59:530.

[21] Wardecki D, Przenioslo R, Fitch AN, Bukowski M, Hempelmann R. Crystal microstructure of annealed nanocrystalline Chromium studied by synchrotron radiation diffraction. Journal of Nanoparticle Research 2011;13:1151.

[22] Hibbard GD, Aust KT, Erb U. The effect of starting nanostructure on the thermal stability of electrodeposited nanocrystalline Co. Acta Materialia 2006;54.

[23] Abdoli H, Ghanbari M, Baghshahi S. Thermal stability of nanostructured aluminum powder synthesized by high-energy milling. Materials Science and Engineering: A 2011;528:6702.
[24] Inami T, Kobiyama M, Okuda S, Maeta H, Ohtsuka H. Grain size measurement of nanocrystalline gold by X-ray diffraction method. Nanostructured Materials 1999;12:657.
[25] Melmed AJ, Tambakis NC, Lau M, Lavernia EJ. APFIM study of impurities in nanocrystalline Fe-Al alloy. Progress in Surface Science 1998;59:313.
[26] Perez RJ, Huang B, Lavernia EJ. Thermal stability of nanocrystalline Fe-10 wt.% Al produced by cryogenic mechanical alloying. Nanostructured Materials 1996;7:565.
[27] Weissmüller J. Alloy effects in nanostructures. Nanostructured Materials 1993;3:261.
[28] Weissmüller J. Some basic notions on nanostructured solids. Materials Science and Engineering: A 1994;179-180:102.
[29] Kirchheim R. Grain coarsening inhibited by solute segregation. Acta Materialia 2002;50:413.
[30] Reiner K. Reducing grain boundary, dislocation line and vacancy formation energies by solute segregation. I. Theoretical background. Acta Materialia 2007;55:5129.
[31] Millett PC, Selvam RP, Bansal S, Saxena A. Atomistic simulation of grain boundary energetics - Effects of dopants. Acta Materialia 2005;53:3671.
[32] Millett PC, Selvam RP, Saxena A. Molecular dynamics simulations of grain size stabilization in nanocrystalline materials by addition of dopants. Acta Materialia 2006;54:297.
[33] Millett PC, Selvam RP, Saxena A. Stabilizing nanocrystalline materials with dopants. Acta Materialia 2007;55:2329.
[34] Bedorf D, Mayr SG. Grain boundary doping of Cu thin films with Bi: A route to create smooth and stable nanocrystalline surfaces. Scripta Materialia 2007;57:853.
[35] Mayr SG, Bedorf D. Stabilization of Cu nanostructures by grain boundary doping with Bi: Experiment versus molecular dynamics simulation. Physical Review B 2007;76:024111.
[36] Vo NQ, Schäfer J, Averback RS, Albe K, Ashkenazy Y, Bellon P. Reaching theoretical strengths in nanocrystalline Cu by grain boundary doping. Scripta Materialia 2011;65:660.
[37] Özerinç S, Tai K, Vo NQ, Bellon P, Averback RS, King WP. Grain boundary doping strengthens nanocrystalline copper alloys. Scripta Materialia 2012;67:720.
[38] Schäfer J, Ashkenazy Y, Albe K, Averback RS. Effect of solute segregation on thermal creep in dilute nanocyrstalline Cu alloys. Materials Science and Engineering: A 2012;546:307.
[39] Frolov T, Darling KA, Kecskes LJ, Mishin Y. Stabilization and strengthening of nanocrystalline copper by alloying with tantalum. Acta Materialia 2012;60:2158.
[40] Rajgarhia R, Saxena A, Spearot D, Hartwig K, More K, Kenik E, Meyer H. Microstructural stability of copper with antimony dopants at grain boundaries: experiments and molecular dynamics simulations. Journal of Materials Science:1.
[41] Rajgarhia R, Spearot D, Saxena A. Molecular Dynamics Simulations of Dislocation Activity in Single-Crystal and Nanocrystalline Copper Doped with Antimony. Metallurgical and Materials Transactions A;41:854.
[42] Purohit Y, Sun L, Irving DL, Scattergood RO, Brenner DW. Computational study of the impurity induced reduction of grain boundary energies in nano- and bi-crystalline Al-Pb alloys. Materials Science and Engineering: A;527:1769.
[43] Purohit Y, Jang S, Irving DL, Padgett CW, Scattergood RO, Brenner DW. Atomistic modeling of the segregation of lead impurities to a grain boundary in an aluminum bicrystalline solid. Materials Science and Engineering: A 2008;493:97.
[44] Purohit Y, Sun L, Shenderova O, Scattergood RO, Brenner DW. First-principles-based mesoscale modeling of the solute-induced stabilization of 〈1 0 0〉 tilt grain boundaries in an Al–Pb alloy. Acta Materialia 2011;59:7022.
[45] Detor. Grain boundary segregation, chemical ordering and stability of nanocrystalline alloys: Atomistic computer simulations in the Ni-W system. Acta Materialia 2007;55:4221.
[46] Trelewicz JR, Schuh CA. Grain boundary segregation and thermodynamically stable binary nanocrystalline alloys. Physical Review B (Condensed Matter and Materials Physics) 2009;79:094112.
[47] VanLeeuwen BK, Darling KA, Koch CC, Scattergood RO, Butler BG. Thermal stability of nanocrystalline Pd81Zr19. Acta Materialia 2010;58.

[48] Atwater MA, Scattergood RO, Koch CC. The stabilization of nanocrystalline copper by zirconium. Materials Science and Engineering: A 2013;559:250.
[49] Chen X, Mao J. Thermal stability and tensile properties of electrodeposited Cu-Bi alloy. Journal of Materials Engineering and Performance 2011;20:481.
[50] Darling KA, VanLeeuwen BK, Semones JE, Koch CC, Scattergood RO, Kecskes LJ, Mathaudhu SN. Stabilized nanocrystalline iron-based alloys: Guiding efforts in alloy selection. Materials Science and Engineering: A 2011;528:4365.
[51] Eckert J, Holzer JC, Johnson WL. THERMAL-STABILITY AND GRAIN-GROWTH BEHAVIOR OF MECHANICALLY ALLOYED NANOCRYSTALLINE FE-CU ALLOYS. Journal of Applied Physics 1993;73:131.
[52] Thuvander M, Abraham M, Cerezo A, Smith GDW. Thermal stability of electrodeposited nanocrystalline nickel and iron-nickel alloys. Materials Science and Technology 2001;17:961.
[53] Kotan H, Saber M, Koch CC, Scattergood RO. Effect of annealing on microstructure, grain growth, and hardness of nanocrystalline Fe–Ni alloys prepared by mechanical alloying. Materials Science and Engineering: A 2012;552:310.
[54] Liu F. Grain growth in nanocrystalline Fe-Ag thin film. Materials Letters 2005;59:1458.
[55] Gupta R, Raman RKS, Koch CC. Grain growth behaviour and consolidation of ball-milled nanocrystalline Fe-10Cr alloy. Materials Science and Engineering a-Structural Materials Properties Microstructure and Processing 2008;494.
[56] Liu F. Precipitation of a metastable Fe(Ag) solid solution upon annealing of supersaturated Fe(Ag) thin film prepared by pulsed laser deposition. Applied Physics A: Materials Science & Processing 2005;81:1095.
[57] Chen Z, Liu F, Yang X, Shen C, Fan Y. Analysis of controlled-mechanism of grain growth in undercooled Fe–Cu alloy. Journal of Alloys and Compounds 2011;509:7109.
[58] Darling KA, VanLeeuwen BK, Koch CC, Scattergood RO. Thermal stability of nanocrystalline Fe-Zr alloys. Materials Science and Engineering: A;527:3572.
[59] Dake JM, Krill Iii CE. Sudden loss of thermal stability in Fe-based nanocrystalline alloys. Scripta Materialia 2012;66:390.
[60] Huang B, Perez RJ, Lavernia EJ. Grain growth of nanocrystalline Fe–Al alloys produced by cryomilling in liquid argon and nitrogen. Materials Science and Engineering: A 1998;255:124.
[61] Atwater MA, Roy D, Darling KA, Butler BG, Scattergood RO, Koch CC. The thermal stability of nanocrystalline copper cryogenically milled with tungsten. Materials Science and Engineering: A 2012;558:226.
[62] Zhu M, Wu Z, Zeng M, Ouyang L, Gao Y. Bimodal growth of the nanophases in the dual-phase composites produced by mechanical alloying in immiscible Cu–Ag system. Journal of Materials Science 2008;43:3259.
[63] Botcharova E, Freudenberger J, Schutz L. High thermal stability of mechanically-alloyed nanocrystalline Cu-Nb alloys. International Journal of Materials Research 2006;97:1350.
[64] Atwater M, Bahmanpour H, Scattergood R, Koch C. The thermal stability of nanocrystalline cartridge brass and the effect of zirconium additions. Journal of Materials Science 2012:1.
[65] Botcharova E, Freudenberger J, Schultz L. Mechanical and electrical properties of mechanically alloyed nanocrystalline Cu-Nb alloys. Acta Materialia 2006;54.
[66] Moon IH, Ryu SS, Kim SW, Won DM, Jang WS. Grain growth in the nanocrystalline W-Cu and Cu-Pb composite powders prepared by mechanical alloying. Zeitschrift Fur Metallkunde 2001;92:986.
[67] Vo NQ, Chee SW, Schwen D, Zhang X, Bellon P, Averback RS. Microstructural stability of nanostructured Cu alloys during high-temperature irradiation. Scripta Materialia 2010;63:929.
[68] Tan LK, Li Y, Ng SC, Lu L. Structures, properties and responses to heat treatment of Cu–Y alloys prepared by mechanical alloying. Journal of Alloys and Compounds 1998;278:201.
[69] Rafailovic LD, Artner W, Nauer GE, Minic DM. Structure, morphology and thermal stability of electrochemically obtained Ni-Co deposits. Thermochimica Acta 2009;496:110.
[70] Detor. Microstructural evolution during the heat treatment of nanocrystalline alloys. Journal of Materials Research 2007;22:3233.
[71] Czerwinski F, Szpunar JA, Erb U. Structural and magnetic characterization of nanocrystalline Ni-20%Fe permalloy films. Journal of Materials Science-Materials in Electronics 2000;11.
[72] Czerwinski F, Li H, Megret M, Szpunar JA, Clark DG, Erb U. THE EVOLUTION OF TEXTURE AND GRAIN SIZE DURING ANNEALING OF NANOCRYSTALLINE Ni-45% Fe ELECTRODEPOSITS. Scripta Materialia 1997;37:1967.

[73] Talin AA, Marquis EA, Goods SH, Kelly JJ, Miller MK. Thermal stability of Ni-Mn electrodeposits. Acta Materialia 2006;54:1935.
[74] Mehta SC, Smith DA, Erb U. Study of grain growth in electrodeposited nanocrystalline nickel-1.2 wt% phosphorus alloy. Materials Science and Engineering a-Structural Materials Properties Microstructure and Processing 1995;204:227.
[75] Hibbard GD, Aust KT, Erb U. Thermal stability of electrodeposited nanocrystalline Ni–Co alloys. Materials Science and Engineering: A 2006;433:195.
[76] Ebrahimi F, Li HQ. Grain growth in electrodeposited nanocrystalline fcc Ni-Fe alloys. Scripta Materialia 2006;55.
[77] Li HQ, Ebrahimi F. An investigation of thermal stability and microhardness of electrodeposited nanocrystalline nickel-21% iron alloys. Acta Materialia 2003;51.
[78] Detor AJ, Miller MK, Schuh CA. Solute distribution in nanocrystalline Ni-W alloys examined through atom probe tomography. Philosophical Magazine 2006;86:4459.
[79] Hentschel T, Isheim D, Kirchheim R, Muller F, Kreye H. Nanocrystalline Ni-3.6 at.% P and its transformation sequence studied by atom-probe field-ion microscopy. Acta Materialia 2000;48:933.
[80] Alfantazi AM, Erb U. Microhardness and thermal stability of pulse-plated Zn-Ni alloy coatings. Materials Science and Engineering a-Structural Materials Properties Microstructure and Processing 1996;212.
[81] Choi P, da Silva M, Klement U, Al-Kassab T, Kirchheim R. Thermal stability of electrodeposited nanocrystalline Co-1.1at.%P. Acta Materialia 2005;53:4473.
[82] da Silva M, Wille C, Klement U, Choi P, Al-Kassab T. Electrodeposited nanocrystalline Co-P alloys: Microstructural characterization and thermal stability. Materials Science and Engineering: A 2007;445-446:31.
[83] Tsyntsaru N, Cesiulis H, Budreika A, Ye X, Juskenas R, Celis JP. The effect of electrodeposition conditions and post-annealing on nanostructure of Co-W coatings. Surface & Coatings Technology 2012;206:4262.
[84] Bryden KJ, Ying JY. Electrodeposition synthesis and hydrogen absorption properties of nanostructured palladium-iron alloys. Nanostructured Materials 1997;9:485.
[85] Bryden KJ, Ying JY. Pulsed electrodeposition synthesis and hydrogen absorption properties of nanostructured palladium-iron alloy films. Journal of the Electrochemical Society 1998;145:3339.
[86] Bryden KJ, Ying JY. Thermal stability and hydrogen absorption characteristics of palladium-yttrium nanoalloys. Acta Materialia 1996;44:3847.
[87] Krill CE, Ehrhardt H, Birringer R. Thermodynamic stabilization of nanocrystallinity. Zeitschrift Fur Metallkunde 2005;96:1134.
[88] Liu F, Kirchheim R. Nano-scale grain growth inhibited by reducing grain boundary energy through solute segregation. Journal of Crystal Growth 2004;264:385.
[89] Rajulapati KV, Scattergood RO, Murty KL, Duscher G, Koch CC. Effect of Pb on the mechanical properties of nanocrystalline Al. Scripta Materialia 2006;55:155.
[90] Wu ZF, Zeng MQ, Ouyang LZ, Zhang XP, Zhu M. Ostwald ripening of Pb nanocrystalline phase in mechanically milled Al-Pb alloys and the influence of Cu additive. Scripta Materialia 2005;53:529.
[91] Zhou F, Liao XZ, Zhu YT, Dallek S, Lavernia EJ. Microstructural evolution during recovery and recrystallization of a nanocrystalline Al-Mg alloy prepared by cryogenic ball milling. Acta Materialia 2003;51.
[92] Hueller M, Vlcek J, Dinkel M, Hoeppel HW, Goeken M. Hardening and thermal stability of nanocrystalline AlMg4.8 powder. Philosophical Magazine 2008;88.
[93] Zhu CJ, Ma XF, Zhao W, Tang HG, Yan JM, Cai SG. Synthesis and thermal stability of Al75W25 alloy obtained by mechanically alloying. Journal of Alloys and Compounds 2005;393:248.
[94] Fogagnolo JB, Amador D, Ruiz-Navas EM, Torralba JM. Solid solution in Al-4.5 wt% Cu produced by mechanical alloying. Materials Science and Engineering a-Structural Materials Properties Microstructure and Processing 2006;433:45.
[95] Rouya E, Stafford GR, Bertocci U, Mallett JJ, Schad R, Begley MR, Kelly RG, Reed ML, Zangari G. Electrodeposition of Metastable Au-Ni Alloys. Journal of the Electrochemical Society 2010;157:D396.
[96] Jankowski AF, Saw CK, Hayes JP. The thermal stability of nanocrystalline Au–Cu alloys. Thin Solid Films 2006;515:1152.
[97] Wang YM, Jankowski AF, Hamza AV. Strength and thermal stability of nanocrystalline gold alloys. Scripta Materialia 2007;57.

[98] Weissmüller J, Krauss W, Haubold T, Birringer R, Gleiter H. Atomic structure and thermal stability of nanostructured Y-Fe alloys. Nanostructured Materials 1992;1:439.
[99] Naka M, Shibayanagi T, Maeda M, Mori M, Mori H. Thermal stability of nanostructured Cr–Ni alloys. Vacuum 2004;73:619.
[100] Alfantazi AM, Page J, Erb U. Pulse plating of Zn-Ni alloy coatings. Journal of Applied Electrochemistry 1996;26:1225.
[101] Abe YR, Holzer JC, Johnson WL. FORMATION AND STABILITY OF NANOCRYSTALLINE NB-CU ALLOYS. Symp on Structure and Properties of Interfaces in Materials, at the 1991 Fall Meeting of the Materials Research Soc, vol. 238. Boston, Ma, 1991. p.721.
[102] Choi P, Al-Kassab T, Gartner F, Kreye H, Kirchheim R. Thermal stability of nanocrystalline nickel-18 at.% tungsten alloy investigated with the tomographic atom probe. Materials Science and Engineering a-Structural Materials Properties Microstructure and Processing 2003;353:74.
[103] Färber B, Cadel E, Menand A, Schmitz G, Kirchheim R. Phosphorus segregation in nanocrystalline Ni-3.6 at.% P alloy investigated with the tomographic atom probe (TAP). Acta Materialia 2000;48:789.
[104] da Silva M, Klement U. A comparison of thermal stability in nanocrystalline Ni- and Co-based materials. Zeitschrift Fur Metallkunde 2005;96:1009.
[105] Detor AJ, Schuh CA. Tailoring and patterning the grain size of nanocrystalline alloys. Acta Materialia 2007;55:371.
[106] Osmola D, Nolan P, Erb U, Palumbo G, Aust KT. Microstructural evolution at large driving forces during grain growth of ultrafine-grained Ni–1.2wt%P. physica status solidi (a) 1992;131:569.
[107] Tsyntsaru N, Cesiulis H, Budreika A, Ye X, Juskenas R, Celis JP. The effect of electrodeposition conditions and post-annealing on nanostructure of Co–W coatings. Surface and Coatings Technology 2012;206:4262.
[108] Hentschel. Nanocrystalline Ni-3.6 at.% P and its transformation sequence studied by atomprobe field-ion microscopy. Acta Materialia 2000;48:933.
[109] Kirchheim R. Reducing grain boundary, dislocation line and vacancy formation energies by solute segregation. I. Theoretical background. Acta Materialia 2007;55:5129.
[110] Fultz B, Frase HN. Grain boundaries of nanocrystalline materials – their widths, compositions, and internal structures. Hyperfine Interactions 2000;130:81.
[111] Ishida K. Effect of grain size on grain boundary segregation. Journal of Alloys and Compounds 1996;235:244.
[112] Murdoch H, Schuh C. Stability of binary nanocrystalline alloys against grain growth and phaseseparation. Acta Materialia 2013;http://dx.doi.org/10.1016/j.actamat.2012.12.033.
[113] Lejcek P, Hofmann S. Thermodynamic State Functions of Interfacial Segregation and Their Role in the Compensation Effect. Reviews on Advanced Materials Science 2009;21:27.
[114] Lejcek P. Grain Boundary Segregation in Metals. Grain Boundary Segregation in Metals 2010;136.
[115] Ikeda T, Numakura H, Koiwa M. A Bragg–Williams model for the thermodynamic activity and the thermodynamic factor in diffusion for ordered alloys with substitutional defects. Acta Materialia 1998;46:6605.
[116] Li JH, Dai Y, Cui YY, Liu BX. Atomistic theory for predicting the binary metallic glass formation. Materials Science and Engineering: R: Reports;72:1.
[117] Menyhard M, Yan M, Vitek V. Atomistic vs phenomenological approaches to grain boundary segregation: Computer modeling of Cu • Ag alloys. Acta Metallurgica et Materialia 1994;42:2783.
[118] Kirchner A, Kieback B. Thermodynamic model of alloy grain boundaries. Scripta Materialia 2011;64:406.
[119] Bakker H. Enthalpies in Alloys: Miedema's Semi-Empirical Model. Enfield, New Hampshire: Trans Tech Publications, 1998.
[120] de Boer FR, Boom R, Mattens WCM, Miedema AR, Niessen AK. Cohesion in Metals: Transition Metal Alloys. 1988.
[121] Udler D, Seidman DN. SOLUTE-ATOM SEGREGATION AT HIGH-ANGLE (002) TWIST BOUNDARIES IN DILUTE AU-PT ALLOYS. Journal of Materials Research 1995;10:1933.
[122] Udler D, Seidman DN. Solute segregation at [001] tilt boundaries in dilute f.c.c. alloys. Acta Materialia 1998;46:1221.
[123] Ruban AV, Skriver HL. Calculated surface segregation in transition metal alloys. Computational Materials Science 1999;15:119.

[124] Ruban AV, Skriver HL, Norskov JK. Surface segregation energies in transition-metal alloys. Physical Review B 1999;59:15990.
[125] Hondros ED, Seah, M.P. The Theory of Grain Boundary Segregation in Terms of Surface Adsorption Analogues. Metallurgical Transactions A 1977;8A:1363.
[126] Seah MP. Grain boundary segregation. Journal of Physics F: Metal Physics 1980;10:1043.
[127] McLean D. Grain Boundaries in Metals: Oxford Clarendon Press, 1957.
[128] Wynblatt P, Chatain D. Anisotropy of segregation at grain boundaries and surfaces. Metallurgical and Materials Transactions A 2006;37:2595.
[129] Foiles SM. CALCULATION OF GRAIN-BOUNDARY SEGREGATION IN NI-CU ALLOYS. Physical Review B 1989;40:11502.
[130] Alber U, Müllejans H, Rühle M. Bismuth segregation at copper grain boundaries. Acta Materialia 1999;47:4047.
[131] Chang LS, Huang KB. Temperature dependence of the grain boundary segregation of Bi in Ni polycrystals. Scripta Materialia 2004;51:551.
[132] Briant CL. Solid solubility and grain boundary segregation. Philosophical Magazine Letters 1996;73.
[133] Friedel J. Electronic structure of primary solid solutions in metals. vol. 3: Taylor & Francis, 1954. p.446
[134] Wynblatt P, Shi Z. Relation between grain boundary segregation and grain boundary character in FCC alloys. Journal of Materials Science 2005;40:2765.
[135] Miedema AR. SURFACE SEGREGATION IN ALLOYS OF TRANSITION-METALS. Zeitschrift Fur Metallkunde 1978;69:455.
[136] Chookajorn T, Murdoch HA, Schuh CA. Design of Stable Nanocrystalline Alloys. Science 2012;337:951.
[137] Kwang Lee S, Nyung Lee D. Calculation of phase diagrams using partial phase diagram data. Calphad 1986;10:61.
[138] Lassner E, Schubert W-D. Tungsten: Properties, Chemistry, Technology of the Element, Alloys, and Chemical Compounds: Springer, 1999.
[139] Skriver HL, Rosengaard NM. Surface energy and work function of elemental metals. Physical Review B 1992;46:7157.
[140] Jones H. The Surface Energy of Solid Metals. Metal Science 1971;5:15.
[141] Senkov ON, Dubois M, Jonas JJ. Elastic moduli of titanium-hydrogen alloys in the temperature range 20 degrees C to 1100 degrees C. Metall. Mater. Trans. A-Phys. Metall. Mater. Sci. 1996;27:3963.
[142] Xu W, Song X, Lu N, Huang C. Thermodynamic and experimental study on phase stability in nanocrystalline alloys. Acta Materialia;58:396.
[143] Xu WW, Song XY, Li ED, Wei J, Zhang JX. Thermodynamic study on phase stability in nanocrystalline Sm--Co alloy system. Journal of Applied Physics 2009;105:104310.
[144] Darling KA, Guduru RK, Reynolds CL, Jr., Bhosle VM, Chan RN, Scattergood RO, Koch CC, Naravan J, Aboelfotoh MO. Thermal stability, mechanical and electrical properties of nanocrystalline Cu3Ge. Intermetallics 2008;16.
[145] Liu KW, Mücklich F. Thermal stability of nano-RuAl produced by mechanical alloying. Acta Materialia 2001;49:395.
[146] CALPHAD. Thermocalc.
[147] Liu XJ, Yamaki T, Ohnuma I, Kainuma R, Ishida K. Thermodynamic calculations of phase equilibria, surface tension and viscosity in the In-Ag-X (X=Bi, Sb) system. Materials Transactions 2004;45:637.
[148] Zhu W, Liu H, Wang J, Dong H, Jin Z. Thermodynamic assessment of the Sn–Ag–Co system and solidification simulation of the ternary alloy. Journal of Alloys and Compounds 2009;481:503.
[149] Saunders N. A review and thermodynamic assessment of the Al-Mg and Mg-Li systems. Calphad 1990;14:61.
[150] Liu XJ, Gao F, Wang CP, Ishida K. Thermodynamic assessments of the Ag-Ni binary and Ag-Cu-Ni ternary systems. Journal of Electronic Materials 2008;37:210.
[151] Oh C-S, Shim J-H, Lee B-J, Dong Nyung L. A thermodynamic study on the Ag • Sb • Sn system. Journal of Alloys and Compounds 1996;238:155.
[152] Gomez-Acebo T. Thermodynamic assessment of the Ag-Zn system. Calphad-Computer Coupling of Phase Diagrams and Thermochemistry 1998;22.

[153] Bo H, Liu LB, Jin ZP. Thermodynamic analysis of Al–Sc, Cu–Sc and Al–Cu–Sc system. Journal of Alloys and Compounds 2010;490:318.
[154] Anglezio JC, Servant C, Ansara I. Contribution to the experimental and thermodynamic assessment of the Al • Ca • Fe • Si system—I. Al • Ca • Fe, Al • Ca • Si, Al • Fe • Si and Ca • Fe • Si systems. Calphad 1994;18:273.
[155] Watson A. Re-assessment of phase diagram and thermodynamic properties of the Al-Ga system. Calphad 1992;16:207.
[156] Li ZS, Liu XJ, Wen MZ, Wang CP, Tang AT, Pan FS. Thermodynamic assessments of the Al–Th and Th–Zn systems. Journal of Nuclear Materials 2010;396:170.
[157] Gao F, Wang C, Liu X, Takaku Y, Ohnuma I, Ishida K. Thermodynamic assessment of phase equilibria in the Sn-Au-Bi system with key experimental verification. Journal of Materials Research 2010;25.
[158] Dong H, Jin S, Zhang L, Wang J, Tao X, Liu H, Jin Z. Thermodynamic Assessment of the Au-Co-Sn Ternary System. Journal of Electronic Materials 2009;38:2158.
[159] Liu Y, Ge Y, Yu D. Thermodynamic descriptions for Au–Fe and Na–Zn binary systems. Journal of Alloys and Compounds 2009;476:79.
[160] Liu J, Guo C, Li C, Du Z. Thermodynamic assessment of the Au-Ga system. Journal of Alloys and Compounds 2010;508.
[161] Wang J, Leinenbach C, Roth M. Thermodynamic modeling of the Au-Ge-Sn ternary system. Journal of Alloys and Compounds 2009;481.
[162] Du ZM, Yang LS. Thermodynamic assessment of the Au-Hf system. Journal of Alloys and Compounds 2003;353:213.
[163] Liu X, Kinaka M, Takaku Y, Ohnuma I, Kainuma R, Ishida K. Experimental investigation and thermodynamic calculation of phase equilibria in the Sn-Au-Ni system. Journal of Electronic Materials 2005;34:670.
[164] Wang J, Liu HS, Jin Z. Thermodynamic assessment of the Au-Pb system. Calphad-Computer Coupling of Phase Diagrams and Thermochemistry 2004;28.
[165] Wang J, Liu YJ, Liu LB, Zhou HY, Jin ZP. Thermodynamic modeling of the Au-Sb-Si ternary system. Journal of Alloys and Compounds 2011;509.
[166] Rudnyi EB, Voronin GF. Thermodynamic assessment of the Ba • Cu • Y ternary system. Direct optimization of the miscibility gap. Calphad 1996;20:297.
[167] Shang S, Liu Z-J, Liu Z-K. Thermodynamic modeling of the Ba–Ni–Ti system. Journal of Alloys and Compounds 2007;430:188.
[168] Manasijevic D, Vrest'al J, Minic D, Kroupa A, Zivkovic D, Zivkovic I. Phase equilibria and thermodynamics of the Bi-Sb-Sn ternary system. Journal of Alloys and Compounds 2007;438.
[169] Bu M, Peng Y, Wang M, Du Y, Xu H, Zhao D, Sha C. Thermodynamic Optimization of the Sc-X (X = La, Li, Ca, Cr) Systems. Journal of Phase Equilibria and Diffusion 2012;33:40.
[170] Oikawa K, Qin GW, Ikeshoji T, Kitakami O, Shimada Y, Ishida K, Fukamichi K. Thermodynamic calculations of phase equilibria of Co-Cr-Pt ternary system and magnetically induced phase separation in the FCC and HCP phases. Journal of Magnetism and Magnetic Materials 2001;236:220.
[171] Wang H, Belegratis MS, Theiner J, Tomiska J. Computer-aided thermodynamic study of solid Co • Pd alloys by Knudsen cell mass spectrometry, and calculation of the phase diagram. Journal of Alloys and Compounds 1995;220:32.
[172] Liu XJ, Zhang HH, Wang CP, Ishida K. Experimental determination and thermodynamic assessment of the phase diagram in the Co–Zr system. Journal of Alloys and Compounds 2009;482:99.
[173] Chan W, Gao MC, Dogan ON, King P, Rollett AD. Thermodynamic Assessment of Cr-Rare Earth Systems. Journal of Phase Equilibria and Diffusion 2009;30:578.
[174] Pérez RJ, Sundman B. Thermodynamic assessment of the CR-SN binary system. Calphad 2001;25:59.
[175] Kaufman L, Turchi PEA, Huang W, Liu Z-K. Thermodynamics of the Cr-Ta-W system by combining the Ab Initio and CALPHAD methods. Calphad 2001;25:419.
[176] Ghosh G. Thermodynamic and kinetic modeling of the Cr-Ti-V system. Journal of Phase Equilibria 2002;23:310.
[177] Wang J, Jin S, Leinenbach C, Jacot A. Thermodynamic assessment of the Cu–Ge binary system. Journal of Alloys and Compounds 2010;504:159.

[178] Liang D, Liu Y. Reevaluation of the Cu–Hf binary system. Journal of Alloys and Compounds 2006;426:101.
[179] Du Z, Xu Y, Zhang W. Thermodynamic assessment of the Cu–La system. Journal of Alloys and Compounds 1999;289:88.
[180] Miettinen J, Vassilev G. THERMODYNAMIC RE-OPTIMIZATION OF THE Cu-Mg-Sn SYSTEM AT THE Cu-Mg SIDE. Journal of Mining and Metallurgy Section B-Metallurgy 2012;48.
[181] Miettinen J. Thermodynamic solution phase data for binary Mn-based systems. Calphad 2001;25:43.
[182] Wang C, Liu X, Ohnuma I, Kainuma R, Ishida K, Hao S. Phase equilibria in the Cu-Fe-Mo and Cu-Fe-Nb systems. Journal of Phase Equilibria 2000;21:54.
[183] Miettinen J, Gandova V, Georgiev S, Vassilev G. Thermodynamic description of the Cu-Ni-Pb system. Central European Journal of Chemistry 2011;9:743.
[184] Gierlotka W, Jendrzejczyk-Handzlik D. Thermodynamic description of the Cu–Sb binary system. Journal of Alloys and Compounds 2009;484:172.
[185] Lany K. Coupled thermochemical and phase diagram data for tantalum based binary alloys. Calphad 1991;15:243.
[186] Wang CP, Li YF, Liu XJ, Ishida K. Thermodynamic assessments of the Cu-Th and Mo-Th systems. Journal of Alloys and Compounds 2008;458:208.
[187] Arroyave R, Eagar TW, Kaufman L. Thermodynamic assessment of the Cu–Ti–Zr system. Journal of Alloys and Compounds 2003;351:158.
[188] Turchanin MA. Phase equilibria and thermodynamics of binary copper systems with 3d-metals. II. The copper-vanadium system. Powder Metallurgy and Metal Ceramics 2006;45:272.
[189] Jantzen T, Spencer PJ. Thermodynamic assessments of the Cu-Pb-Zn and Cu-Sn-Zn systems. Calphad 1998;22:417.
[190] Miettinen J. Thermodynamic reassessment of Fe-Cr-Ni system with emphasis on the iron-rich corner. Calphad-Computer Coupling of Phase Diagrams and Thermochemistry 1999;23.
[191] Ohno M, Yoh K. Thermodynamic Calculation of Phase Equilibria in As-Fe-In Ternary System Based on CALPHAD Approach. Materials Transactions 2009;50:1202.
[192] Povoden-Karadeniz E, Grundy AN, Chen M, Ivas T, Gauckler LJ. Thermodynamic Assessment of the La-Fe-O System. Journal of Phase Equilibria and Diffusion 2009;30:351.
[193] Wang CP, Liu XJ, Ohnuma I, Kainuma R, Hao SM, Ishida K. Phase equilibria in the Cu-Fe-Mo and Cu-Fe-Nb systems. Journal of Phase Equilibria 2000;21:54.
[194] Fredriksson P, Sundman B. A thermodynamic assessment of the Fe-Pt system. Calphad-Computer Coupling of Phase Diagrams and Thermochemistry 2001;25:535.
[195] Pei BY, Bjorkman B, Sundman B, Jansson B. A THERMODYNAMIC ASSESSMENT OF THE IRON - ANTIMONY SYSTEM. Calphad-Computer Coupling of Phase Diagrams and Thermochemistry 1995;19:1.
[196] Liu XJ, Yu P, Wang CP, Ishida K. Thermodynamic evaluation of the Co-Sc and Fe-Sc systems. Journal of Alloys and Compounds 2008;466:169.
[197] Peng Y, Zhao D, Hu B, Zhou L, Du Y, Gang T, Liu S, Chang K. Thermodynamic Modeling of the Sr-M (M = Fe, Mn, Ni, Ti, V) Systems. Journal of Phase Equilibria and Diffusion 2011;32:42.
[198] Witusiewicz VT, Bondar AA, Hecht U, Voblikov VM, Fomichov OS, Petyukh VM, Rex S. Experimental study and thermodynamic re-assessment of the binary Fe-Ta system. Intermetallics 2011;19:1059.
[199] Jonsson S. Assessment of the Fe-Ti system. Metallurgical and Materials Transactions B-Process Metallurgy and Materials Processing Science 1998;29.
[200] Tang Y, Yuan X, Du Y, Xiong W. THERMODYNAMIC MODELING OF THE Fe-Zn SYSTEM USING EXPONENTIAL TEMPERATURE DEPENDENCE FOR THE EXCESS GIBBS ENERGY. Journal of Mining and Metallurgy Section B-Metallurgy 2011;47:1.
[201] Servant C, Gueneau C, Ansara I. EXPERIMENTAL AND THERMODYNAMIC ASSESSMENT OF THE FE-ZR SYSTEM. Journal of Alloys and Compounds 1995;220:19.
[202] Ghosh G, van de Walle A, Asta M, Olson GB. Phase stability of the Hf-Nb system: From first-principles to CALPHAD. Calphad 2002;26:491.
[203] Guillermet AF. Gibbs energy coupling of phase stability and thermochemistry in the Hf-Nb system. Journal of Alloys and Compounds 1996;234:111.
[204] Witusiewicz VT, Hecht U, Boettger B, Rex S. Thermodynamic re-optimisation of the Bi-In-Sn system based on new experimental data. Journal of Alloys and Compounds 2007;428.

[205] Lee BJ. Thermodynamic assessments of the Sn-Zn and In-Zn binary systems. Calphad-Computer Coupling of Phase Diagrams and Thermochemistry 1996;20.
[206] Povoden E, Chen M, Grundy AN, Ivas T, Gauckler LJ. Thermodynamic Assessment of the La-Cr-O System. Journal of Phase Equilibria and Diffusion 2009;30:12.
[207] Chan W, Gao MC, Dogan ON, King P. Thermodynamic Assessment of V-Rare Earth Systems. Journal of Phase Equilibria and Diffusion 2010;31:425.
[208] Oh CS, Kang SY, Lee DN. ASSESSMENT OF THE MG-BI SYSTEM. Calphad-Computer Coupling of Phase Diagrams and Thermochemistry 1992;16.
[209] Grobner J, Mirkovic D, Ohno M, Schmid-Fetzer R. Experimental investigation and thermodynamic calculation of binary Mg-Mn phase equilibria. Journal of Phase Equilibria and Diffusion 2005;26:234.
[210] Miettinen J, Vassilev G. Thermodynamic assessment of the Cu-Mg-Si system in its copper-rich region. Crystal Research and Technology 2011;46:1122.
[211] Qi HY, Huang GX, Bo H, Xu GL, Liu LB, Jin ZP. Experimental investigation and thermodynamic assessment of the Mg-Zn-Gd system focused on Mg-rich corner. Journal of Materials Science 2012;47.
[212] Hamalainen M, Bochvar N, Rokhlin LL, Zeng K. Thermodynamic evaluation of the Cu-Mg-Zr system. Journal of Alloys and Compounds 1999;285:162.
[213] Wang CP, Wang J, Liu XJ, Ohnuma I, Kainuma R, Ishida K. Thermodynamic assessment of the Co-La and Mo-La systems. Journal of Alloys and Compounds 2008;453:174.
[214] Bratberg J, Frisk K. A thermodynamic analysis of the Mo-V and Mo-V-C systems. Calphad-Computer Coupling of Phase Diagrams and Thermochemistry 2002;26:459.
[215] Chan W, Gao MC, Dogan ON, King P. Thermodynamic Assessment of Mo-Ce and Mo-Y Systems. Journal of Phase Equilibria and Diffusion 2010;31:414.
[216] Liu XJ, Jiang ZP, Wang CP, Ishida K. Experimental determination and thermodynamic calculation of the phase equilibria in the Cu–Cr–Nb and Cu–Cr–Co systems. Journal of Alloys and Compounds 2009;478:287.
[217] Zhang YL, Liu HS, Jin ZP. Thermodynamic assessment of the Nb-Ti system. Calphad-Computer Coupling of Phase Diagrams and Thermochemistry 2001;25:305.
[218] Kumar KCH, Wollants P, Delaey L. THERMODYNAMIC CALCULATION OF NB-TI-V PHASE-DIAGRAM. Calphad-Computer Coupling of Phase Diagrams and Thermochemistry 1994;18:71.
[219] Mattern N, Zinkevich M, Loeser W, Behr G, Acker J. Experimental and thermodynamic assessment of the Nb-Ni-Y system. Journal of Phase Equilibria and Diffusion 2008;29:141.
[220] Kumar KCH, Wollants P, Delaey L. THERMODYNAMIC ASSESSMENT OF THE TI-ZR SYSTEM AND CALCULATION OF THE NB-TI-ZR PHASE-DIAGRAM. Journal of Alloys and Compounds 1994;206:121.
[221] Wang CP, Liu XJ, Ohnuma I, Kainuma R, Ishida K. Thermodynamic assessment of the Cu-Ni-Pb system. Calphad-Computer Coupling of Phase Diagrams and Thermochemistry 2000;24:149.
[222] Gürler R. A computer assessment of the ternary Ru-Rh-Pd system. Journal of Nuclear Materials 1992;199:22.
[223] Du ZM. Thermodynamic assessment of the Pd-Zr system. Zeitschrift Fur Metallkunde 2003;94:864.
[224] Wang SL, Wang CP, Liu XJ, Ishida K. Thermodynamic assessments of the Ag-Y and Sc-Y systems. Journal of Alloys and Compounds 2009;476:187.
[225] Liu ZK, Chang YA. Thermodynamic assessment of the Al-Fe-Si system. Metallurgical and Materials Transactions a-Physical Metallurgy and Materials Science 1999;30.
[226] Meng FG, Liu HS, Liu LB, Jin ZP. Thermodynamic description of the Au-Si-Sn system. Journal of Alloys and Compounds 2007;431:292.
[227] Guillermet AF. PHASE-DIAGRAM AND THERMOCHEMICAL PROPERTIES OF THE ZR-TA SYSTEM - AN ASSESSMENT BASED ON GIBBS ENERGY MODELING. Journal of Alloys and Compounds 1995;226:174.
[228] Li ZS, Liu XJ, Wang CP. Thermodynamic modeling of the Th-U, Th-Zr and Th-U-Zr systems. Journal of Alloys and Compounds 2009;476:193.
[229] Kwang Lee S, Nyung Lee D. Calculation of phase diagrams using partial phase diagram data. Calphad;10:61.
[230] Turchanin MA, Agraval PG, Abdulov AR. Thermodynamic assessment of the Cu-Ti-Zr system. II. Cu-Zr and Ti-Zr systems. Powder Metallurgy and Metal Ceramics 2008;47:428.
[231] Chan W, Gao M, Doğan Ö, King P, Rollett A. Thermodynamic Assessment of Cr-Rare Earth Systems. Journal of Phase Equilibria and Diffusion 2009;30:578.

[232] Bu MJ, Wang PS, Xu HH, Liu SH, Sha CS, Du Y, Pan FS, Tang AT. EXPERIMENTAL INVESTIGATION AND THERMODYNAMIC MODELING OF THE Zr-Y SYSTEM. Journal of Mining and Metallurgy Section B-Metallurgy 2010;46:181.
[233] Mathon M, Jardet K, Aragon E, Satre P, Sebaoun A. Al-Ga-Zn System: Reassessments of the Three Binary Systems and Discussion on Possible Estimations and on Optimisation of the Ternary System. Calphad 2000;24:253.

Appendix A

Appendix A contains the table of all enthalpy values (Miedema and RKM sourced) for the alloys

Alloy	Miedema model			RKM model			Source
	ΔH^{mix}	ΔH^{seg}	ΔH^{int}	ΔH^{mix}	ΔH^{seg}	ΔH^{int}	
Ag-Ag	0	0	0	0	0	0	
Ag-Al	-	-	-	99	99	10.5454 - 0.0058 T	[146]
Ag-As	-	-	-	0	0	0	
Ag-Au	-	-	-	-15599	-7889	-16	[146]
Ag-Ba	-	-	-	0	0	0	
Ag-Be	-	-	-	0	0	0	
Ag-Bi	-	-	-	11976	25074	-18.5568 - 0.0160 T	[147]
Ag-Ca	-	-	-	0	0	0	
Ag-Cd	-	-	-	0	0	0	
Ag-Co	112335	9638	69	77000	19920	76	[148]
Ag-Cr	133669	7220	98	0	0	0	
Ag-Cs	-	-	-	0	0	0	
Ag-Cu	-	-	-	25696	12170	23.5277 - 0.0094 T	[146]
Ag-Fe	140903	11015	103	0	0	0	
Ag-Ga	-	-	-	0	0	0	
Ag-Ge	-	-	-	14126	99	19.1808 + 0.0111 T	[146]
Ag-Hf	-28921	-24196	-53	0	0	0	
Ag-In	-	-	-	99	99	-2.5331 - 0.0020 T	[147]
Ag-Ir	83405	-24308	62	0	0	0	
Ag-K	-	-	-	0	0	0	
Ag-La	-56831	25961	-143	0	0	0	
Ag-Li	-	-	-	0	0	0	
Ag-Mg	-	-	-	1607	15192	-2.2256 - 0.0040 T	[149]
Ag-Mn	68971	15096	46	0	0	0	
Ag-Mo	151614	-20987	147	0	0	0	
Ag-Na	-	-	-	0	0	0	
Ag-Nb	67112	-30569	66	0	0	0	
Ag-Ni	100650	10361	56	57720	16142	23.2292 + 0.0031 T	[150]
Ag-Os	132862	-27065	111	0	0	0	
Ag-P	-	-	-	0	0	0	
Ag-Pb	-	-	-	32469	19622	-32.7331 + 0.0303 T	[146]
Ag-Pd	-20000	-16402	-29	0	0	0	
Ag-Pt	8093	-25026	-3	0	0	0	
Ag-Rb	-	-	-	0	0	0	
Ag-Re	165051	-29982	151	0	0	0	
Ag-Rh	57296	-17732	37	0	0	0	
Ag-Ru	115647	-18333	91	0	0	0	
Ag-Sb	-	-	-	99	99	-99.3336 + 0.0837 T	[147]
Ag-Sc	-89913	-6552	-119	0	0	0	

Ag-Si	-	-	-	0	0	0	
Ag-Sn	-	-	-	99	99	-2.6560 + 0.0087 T	[151]
Ag-Sr	-	-	-	0	0	0	
Ag-Ta	61885	-42062	61	0	0	0	
Ag-Tc	112124	-23413	96	0	0	0	
Ag-Th	-	-	-	0	0	0	
Ag-Ti	-5301	-22780	-6	0	0	0	
Ag-Tl	-	-	-	0	0	0	
Ag-V	73839	-13872	63	0	0	0	
Ag-W	175584	-35824	172	0	0	0	
Ag-Y	-54585	10456	-136	0	0	0	
Ag-Zn	-	-	-	-23700	7938	-26.0733 + 0.0008 T	[152]
Ag-Zr	-59694	-29437	-87	0	0	0	
Al-Ag	-	-	-	99	99	10.7354 - 0.0058 T	[146]
Al-Al	0	0	-	0	0	0	
Al-As	-	-	-	0	0	0	
Al-Au	-	-	-	-68204	-20862	-151.0210 + 0.0469 T	[146]
Al-Ba	-	-	-	0	0	0	
Al-Be	-	-	-	0	0	0	
Al-Bi	-	-	-	0	0	0	
Al-Ca	-	-	-	0	0	0	
Al-Cd	-	-	-	0	0	0	
Al-Co	-85043	-16631	-105	0	0	0	
Al-Cr	-60442	-17810	-74	0	0	0	
Al-Cs	-	-	-	0	0	0	
Al-Cu	-	-	-	-51353	-7886	-101.6454 + 0.0001 T	[153]
Al-Fe	-62118	-15899	-79	-47330	-10094	-103.0999 + 0.0267 T	[154]
Al-Ga	-	-	-	17383	1080	13.8820 + 0.0082 T	[155]
Al-Ge	-	-	-	10460	7152	10	[146]
Al-Hf	-180709	-45388	-215	0	0	0	
Al-In	-	-	-	0	0	0	
Al-Ir	-144273	-54706	-163	0	0	0	
Al-K	-	-	-	0	0	0	
Al-La	-125023	13202	-231	0	0	0	
Al-Li	-	-	-	0	0	0	
Al-Mg	-	-	-	1607	12744	-3.4082 - 0.0040 T	[149]
Al-Mn	-102012	-7256	-106	0	0	0	
Al-Mo	-62427	-49362	-65	0	0	0	
Al-Na	-	-	-	0	0	0	
Al-Nb	-117205	-55130	-121	0	0	0	
Al-Ni	-96829	-15887	-118	0	0	0	

Al-Os	-98844	-57774	-115	0	0	0	
Al-P	-	-	-	0	0	0	
Al-Pb	-	45717	-	100000	23455	50	[146]
Al-Pd	-217306	-43708	-230	0	0	0	
Al-Pt	-210397	-55059	-229	0	0	0	
Al-Rb	-	-	-	0	0	0	
Al-Re	-68470	-60813	-79	0	0	0	
Al-Rh	-153982	-46178	-169	0	0	0	
Al-Ru	-109210	-48114	-126	0	0	0	
Al-Sb	-	-	-	0	0	0	
Al-Sc	-158288	-17560	-195	-107000	-6026	-131.3042 + 0.0025 T	[153]
Al-Si	-	-	-	-6340	5321	-7.7724 - 0.0026 T	[154]
Al-Sn	-	-	-	0	0	0	
Al-Sr	-	-	-	0	0	0	
Al-Ta	-69329	-66238	-124	0	0	0	
Al-Tc	-111444	-53361	-124	0	0	0	
Al-Th	-	-	-	99	99	-96.0958 - 0.0083 T	[156]
Al-Ti	-161647	-43698	-162	0	0	0	
Al-Tl	-	-	-	0	0	0	
Al-V	-102059	-36921	-101	0	0	0	
Al-W	-50679	-65599	-54	0	0	0	
Al-Y	-124700	-1831	-221	0	0	0	
Al-Zn	-	7092	-	7802	7859	-1.1631 + 0.0062 T	[146]
Al-Zr	-201005	-49546	-240	0	0	0	
Au-Ag	-	-	-	-15599	4472	-16	[146]
Au-Al	-	-	-	-68204	-3030	-151.2387 + 0.0468 T	[146]
Au-As	-	-	-	0	0	0	
Au-Au	0	0	0	0	0	0	
Au-Ba	-	-	-	0	0	0	
Au-Be	-	-	-	0	0	0	
Au-Bi	-	-	-	48000	36008	18	[157]
Au-Ca	-	-	-	0	0	0	
Au-Cd	-	-	-	0	0	0	
Au-Co	62781	14206	25	27766	35139	9.3331 + 0.0051 T	[158]
Au-Cr	25752	4467	-1	0	0	0	
Au-Cs	-	-	-	0	0	0	
Au-Cu	-	-	-	-18278	19794	-51.4656 + 0.0788 T - 0.0100 T Log[T]	[146]
Au-Fe	58397	11681	28	16677	29864	1.5948 - 0.0081 T	[159]
Au-Ga	-	-	-	-61363	-767	-25.4244 - 0.0551 T	[160]
Au-Ge	-	-	-	-12915	16764	9.4825 - 0.0231 T	[161]
Au-Hf	-240702	-45640	-257	-85110	-8470	-10.9738 - 0.0160 T	[162]

Au-In	-	-	-	0	0	0	
Au-Ir	62129	-17911	48	0	0	0	
Au-K	-	-	-	0	0	0	
Au-La	-127920	4799	-328	0	0	0	
Au-Li	-	-	-	0	0	0	
Au-Mg	-	-	-	0	0	0	
Au-Mn	-23626	13615	-39	0	0	0	
Au-Mo	14535	-29433	13	0	0	0	
Au-Na	-	-	-	0	0	0	
Au-Nb	-127832	-47304	-124	0	0	0	
Au-Ni	64918	16451	25	18378	35253	17.0636 - 0.0176 T	[163]
Au-Os	83846	-23873	68	0	0	0	
Au-P	-	-	-	0	0	0	
Au-Pb	-	-	-	30000	25535	4	[164]
Au-Pd	3759	-5259	0	0	0	0	
Au-Pt	21216	-15246	17	0	0	0	
Au-Rb	-	-	-	0	0	0	
Au-Re	85828	-30996	76	0	0	0	
Au-Rh	41090	-10537	27	0	0	0	
Au-Ru	74589	-14053	56	0	0	0	
Au-Sb	-	-	-	49513	28279	0.0604 + 0.0250 T	[165]
Au-Sc	-285142	-24138	-291	0	0	0	
Au-Si	-	-	-	2000	22076	-3	[165]
Au-Sn	-	-	-	-34325	16832	-65.6840 + 0.0076 T	[157]
Au-Sr	-	-	-	0	0	0	
Au-Ta	-128502	-58766	-125	0	0	0	
Au-Tc	63243	-20407	52	0	0	0	
Au-Th	-	-	-	0	0	0	
Au-Ti	-191555	-37580	-180	0	0	0	
Au-Tl	-		-	0	0	0	
Au-V	-70788	-21633	-69	0	0	0	
Au-W	46703	-43951	44	0	0	0	
Au-Y	-256456	-9853	-318	0	0	0	
Au-Zn	-	-	-	0	0	0	
Au-Zr	-285377	-51640	-303	0	0	0	
Ba-Ag	-	-	-	0	0	0	
Ba-Al	-	-	-	0	0	0	
Ba-As	-	-	-	0	0	0	
Ba-Au	-	-	-	0	0	0	
Ba-Ba	0	0	-	0	0	0	
Ba-Be	-	-	-	0	0	0	

Ba-Bi	-	-	-	0	0	0	
Ba-Ca	-	-	-	0	0	0	
Ba-Cd	-	-	-	0	0	0	
Ba-Co	200605	123986	32	0	0	0	
Ba-Cr	334628	124915	141	0	0	0	
Ba-Cs	-	-	-	0	0	0	
Ba-Cu	-	-	-	-3828	92697	-121.3380 + 0.0034 T	[166]
Ba-Fe	290225	128081	104	0	0	0	
Ba-Ga	-	-	-	0	0	0	
Ba-Ge	-	-	-	0	0	0	
Ba-Hf	301739	32357	169	0	0	0	
Ba-In	-	-	-	0	0	0	
Ba-Ir	118878	68874	-43	0	0	0	
Ba-K	-	-	-	0	0	0	
Ba-La	96619	153	57	0	0	0	
Ba-Li	-	-	-	0	0	0	
Ba-Mg	-	-	-	0	0	0	
Ba-Mn	248639	124467	81	0	0	0	
Ba-Mo	413221	86024	216	0	0	0	
Ba-Na	-	-	-	0	0	0	
Ba-Nb	426531	68527	244	0	0	0	
Ba-Ni	162765	122445	1	341686	144262	320	[167]
Ba-Os	220094	72871	44	0	0	0	
Ba-P	-	-	-	0	0	0	
Ba-Pb	-	-	-	0	0	0	
Ba-Pd	-60419	65981	-185	0	0	0	
Ba-Pt	-8747	56269	-152	0	0	0	
Ba-Rb	-	-	-	0	0	0	
Ba-Re	311710	70696	124	0	0	0	
Ba-Rh	87860	78586	-63	0	0	0	
Ba-Ru	189496	81930	19	0	0	0	
Ba-Sb	-	-	-	0	0	0	
Ba-Sc	179744	37959	89	0	0	0	
Ba-Si	-	-	-	0	0	0	
Ba-Sn	-	-	-	0	0	0	
Ba-Sr	-	-	-	0	0	0	
Ba-Ta	413959	51593	233	0	0	0	
Ba-Tc	203847	76050	34	0	0	0	
Ba-Th	-	-	-	0	0	0	
Ba-Ti	330416	73251	170	403506	96059	356	[167]
Ba-Tl	-	-	-	0	0	0	

Ba-V	348346	99981	163	0	0	0	
Ba-W	283628	41581	22	0	0	0	
Ba-Y	124654	12449	68	0	0	0	
Ba-Zn	-	-	-	0	0	0	
Ba-Zr	286081	36846	163	0	0	0	
Be-Ag	-	-	-	0	0	0	
Be-Al	-	-	-	0	0	0	
Be-As	-	-	-	0	0	0	
Be-Au	-	-	-	0	0	0	
Be-Ba	-	-	-	0	0	0	
Be-Be	0	0	-	0	0	0	
Be-Bi	-	-	-	0	0	0	
Be-Ca	-	-	-	0	0	0	
Be-Cd	-	-	-	0	0	0	
Be-Co	-3155	11802	-26	0	0	0	
Be-Cr	2856	33002	-41	0	0	0	
Be-Cs	-	-	-	0	0	0	
Be-Cu	-	-	-	0	0	0	
Be-Fe	7020	13560	-25	0	0	0	
Be-Ga	-	-	-	0	0	0	
Be-Ge	-	-	-	0	0	0	
Be-Hf	49285	226231	-209	0	0	0	
Be-In	-	-	-	0	0	0	
Be-Ir	61080	67216	-38	0	0	0	
Be-K	-	-	-	0	0	0	
Be-La	-8550	223070	-184	0	0	0	
Be-Li	-	-	-	0	0	0	
Be-Mg	-	-	-	0	0	0	
Be-Mn	-248462	17165	-54	0	0	0	
Be-Mo	109568	78317	-43	0	0	0	
Be-Na	-	-	-	0	0	0	
Be-Nb	45080	115688	-134	0	0	0	
Be-Ni	-6972	13763	-27	0	0	0	
Be-Os	79969	55979	-20	0	0	0	
Be-P	-	-	-	0	0	0	
Be-Pb	-	-	-	0	0	0	
Be-Pd	31592	70093	-50	0	0	0	
Be-Pt	41307	90751	-61	0	0	0	
Be-Rb	-	-	-	0	0	0	
Be-Re	109390	64974	-11	0	0	0	
Be-Rh	44161	51802	-39	0	0	0	

Be-Ru	54578	50915	-25	0	0	0	
Be-Sb	-	-	-	0	0	0	
Be-Sc	-28353	188061	-191	0	0	0	
Be-Si	-	-	-	0	0	0	
Be-Sn	-	-	-	0	0	0	
Be-Sr	-	-	-	0	0	0	
Be-Ta	83256	137301	-132	0	0	0	
Be-Tc	73191	51628	-25	0	0	0	
Be-Th	-	-	-	0	0	0	
Be-Ti	-27436	93639	-158	0	0	0	
Be-Tl	-	-	-	0	0	0	
Be-V	-12028	46533	-84	0	0	0	
Be-W	144692	89107	-27	0	0	0	
Be-Y	15504	221933	-190	0	0	0	
Be-Zn	-	-	-	0	0	0	
Be-Zr	-16441	166075	-239	0	0	0	
Bi-Ag	-	-	-	0	0	0	
Bi-Al	-	-	-	0	0	0	
Bi-As	-	-	-	0	0	0	
Bi-Au	-	-	-	8000	-5775	-36	[157]
Bi-Ba	-	-	-	0	0	0	
Bi-Be	-	-	-	0	0	0	
Bi-Bi	0	0	-	0	0	0	
Bi-Ca	-	-	-	0	0	0	
Bi-Cd	-	-	-	0	0	0	
Bi-Co	111133	30670	4	0	0	0	
Bi-Cr	136838	24210	33	0	0	0	
Bi-Cs	-	-	-	0	0	0	
Bi-Cu	-	-	-	0	0	0	
Bi-Fe	148850	31022	39	0	0	0	
Bi-Ga	-	-	-	0	0	0	
Bi-Ge	-	-	-	0	0	0	
Bi-Hf	-89635	-45923	-15	0	0	0	
Bi-In	-	-	-	0	0	0	
Bi-Ir	91641	-12174	-3	0	0	0	
Bi-K	-	-	-	0	0	0	
Bi-La	-272577	-50687	-276	0	0	0	
Bi-Li	-	-	-	0	0	0	
Bi-Mg	-	-	-	0	0	0	
Bi-Mn	43161	27055	-31	0	0	0	
Bi-Mo	156617	-14114	74	0	0	0	

Bi-Na	-	-	-	0	0	0	
Bi-Nb	21796	-37219	-12	0	0	0	
Bi-Ni	97928	31428	-8	0	0	0	
Bi-Os	151556	-13367	47	0	0	0	
Bi-P	-	-	-	0	0	0	
Bi-Pb	-	-	-	0	0	0	
Bi-Pd	-64797	-9850	-118	0	0	0	
Bi-Pt	-6096	-17995	-75	0	0	0	
Bi-Rb	-	-	-	0	0	0	
Bi-Re	187015	-19247	84	0	0	0	
Bi-Rh	48262	-4763	-36	0	0	0	
Bi-Ru	128924	-3944	27	0	0	0	
Bi-Sb	-	-	-	16450	4945	7.9735 + 0.0063 T	[168]
Bi-Sc	-218814	-45241	-197	0	0	0	
Bi-Si	-	-	-	0	0	0	
Bi-Sn	-	-	-	99	99	99	[168]
Bi-Sr	-	-	-	0	0	0	
Bi-Ta	16020	-52189	-19	0	0	0	
Bi-Tc	120447	-10898	27	0	0	0	
Bi-Th	-	-	-	0	0	0	
Bi-Ti	-77967	-31398	-93	0	0	0	
Bi-Tl	-	-	-	0	0	0	
Bi-V	54096	-4583	-10	0	0	0	
Bi-W	190037	-31222	101	0	0	0	
Bi-Y	-260105	-53208	-249	0	0	0	
Bi-Zn	-	-	-	0	0	0	
Bi-Zr	-213843	-63557	-196	0	0	0	
Ca-Ag	-	-	-	0	0	0	
Ca-Al	-	-	-	0	0	0	
Ca-As	-	-	-	0	0	0	
Ca-Au	-	-	-	0	0	0	
Ca-Ba	-	-	-	0	0	0	
Ca-Be	-	-	-	0	0	0	
Ca-Bi	-	-	-	0	0	0	
Ca-Ca	0	0	-	0	0	0	
Ca-Cd	-	-	-	0	0	0	
Ca-Co	146516	80903	8	0	0	0	
Ca-Cr	266073	82029	114	0	0	0	
Ca-Cs	-	-	-	0	0	0	
Ca-Cu	-	-	-	0	0	0	
Ca-Fe	226060	84810	77	120705	76252	11	[154]

Ca-Ga	-	-	-	0	0	0	
Ca-Ge	-	-	-	0	0	0	
Ca-Hf	207487	-1781	133	0	0	0	
Ca-In	-	-	-	0	0	0	
Ca-Ir	62526	26205	-73	0	0	0	
Ca-K	-	-	-	0	0	0	
Ca-La	37538	-15301	32	0	0	0	
Ca-Li	-	-	-	0	0	0	
Ca-Mg	-	-	-	0	0	0	
Ca-Mn	187280	83298	58	0	0	0	
Ca-Mo	325943	43597	182	0	0	0	
Ca-Na	-	-	-	0	0	0	
Ca-Nb	326665	28163	207	0	0	0	
Ca-Ni	112607	79493	-22	0	0	0	
Ca-Os	155715	29851	13	0	0	0	
Ca-P	-	-	-	0	0	0	
Ca-Pb	-	-	-	0	0	0	
Ca-Pd	-101777	24763	-208	0	0	0	
Ca-Pt	-58803	14302	-182	0	0	0	
Ca-Rb	-	-	-	0	0	0	
Ca-Re	238101	27950	92	0	0	0	
Ca-Rh	36062	36068	-90	0	0	0	
Ca-Ru	128459	38973	-11	0	0	0	
Ca-Sb	-	-	-	0	0	0	
Ca-Sc	102915	7566	61	56572	7223	27	[169]
Ca-Si	-	-	-	0	0	0	
Ca-Sn	-	-	-	0	0	0	
Ca-Sr	-	-	-	0	0	0	
Ca-Ta	316233	11657	196	0	0	0	
Ca-Tc	140301	33292	4	0	0	0	
Ca-Th	-	-	-	0	0	0	
Ca-Ti	242449	34191	138	0	0	0	
Ca-Tl	-	-	-	0	0	0	
Ca-V	270729	58084	135	0	0	0	
Ca-W	333330	23037	187	0	0	0	
Ca-Y	56726	-9898	42	0	0	0	
Ca-Zn	-	-	-	0	0	0	
Ca-Zr	191470	2405	127	0	0	0	
Cd-Ag	-	-	-	0	0	0	
Cd-Al	-	-	-	0	0	0	
Cd-As	-	-	-	0	0	0	

Cd-Au	-	-	-	0	0	0	
Cd-Ba	-	-	-	0	0	0	
Cd-Be	-	-	-	0	0	0	
Cd-Bi	-	-	-	0	0	0	
Cd-Ca	-	-	-	0	0	0	
Cd-Cd	0	0	-	0	0	0	
Cd-Co	61538	12229	-4	0	0	0	
Cd-Cr	91769	6997	34	0	0	0	
Cd-Cs	-	-	-	0	0	0	
Cd-Cu	-	-	-	0	0	0	
Cd-Fe	93846	12663	32	0	0	0	
Cd-Ga	-	-	-	0	0	0	
Cd-Ge	-	-	-	0	0	0	
Cd-Hf	-110022	-53053	-109	0	0	0	
Cd-In	-	-	-	0	0	0	
Cd-Ir	22733	-31882	-30	0	0	0	
Cd-K	-	-	-	0	0	0	
Cd-La	-133976	-13108	-192	0	0	0	
Cd-Li	-	-	-	0	0	0	
Cd-Mg	-	-	-	0	0	0	
Cd-Mn	20736	12231	-18	0	0	0	
Cd-Mo	101524	-29659	72	0	0	0	
Cd-Na	-	-	-	0	0	0	
Cd-Nb	14510	-45097	9	0	0	0	
Cd-Ni	48425	12744	-18	0	0	0	
Cd-Os	75527	-33168	22	0	0	0	
Cd-P	-	-	-	0	0	0	
Cd-Pb	-	-	-	0	0	0	
Cd-Pd	-97279	-26819	-129	0	0	0	
Cd-Pt	-61285	-36515	-102	0	0	0	
Cd-Rb	-	-	-	0	0	0	
Cd-Re	109794	-37852	64	0	0	0	
Cd-Rh	-5412	-23639	-53	0	0	0	
Cd-Ru	58411	-23618	4	0	0	0	
Cd-Sb	-	-	-	0	0	0	
Cd-Sc	-142160	-32123	-144	0	0	0	
Cd-Si	-	-	-	0	0	0	
Cd-Sn	-	-	-	0	0	0	
Cd-Sr	-	-	-	0	0	0	
Cd-Ta	8644	-58660	3	0	0	0	
Cd-Tc	53044	-29947	7	0	0	0	

Cd-Th	-	-	-	0	0	0	
Cd-Ti	-58371	-36883	-58	0	0	0	
Cd-Tl	-	-	-	0	0	0	
Cd-V	32263	-18683	5	0	0	0	
Cd-W	122988	-46844	92	0	0	0	
Cd-Y	-133719	-24752	-177	0	0	0	
Cd-Zn	-	-	-	0	0	0	
Cd-Zr	-137615	-54932	-138	0	0	0	
Co-Ag	95264	54567	84	0	0	0	
Co-Al	-99335	25977	-124	0	0	0	
Co-As	-95970	15622	-149	0	0	0	
Co-Au	63040	56984	33	0	0	0	
Co-Ba	-23686	240619	65	0	0	0	
Co-Be	-2601	15749	-21	0	0	0	
Co-Bi	72255	117008	8	0	0	0	
Co-Ca	-236893	169473	13	0	0	0	
Co-Cd	25387	69775	-5	0	0	0	
Co-Co	0	0	0	0	0	0	
Co-Cr	-16450	2720	-18	8045	99	-11.0298 + 0.0194 T	[170]
Co-Cs	97766	200456	353	0	0	0	
Co-Cu	25520	15989	25	30543	16643	32	[146]
Co-Fe	-1231	-527	-2	0	0	0	
Co-Ga	-52909	20804	-96	0	0	0	
Co-Ge	-61624	22670	-89	0	0	0	
Co-Hf	-46214	78532	-168	0	0	0	
Co-In	14610	108277	-18	0	0	0	
Co-Ir	5363	-6318	-15	0	0	0	
Co-K	120810	170954	293	0	0	0	
Co-La	1855	145336	-93	0	0	0	
Co-Li	107997	52419	30	0	0	0	
Co-Mg	16641	79646	3	0	0	0	
Co-Mn	-20046	13781	-21	0	0	0	
Co-Mo	20358	-4296	-22	0	0	0	
Co-Na	98422	114475	180	0	0	0	
Co-Nb	-46908	11239	-111	0	0	0	
Co-Ni	-951	2237	-1	0	0	0	
Co-Os	18762	-16166	0	0	0	0	
Co-P	-190383	-1323	-213	0	0	0	
Co-Pb	77305	164046	32	0	0	0	
Co-Pd	11917	14296	-7	99	99	99	[171]
Co-Pt	-7017	8221	-33	0	0	0	

Co-Rb	99468	204073	323	0	0	0	
Co-Re	36548	-16047	9	0	0	0	
Co-Rh	5774	-3081	-9	0	0	0	
Co-Ru	9614	-9108	-3	0	0	0	
Co-Sb	31185	76157	-62	0	0	0	
Co-Sc	-66424	89592	-139	0	0	0	
Co-Si	14965	43724	138	0	0	0	
Co-Sn	57893	133594	-62	0	0	0	
Co-Sr	-22979	223622	53	0	0	0	
Co-Ta	-31549	11684	-109	0	0	0	
Co-Tc	19597	-11517	-1	0	0	0	
Co-Th	6481	158017	-166	0	0	0	
Co-Ti	-81386	17815	-126	0	0	0	
Co-Tl	59797	132085	40	0	0	0	
Co-V	-46872	-3455	-58	0	0	0	
Co-W	43800	-11619	-6	0	0	0	
Co-Y	-2025	128449	-112	0	0	0	
Co-Zn	-42355	27515	-49	0	0	0	
Co-Zr	-87071	53642	-197	-47428	37602	-131	[172]
Cr-Ag	127130	47370	120	0	0	0	
Cr-Al	-67078	20010	-87	0	0	0	
Cr-As	-105994	7770	-156	0	0	0	
Cr-Au	28398	40754	-1	0	0	0	
Cr-Ba	131195	256178	299	0	0	0	
Cr-Be	-3615	26982	-33	0	0	0	
Cr-Bi	116461	111060	61	0	0	0	
Cr-Ca	140522	178909	196	0	0	0	
Cr-Cd	71572	64156	46	0	0	0	
Cr-Co	-16469	-1485	-18	8045	99	-10.9162 + 0.0188 T	[170]
Cr-Cr	0	0	0	0	0	0	
Cr-Cs	254655	224003	628	0	0	0	
Cr-Cu	50195	16041	49	85330	20164	95.0886 - 0.0100 T	[146]
Cr-Fe	-5874	-1676	-6	10820	32	20.3649 - 0.0097 T	[146]
Cr-Ga	-12483	17370	-50	0	0	0	
Cr-Ge	-52729	16043	-77	0	0	0	
Cr-Hf	49497	85334	-44	0	0	0	
Cr-In	72255	104141	50	0	0	0	
Cr-Ir	-62828	-24252	-78	0	0	0	
Cr-K	267726	188120	516	0	0	0	
Cr-La	138801	155706	93	40000	85451	-76	[173]
Cr-Li	135747	57531	131	0	0	0	

Cr-Mg	102591	79113	98	0	0	0	
Cr-Mn	8525	15095	8	0	0	0	
Cr-Mo	27912	-13001	2	20928	-16300	-6.6997 - 0.0054 T	[146]
Cr-Na	97760	123003	329	0	0	0	
Cr-Nb	13612	8449	-32	30414	-11613	-31.8768 - 0.0057 T	
Cr-Ni	-24868	-233	-27	99	99	-18.9776 - 0.0002 T	[146]
Cr-Os	-34566	-31641	-46	0	0	0	
Cr-P	-248816	-11117	-274	0	0	0	
Cr-Pb	125873	160044	88	0	0	0	
Cr-Pd	-47157	-2586	-65	0	0	0	
Cr-Pt	-84231	-12458	-110	-105000	-19242	-123	[170]
Cr-Rb	254189	223441	571	0	0	0	
Cr-Re	-2796	-30424	-19	0	0	0	
Cr-Rh	-47689	-17651	-58	0	0	0	
Cr-Ru	-41470	-23550	-49	0	0	0	
Cr-Sb	53568	67631	-34	0	0	0	
Cr-Sc	54588	95020	3	38778	64650	-35.6913 + 0.0012 T	[169]
Cr-Si	-113321	2914	-134	-93843	8856	-76.1507 - 0.0020 T	
Cr-Sn	108192	132065	-10	26991	36290	-189.7966 + 0.0204 T	[174]
Cr-Sr	378859	237288	271	0	0	0	
Cr-Ta	26315	9606	-30	36943	-7597	-53.9542 + 0.0056 T	[175]
Cr-Tc	-25707	-25634	-39	0	0	0	
Cr-Th	136727	173727	12	0	0	0	
Cr-Ti	-3169	16737	-33	6894	6713	-35.9096 + 0.0091 T	[176]
Cr-Tl	119082	128278	110	0	0	0	
Cr-V	-3245	-6777	-8	-12937	-10218	-12.9202 - 0.0090 T	[176]
Cr-W	36290	-22583	4	31520	-24125	-1	[175]
Cr-Y	130699	137670	59	69000	104820	-2	[173]
Cr-Zn	-4557	24877	-9	0	0	0	
Cr-Zr	22694	59148	-58	0	0	0	
Cu-Ag	-	-	-	25745	15672	9.3077 - 0.0107 T	
Cu-Al	-	-	-	-51353	3437	-111.2690 - 0.0002 T	[153]
Cu-As	-	-	-	0	0	0	
Cu-Au	-	-	-	-18278	6894	-55.2644 + 0.0788 T - 0.0100 T Log[T]	[146]
Cu-Ba	-	-	-	-3828	94372	-10.7387 + 0.0034 T	
Cu-Be	-	-	-	0	0	0	
Cu-Bi	-	-	-	77869	54121	-26	
Cu-Ca	-	-	-	0	0	0	
Cu-Cd	-	-	-	0	0	0	
Cu-Co	27524	-8620	26	0	0	0	[146]
Cu-Cr	49996	-3525	51	0	0	0	[146]

Cu-Cs	-	-	-	0	0	0	
Cu-Cu	0	0	0	0	0	0	
Cu-Fe	51841	-6145	53	5561873	645791	-0.2917 + 5.5619 T	[146]
Cu-Ga	-	-	-	0	0	0	
Cu-Ge	-	-	-	99	99	-12.4755 + 0.0283 T	[177]
Cu-Hf	29082	31961	-81	-26000	39577	-125	[178]
Cu-In	-	-	-	0	0	0	
Cu-Ir	2182	-25730	1	0	0	0	
Cu-K	-	-	-	0	0	0	
Cu-La	16348	96148	-115	100000	85962	-7	[179]
Cu-Li	-	-	-	0	0	0	
Cu-Mg	-	-	-	-15227	36699	-58.3115 + 0.0083 T	[180]
Cu-Mn	15159	5577	15	9300	5763	19.7494 - 0.0035 T	[181]
Cu-Mo	90652	-16694	82	83144	-14012	69	[182]
Cu-Na	-	-	-	0	0	0	
Cu-Nb	47642	-8733	12	40472	-15258	-0.2035 - 0.0052 T	[182]
Cu-Ni	16829	-7689	14	11168	-7877	10.1863 + 0.0010 T	[183]
Cu-Os	42601	-31037	46	0	0	0	
Cu-P	-	-	-	0	0	0	
Cu-Pb	-	-	-	49394	27603	-46.1626 - 0.0247 T	[183]
Cu-Pd	-50600	-12850	-62	0	0	0	
Cu-Pt	-45274	-19285	-56	0	0	0	
Cu-Rb	-	-	-	0	0	0	
Cu-Re	77844	-30200	82	0	0	0	
Cu-Rh	-8785	-21679	-11	0	0	0	
Cu-Ru	28383	-23740	31	0	0	0	
Cu-Sb	-	-	-	-19910	36394	-101.5515 - 0.0064 T	[184]
Cu-Sc	-20609	47263	-115	-3890	51189	-84	[153]
Cu-Si	-	-	-	-28313	6920	-49.6755 + 0.0329 T	[146]
Cu-Sn	-	-	-	-12159	99	-159.7593 - 0.0101 T	[180]
Cu-Sr	-	-	-	0	0	0	
Cu-Ta	55045	-14344	9	104600	-2663	57	[185]
Cu-Tc	35626	-26689	37	0	0	0	
Cu-Th	-	-	-	1600	75685	-180	[186]
Cu-Ti	-5591	-1598	-40	-9882	-2667	-43	[187]
Cu-Tl	-	-	-	54500	21827	-28	
Cu-V	25023	-13336	21	55000	-10105	50	[188]
Cu-W	107666	-27533	101	0	0	0	
Cu-Y	31102	78285	-117	-67720	70358	-248.9774 + 0.0234 T	[166]
Cu-Zn	-	-	-	-32261	12662	-49.5023 + 0.0113 T	[189]
Cu-Zr	-5993	17819	-110	2233	15681	-96	[187]

Fe-Ag	127798	57682	123	0	0	0	
Fe-Al	-73627	28598	-91	-83930	22134	-121.2022 + 0.0351 T	[154]
Fe-As	-86318	17117	-131	0	0	0	
Fe-Au	59952	55775	37	22347	27848	4.6406 - 0.0124 T	[159]
Fe-Ba	71499	256451	213	0	0	0	
Fe-Be	5171	18529	-20	0	0	0	
Fe-Bi	115696	122789	71	0	0	0	
Fe-Ca	126868	181519	129	120233	103483	82	[154]
Fe-Cd	63068	73804	42	0	0	0	
Fe-Co	-1302	243	-2	0	0	0	
Fe-Cr	-5919	3737	-6	10820	5995	20.4249 - 0.0097 T	[190]
Fe-Cs	195774	219502	522	0	0	0	
Fe-Cu	51764	18932	50	35108	17047	38.9591 - 0.0041 T	[146]
Fe-Fe	0	0	0	0	0	0	
Fe-Ga	-22175	24654	-55	0	0	0	
Fe-Ge	-43740	24761	-64	0	0	0	
Fe-Hf	-3992	85679	-98	0	0	0	
Fe-In	60870	113811	43	41457	35934	-32.8661 + 0.0224 T	[191]
Fe-Ir	-23989	-10389	-38	0	0	0	
Fe-K	214003	186519	433	0	0	0	
Fe-La	81364	157672	25	54028	104530	-40.5965 + 0.0237 T	[192]
Fe-Li	127374	59451	94	0	0	0	
Fe-Mg	72131	85781	68	0	0	0	
Fe-Mn	1057	16605	1	-1522	16338	-2.8021 + 0.0012 T	[146]
Fe-Mo	19429	-4287	-9	27678	-1398	9.3429 - 0.0030 T	[146]
Fe-Na	170873	124969	277	0	0	0	
Fe-Nb	-23032	14408	-70	1933	-2724	-58.9598 + 0.0063 T	[193]
Fe-Ni	-4922	2124	-6	-2244	99	-3.8354 + 0.0006 T	[146]
Fe-Os	-5767	-19458	-17	0	0	0	
Fe-P	-208119	-2951	-229	0	0	0	
Fe-Pb	122094	170008	95	0	0	0	
Fe-Pd	-5043	11622	-19	0	0	0	
Fe-Pt	-37333	3611	-59	-175000	-23575	-311.3234 + 0.0710 T	[194]
Fe-Rb	196125	221137	477	0	0	0	
Fe-Re	16132	-18678	-1	0	0	0	
Fe-Rh	-13643	-5801	-23	0	0	0	
Fe-Ru	-12160	-12227	-20	0	0	0	
Fe-Sb	60533	80029	-16	31044	99	-36.2872 + 0.0263 T	[195]
Fe-Sc	-1792	98170	-53	-17527500	-1996183	-75.4391 - 17.5000 T	[196]
Fe-Si	-105822	11852	-122	-97767	22436	-49.5270 + 0.0465 T	[154]
Fe-Sn	92310	138873	-8	0	0	0	

Fe-Sr	64005	238271	191	93199	124316	181	[197]
Fe-Ta	-10123	15039	-67	12871	8790	-54.0047 + 0.0094 T	[198]
Fe-Tc	279	-14141	-13	0	0	0	
Fe-Th	73439	170073	-58	0	0	0	
Fe-Ti	-43355	22337	-74	-51247	12146	-72.9277 - 0.0006 T	[199]
Fe-Tl	109846	138216	106	0	0	0	
Fe-V	-23701	-1141	-29	0	0	0	
Fe-W	33806	-12559	0	41544	-5296	22	[146]
Fe-Y	70530	139447	-6	0	0	0	
Fe-Zn	-10582	30929	-14	7642	31981	-3	[200]
Fe-Zr	-35220	61444	-118	-19000	37318	-97	[201]
Ga-Ag	-	-	-	0	0	0	
Ga-Al	-	-	-	0	0	0	
Ga-As	-	-	-	0	0	0	
Ga-Au	-	-	-	-61363	-16773	-35.7811 - 0.0530 T	[160]
Ga-Ba	-	-	-	0	0	0	
Ga-Be	-	-	-	0	0	0	
Ga-Bi	-	-	-	0	0	0	
Ga-Ca	-	-	-	0	0	0	
Ga-Cd	-	-	-	0	0	0	
Ga-Co	-22518	-10811	-74	0	0	0	
Ga-Cr	3574	-12368	-38	0	0	0	
Ga-Cs	-	-	-	0	0	0	
Ga-Cu	-	-	-	0	0	0	
Ga-Fe	3353	-9833	-43	0	0	0	
Ga-Ga	0	0	-	0	0	0	
Ga-Ge	-	-	-	0	0	0	
Ga-Hf	-176223	-31055	-185	0	0	0	
Ga-In	-	-	-	20000	13382	8	[146]
Ga-Ir	-80307	-48938	-122	0	0	0	
Ga-K	-	-	-	0	0	0	
Ga-La	-151446	28934	-233	0	0	0	
Ga-Li	-	-	-	0	0	0	
Ga-Mg	-	-	-	0	0	0	
Ga-Mn	-56978	-3161	-80	0	0	0	
Ga-Mo	-2130	-42619	-18	0	0	0	
Ga-Na	-	-	-	0	0	0	
Ga-Nb	-78108	-46720	-77	0	0	0	
Ga-Ni	-35098	-10210	-88	0	0	0	
Ga-Os	-28790	-51546	-70	0	0	0	
Ga-P	-	-	-	0	0	0	

Ga-Pb	-	-	-	0	0	0	
Ga-Pd	-183143	-39750	-205	0	0	0	
Ga-Pt	-161100	-49501	-192	0	0	0	
Ga-Rb	-	-	-	0	0	0	
Ga-Re	2094	-54170	-31	0	0	0	
Ga-Rh	-99543	-41240	-135	0	0	0	
Ga-Ru	-42065	-42224	-84	0	0	0	
Ga-Sb	-	-	-	0	0	0	
Ga-Sc	-171494	-6460	-186	0	0	0	
Ga-Si	-	-	-	0	0	0	
Ga-Sn	-	-	-	6700	17523	-20	[146]
Ga-Sr	-	-	-	0	0	0	
Ga-Ta	-83432	-57177	-82	0	0	0	
Ga-Tc	-48236	-47489	-82	0	0	0	
Ga-Th	-	-	-	0	0	0	
Ga-Ti	-135848	-36905	-130	0	0	0	
Ga-Tl	-	-	-	0	0	0	
Ga-V	-53906	-31952	-67	0	0	0	
Ga-W	14701	-58048	-3	0	0	0	
Ga-Y	-151238	13081	-219	0	0	0	
Ga-Zn	-	-	-	0	0	0	
Ga-Zr	-199334	-37674	-212	0	0	0	
Ge-Ag	-	-	-	0	0	0	
Ge-Al	-	-	-	0	0	0	
Ge-As	-	-	-	0	0	0	
Ge-Au	-	-	-	0	0	0	
Ge-Ba	-	-	-	0	0	0	
Ge-Be	-	-	-	0	0	0	
Ge-Bi	-	-	-	0	0	0	
Ge-Ca	-	-	-	0	0	0	
Ge-Cd	-	-	-	0	0	0	
Ge-Co	-50282	-23264	-72	0	0	0	
Ge-Cr	-50838	-25657	-63	0	0	0	
Ge-Cs	-	-	-	0	0	0	
Ge-Cu	-	-	-	0	0	0	
Ge-Fe	-36104	-23054	-53	0	0	0	
Ge-Ga	-	-	-	0	0	0	
Ge-Ge	0	0	-	0	0	0	
Ge-Hf	-229598	-36997	-278	0	0	0	
Ge-In	-	-	-	0	0	0	
Ge-Ir	-79821	-53072	-93	0	0	0	

Ge-K	-	-	-	0	0	0	
Ge-La	-209091	22910	-343	0	0	0	
Ge-Li	-	-	-	0	0	0	
Ge-Mg	-	-	-	0	0	0	
Ge-Mn	-106400	-16306	-108	0	0	0	
Ge-Mo	-51691	-52531	-52	0	0	0	
Ge-Na	-	-	-	0	0	0	
Ge-Nb	-141907	-56818	-147	0	0	0	
Ge-Ni	-56656	-21912	-80	0	0	0	
Ge-Os	-42254	-57933	-55	0	0	0	
Ge-P	-	-	-	0	0	0	
Ge-Pb	-	-	-	0	0	0	
Ge-Pd	-165246	-42615	-171	0	0	0	
Ge-Pt	-141108	-50538	-151	0	0	0	
Ge-Rb	-	-	-	0	0	0	
Ge-Re	-22858	-61068	-30	0	0	0	
Ge-Rh	-101743	-47079	-112	0	0	0	
Ge-Ru	-54281	-48961	-68	0	0	0	
Ge-Sb	-	-	-	0	0	0	
Ge-Sc	-228637	-13069	-276	0	0	0	
Ge-Si	-	-	-	0	0	0	
Ge-Sn	-	-	-	25091	15737	-48.4776 + 0.0106 T	[161]
Ge-Sr	-	-	-	0	0	0	
Ge-Ta	-145227	-65930	-151	0	0	0	
Ge-Tc	-61386	-54133	-70	0	0	0	
Ge-Th	-	-	-	0	0	0	
Ge-Ti	-203199	-47973	-204	0	0	0	
Ge-Tl	-	-	-	0	0	0	
Ge-V	-117161	-44741	-113	0	0	0	
Ge-W	-29082	-66011	-30	0	0	0	
Ge-Y	-201180	7526	-322	0	0	0	
Ge-Zn	-	-	-	0	0	0	
Ge-Zr	-260495	-46533	-314	0	0	0	
Hf-Ag	-38726	51175	-48	0	0	0	
Hf-Al	-186957	36044	-189	0	0	0	
Hf-As	-359833	20391	-364	0	0	0	
Hf-Au	-235109	20127	-253	-85110	34073	-38.1400 - 0.0100 T	[162]
Hf-Ba	220110	153426	280	0	0	0	
Hf-Be	40647	168890	-129	0	0	0	
Hf-Bi	-80574	23524	-212	0	0	0	
Hf-Ca	160343	95922	179	0	0	0	

Hf-Cd	-111018	32801	-113	0	0	0	
Hf-Co	-16246	122669	-119	0	0	0	
Hf-Cr	70824	106075	-32	0	0	0	
Hf-Cs	349545	194921	625	0	0	0	
Hf-Cu	7960	111132	-58	4006	95567	-71.0668 - 0.0005 T	[178]
Hf-Fe	27423	117002	-71	0	0	0	
Hf-Ga	-179776	36774	-179	0	0	0	
Hf-Ge	-244471	50364	-244	0	0	0	
Hf-Hf	0	0	0	0	0	0	
Hf-In	-115752	27795	-128	0	0	0	
Hf-Ir	-173091	39128	-253	0	0	0	
Hf-K	363178	155341	482	0	0	0	
Hf-La	91954	54961	72	0	0	0	
Hf-Li	121358	62936	108	0	0	0	
Hf-Mg	29071	44846	29	0	0	0	
Hf-Mn	30156	91059	-41	0	0	0	
Hf-Mo	36059	44574	-15	0	0	0	
Hf-Na	243334	95957	273	0	0	0	
Hf-Nb	29675	16326	15	22445	9035	3.2977 + 0.0035 T	[202]
Hf-Ni	-42522	120892	-145	0	0	0	
Hf-Os	-92556	46160	-178	0	0	0	
Hf-P	-505860	8942	-488	0	0	0	
Hf-Pb	-133037	31285	-169	0	0	0	
Hf-Pd	-267221	37766	-301	0	0	0	
Hf-Pt	-292778	20080	-340	0	0	0	
Hf-Rb	324912	182652	551	0	0	0	
Hf-Re	-36318	35857	-111	0	0	0	
Hf-Rh	-161554	55732	-232	0	0	0	
Hf-Ru	-104082	56856	-188	0	0	0	
Hf-Sb	-251797	11449	-295	0	0	0	
Hf-Sc	22229	26417	21	0	0	0	
Hf-Si	-240237	122553	-262	0	0	0	
Hf-Sn	-185410	16083	-216	0	0	0	
Hf-Sr	204694	136694	249	0	0	0	
Hf-Ta	27645	-98	11	21867	-1710	6	[203]
Hf-Tc	-101324	47415	-172	0	0	0	
Hf-Th	54043	26678	25	0	0	0	
Hf-Ti	14472	27766	1	0	0	0	
Hf-Tl	-84745	35810	-103	0	0	0	
Hf-V	45280	65638	-8	0	0	0	
Hf-W	29900	19591	-24	0	0	0	

Hf-Y	70579	38856	51	0	0	0	
Hf-Zn	-104544	61684	-117	0	0	0	
Hf-Zr	-643	3048	-1	0	0	0	
In-Ag	-	-	-	0	0	0	
In-Al	-	-	-	0	0	0	
In-As	-	-	-	0	0	0	
In-Au	-	-	-	0	0	0	
In-Ba	-	-	-	0	0	0	
In-Be	-	-	-	0	0	0	
In-Bi	-	-	-	-21139	1479	-23	[204]
In-Ca	-	-	-	0	0	0	
In-Cd	-	-	-	0	0	0	
In-Co	52120	-11761	-11	0	0	0	
In-Cr	95821	-7680	32	0	0	0	
In-Cs	-	-	-	0	0	0	
In-Cu	-	-	-	0	0	0	
In-Fe	93993	-8322	28	0	0	0	
In-Ga	-	-	-	0	0	0	
In-Ge	-	-	-	0	0	0	
In-Hf	-117859	-55276	-112	0	0	0	
In-In	-	0	-	0	0	0	
In-Ir	14630	-40622	-41	0	0	0	
In-K	-	-	-	0	0	0	
In-La	-177335	-41188	-205	0	0	0	
In-Li	-	-	-	0	0	0	
In-Mg	-	-	-	0	0	0	
In-Mn	18552	261	-25	0	0	0	
In-Mo	117924	-33250	73	0	0	0	
In-Na	-	-	-	0	0	0	
In-Nb	27621	-42853	13	0	0	0	
In-Ni	35277	-11313	-27	0	0	0	
In-Os	76133	-42988	15	0	0	0	
In-P	-	-	-	0	0	0	
In-Pb	-	-	-	0	0	0	
In-Pd	-123435	-34545	-151	0	0	0	
In-Pt	-80598	-42259	-119	0	0	0	
In-Rb	-	-	-	0	0	0	
In-Re	118208	-44586	60	0	0	0	
In-Rh	-17442	-34790	-66	0	0	0	
In-Ru	55586	-34525	-4	0	0	0	
In-Sb	-	-	-	40000	9977	19.9173 + 0.0200 T	[147]

In-Sc	-154349	-35915	-145	0	0	0	
In-Si	-	-	-	0	0	0	
In-Sn	-	-	-	0	0	0	
In-Sr	-	-	-	0	0	0	
In-Ta	21825	-56079	6	0	0	0	
In-Tc	52187	-39345	-1	0	0	0	
In-Th	-	-	-	0	0	0	
In-Ti	-54571	-35081	-59	0	0	0	
In-Tl	-	-	-	0	0	0	
In-V	38633	-24752	4	0	0	0	
In-W	141603	-48750	93	0	0	0	
In-Y	-172075	-42102	-185	0	0	0	
In-Zn	-	-	-	99	99	99	[205]
In-Zr	-149624	-55647	-141	0	0	0	
Ir-Ag	61643	50076	61	0	0	0	
Ir-Al	-159649	24054	-156	0	0	0	
Ir-As	-123522	26563	-144	0	0	0	
Ir-Au	58011	52466	52	0	0	0	
Ir-Ba	-167788	217077	-70	0	0	0	
Ir-Be	90739	79058	-24	0	0	0	
Ir-Bi	26187	108808	-5	0	0	0	
Ir-Ca	-202089	149429	-97	0	0	0	
Ir-Cd	-27949	63326	-32	0	0	0	
Ir-Co	10462	37020	-13	0	0	0	
Ir-Cr	-54844	19279	-65	0	0	0	
Ir-Cs	25286	187499	214	0	0	0	
Ir-Cu	27747	39245	1	0	0	0	
Ir-Fe	-20050	29667	-32	0	0	0	
Ir-Ga	-122499	22979	-128	0	0	0	
Ir-Ge	-93902	30990	-95	0	0	0	
Ir-Hf	-240163	59687	-293	0	0	0	
Ir-In	-40282	96976	-52	0	0	0	
Ir-Ir	0	0	0	0	0	0	
Ir-K	48676	160443	179	0	0	0	
Ir-La	-158850	121223	-230	0	0	0	
Ir-Li	-184083	55010	-27	0	0	0	
Ir-Mg	-56745	68525	-58	0	0	0	
Ir-Mn	-60172	32431	-66	0	0	0	
Ir-Mo	-80809	-12632	-85	0	0	0	
Ir-Na	24815	108708	102	0	0	0	
Ir-Nb	-198283	-8433	-216	0	0	0	

Ir-Ni	20380	39988	-5	0	0	0	
Ir-Os	-1958	-9554	-2	0	0	0	
Ir-P	-177496	22783	-177	0	0	0	
Ir-Pb	33714	154780	16	0	0	0	
Ir-Pd	24594	22769	24	0	0	0	
Ir-Pt	3476	11391	2	0	0	0	
Ir-Rb	22652	190162	197	0	0	0	
Ir-Re	-11951	-16671	-13	0	0	0	
Ir-Rh	2945	8780	2	0	0	0	
Ir-Ru	-1119	1276	-2	0	0	0	
Ir-Sb	-16733	71538	-66	0	0	0	
Ir-Sc	-232941	68014	-255	0	0	0	
Ir-Si	-150823	27958	-149	0	0	0	
Ir-Sn	-28798	126860	-87	0	0	0	
Ir-Sr	-163619	201150	-73	0	0	0	
Ir-Ta	-190797	-8273	-211	0	0	0	
Ir-Tc	-5899	-4476	-6	0	0	0	
Ir-Th	-196526	139662	-316	0	0	0	
Ir-Ti	-224957	866	-228	0	0	0	
Ir-Tl	15970	121170	12	0	0	0	
Ir-V	-135934	-4676	-130	0	0	0	
Ir-W	-53998	-23018	-63	0	0	0	
Ir-Y	-177583	105410	-242	0	0	0	
Ir-Zn	-74960	34746	-75	0	0	0	
Ir-Zr	-280309	30157	-331	0	0	0	
La-Ag	-52417	65392	-100	0	0	0	
La-Al	-117967	59536	-155	0	0	0	
La-As	-312083	42259	-322	0	0	0	
La-Au	-79428	64456	-55	0	0	0	
La-Ba	67909	47819	69	0	0	0	
La-Be	43533	174961	-91	0	0	0	
La-Bi	-274461	-122	-277	0	0	0	
La-Ca	32070	25651	32	0	0	0	
La-Cd	-138897	35498	-155	0	0	0	
La-Co	74246	134654	-51	0	0	0	
La-Cr	193880	127656	52	99571	104205	-18	[206]
La-Cs	297222	102782	291	0	0	0	
La-Cu	30665	124662	-64	0	0	0	
La-Fe	150593	134968	14	54028	102636	-93.2013 + 0.0237 T	[192]
La-Ga	-150819	56398	-173	0	0	0	
La-Ge	-203399	73034	-231	0	0	0	

La-Hf	99006	8532	53	0	0	0	
La-In	-181042	12966	-178	0	0	0	
La-Ir	-53263	64457	-158	0	0	0	
La-K	177632	74611	207	0	0	0	
La-La	0	0	0	0	0	0	
La-Li	44982	45129	19	0	0	0	
La-Mg	-12637	36217	-31	0	0	0	
La-Mn	124626	117777	8	0	0	0	
La-Mo	225661	77073	103	0	0	0	
La-Na	95598	42834	92	0	0	0	
La-Nb	211759	49336	120	0	0	0	
La-Ni	39059	132923	-81	0	0	0	
La-Os	48121	70583	-70	0	0	0	
La-P	-394901	31863	-401	0	0	0	
La-Pb	-242063	-2548	-241	0	0	0	
La-Pd	-203935	60376	-270	0	0	0	
La-Pt	-186402	47171	-267	0	0	0	
La-Rb	199531	90361	247	0	0	0	
La-Re	132996	65167	9	0	0	0	
La-Rh	-65363	77357	-162	0	0	0	
La-Ru	24669	80439	-90	0	0	0	
La-Sb	-315952	8906	-319	0	0	0	
La-Sc	29484	18960	7	20485	99	-15.3948 + 0.0190 T	[169]
La-Si	-155032	123878	-207	0	0	0	
La-Sn	-237534	15696	-239	0	0	0	
La-Sr	57018	39721	58	0	0	0	
La-Ta	204357	31802	111	0	0	0	
La-Tc	35395	72830	-75	0	0	0	
La-Th	13197	-13909	10	0	0	0	
La-Ti	143488	54449	64	0	0	0	
La-Tl	-184753	9011	-182	0	0	0	
La-V	187603	93631	69	55758	61635	-40	[207]
La-W	228604	54158	104	0	0	0	
La-Y	3215	2175	1	0	0	0	
La-Zn	-73642	81592	-122	0	0	0	
La-Zr	81770	12785	45	0	0	0	
Li-Ag	-	-	-	0	0	0	
Li-Al	-	-	-	0	0	0	
Li-As	-	-	-	0	0	0	
Li-Au	-	-	-	0	0	0	
Li-Ba	-	-	-	0	0	0	

Li-Be	-	-	-	0	0	0	
Li-Bi	-	-	-	0	0	0	
Li-Ca	-	-	-	0	0	0	
Li-Cd	-	-	-	0	0	0	
Li-Co	63636	-20525	31	0	0	0	
Li-Cr	155697	-9323	127	0	0	0	
Li-Cs	-	-	-	0	0	0	
Li-Cu	-	-	-	0	0	0	
Li-Fe	125713	-13815	96	0	0	0	
Li-Ga	-	-	-	0	0	0	
Li-Ge	-	-	-	0	0	0	
Li-Hf	118607	-33802	127	0	0	0	
Li-In	-	-	-	0	0	0	
Li-Ir	2894	-51928	-36	0	0	0	
Li-K	-	-	-	0	0	0	
Li-La	36103	-15282	30	0	0	0	
Li-Li	-	0	-	0	0	0	
Li-Mg	-	-	-	-9449	-9173	-20.9311 + 0.0085 T	[149]
Li-Mn	95716	-1380	71	0	0	0	
Li-Mo	204271	-30140	195	0	0	0	
Li-Na	-	-	-	0	0	0	
Li-Nb	205440	-29802	206	0	0	0	
Li-Ni	37281	-21491	3	0	0	0	
Li-Os	73360	-51647	44	0	0	0	
Li-P	-	-	-	0	0	0	
Li-Pb	-	-	-	0	0	0	
Li-Pd	-118102	-47847	-165	0	0	0	
Li-Pt	-86506	-55837	-138	0	0	0	
Li-Rb	-	-	-	0	0	0	
Li-Re	137579	-49442	118	0	0	0	
Li-Rh	-17580	-45721	-55	0	0	0	
Li-Ru	52155	-43935	20	0	0	0	
Li-Sb	-	-	-	0	0	0	
Li-Sc	49488	-18595	54	47776	-16800	63	[169]
Li-Si	-	-	-	0	0	0	
Li-Sn	-	-	-	0	0	0	
Li-Sr	-	-	-	0	0	0	
Li-Ta	196188	-43010	196	0	0	0	
Li-Tc	62055	-47266	34	0	0	0	
Li-Th	-	-	-	0	0	0	
Li-Ti	139673	-21861	135	0	0	0	

Li-Tl	-	-	-	0	0	0	
Li-V	160120	-20348	141	0	0	0	
Li-W	211061	-46584	204	0	0	0	
Li-Y	38347	-19414	38	0	0	0	
Li-Zn	-	-	-	0	0	0	
Li-Zr	108611	-32330	117	0	0	0	
Mg-Ag	-	-	-	0	0	0	
Mg-Al	-	-	-	4450	2193	-12.0719 + 0.0001 T	[149]
Mg-As	-	-	-	0	0	0	
Mg-Au	-	-	-	0	0	0	
Mg-Ba	-	-	-	0	0	0	
Mg-Be	-	-	-	0	0	0	
Mg-Bi	-	-	-	-54819	-841	-44.0306 - 0.0210 T	[208]
Mg-Ca	-	-	-	0	0	0	
Mg-Cd	-	-	-	0	0	0	
Mg-Co	76871	20187	3	0	0	0	
Mg-Cr	145852	19487	75	0	0	0	
Mg-Cs	-	-	-	0	0	0	
Mg-Cu	-	-	-	10000	19521	-33	[180]
Mg-Fe	126691	22616	54	0	0	0	
Mg-Ga	-	-	-	0	0	0	
Mg-Ge	-	-	-	0	0	0	
Mg-Hf	29471	-37671	29	0	0	0	
Mg-In	-	-	-	0	0	0	
Mg-Ir	10072	-27394	-57	0	0	0	
Mg-K	-	-	-	0	0	0	
Mg-La	-9623	-6500	-41	0	0	0	
Mg-Li	-	-	-	-6285	6967	-11	[149]
Mg-Mg	-	0	-	0	0	0	
Mg-Mn	81564	25355	28	35338	34320	-3.0803 - 0.0018 T	[209]
Mg-Mo	168710	-15970	125	0	0	0	
Mg-Na	-	-	-	0	0	0	
Mg-Nb	129168	-27418	111	0	0	0	
Mg-Ni	54560	19658	-20	0	0	0	
Mg-Os	77759	-26758	11	0	0	0	
Mg-P	-	-	-	0	0	0	
Mg-Pb	-	-	-	0	0	0	
Mg-Pd	-113433	-23084	-161	0	0	0	
Mg-Pt	-85576	-34063	-144	0	0	0	
Mg-Rb	-	-	-	0	0	0	
Mg-Re	130901	-29267	72	0	0	0	

Mg-Rh	-10235	-18056	-71	0	0	0	
Mg-Ru	58974	-17326	-8	0	0	0	
Mg-Sb	-	-	-	0	0	0	
Mg-Sc	-19092	-19451	-20	0	0	0	
Mg-Si	-	-	-	-6255	17618	-41.1743 + 0.0009 T	[210]
Mg-Sn	-	-	-	-22000	108	-3	[180]
Mg-Sr	-	-	-	0	0	0	
Mg-Ta	122921	-41668	104	0	0	0	
Mg-Tc	61455	-22837	2	0	0	0	
Mg-Th	-	-	-	0	0	0	
Mg-Ti	65209	-18738	50	0	0	0	
Mg-Tl	-	-	-	0	0	0	
Mg-V	118583	-2945	74	0	0	0	
Mg-W	180858	-34455	136	0	0	0	
Mg-Y	-13560	-15943	-35	0	0	0	
Mg-Zn	-	-	-	2543	16504	-17.1382 + 0.0004 T	[211]
Mg-Zr	13000	-36817	13	40148	-33605	40	[212]
Mn-Ag	67790	29985	57	0	0	0	
Mn-Al	-103898	5279	-127	0	0	0	
Mn-As	-156741	-10231	-213	0	0	0	
Mn-Au	-25907	23465	-53	0	0	0	
Mn-Ba	112189	229772	176	0	0	0	
Mn-Be	-250231	-46557	-445	0	0	0	
Mn-Bi	34026	86022	-58	0	0	0	
Mn-Ca	79415	156575	102	0	0	0	
Mn-Cd	11576	45748	-25	0	0	0	
Mn-Co	-18827	-18154	-21	0	0	0	
Mn-Cr	8600	-11652	9	0	0	0	
Mn-Cs	183587	196187	480	0	0	0	
Mn-Cu	15159	-1901	15	99	99	12	[181]
Mn-Fe	1510	-16222	1	-1522	-16632	-3.3938 + 0.0012 T	[146]
Mn-Ga	-62955	291	-106	0	0	0	
Mn-Ge	-105410	-1304	-132	0	0	0	
Mn-Hf	29486	64558	-57	0	0	0	
Mn-In	5421	82134	-39	0	0	0	
Mn-Ir	-70847	-34508	-80	0	0	0	
Mn-K	194451	162624	387	0	0	0	
Mn-La	91022	133126	14	0	0	0	
Mn-Li	73974	39770	76	0	0	0	
Mn-Mg	54184	61819	37	85000	43186	57	[209]
Mn-Mn	0	0	0	0	0	0	

Mn-Mo	33978	-20564	22	0	0	0	
Mn-Na	185069	101601	235	0	0	0	
Mn-Nb	18629	-1297	-17	0	0	0	
Mn-Ni	-30160	-17223	-33	0	0	0	
Mn-Os	-33118	-40852	-38	0	0	0	
Mn-P	-277519	-28448	-305	0	0	0	
Mn-Pb	45049	131400	-26	41100	16836	-128	
Mn-Pd	-85201	-16851	-100	0	0	0	
Mn-Pt	-108482	-24522	-128	0	0	0	
Mn-Rb	184049	196971	432	0	0	0	
Mn-Re	3014	-38327	-2	0	0	0	
Mn-Rh	-63265	-29706	-70	0	0	0	
Mn-Ru	-42116	-33742	-46	0	0	0	
Mn-Sb	-22927	45919	-132	0	0	0	
Mn-Sc	23464	76249	-40	0	0	0	
Mn-Si	-149295	-11822	-167	0	0	0	
Mn-Sn	34287	102030	-99	0	0	0	
Mn-Sr	100052	211836	156	81258	91630	80	[197]
Mn-Ta	23817	-2204	-17	0	0	0	
Mn-Tc	-30090	-35685	-37	0	0	0	
Mn-Th	101396	144399	-42	0	0	0	
Mn-Ti	-9357	6056	-36	0	0	0	
Mn-Tl	43519	104053	6	0	0	0	
Mn-V	228	-16580	-3	0	0	0	
Mn-W	41047	-30126	28	0	0	0	
Mn-Y	88099	115266	-8	0	0	0	
Mn-Zn	-47725	8302	-55	0	0	0	
Mn-Zr	7502	42800	-74	0	0	0	
Mo-Ag	149078	59949	150	0	0	0	
Mo-Al	-64468	36181	-64	0	0	0	
Mo-As	-115254	31888	-133	0	0	0	
Mo-Au	16358	41697	14	0	0	0	
Mo-Ba	162937	256059	386	0	0	0	
Mo-Be	86660	87164	-30	0	0	0	
Mo-Bi	135324	112804	116	0	0	0	
Mo-Ca	219365	179624	263	0	0	0	
Mo-Cd	84920	72834	82	0	0	0	
Mo-Co	15269	45932	-18	0	0	0	
Mo-Cr	27912	36040	1	0	0	0	
Mo-Cs	356431	247293	730	0	0	0	
Mo-Cu	96512	56039	67	82313	51169	57	[193]

Mo-Fe	17621	42140	-7	0	0	0	
Mo-Ga	-13811	38657	-20	0	0	0	
Mo-Ge	-52173	40701	-53	0	0	0	
Mo-Hf	10681	62514	-17	0	0	0	
Mo-In	95839	102627	95	0	0	0	
Mo-Ir	-79729	-4146	-86	0	0	0	
Mo-K	361353	208907	601	0	0	0	
Mo-La	165253	148882	156	130000	109110	83	[213]
Mo-Li	211278	80507	169	0	0	0	
Mo-Mg	132707	86302	137	0	0	0	
Mo-Mn	36765	50226	18	0	0	0	
Mo-Mo	0	0	0	0	0	0	
Mo-Na	54812	141906	390	0	0	0	
Mo-Nb	-17589	6575	-23	0	0	0	
Mo-Ni	7900	46901	-27	0	0	0	
Mo-Os	-48478	-8748	-55	0	0	0	
Mo-P	-269274	17642	-270	0	0	0	
Mo-Pb	148511	147707	142	0	0	0	
Mo-Pd	-57599	17812	-59	0	0	0	
Mo-Pt	-110633	217	-114	0	0	0	
Mo-Rb	352245	242730	665	0	0	0	
Mo-Re	-24657	-13376	-27	0	0	0	
Mo-Rh	-53441	9057	-59	0	0	0	
Mo-Ru	-47522	2544	-56	0	0	0	
Mo-Sb	52787	75065	10	0	0	0	
Mo-Sc	55742	85851	45	0	0	0	
Mo-Si	-119754	40926	-120	0	0	0	
Mo-Sn	83995	110654	33	0	0	0	
Mo-Sr	-771653	236478	351	0	0	0	
Mo-Ta	-13328	940	-20	0	0	0	
Mo-Tc	-41452	-2261	-45	0	0	0	
Mo-Th	121628	146284	63	49000	96027	-26.1842 - 0.0062 T	[186]
Mo-Ti	-13211	22013	-15	0	0	0	
Mo-Tl	152312	125400	162	0	0	0	
Mo-V	5044	16331	0	19245	17499	13	[214]
Mo-W	-888	-16390	-1	2000	-15969	2	[146]
Mo-Y	138562	126945	114	100000	108824	55	[215]
Mo-Zn	18725	50220	16	0	0	0	
Mo-Zr	-2217	47254	-27	0	0	0	
Na-Ag	-	-	-	0	0	0	
Na-Al	-	-	-	0	0	0	

Na-As	-	-	-	0	0	0	
Na-Au	-	-	-	0	0	0	
Na-Ba	-	-	-	0	0	0	
Na-Be	-	-	-	0	0	0	
Na-Bi	-	-	-	0	0	0	
Na-Ca	-	-	-	0	0	0	
Na-Cd	-	-	-	0	0	0	
Na-Co	207554	18464	127	0	0	0	
Na-Cr	313898	26138	221	0	0	0	
Na-Cs	-	-	-	0	0	0	
Na-Cu	-	-	-	0	0	0	
Na-Fe	283156	24725	195	0	0	0	
Na-Ga	-	-	-	0	0	0	
Na-Ge	-	-	-	0	0	0	
Na-Hf	266311	-19774	221	0	0	0	
Na-In	-	-	-	0	0	0	
Na-Ir	166261	-15673	95	0	0	0	
Na-K	-	-	-	0	0	0	
Na-La	96687	-20274	98	0	0	0	
Na-Li	-	-	-	0	0	0	
Na-Mg	-	-	-	0	0	0	
Na-Mn	231843	32374	152	0	0	0	
Na-Mo	393061	2198	311	0	0	0	
Na-Na	-	0	-	0	0	0	
Na-Nb	388185	-4121	313	0	0	0	
Na-Ni	177588	17585	100	0	0	0	
Na-Os	247468	-14887	173	0	0	0	
Na-P	-	-	-	0	0	0	
Na-Pb	-	-	-	0	0	0	
Na-Pd	11619	-14560	-50	0	0	0	
Na-Pt	65005	-21240	-3	0	0	0	
Na-Rb	-	-	-	0	0	0	
Na-Re	322105	-14197	246	0	0	0	
Na-Rh	132226	-9684	64	0	0	0	
Na-Ru	219247	-7092	145	0	0	0	
Na-Sb	-	-	-	0	0	0	
Na-Sc	149535	-9454	125	0	0	0	
Na-Si	-	-	-	0	0	0	
Na-Sn	-	-	-	0	0	0	
Na-Sr	-	-	-	0	0	0	
Na-Ta	376003	-18697	302	0	0	0	

Na-Tc	230983	-11135	159	0	0	0	
Na-Th	-	-	-	0	0	0	
Na-Ti	292872	1462	225	0	0	0	
Na-Tl	-	-	-	0	0	0	
Na-V	317929	10544	231	0	0	0	
Na-W	406325	-14685	327	0	0	0	
Na-Y	113592	-18509	108	0	0	0	
Na-Zn	-	-	-	0	0	0	
Na-Zr	248359	-17461	208	0	0	0	
Nb-Ag	66116	47147	66	0	0	0	
Nb-Al	-117786	28632	-116	0	0	0	
Nb-As	-235326	19181	-252	0	0	0	
Nb-Au	-128848	16888	-134	0	0	0	
Nb-Ba	307404	210950	437	0	0	0	
Nb-Be	13697	79875	-90	0	0	0	
Nb-Bi	24824	68032	-17	0	0	0	
Nb-Ca	244893	142984	299	0	0	0	
Nb-Cd	14510	51666	10	0	0	0	
Nb-Co	-49420	42441	-88	30414	69083	-3.1545 - 0.0069 T	[216]
Nb-Cr	12455	39949	-26	0	0	0	
Nb-Cs	427970	241231	820	0	0	0	
Nb-Cu	37474	56267	9	49480	63256	27	[193]
Nb-Fe	-22191	42161	-57	1933	64340	-32.5147 + 0.0063 T	[193]
Nb-Ga	-77785	31717	-82	0	0	0	
Nb-Ge	-145045	33625	-144	0	0	0	
Nb-Hf	26154	20749	17	22714	26400	14	[203]
Nb-In	24993	64043	16	0	0	0	
Nb-Ir	-186361	-12134	-207	0	0	0	
Nb-K	410707	198723	657	0	0	0	
Nb-La	185141	101564	177	0	0	0	
Nb-Li	200623	77731	185	0	0	0	
Nb-Mg	118511	67194	121	0	0	0	
Nb-Mn	14111	53430	-13	0	0	0	
Nb-Mo	-15642	959	-22	0	0	0	
Nb-Na	350848	130180	408	0	0	0	
Nb-Nb	0	0	0	0	0	0	
Nb-Ni	-68842	42351	-107	0	0	0	
Nb-Os	-129788	-13336	-152	0	0	0	
Nb-P	-412762	5039	-407	0	0	0	
Nb-Pb	43106	83268	18	0	0	0	
Nb-Pd	-202318	5182	-208	0	0	0	

Nb-Pt	-256138	-14310	-267	0	0	0	
Nb-Rb	417800	230377	736	0	0	0	
Nb-Re	-84493	-16322	-100	0	0	0	
Nb-Rh	-158449	2194	-176	0	0	0	
Nb-Ru	-133647	-2226	-156	0	0	0	
Nb-Sb	-73118	42097	-125	0	0	0	
Nb-Sc	81327	53160	76	0	0	0	
Nb-Si	-196632	37973	-195	0	0	0	
Nb-Sn	-25527	52404	-68	0	0	0	
Nb-Sr	292385	192039	396	0	0	0	
Nb-Ta	0	-11491	0	0	0	0	
Nb-Tc	-123764	-6684	-139	0	0	0	
Nb-Th	134380	72895	95	0	0	0	
Nb-Ti	8165	17302	8	13045	17881	13	[217]
Nb-Tl	72457	79616	67	0	0	0	
Nb-V	8294	21405	-4	9080	23072	-2	[218]
Nb-W	-26650	-19161	-33	0	0	0	
Nb-Y	158775	80362	139	150000	86867	113	[219]
Nb-Zn	-32742	47406	-35	0	0	0	
Nb-Zr	26461	19478	17	1143	17603	-14.6427 + 0.0055 T	[220]
Ni-Ag	81153	50052	68	57720	34474	25.4002 + 0.0031 T	[150]
Ni-Al	-112848	21675	-139	0	0	0	
Ni-As	-100697	12510	-155	0	0	0	
Ni-Au	64670	54120	33	18378	24312	-14.1772 - 0.0171 T	[163]
Ni-Ba	-68074	230117	1	0	0	0	
Ni-Be	-5465	13179	-22	0	0	0	
Ni-Bi	55090	111466	-15	0	0	0	
Ni-Ca	-112270	160707	-37	0	0	0	
Ni-Cd	8804	64885	-24	0	0	0	
Ni-Co	-950	-2473	-1	0	0	0	
Ni-Cr	-24788	-728	-27	99	99	-27.6618 + 0.0035 T	[146]
Ni-Cs	57804	189848	284	0	0	0	
Ni-Cu	14038	12325	14	11168	12144	12.7562 + 0.0010 T	[183]
Ni-Fe	-4765	-3357	-6	0	0	0	
Ni-Ga	-68590	16218	-114	0	0	0	
Ni-Ge	-70201	19054	-99	0	0	0	
Ni-Hf	-73746	70712	-204	0	0	0	
Ni-In	-5296	102546	-42	0	0	0	
Ni-Ir	16098	-7923	-7	0	0	0	
Ni-K	81775	161638	235	0	0	0	
Ni-La	-36738	135983	-146	0	0	0	

Ni-Li	359317	46833	3	0	0	0	
Ni-Mg	-9284	73673	-25	0	0	0	
Ni-Mn	-31712	10005	-33	0	0	0	
Ni-Mo	14587	-8120	-32	0	0	0	
Ni-Na	66611	107292	140	0	0	0	
Ni-Nb	-65495	5372	-136	0	0	0	
Ni-Ni	0	0	0	0	0	0	
Ni-Os	27050	-17984	6	0	0	0	
Ni-P	-183571	-2851	-206	0	0	0	
Ni-Pb	58995	157948	8	30570	39574	-43.7160 - 0.0322 T	[221]
Ni-Pd	19417	12606	0	0	0	0	
Ni-Pt	5161	6879	-22	0	0	0	
Ni-Rb	58728	194012	259	0	0	0	
Ni-Re	40451	-18523	10	0	0	0	
Ni-Rh	12795	-4960	-4	0	0	0	
Ni-Ru	16762	-10997	2	0	0	0	
Ni-Sb	18319	71474	-79	0	0	0	
Ni-Sc	-100998	81615	-180	0	0	0	
Ni-Si	-118592	7754	-145	0	0	0	
Ni-Sn	40563	127412	-84	0	0	0	
Ni-Sr	-64137	213712	-6	0	0	0	
Ni-Ta	-49022	5753	-133	0	0	0	
Ni-Tc	25705	-13548	3	0	0	0	
Ni-Th	-30196	148016	-218	0	0	0	
Ni-Ti	-104978	11767	-154	0	0	0	
Ni-Tl	38845	126066	14	0	0	0	
Ni-V	-61654	-7949	-75	0	0	0	
Ni-W	41385	-15328	-14	0	0	0	
Ni-Y	-39936	119333	-162	0	0	0	
Ni-Zn	-56940	23446	-63	0	0	0	
Ni-Zr	-118196	45716	-237	0	0	0	
Pb-Ag	-	-	-	0	0	0	
Pb-Al	-	12468	-	0	0	0	
Pb-As	-	-	-	0	0	0	
Pb-Au	-	-	-	30000	16239	11	[164]
Pb-Ba	-	-	-	0	0	0	
Pb-Be	-	-	-	0	0	0	
Pb-Bi	-	-	-	0	0	0	
Pb-Ca	-	-	-	0	0	0	
Pb-Cd	-	-	-	0	0	0	
Pb-Co	118307	9975	18	0	0	0	

Pb-Cr	148622	9824	50	0	0	0	
Pb-Cs	-	-	-	0	0	0	
Pb-Cu	-	-	-	0	0	0	
Pb-Fe	157374	12302	54	0	0	0	
Pb-Ga	-	-	-	0	0	0	
Pb-Ge	-	-	-	0	0	0	
Pb-Hf	-140390	-55945	-132	0	0	0	
Pb-In	-	-	-	0	0	0	
Pb-Ir	101193	-21988	11	0	0	0	
Pb-K	-	-	-	0	0	0	
Pb-La	-239135	-48872	-250	0	0	0	
Pb-Li	-	-	-	0	0	0	
Pb-Mg	-	-	-	0	0	0	
Pb-Mn	56062	16416	-15	0	0	0	
Pb-Mo	171470	-19819	95	0	0	0	
Pb-Na	-	-	-	0	0	0	
Pb-Nb	41746	-35874	13	0	0	0	
Pb-Ni	103972	10746	5	30570	91086	4.9726 - 0.0204 T	[221]
Pb-Os	161343	-24347	62	0	0	0	
Pb-P	-	-	-	0	0	0	
Pb-Pb	-	0	-	0	0	0	
Pb-Pd	-58071	-17502	-105	0	0	0	
Pb-Pt	124	-24678	-62	0	0	0	
Pb-Rb	-	-	-	0	0	0	
Pb-Re	198290	-27764	101	0	0	0	
Pb-Rh	57982	-16160	-22	0	0	0	
Pb-Ru	137870	-15687	41	0	0	0	
Pb-Sb	-	-	-	0	0	0	
Pb-Sc	-193843	-38743	-176	0	0	0	
Pb-Si	-	-	-	0	0	0	
Pb-Sn	-	-	-	6696	4866	4.3696 + 0.0016 T	[146]
Pb-Sr	-	-	-	0	0	0	
Pb-Ta	36284	-49977	5	0	0	0	
Pb-Tc	130850	-21204	43	0	0	0	
Pb-Th	-	-	-	0	0	0	
Pb-Ti	-57301	-29647	-70	0	0	0	
Pb-Tl	-	-	-	0	0	0	
Pb-V	66522	-12140	9	0	0	0	
Pb-W	203781	-35526	121	0	0	0	
Pb-Y	-228216	-48338	-225	0	0	0	
Pb-Zn	-	19918	-	0	0	0	

Pb-Zr	-181838	-56517	-167	0	0	0	
Pd-Ag	-28331	15318	-28	0	0	0	
Pd-Al	-223222	-5339	-216	0	0	0	
Pd-As	-193221	-1930	-215	0	0	0	
Pd-Au	3266	15581	0	0	0	0	
Pd-Ba	-315043	139895	-298	0	0	0	
Pd-Be	39736	37794	-32	0	0	0	
Pd-Bi	-109781	49067	-178	0	0	0	
Pd-Ca	-352838	84342	-272	0	0	0	
Pd-Cd	-128127	22332	-136	0	0	0	
Pd-Co	11928	9006	-5	0	0	0	
Pd-Cr	-47222	-1415	-53	0	0	0	
Pd-Cs	-135024	131858	-40	0	0	0	
Pd-Cu	-38169	10747	-48	0	0	0	
Pd-Fe	-5894	5249	-16	0	0	0	
Pd-Ga	-205801	-7934	-213	0	0	0	
Pd-Ge	-170458	2263	-170	0	0	0	
Pd-Hf	-290164	-15040	-342	0	0	0	
Pd-In	-159074	39900	-186	0	0	0	
Pd-Ir	24783	-16830	24	0	0	0	
Pd-K	-109771	108907	-38	0	0	0	
Pd-La	-278945	48149	-388	0	0	0	
Pd-Li	-1.3203197554458831*^6	22405	-123	0	0	0	
Pd-Mg	-161381	25380	-162	0	0	0	
Pd-Mn	-80726	9716	-82	0	0	0	
Pd-Mo	-56191	-30677	-57	0	0	0	
Pd-Na	-117023	65416	-53	0	0	0	
Pd-Nb	-200992	-40737	-212	0	0	0	
Pd-Ni	19489	11869	0	0	0	0	
Pd-Os	32406	-25302	31	0	0	0	
Pd-P	-199416	770	-197	0	0	0	
Pd-Pb	-102453	74988	-152	0	0	0	
Pd-Pd	0	0	0	0	0	0	
Pd-Pt	8075	-9276	8	0	0	0	
Pd-Rb	-135594	134325	-39	0	0	0	
Pd-Re	26004	-32062	26	0	0	0	
Pd-Rh	8999	-10471	7	18507	-9017	17.9814 - 0.0033 T	[222]
Pd-Ru	26598	-15539	24	12541	-16506	-6.5768 + 0.0176 T	[222]
Pd-Sb	-132813	24182	-204	0	0	0	
Pd-Sc	-322485	5893	-352	0	0	0	

Pd-Si	-196668	-895	-190	0	0	0	
Pd-Sn	-150402	41312	-220	0	0	0	
Pd-Sr	-308330	126341	-285	0	0	0	
Pd-Ta	-196820	-48357	-210	0	0	0	
Pd-Tc	17211	-21391	17	0	0	0	
Pd-Th	-292401	34584	-440	0	0	0	
Pd-Ti	-255275	-30699	-256	0	0	0	
Pd-Tl	-116283	58023	-144	0	0	0	
Pd-V	-140106	-24597	-132	0	0	0	
Pd-W	-22908	-42876	-26	0	0	0	
Pd-Y	-286094	31259	-379	0	0	0	
Pd-Zn	-153507	6864	-143	0	0	0	
Pd-Zr	-337979	-28286	-391	-222417	17471	-55.7322 + 0.0697 T	[223]
Pt-Ag	-2569	27485	-3	0	0	0	
Pt-Al	-217364	5264	-207	0	0	0	
Pt-As	-176485	11318	-191	0	0	0	
Pt-Au	19288	26353	18	0	0	0	
Pt-Ba	-300141	156251	-233	0	0	0	
Pt-Be	67783	58232	-37	0	0	0	
Pt-Bi	-67356	65255	-110	0	0	0	
Pt-Ca	-331866	98107	-226	0	0	0	
Pt-Cd	-101451	34821	-102	0	0	0	
Pt-Co	-2646	23192	-26	-49573	23164	-71	[170]
Pt-Cr	-77114	8490	-87	-146232	4695	-164	[170]
Pt-Cs	-89156	150401	45	0	0	0	
Pt-Cu	-20068	25782	-42	0	0	0	
Pt-Fe	-34050	17388	-47	-169314	5171	-281.5713 + 0.0797 T	[194]
Pt-Ga	-191796	4544	-192	0	0	0	
Pt-Ge	-147460	16033	-145	0	0	0	
Pt-Hf	-338797	-10194	-374	0	0	0	
Pt-In	-126223	53372	-141	0	0	0	
Pt-Ir	3409	-8140	1	0	0	0	
Pt-K	-64483	126011	35	0	0	0	
Pt-La	-285256	59200	-368	0	0	0	
Pt-Li	-308919	35129	-96	0	0	0	
Pt-Mg	-138695	36507	-138	0	0	0	
Pt-Mn	-95390	20700	-101	0	0	0	
Pt-Mo	-110632	-26487	-108	0	0	0	
Pt-Na	-80768	79941	-3	0	0	0	
Pt-Nb	-261140	-38385	-264	0	0	0	
Pt-Ni	9006	26463	-17	0	0	0	

Pt-Os	339	-17296	-2	0	0	0	
Pt-P	-193212	13382	-188	0	0	0	
Pt-Pb	-59319	91419	-87	0	0	0	
Pt-Pd	8184	11863	8	0	0	0	
Pt-Pt	0	0	0	0	0	0	
Pt-Rb	-92445	151967	40	0	0	0	
Pt-Re	-17269	-26166	-17	0	0	0	
Pt-Rh	-3065	242	-6	0	0	0	
Pt-Ru	250	-6531	-4	0	0	0	
Pt-Sb	-100171	38742	-151	0	0	0	
Pt-Sc	-340010	13939	-354	0	0	0	
Pt-Si	-190196	14015	-184	0	0	0	
Pt-Sn	-128249	55173	-176	0	0	0	
Pt-Sr	-294690	142056	-225	0	0	0	
Pt-Ta	-256080	-46024	-260	0	0	0	
Pt-Tc	-11479	-13000	-12	0	0	0	
Pt-Th	-325740	44376	-445	0	0	0	
Pt-Ti	-297025	-26020	-290	0	0	0	
Pt-Tl	-73533	73103	-86	0	0	0	
Pt-V	-177648	-17485	-167	0	0	0	
Pt-W	-79191	-39579	-79	0	0	0	
Pt-Y	-301364	41393	-367	0	0	0	
Pt-Zn	-130409	19655	-126	0	0	0	
Pt-Zr	-384101	-23613	-421	0	0	0	
Rb-Ag	-	-	-	0	0	0	
Rb-Al	-	-	-	0	0	0	
Rb-As	-	-	-	0	0	0	
Rb-Au	-	-	-	0	0	0	
Rb-Ba	-	-	-	0	0	0	
Rb-Be	-	-	-	0	0	0	
Rb-Bi	-	-	-	0	0	0	
Rb-Ca	-	-	-	0	0	0	
Rb-Cd	-	-	-	0	0	0	
Rb-Co	271963	34239	151	0	0	0	
Rb-Cr	401792	43860	249	0	0	0	
Rb-Cs	-	-	-	0	0	0	
Rb-Cu	-	-	-	0	0	0	
Rb-Fe	361230	41137	221	0	0	0	
Rb-Ga	-	-	-	0	0	0	
Rb-Ge	-	-	-	0	0	0	
Rb-Hf	425466	4823	285	0	0	0	

Rb-In	-	-	-	0	0	0	
Rb-Ir	232749	3290	123	0	0	0	
Rb-K	-	-	-	0	0	0	
Rb-La	237721	-2047	170	0	0	0	
Rb-Li	-	-	-	0	0	0	
Rb-Mg	-	-	-	0	0	0	
Rb-Mn	314887	50599	182	0	0	0	
Rb-Mo	508259	22491	345	0	0	0	
Rb-Na	-	-	-	0	0	0	
Rb-Nb	536958	19221	364	0	0	0	
Rb-Ni	236564	33260	123	0	0	0	
Rb-Os	323383	3712	200	0	0	0	
Rb-P	-	-	-	0	0	0	
Rb-Pb	-	-	-	0	0	0	
Rb-Pd	60129	4527	-24	0	0	0	
Rb-Pt	122913	-1423	27	0	0	0	
Rb-Rb	-	0	-	0	0	0	
Rb-Re	411053	4845	273	0	0	0	
Rb-Rh	193882	8663	90	0	0	0	
Rb-Ru	290105	11212	171	0	0	0	
Rb-Sb	-	-	-	0	0	0	
Rb-Sc	295362	14960	192	0	0	0	
Rb-Si	-	-	-	0	0	0	
Rb-Sn	-	-	-	0	0	0	
Rb-Sr	-	-	-	0	0	0	
Rb-Ta	522026	4636	352	0	0	0	
Rb-Tc	307153	7531	186	0	0	0	
Rb-Th	-	-	-	0	0	0	
Rb-Ti	431085	24978	277	0	0	0	
Rb-Tl	-	-	-	0	0	0	
Rb-V	427989	30898	269	0	0	0	
Rb-W	519909	5668	359	0	0	0	
Rb-Y	258589	3285	179	0	0	0	
Rb-Zn	-	-	-	0	0	0	
Rb-Zr	413510	7877	277	0	0	0	
Re-Ag	151716	74179	152	0	0	0	
Re-Al	-78033	47461	-77	0	0	0	
Re-As	-74984	48056	-90	0	0	0	
Re-Au	85379	67364	83	0	0	0	
Re-Ba	46459	259743	210	0	0	0	
Re-Be	119915	99013	-7	0	0	0	

Re-Bi	137094	135424	130	0	0	0	
Re-Ca	-83716	185896	125	0	0	0	
Re-Cd	71272	87857	70	0	0	0	
Re-Co	38084	57263	8	0	0	0	
Re-Cr	4249	42154	-16	0	0	0	
Re-Cs	223176	236556	514	0	0	0	
Re-Cu	99202	63922	65	0	0	0	
Re-Fe	18699	50904	-1	0	0	0	
Re-Ga	-28864	48889	-33	0	0	0	
Re-Ge	-30356	53849	-31	0	0	0	
Re-Hf	-91744	83194	-129	0	0	0	
Re-In	74604	122261	76	0	0	0	
Re-Ir	-12144	14062	-13	0	0	0	
Re-K	240429	203749	431	0	0	0	
Re-La	40820	158588	14	0	0	0	
Re-Li	2.3174966197 41846*^6	83941	94	0	0	0	
Re-Mg	73309	96382	75	0	0	0	
Re-Mn	13101	56552	-2	0	0	0	
Re-Mo	-25443	8467	-27	0	0	0	
Re-Na	186724	143530	281	0	0	0	
Re-Nb	-93710	15416	-105	0	0	0	
Re-Ni	40451	59268	8	0	0	0	
Re-Os	-2592	6269	-4	0	0	0	
Re-P	-185988	37522	-186	0	0	0	
Re-Pb	146526	177880	151	0	0	0	
Re-Pd	26074	38215	26	0	0	0	
Re-Pt	-17027	23247	-18	0	0	0	
Re-Rb	219923	235792	472	0	0	0	
Re-Re	0	0	0	0	0	0	
Re-Rh	5988	25307	4	0	0	0	
Re-Ru	-749	17397	-4	0	0	0	
Re-Sb	71910	96012	39	0	0	0	
Re-Sc	-58943	97900	-72	0	0	0	
Re-Si	-100815	51355	-101	0	0	0	
Re-Sn	76413	144968	33	0	0	0	
Re-Sr	39500	241587	188	0	0	0	
Re-Ta	-87125	13628	-100	0	0	0	
Re-Tc	1303	12327	1	0	0	0	
Re-Th	-5082	169781	-81	0	0	0	
Re-Ti	-98868	28078	-101	0	0	0	
Re-Tl	134779	146924	148	0	0	0	

Re-V	-47409	20556	-48	0	0	0	
Re-W	-13030	-4628	-17	0	0	0	
Re-Y	14635	139283	-20	0	0	0	
Re-Zn	7422	59160	2	0	0	0	
Re-Zr	-118626	58866	-153	0	0	0	
Rh-Ag	39196	42634	38	0	0	0	
Rh-Al	-167387	17362	-167	0	0	0	
Rh-As	-141288	16701	-169	0	0	0	
Rh-Au	39319	45987	30	0	0	0	
Rh-Ba	-174240	208712	-108	0	0	0	
Rh-Be	57242	57646	-26	0	0	0	
Rh-Bi	-5273	98802	-57	0	0	0	
Rh-Ca	-212873	142396	-124	0	0	0	
Rh-Cd	-48278	55826	-59	0	0	0	
Rh-Co	7082	21252	-8	0	0	0	
Rh-Cr	-45312	9543	-50	0	0	0	
Rh-Cs	-878	176888	168	0	0	0	
Rh-Cu	5199	26090	-9	0	0	0	
Rh-Fe	-12912	16458	-20	0	0	0	
Rh-Ga	-134594	14450	-148	0	0	0	
Rh-Ge	-113572	21244	-118	0	0	0	
Rh-Hf	-208510	55347	-277	0	0	0	
Rh-In	-64129	89113	-86	0	0	0	
Rh-Ir	2814	-6573	3	0	0	0	
Rh-K	22466	150610	139	0	0	0	
Rh-La	-154988	115387	-245	0	0	0	
Rh-Li	-292272	46802	-43	0	0	0	
Rh-Mg	-72765	62219	-76	0	0	0	
Rh-Mn	-58209	22902	-60	0	0	0	
Rh-Mo	-51785	-15028	-61	0	0	0	
Rh-Na	2464	99938	72	0	0	0	
Rh-Nb	-162761	-8960	-188	0	0	0	
Rh-Ni	13773	24036	-3	0	0	0	
Rh-Os	8182	-16126	8	0	0	0	
Rh-P	-191391	12313	-194	0	0	0	
Rh-Pb	2352	144449	-33	0	0	0	
Rh-Pd	9066	14307	8	18507	14426	16.9964 - 0.0033 T	[222]
Rh-Pt	-3395	5107	-7	0	0	0	
Rh-Rb	-2456	180290	154	0	0	0	
Rh-Re	6568	-20836	4	0	0	0	
Rh-Rh	0	0	0	0	0	0	

Rh-Ru	5073	-6513	5	0	0	0	
Rh-Sb	-41869	62304	-109	0	0	0	
Rh-Sc	-221517	63617	-257	0	0	0	
Rh-Si	-162445	13257	-160	0	0	0	
Rh-Sn	-44357	116238	-123	0	0	0	
Rh-Sr	-170326	193141	-108	0	0	0	
Rh-Ta	-155244	-9282	-185	0	0	0	
Rh-Tc	1833	-11390	1	0	0	0	
Rh-Th	-174978	132095	-317	0	0	0	
Rh-Ti	-200716	-1247	-211	0	0	0	
Rh-Tl	-14234	112334	-30	0	0	0	
Rh-V	-117811	-9821	-113	0	0	0	
Rh-W	-24199	-24253	-37	0	0	0	
Rh-Y	-167855	99766	-253	0	0	0	
Rh-Zn	-94280	25831	-90	0	0	0	
Rh-Zr	-251230	27561	-316	0	0	0	
Ru-Ag	93995	56673	94	0	0	0	
Ru-Al	-125464	29476	-126	0	0	0	
Ru-As	-100425	29148	-124	0	0	0	
Ru-Au	71891	57968	64	0	0	0	
Ru-Ba	-82300	233565	32	0	0	0	
Ru-Be	71387	66869	-17	0	0	0	
Ru-Bi	70393	118630	43	0	0	0	
Ru-Ca	-131261	163273	-16	0	0	0	
Ru-Cd	10628	70831	4	0	0	0	
Ru-Co	11969	29401	-3	0	0	0	
Ru-Cr	-37230	17568	-43	0	0	0	
Ru-Cs	92185	202150	320	0	0	0	
Ru-Cu	43616	37351	25	0	0	0	
Ru-Fe	-10248	24231	-17	0	0	0	
Ru-Ga	-82364	28127	-93	0	0	0	
Ru-Ge	-68619	33810	-72	0	0	0	
Ru-Hf	-165399	71462	-227	0	0	0	
Ru-In	4696	106849	-5	0	0	0	
Ru-Ir	-1147	-18	-2	0	0	0	
Ru-K	113969	173164	268	0	0	0	
Ru-La	-74109	136803	-137	0	0	0	
Ru-Li	-194877	60931	16	0	0	0	
Ru-Mg	-8343	77763	-9	0	0	0	
Ru-Mn	-36019	32432	-40	0	0	0	
Ru-Mo	-48222	-7352	-58	0	0	0	

Ru-Na	85095	118330	166	0	0	0	
Ru-Nb	-144084	1384	-169	0	0	0	
Ru-Ni	18480	32172	2	0	0	0	
Ru-Os	547	-9957	0	0	0	0	
Ru-P	-177805	20962	-181	0	0	0	
Ru-Pb	77244	165038	64	0	0	0	
Ru-Pd	26747	23476	25	13408	21177	-4.4298 + 0.0149 T	[222]
Ru-Pt	396	12787	-4	0	0	0	
Ru-Rb	90279	204217	294	0	0	0	
Ru-Re	-478	-14580	-4	0	0	0	
Ru-Rh	5073	7696	5	-15995	5203	-26.5123 + 0.0104 T	[222]
Ru-Ru	0	0	0	0	0	0	
Ru-Sb	21786	79406	-29	0	0	0	
Ru-Sc	-157062	80895	-185	0	0	0	
Ru-Si	-131463	24014	-130	0	0	0	
Ru-Sn	19769	135854	-44	0	0	0	
Ru-Sr	-81422	216807	22	0	0	0	
Ru-Ta	-135214	1879	-164	0	0	0	
Ru-Tc	393	-4513	-1	0	0	0	
Ru-Th	-107368	153848	-225	0	0	0	
Ru-Ti	-166626	10565	-176	0	0	0	
Ru-Tl	59639	131269	60	0	0	0	
Ru-V	-98749	-566	-95	0	0	0	
Ru-W	-25415	-17012	-40	0	0	0	
Ru-Y	-93964	119951	-158	0	0	0	
Ru-Zn	-47306	38036	-47	0	0	0	
Ru-Zr	-202654	43156	-260	0	0	0	
Sb-Ag	-	-	-	0	0	0	
Sb-Al	-	-	-	0	0	0	
Sb-As	-	-	-	0	0	0	
Sb-Au	-	-	-	0	0	0	
Sb-Ba	-	-	-	0	0	0	
Sb-Be	-	-	-	0	0	0	
Sb-Bi	-	-	-	3850	2856	8.0579 - 0.0063 T	[168]
Sb-Ca	-	-	-	0	0	0	
Sb-Cd	-	-	-	0	0	0	
Sb-Co	53754	13668	-35	0	0	0	
Sb-Cr	61550	5314	-19	0	0	0	
Sb-Cs	-	-	-	0	0	0	
Sb-Cu	-	-	-	0	0	0	
Sb-Fe	78562	12776	-9	0	0	0	

Sb-Ga	-	-	-	0	0	0	
Sb-Ge	-	-	-	0	0	0	
Sb-Hf	-257965	-73647	-237	0	0	0	
Sb-In	-	-	-	0	0	0	
Sb-Ir	28288	-29876	-46	0	0	0	
Sb-K	-	-	-	0	0	0	
Sb-La	-317761	-43323	-336	0	0	0	
Sb-Li	-	-	-	0	0	0	
Sb-Mg	-	-	-	0	0	0	
Sb-Mn	-21925	9199	-76	0	0	0	
Sb-Mo	61263	-34210	7	0	0	0	
Sb-Na	-	-	-	0	0	0	
Sb-Nb	-80463	-56172	-90	0	0	0	
Sb-Ni	43995	14645	-45	0	0	0	
Sb-Os	79309	-31866	-2	0	0	0	
Sb-P	-	-	-	0	0	0	
Sb-Pb	-	-	-	0	0	0	
Sb-Pd	-105898	-25230	-144	0	0	0	
Sb-Pt	-59215	-34311	-110	0	0	0	
Sb-Rb	-	-	-	0	0	0	
Sb-Re	103756	-38519	27	0	0	0	
Sb-Rh	-7343	-21844	-73	0	0	0	
Sb-Ru	60936	-22109	-19	0	0	0	
Sb-Sb	-	0	-	0	0	0	
Sb-Sc	-282462	-51644	-256	0	0	0	
Sb-Si	-	-	-	0	0	0	
Sb-Sn	-	-	-	-1732	-4307	3.6820 - 0.0057 T	[168]
Sb-Sr	-	-	-	0	0	0	
Sb-Ta	-84929	-70354	-96	0	0	0	
Sb-Tc	49621	-29238	-21	0	0	0	
Sb-Th	-	-	-	0	0	0	
Sb-Ti	-166619	-48825	-162	0	0	0	
Sb-Tl	-	-	-	0	0	0	
Sb-V	-29753	-24064	-70	0	0	0	
Sb-W	92406	-51234	32	0	0	0	
Sb-Y	-311204	-51350	-310	0	0	0	
Sb-Zn	-	-	-	0	0	0	
Sb-Zr	-300736	-75570	-275	0	0	0	
Sc-Ag	-89187	20520	-108	0	0	0	
Sc-Al	-155278	15321	-170	-106397	15742	-133	[153]
Sc-As	-331113	520	-344	0	0	0	

Sc-Au	-251734	-8725	-293	0	0	0	
Sc-Ba	132561	99007	141	0	0	0	
Sc-Be	24519	121537	-122	0	0	0	
Sc-Bi	-215450	-7113	-258	0	0	0	
Sc-Ca	81434	51820	78	65910	40739	50	[169]
Sc-Cd	-144244	6763	-149	0	0	0	
Sc-Co	10866	78325	-100	0	0	0	
Sc-Cr	112565	70651	2	43195	70066	-54	[169]
Sc-Cs	234358	141365	416	0	0	0	
Sc-Cu	-13123	71374	-83	11500	63276	-64.9610 - 0.0030 T	[153]
Sc-Fe	71213	77789	-39	5700	70516	-99	[196]
Sc-Ga	-172245	14108	-178	0	0	0	
Sc-Ge	-227697	25315	-242	0	0	0	
Sc-Hf	24144	-20528	20	0	0	0	
Sc-In	-153827	-603	-164	0	0	0	
Sc-Ir	-125349	5346	-227	0	0	0	
Sc-K	225270	106063	305	0	0	0	
Sc-La	29394	15664	10	20485	99	-16.3184 + 0.0190 T	[169]
Sc-Li	-	-	45	58238	33308	55	[169]
Sc-Mg	-19535	16357	-20	0	0	0	
Sc-Mn	53812	64933	-28	0	0	0	
Sc-Mo	111280	19380	38	0	0	0	
Sc-Na	138508	55382	150	0	0	0	
Sc-Nb	98729	-1238	66	0	0	0	
Sc-Ni	-19775	76540	-130	0	0	0	
Sc-Os	-36468	11106	-141	0	0	0	
Sc-P	-434758	-7773	-445	0	0	0	
Sc-Pb	-190824	-2776	-220	0	0	0	
Sc-Pd	-257098	4648	-319	0	0	0	
Sc-Pt	-253553	-10671	-333	0	0	0	
Sc-Rb	245474	130016	359	0	0	0	
Sc-Re	32885	5825	-63	0	0	0	
Sc-Rh	-130186	19349	-221	0	0	0	
Sc-Ru	-54270	21436	-157	0	0	0	
Sc-Sb	-283018	-13523	-316	0	0	0	
Sc-Sc	0	0	0	0	0	0	
Sc-Si	-192537	70977	-232	0	0	0	
Sc-Sn	-215696	-8940	-234	0	0	0	
Sc-Sr	118888	84905	122	0	0	0	
Sc-Ta	94163	-17429	59	0	0	0	
Sc-Tc	-48850	14044	-141	0	0	0	

Sc-Th	14855	-8747	0	0	0	0	
Sc-Ti	55338	8283	28	0	0	0	
Sc-Tl	-141622	3553	-158	0	0	0	
Sc-V	95101	38429	25	0	0	0	
Sc-W	110918	-3624	34	0	0	0	
Sc-Y	17088	4251	4	11412	4196	-11.4565 + 0.0099 T	[224]
Sc-Zn	-105373	36398	-128	0	0	0	
Sc-Zr	17235	-17333	16	0	0	0	
Si-Ag	-	-	-	0	0	0	
Si-Al	-	-	-	65279	13099	108.7261 - 0.0461 T	[225]
Si-As	-	-	-	0	0	0	
Si-Au	-	-	-	40000	5328	35	[165]
Si-Ba	-	-	-	0	0	0	
Si-Be	-	-	-	0	0	0	
Si-Bi	-	-	-	0	0	0	
Si-Ca	-	-	-	0	0	0	
Si-Cd	-	-	-	0	0	0	
Si-Co	20838	-31510	-120	0	0	0	
Si-Cr	-114047	-31688	-119	0	0	0	
Si-Cs	-	-	-	0	0	0	
Si-Cu	-	-	-	0	0	0	
Si-Fe	-102624	-31568	-110	0	0	0	
Si-Ga	-	-	-	0	0	0	
Si-Ge	-	-	-	0	0	0	
Si-Hf	-231188	-23890	-323	0	0	0	
Si-In	-	-	-	0	0	0	
Si-Ir	-149686	-56287	-158	0	0	0	
Si-K	-	-	-	0	0	0	
Si-La	-182716	43747	-331	0	0	0	
Si-Li	-	-	-	0	0	0	
Si-Mg	-	-	-	0	0	0	
Si-Mn	-150191	-20631	-147	0	0	0	
Si-Mo	-119189	-54841	-126	0	0	0	
Si-Na	-	-	-	0	0	0	
Si-Nb	-189685	-53913	-216	0	0	0	
Si-Ni	-111095	-29883	-126	0	0	0	
Si-Os	-119258	-62550	-126	0	0	0	
Si-P	-	-	-	0	0	0	
Si-Pb	-	-	-	0	0	0	
Si-Pd	-197921	-41771	-206	0	0	0	
Si-Pt	-194791	-50589	-206	0	0	0	

Si-Rb	-	-	-	0	0	0	
Si-Re	-103872	-64997	-107	0	0	0	
Si-Rh	-159347	-50258	-165	0	0	0	
Si-Ru	-126064	-53568	-133	0	0	0	
Si-Sb	-	-	-	67796	39691	12	[165]
Si-Sc	-214523	2646	-286	0	0	0	
Si-Si	-	0	-	0	0	0	
Si-Sn	-	-	-	49105	33049	-65.4353 + 0.0238 T	[226]
Si-Sr	-	-	-	0	0	0	
Si-Ta	-184671	-61170	-217	0	0	0	
Si-Tc	-131693	-58172	-136	0	0	0	
Si-Th	-	-	-	0	0	0	
Si-Ti	-232966	-43478	-252	0	0	0	
Si-Tl	-	-	-	0	0	0	
Si-V	-170438	-46672	-166	0	0	0	
Si-W	-100807	-67591	-110	0	0	0	
Si-Y	-174765	27321	-318	0	0	0	
Si-Zn	-	-	-	0	0	0	
Si-Zr	-266042	-35122	-355	0	0	0	
Sn-Ag	-	-	-	18359	7310	-7	[151]
Sn-Al	-	-	-	0	0	0	
Sn-As	-	-	-	0	0	0	
Sn-Au	-	-	-	-18000	-7961	-52	[157]
Sn-Ba	-	-	-	0	0	0	
Sn-Be	-	-	-	0	0	0	
Sn-Bi	-	-	-	99	99	3.7814 - 0.0010 T	[168]
Sn-Ca	-	-	-	0	0	0	
Sn-Cd	-	-	-	0	0	0	
Sn-Co	115513	23518	-37	0	0	0	
Sn-Cr	139750	16467	-6	26991	78217	-68.2664 + 0.0204 T	[174]
Sn-Cs	-	-	-	0	0	0	
Sn-Cu	-	-	-	0	0	0	
Sn-Fe	142159	23189	-5	0	0	0	
Sn-Ga	-	-	-	0	0	0	
Sn-Ge	-	-	-	0	0	0	
Sn-Hf	-191748	-63061	-181	0	0	0	
Sn-In	-	-	-	0	0	0	
Sn-Ir	79237	-22762	-63	0	0	0	
Sn-K	-	-	-	0	0	0	
Sn-La	-237135	-35400	-266	0	0	0	
Sn-Li	-	-	-	0	0	0	

Sn-Mg	-	-	-	0	0	0	
Sn-Mn	46180	20091	-60	0	0	0	
Sn-Mo	115182	-23571	24	0	0	0	
Sn-Na	-	-	-	0	0	0	
Sn-Nb	-28578	-44402	-51	0	0	0	
Sn-Ni	103943	24129	-50	0	0	0	
Sn-Os	135431	-23871	-13	0	0	0	
Sn-P	-	-	-	0	0	0	
Sn-Pb	-	-	-	0	0	0	
Sn-Pd	-95325	-18725	-163	0	0	0	
Sn-Pt	-47710	-28517	-134	0	0	0	
Sn-Rb	-	-	-	0	0	0	
Sn-Re	157024	-29873	24	0	0	0	
Sn-Rh	39731	-14199	-87	0	0	0	
Sn-Ru	114919	-14055	-30	0	0	0	
Sn-Sb	-	-	-	-17728	99	25.5455 - 0.0666 T	[168]
Sn-Sc	-216065	-41740	-201	0	0	0	
Sn-Si	-	-	-	0	0	0	
Sn-Sn	-	0	-	0	0	0	
Sn-Sr	-	-	-	0	0	0	
Sn-Ta	-28592	-59024	-58	0	0	0	
Sn-Tc	97213	-20978	-29	0	0	0	
Sn-Th	-	-	-	0	0	0	
Sn-Ti	-107322	-36780	-119	0	0	0	
Sn-Tl	-	-	-	0	0	0	
Sn-V	25779	-12156	-44	0	0	0	
Sn-W	146006	-41325	45	0	0	0	
Sn-Y	-234171	-42694	-245	0	0	0	
Sn-Zn	-	-	-	0	0	0	
Sn-Zr	-228171	-63822	-213	0	0	0	
Sr-Ag	-	-	-	0	0	0	
Sn-Zn	-	-	-	26346	36421	-26.8830 + 0.0197 T	[205]
Sr-As	-	-	-	0	0	0	
Sr-Au	-	-	-	0	0	0	
Sr-Ba	-	-	-	0	0	0	
Sr-Be	-	-	-	0	0	0	
Sr-Bi	-	-	-	0	0	0	
Sr-Ca	-	-	-	0	0	0	
Sr-Cd	-	-	-	0	0	0	
Sr-Co	184296	107476	27	0	0	0	
Sr-Cr	315105	109055	136	0	0	0	

Sr-Cs	-	-	-	0	0	0	
Sr-Cu	-	-	-	0	0	0	
Sr-Fe	271798	111795	99	93941	95247	-24	[197]
Sr-Ga	-	-	-	0	0	0	
Sr-Ge	-	-	-	0	0	0	
Sr-Hf	273206	21103	160	0	0	0	
Sr-In	-	-	-	0	0	0	
Sr-Ir	103894	53641	-47	0	0	0	
Sr-K	-	-	-	0	0	0	
Sr-La	76658	-5218	50	0	0	0	
Sr-Li	-	-	-	0	0	0	
Sr-Mg	-	-	-	0	0	0	
Sr-Mn	230268	109637	76	60932	106989	-44	[197]
Sr-Mo	388158	70969	209	0	0	0	
Sr-Na	-	-	-	0	0	0	
Sr-Nb	397647	54770	236	0	0	0	
Sr-Ni	148197	106073	-3	0	0	0	
Sr-Os	202545	57325	39	0	0	0	
Sr-P	-	-	-	0	0	0	
Sr-Pb	-	-	-	0	0	0	
Sr-Pd	-71801	51338	-188	0	0	0	
Sr-Pt	-22523	41442	-157	0	0	0	
Sr-Rb	-	-	-	0	0	0	
Sr-Re	291495	55472	119	0	0	0	
Sr-Rh	73572	63184	-67	0	0	0	
Sr-Ru	172454	66336	14	0	0	0	
Sr-Sb	-	-	-	0	0	0	
Sr-Sc	156094	27994	82	0	0	0	
Sr-Si	-	-	-	0	0	0	
Sr-Sn	-	-	-	0	0	0	
Sr-Sr	-	0	-	0	0	0	
Sr-Ta	384851	37929	224	0	0	0	
Sr-Tc	186258	60627	29	0	0	0	
Sr-Th	-	-	-	0	0	0	
Sr-Ti	304001	59861	162	54816	43798	-26	[197]
Sr-Tl	-	-	-	0	0	0	
Sr-V	325449	84922	157	54048	61602	-46	[197]
Sr-W	396759	50534	216	0	0	0	
Sr-Y	102480	5041	61	0	0	0	
Sr-Zn	-	-	-	0	0	0	
Sr-Zr	257306	25497	154	0	0	0	

Ta-Ag	60655	59692	60	0	0	0	
Ta-Al	-70018	53381	-20	0	0	0	
Ta-As	-238166	32741	-255	0	0	0	
Ta-Au	-129717	29369	-135	0	0	0	
Ta-Ba	293597	227466	417	0	0	0	
Ta-Be	44223	125753	-89	0	0	0	
Ta-Bi	19202	79141	-28	0	0	0	
Ta-Ca	232761	156827	284	0	0	0	
Ta-Cd	8644	61912	3	0	0	0	
Ta-Co	-33584	80369	-86	0	0	0	
Ta-Cr	25498	69394	-24	36943	83938	-23.6430 + 0.0026 T	[175]
Ta-Cs	413515	249800	794	0	0	0	
Ta-Cu	42423	84511	7	104600	87538	70	[185]
Ta-Fe	-8162	76810	-54	12871	88830	-40.9515 + 0.0094 T	[198]
Ta-Ga	-83076	44868	-88	0	0	0	
Ta-Ge	-148923	49729	-148	0	0	0	
Ta-Hf	23727	33430	12	0	0	0	
Ta-In	18860	75163	7	0	0	0	
Ta-Ir	-174157	11744	-203	0	0	0	
Ta-K	396396	207733	635	0	0	0	
Ta-La	177125	117128	164	0	0	0	
Ta-Li	191368	88025	176	0	0	0	
Ta-Mg	111407	77370	113	0	0	0	
Ta-Mn	18747	74899	-14	0	0	0	
Ta-Mo	-10547	19988	-19	0	0	0	
Ta-Na	338270	139627	393	0	0	0	
Ta-Nb	0	12159	0	0	0	0	
Ta-Ni	-51995	79917	-105	0	0	0	
Ta-Os	-116470	12829	-147	0	0	0	
Ta-P	-410370	19910	-405	0	0	0	
Ta-Pb	37790	97861	7	0	0	0	
Ta-Pd	-197830	25126	-206	0	0	0	
Ta-Pt	-248769	4885	-263	0	0	0	
Ta-Rb	403314	239850	713	0	0	0	
Ta-Re	-74410	6210	-96	0	0	0	
Ta-Rh	-148532	27905	-173	0	0	0	
Ta-Ru	-120542	24419	-152	0	0	0	
Ta-Sb	-77157	52246	-133	0	0	0	
Ta-Sc	75065	64911	67	0	0	0	
Ta-Si	-194193	75447	-197	0	0	0	
Ta-Sn	-24908	64776	-76	0	0	0	

Ta-Sr	278260	208112	377	0	0	0	
Ta-Ta	0	0	0	0	0	0	
Ta-Tc	-113476	18047	-135	0	0	0	
Ta-Th	132718	93746	85	0	0	0	
Ta-Ti	5704	29034	5	0	0	0	
Ta-Tl	65765	91591	57	0	0	0	
Ta-V	12446	41758	-4	0	0	0	
Ta-W	-20489	-1887	-29	0	0	0	
Ta-Y	152119	95136	127	0	0	0	
Ta-Zn	-36971	62546	-40	0	0	0	
Ta-Zr	23469	30822	12	31965	29905	17.8190 - 0.0003 T	[227]
Tc-Ag	97015	59205	97	0	0	0	
Tc-Al	-122506	33013	-121	0	0	0	
Tc-As	-107706	32774	-128	0	0	0	
Tc-Au	62036	57389	58	0	0	0	
Tc-Ba	-61308	235351	57	0	0	0	
Tc-Be	86063	74035	-17	0	0	0	
Tc-Bi	68333	118337	42	0	0	0	
Tc-Ca	-139324	165205	5	0	0	0	
Tc-Cd	12627	72806	8	0	0	0	
Tc-Co	21498	36286	-1	0	0	0	
Tc-Cr	-20742	24497	-33	0	0	0	
Tc-Cs	114876	207984	346	0	0	0	
Tc-Cu	53769	43725	29	0	0	0	
Tc-Fe	2235	31346	-11	0	0	0	
Tc-Ga	-80903	32315	-88	0	0	0	
Tc-Ge	-70612	37945	-72	0	0	0	
Tc-Hf	-153184	68485	-201	0	0	0	
Tc-In	7207	106655	-1	0	0	0	
Tc-Ir	-5876	3467	-6	0	0	0	
Tc-K	135520	178448	290	0	0	0	
Tc-La	-56393	137703	-111	0	0	0	
Tc-Li	-524215	65979	27	0	0	0	
Tc-Mg	2033	80278	2	0	0	0	
Tc-Mn	-22104	39116	-30	0	0	0	
Tc-Mo	-41736	-3077	-45	0	0	0	
Tc-Na	97645	122797	180	0	0	0	
Tc-Nb	-131298	3665	-147	0	0	0	
Tc-Ni	26733	38801	2	0	0	0	
Tc-Os	1305	-5470	1	0	0	0	
Tc-P	-189500	24803	-190	0	0	0	

Tc-Pb	77055	161593	64	0	0	0	
Tc-Pd	17368	26329	17	0	0	0	
Tc-Pt	-11402	14441	-13	0	0	0	
Tc-Rb	112756	209347	318	0	0	0	
Tc-Re	1349	-10501	1	0	0	0	
Tc-Rh	1738	11977	1	0	0	0	
Tc-Ru	401	4648	-1	0	0	0	
Tc-Sb	16013	80307	-31	0	0	0	
Tc-Sc	-140272	81174	-162	0	0	0	
Tc-Si	-131122	30031	-129	0	0	0	
Tc-Sn	15412	129993	-41	0	0	0	
Tc-Sr	-63100	218490	46	0	0	0	
Tc-Ta	-124083	2449	-142	0	0	0	
Tc-Tc	0	0	0	0	0	0	
Tc-Th	-91996	149652	-195	0	0	0	
Tc-Ti	-151031	14145	-155	0	0	0	
Tc-Tl	62832	130522	63	0	0	0	
Tc-V	-82725	5363	-80	0	0	0	
Tc-W	-22185	-14077	-28	0	0	0	
Tc-Y	-76425	120020	-132	0	0	0	
Tc-Zn	-41820	42843	-42	0	0	0	
Tc-Zr	-186679	43493	-232	0	0	0	
Th-Ag	-	-	-	0	0	0	
Th-Al	-	-	-	99	99	-82.9590 - 0.0062 T	[156]
Th-As	-	-	-	0	0	0	
Th-Au	-	-	-	0	0	0	
Th-Ba	-	-	-	0	0	0	
Th-Be	-	-	-	0	0	0	
Th-Bi	-	-	-	0	0	0	
Th-Ca	-	-	-	0	0	0	
Th-Cd	-	-	-	0	0	0	
Th-Co	81258	180549	-93	0	0	0	
Th-Cr	193167	164767	7	0	0	0	
Th-Cs	-	-	-	0	0	0	
Th-Cu	-	-	-	0	0	0	
Th-Fe	146854	176072	-33	0	0	0	
Th-Ga	-	-	-	0	0	0	
Th-Ge	-	-	-	0	0	0	
Th-Hf	57047	15851	20	0	0	0	
Th-In	-	-	-	0	0	0	
Th-Ir	-69990	97235	-216	0	0	0	

Th-K	-	-	-	0	0	0	
Th-La	12865	20328	11	0	0	0	
Th-Li	-	-	-	0	0	0	
Th-Mg	-	-	-	0	0	0	
Th-Mn	125932	138586	-24	0	0	0	
Th-Mo	187078	102756	43	46286	94075	-71	[186]
Th-Na	-	-	-	0	0	0	
Th-Nb	156164	63298	67	0	0	0	
Th-Ni	47977	178407	-122	0	0	0	
Th-Os	29323	106055	-131	0	0	0	
Th-P	-	-	-	0	0	0	
Th-Pb	-	-	-	0	0	0	
Th-Pd	-220275	87799	-306	0	0	0	
Th-Pt	-216745	73848	-320	0	0	0	
Th-Rb	-	-	-	0	0	0	
Th-Re	104530	95891	-55	0	0	0	
Th-Rh	-74366	112172	-210	0	0	0	
Th-Ru	9336	115913	-147	0	0	0	
Th-Sb	-	-	-	0	0	0	
Th-Sc	15167	29103	0	0	0	0	
Th-Si	-	-	-	0	0	0	
Th-Sn	-	-	-	0	0	0	
Th-Sr	-	-	-	0	0	0	
Th-Ta	155963	45059	60	0	0	0	
Th-Tc	14395	105857	-132	0	0	0	
Th-Th	0	0	0	0	0	0	
Th-Ti	107396	67514	28	0	0	0	
Th-Tl	-	-	-	0	0	0	
Th-V	165653	120480	28	0	0	0	
Th-W	188156	77696	40	0	0	0	
Th-Y	5001	17157	5	0	0	0	
Th-Zn	-	-	-	20000	115556	-58	[156]
Th-Zr	41664	20534	15	20704	17433	-11.6578 + 0.0095 T	[228]
Ti-Ag	-6000	22288	-6	0	0	0	
Ti-Al	-162292	6737	-163	0	0	0	
Ti-As	-294495	-5174	-320	0	0	0	
Ti-Au	-191171	-7629	-203	0	0	0	
Ti-Ba	230690	182139	321	0	0	0	
Ti-Be	-35105	62863	-111	0	0	0	
Ti-Bi	-69961	37147	-143	0	0	0	
Ti-Ca	178417	116940	210	0	0	0	

Ti-Cd	-55821	26012	-69	0	0	0	
Ti-Co	-69372	25476	-103	0	0	0	
Ti-Cr	4432	24182	-27	23900	35856	-3	[176]
Ti-Cs	341647	208224	677	0	0	0	
Ti-Cu	-13912	35657	-33	16334	39275	-4	[187]
Ti-Fe	-31159	26213	-62	3061	38348	-49.7837 + 0.0231 T	[199]
Ti-Ga	-134371	7946	-145	0	0	0	
Ti-Ge	-205381	9957	-207	0	0	0	
Ti-Hf	14337	2960	1	0	0	0	
Ti-In	-53151	36904	-78	0	0	0	
Ti-Ir	-202908	-30479	-227	0	0	0	
Ti-K	311668	167602	530	0	0	0	
Ti-La	130197	76976	99	0	0	0	
Ti-Li	133340	54877	130	0	0	0	
Ti-Mg	59974	43514	58	0	0	0	
Ti-Mn	-9596	35482	-30	0	0	0	
Ti-Mo	-7990	-14264	-14	0	0	0	
Ti-Na	260047	102749	313	0	0	0	
Ti-Nb	8031	-15408	8	11742	-14970	12	[217]
Ti-Ni	-92257	24897	-126	0	0	0	
Ti-Os	-136972	-30290	-161	0	0	0	
Ti-P	-450595	-16550	-452	0	0	0	
Ti-Pb	-50874	53410	-103	0	0	0	
Ti-Pd	-249276	-17082	-260	0	0	0	
Ti-Pt	-285580	-34857	-304	0	0	0	
Ti-Rb	331100	198421	601	0	0	0	
Ti-Re	-82777	-32361	-100	0	0	0	
Ti-Rh	-184851	-16992	-204	0	0	0	
Ti-Ru	-145006	-19611	-169	0	0	0	
Ti-Sb	-158541	13082	-233	0	0	0	
Ti-Sc	47271	32138	33	0	0	0	
Ti-Si	-236245	17701	-236	0	0	0	
Ti-Sn	-99811	25272	-163	0	0	0	
Ti-Sr	218179	164099	288	86242	90596	69	[197]
Ti-Ta	5544	-27126	6	0	0	0	[185]
Ti-Tc	-134981	-24271	-153	0	0	0	
Ti-Th	99905	51596	41	0	0	0	
Ti-Ti	0	0	0	0	0	0	
Ti-Tl	-16541	50728	-43	0	0	0	
Ti-V	4193	5093	-6	23200	7132	13	[220]
Ti-W	-16121	-34222	-23	0	0	0	[229]

Ti-Y	112452	57058	73	0	0	0	
Ti-Zn	-88233	24893	-88	0	0	0	
Ti-Zr	13533	1280	-1	3460	-191	-12	[230]
Tl-Ag	-	-	-	0	0	0	
Tl-Al	-	-	-	0	0	0	
Tl-As	-	-	-	0	0	0	
Tl-Au	-	-	-	0	0	0	
Tl-Ba	-	-	-	0	0	0	
Tl-Be	-	-	-	0	0	0	
Tl-Bi	-	-	-	0	0	0	
Tl-Ca	-	-	-	0	0	0	
Tl-Cd	-	-	-	0	0	0	
Tl-Co	102210	-10220	25	0	0	0	
Tl-Cr	145770	-5788	67	0	0	0	
Tl-Cs	-	-	-	0	0	0	
Tl-Cu	-	-	-	0	0	0	
Tl-Fe	147234	-6425	66	0	0	0	
Tl-Ga	-	-	-	0	0	0	
Tl-Ge	-	-	-	0	0	0	
Tl-Hf	-88319	-53708	-84	0	0	0	
Tl-In	-	-	-	0	0	0	
Tl-Ir	77766	-36554	9	0	0	0	
Tl-K	-	-	-	0	0	0	
Tl-La	-180760	-44432	-197	0	0	0	
Tl-Li	-	-	-	0	0	0	
Tl-Mg	-	-	-	0	0	0	
Tl-Mn	59097	1282	3	0	0	0	
Tl-Mo	178066	-29723	117	0	0	0	
Tl-Na	-	-	-	0	0	0	
Tl-Nb	75852	-39912	50	0	0	0	
Tl-Ni	84702	-9768	9	0	0	0	
Tl-Os	140402	-38988	65	0	0	0	
Tl-P	-	-	-	0	0	0	
Tl-Pb	-	-	-	0	0	0	
Tl-Pd	-73636	-31459	-110	0	0	0	
Tl-Pt	-20024	-38023	-69	0	0	0	
Tl-Rb	-	-	-	0	0	0	
Tl-Re	184191	-40461	110	0	0	0	
Tl-Rh	38844	-31552	-22	0	0	0	
Tl-Ru	116770	-30939	43	0	0	0	
Tl-Sb	-	-	-	0	0	0	

Tl-Sc	-143705	-36304	-132	0	0	0	
Tl-Si	-	-	-	0	0	0	
Tl-Sn	-	-	-	0	0	0	
Tl-Sr	-	-	-	0	0	0	
Tl-Ta	69524	-53242	42	0	0	0	
Tl-Tc	113964	-35571	47	0	0	0	
Tl-Th	-	-	-	0	0	0	
Tl-Ti	-18426	-33201	-31	0	0	0	
Tl-Tl	-	0	-	0	0	0	
Tl-V	83835	-22781	36	0	0	0	
Tl-W	205999	-44667	141	0	0	0	
Tl-Y	-171239	-43957	-175	0	0	0	
Tl-Zn	-	-	-	0	0	0	
Tl-Zr	-124042	-54225	-115	0	0	0	
V-Ag	74784	37034	73	0	0	0	
V-Al	-102373	16480	-113	0	0	0	
V-As	-181439	6239	-224	0	0	0	
V-Au	-70246	15246	-87	0	0	0	
V-Ba	214371	224468	337	0	0	0	
V-Be	-22250	38140	-66	0	0	0	
V-Bi	50830	78078	-17	0	0	0	
V-Ca	172492	152769	224	0	0	0	
V-Cd	27672	49135	6	0	0	0	
V-Co	-45146	9845	-54	0	0	0	
V-Cr	-2583	11761	-8	-12937	12125	-11.2004 - 0.0085 T	[176]
V-Cs	307035	227634	685	0	0	0	
V-Cu	23628	26289	19	42475	28840	39	[188]
V-Fe	-21879	10825	-28	0	0	0	
V-Ga	-56560	16883	-83	0	0	0	
V-Ge	-114760	16219	-129	0	0	0	
V-Hf	39840	33763	-10	0	0	0	
V-In	30573	72567	6	0	0	0	
V-Ir	-137631	-27984	-146	0	0	0	
V-K	308404	188714	552	0	0	0	
V-La	155074	117459	118	98843	97619	75	[207]
V-Li	143500	63578	144	0	0	0	
V-Mg	97016	65589	93	0	0	0	
V-Mn	-102	27038	-3	0	0	0	
V-Mo	3061	-14516	0	19245	-12120	17	[214]
V-Na	271646	122223	343	0	0	0	
V-Nb	8989	-6247	-5	9080	-7829	-7	[218]

V-Ni	-59804	10365	-69	0	0	0	
V-Os	-92024	-31678	-97	0	0	0	
V-P	-335324	-9163	-354	0	0	0	
V-Pb	61790	104158	15	0	0	0	
V-Pd	-140829	-8746	-151	0	0	0	
V-Pt	-181806	-24236	-198	0	0	0	
V-Rb	304077	221984	617	0	0	0	
V-Re	-50890	-32395	-54	0	0	0	
V-Rh	-117640	-17251	-123	0	0	0	
V-Ru	-97898	-21979	-103	0	0	0	
V-Sb	-26267	44985	-113	0	0	0	
V-Sc	66736	61238	33	0	0	0	
V-Si	-170024	8814	-175	0	0	0	
V-Sn	21859	68799	-68	0	0	0	
V-Sr	204712	205512	304	87611	108437	85	[197]
V-Ta	13222	-13942	-4	6929	-11426	-9	[185]
V-Tc	-84448	-25147	-89	0	0	0	
V-Th	138679	100288	45	0	0	0	
V-Ti	2974	8704	-7	14000	9886	3	[218]
V-Tl	74167	91539	56	0	0	0	
V-V	0	0	0	0	0	0	
V-W	808	-30491	-3	0	0	0	
V-Y	142715	95588	85	113047	94588	18	[207]
V-Zn	-34110	28624	-36	0	0	0	
V-Zr	28536	25822	-17	0	0	0	
W-Ag	172050	78017	172	0	0	0	
W-Al	-52903	53610	-52	0	0	0	
W-As	-90688	52463	-104	0	0	0	
W-Au	48087	60017	48	0	0	0	
W-Ba	36690	268802	383	0	0	0	
W-Be	125760	121630	-18	0	0	0	
W-Bi	160880	130465	153	0	0	0	
W-Ca	259457	192523	261	0	0	0	
W-Cd	101524	89295	101	0	0	0	
W-Co	38410	77189	-5	0	0	0	
W-Cr	38679	61028	4	31520	62074	0	[175]
W-Cs	356782	260596	720	0	0	0	
W-Cu	120774	81901	80	0	0	0	
W-Fe	32314	70613	0	0	0	0	
W-Ga	-616	57220	-4	0	0	0	
W-Ge	-29999	61440	-30	0	0	0	

W-Hf	-3757	74863	-27	0	0	0	
W-In	113866	118569	118	0	0	0	
W-Ir	-54559	19225	-62	0	0	0	
W-K	364346	222879	597	0	0	0	
W-La	158208	161777	154	0	0	0	
W-Li	247384	96387	169	0	0	0	
W-Mg	140166	101022	144	0	0	0	
W-Mn	47548	71941	23	0	0	0	
W-Mo	-847	17558	-1	0	0	0	
W-Na	247099	156675	391	0	0	0	
W-Nb	-30034	19284	-34	0	0	0	
W-Ni	33748	78276	-11	0	0	0	
W-Os	-28856	15157	-38	0	0	0	
W-P	-241052	39558	-239	0	0	0	
W-Pb	172930	164970	176	0	0	0	
W-Pd	-25100	40546	-26	0	0	0	
W-Pt	-79777	21687	-82	0	0	0	
W-Rb	352612	256024	658	0	0	0	
W-Re	-12812	7512	-16	0	0	0	
W-Rh	-27398	33807	-36	0	0	0	
W-Ru	-26387	27130	-38	0	0	0	
W-Sb	77838	93205	46	0	0	0	
W-Sc	45752	98239	39	0	0	0	
W-Si	-98964	74457	-102	0	0	0	
W-Sn	101488	127538	61	0	0	0	
W-Sr	118448	249220	348	0	0	0	
W-Ta	-25181	13163	-30	0	0	0	
W-Tc	-22792	20990	-28	0	0	0	
W-Th	108427	160317	57	0	0	0	
W-Ti	-22633	35581	-23	18212	38345	14.7820 - 0.0018 T	[229]
W-Tl	173829	141730	189	0	0	0	
W-V	5069	35339	-3	0	0	0	
W-W	0	0	0	0	0	0	
W-Y	128989	139783	111	0	0	0	
W-Zn	34869	69463	28	0	0	0	
W-Zr	-18384	58933	-39	0	0	0	
Y-Ag	-51908	56870	-103	0	0	0	
Y-Al	-118624	49866	-161	0	0	0	
Y-As	-314852	31325	-330	0	0	0	
Y-Au	-200817	31991	-268	0	0	0	
Y-Ba	88002	68909	90	0	0	0	

Y-Be	78608	186522	-101	0	0	0	
Y-Bi	-260593	-4908	-272	0	0	0	
Y-Ca	45316	34541	45	0	0	0	
Y-Cd	-139717	25610	-154	0	0	0	
Y-Co	89742	143225	-67	0	0	0	
Y-Cr	200213	130666	35	63000	93676	-91	[231]
Y-Cs	29834	119150	329	0	0	0	
Y-Cu	44811	126983	-70	0	0	0	
Y-Fe	158166	140664	-4	0	0	0	
Y-Ga	-152094	46837	-175	0	0	0	
Y-Ge	-197765	65669	-235	0	0	0	
Y-Hf	77427	-2702	41	0	0	0	
Y-In	-175241	5972	-175	0	0	0	
Y-Ir	-42609	64828	-180	0	0	0	
Y-K	194025	87738	237	0	0	0	
Y-La	3209	3726	1	0	0	0	
Y-Li	46751	39944	26	0	0	0	
Y-Mg	-16328	27876	-29	0	0	0	
Y-Mn	127449	111150	-5	0	0	0	
Y-Mo	213658	73405	81	100000	44742	-19	[215]
Y-Na	108950	47307	110	0	0	0	
Y-Nb	189116	39465	102	150000	18947	73	[219]
Y-Ni	56196	141169	-97	0	0	0	
Y-Os	54400	72666	-93	0	0	0	
Y-P	-400170	19910	-416	0	0	0	
Y-Pb	-229778	-5643	-235	0	0	0	
Y-Pd	-194816	56927	-286	0	0	0	
Y-Pt	-179313	43593	-289	0	0	0	
Y-Rb	215871	107131	281	0	0	0	
Y-Re	131942	64582	-14	0	0	0	
Y-Rh	-54050	78719	-181	0	0	0	
Y-Ru	32541	82446	-112	0	0	0	
Y-Sb	-310281	-49	-319	0	0	0	
Y-Sc	17104	10155	3	11412	8726	-12.5041 + 0.0099 T	[224]
Y-Si	-142661	137448	-216	0	0	0	
Y-Sn	-234937	5869	-239	0	0	0	
Y-Sr	75493	57667	76	0	0	0	
Y-Ta	183768	21469	93	0	0	0	
Y-Tc	40009	73467	-96	0	0	0	
Y-Th	5013	-15653	5	0	0	0	
Y-Ti	126875	43967	51	0	0	0	

Y-Tl	-173944	4563	-175	0	0	0	
Y-V	181649	90361	54	70170	50907	-49	[207]
Y-W	217059	49347	81	0	0	0	
Y-Y	0	0	0	0	0	0	
Y-Zn	-69742	72970	-125	0	0	0	
Y-Zr	60818	1580	34	40000	-3551	15	[232]
Zn-Ag	-	-	-	-18700	-8926	-20	[152]
Zn-Al	-	-	-	9868	-3257	17.8464 - 0.0090 T	[146]
Zn-As	-	-	-	0	0	0	
Zn-Au	-	-	-	0	0	0	
Zn-Ba	-	-	-	0	0	0	
Zn-Be	-	-	-	0	0	0	
Zn-Bi	-	-	-	0	0	0	
Zn-Ca	-	-	-	0	0	0	
Zn-Cd	-	-	-	0	0	0	
Zn-Co	-23476	-21843	-45	0	0	0	
Zn-Cr	4469	-20800	-9	0	0	0	
Zn-Cs	-	-	-	0	0	0	
Zn-Cu	-	-	-	-25214	-13340	-24.0248 - 0.0108 T	[189]
Zn-Fe	3754	-20019	-13	23602	-17870	7	[200]
Zn-Ga	-	-	-	11756	-6279	3	[233]
Zn-Ge	-	-	-	0	0	0	
Zn-Hf	-91353	-23561	-141	0	0	0	
Zn-In	-	-	-	23114	4645	-16	[205]
Zn-Ir	-68962	-53890	-88	0	0	0	
Zn-K	-	-	-	0	0	0	
Zn-La	-69538	37752	-191	0	0	0	
Zn-Li	-	-	-	0	0	0	
Zn-Mg	-	-	-	2543	11723	-17.5956 - 0.0007 T	[211]
Zn-Mn	-44350	-10965	-50	0	0	0	
Zn-Mo	16968	-45784	17	0	0	0	
Zn-Na	-	-	-	0	0	0	
Zn-Nb	-32075	-45705	-39	0	0	0	
Zn-Ni	-35782	-21315	-60	0	0	0	
Zn-Os	-22911	-57223	-37	0	0	0	
Zn-P	-	-	-	0	0	0	
Zn-Pb	-	61304	-	0	0	0	
Zn-Pd	-152729	-44020	-171	0	0	0	
Zn-Pt	-134813	-52666	-157	0	0	0	
Zn-Rb	-	-	-	0	0	0	
Zn-Re	9291	-58569	3	0	0	0	

Zn-Rh	-85148	-47329	-102	0	0	0	
Zn-Ru	-35996	-48502	-52	0	0	0	
Zn-Sb	-	-	-	0	0	0	
Zn-Sc	-98626	-1157	-154	0	0	0	
Zn-Si	-	-	-	0	0	0	
Zn-Sn	-	-	-	30453	11900	-49	[205]
Zn-Sr	-	-	-	0	0	0	
Zn-Ta	-36197	-55078	-44	0	0	0	
Zn-Tc	-37210	-53066	-49	0	0	0	
Zn-Th	-	-	-	0	0	0	[156]
Zn-Ti	-85886	-36447	-93	0	0	0	
Zn-Tl	-	-	-	0	0	0	
Zn-V	-33280	-36801	-34	0	0	0	
Zn-W	30683	-60131	32	0	0	0	
Zn-Y	-61778	21249	-180	0	0	0	
Zn-Zn	-	0	-	0	0	0	
Zn-Zr	-111664	-31399	-166	0	0	0	
Zr-Ag	-68797	35309	-78	0	0	0	
Zr-Al	-206788	22633	-208	0	0	0	
Zr-As	-394173	7007	-397	0	0	0	
Zr-Au	-275895	2083	-294	0	0	0	
Zr-Ba	217299	147295	269	0	0	0	
Zr-Be	-11005	118556	-147	0	0	0	
Zr-Bi	-205206	16284	-256	0	0	0	
Zr-Ca	154585	91824	169	0	0	0	
Zr-Cd	-139883	24753	-142	0	0	0	
Zr-Co	-51191	75016	-137	-47428	86132	-134	[172]
Zr-Cr	48989	68682	-41	0	0	0	
Zr-Cs	347333	191412	613	0	0	0	
Zr-Cu	-21772	75668	-78	11337	78639	-51	[187]
Zr-Fe	1112	74279	-85	0	0	0	
Zr-Ga	-203765	23086	-203	0	0	0	
Zr-Ge	-273738	31071	-272	0	0	0	
Zr-Hf	-585	-2771	-1	0	0	0	
Zr-In	-147730	21785	-160	0	0	0	
Zr-Ir	-212231	3338	-281	0	0	0	
Zr-K	334899	151404	466	0	0	0	
Zr-La	78304	50587	60	0	0	0	
Zr-Li	111528	58649	100	0	0	0	
Zr-Mg	13000	39894	13	40148	43106	40	[212]
Zr-Mn	13198	69396	-52	0	0	0	

Zr-Mo	26869	18560	-23	0	0	0	
Zr-Na	230121	92057	257	0	0	0	
Zr-Nb	32136	4210	15	5133	-445	-11	[220]
Zr-Ni	-80685	73566	-165	0	0	0	
Zr-Os	-127269	7492	-202	0	0	0	
Zr-P	-541914	-3032	-521	0	0	0	
Zr-Pb	-175061	24291	-210	0	0	0	
Zr-Pd	-309480	8657	-339	-106109	30245	-154	[223]
Zr-Pt	-334680	-9520	-377	0	0	0	
Zr-Rb	-15045	178736	537	0	0	0	
Zr-Re	-61530	2829	-129	0	0	0	
Zr-Rh	-200496	18563	-261	0	0	0	
Zr-Ru	-139629	18510	-212	0	0	0	
Zr-Sb	-296217	3225	-337	0	0	0	
Zr-Sc	16719	23580	16	0	0	0	
Zr-Si	-269761	65075	-284	0	0	0	
Zr-Sn	-223668	9408	-250	0	0	0	
Zr-Sr	200707	130998	238	0	0	0	
Zr-Ta	29800	-10923	10	30052	-9341	13	[227]
Zr-Tc	-132239	11879	-195	0	0	0	
Zr-Th	40864	22645	19	0	0	0	[228]
Zr-Ti	14527	17348	-1	3460	16180	-11	[230]
Zr-Tl	-120285	29565	-139	0	0	0	
Zr-V	37371	40170	-13	0	0	0	
Zr-W	18559	-4522	-34	0	0	0	
Zr-Y	57806	35488	42	40000	35145	21	[232]
Zr-Zn	-125703	45709	-137	0	0	0	
Zr-Zr	0	0	0	0	0	0	

Appendix B

This appendix contains example programs of the type used to make the calculations in this work.

B.1 is the program for calculating enthalpies from RKM data

B.2 is an example program to find the minimum in the free energy curves

B.3 is an example program to compare the nanocrystallline free energies with other phases in order to construct a stability map

B.4 is an example program to create a nanocrystalline stability map

APPENDIX B .1

```
R = 8.314;
```

Data sources

```
(*List of element text labels*)
elementlist = Import["C:\\Documents and Settings\\Heather\\My
      Documents\\My Dropbox\\inputfiles\\element list.txt", "Table"];
(*Elastic moduli for the pure elements*)
ModulusArray = Import[
    "C:\\Documents and Settings\\Heather\\My Documents\\My Dropbox\\inputfiles\\bulk
      and shear modulus table.txt", "Table"];
(*Atomic volume and Miedema-model parameters for the pure elements *)
ParameterArray = Import["C:\\Documents and Settings\\Heather\\My
      Documents\\My Dropbox\\inputfiles\\parameter table.txt", "Table"];
(*Miedema model chemical interaction paramter*)
ΔHintAinBArray = Import[
    "C:\\Documents and Settings\\Heather\\My Documents\\My Dropbox\\inputfiles\\deltaHint
      solute row - solvent column.txt", "Table"];
(*pure element surface energies*)
surfaceE = Import["C:\\Documents and Settings\\Heather\\My
      Documents\\My Dropbox\\inputfiles\\surface energy.txt", "Table"];
(*pure element radii*)
RadiusArray = Import["C:\\Documents and Settings\\Heather\\My
      Documents\\My Dropbox\\inputfiles\\atomicradii.txt", "Table"];
(*non-Miedema coefficients to RKM enthalpy models*)
testRKM = Import["C:\\Documents and Settings\\Heather\\My
      Documents\\My Dropbox\\Miedema paper\\testrkm.txt", "Table"];
```

Calculation of Mixing Enthalpies for RKM

```
Hmix = ConstantArray[0, {Length[testRKM], 5}];
Hseg = ConstantArray[0, {Length[testRKM], 5}];
ΔHint = ConstantArray[0, Length[testRKM]];
Hmixtable = ConstantArray[0, {71, 71}];
Hsegtable = ConstantArray[0, {71, 71}];
For[li = 1, li ≤ (Length[testRKM]), li++,
  (*extracting binary system from label*)
  name = StringSplit[testRKM[[li, 1]], "-"];
  For[ei = 1, ei ≤ Length[elementlist],
   ei++, If[name[[1]] == elementlist[[ei, 1]], solvent = ei;];
   If[name[[2]] == elementlist[[ei, 1]], solute = ei;];];

  (*RKM parameters*)
  L0a = ToExpression[testRKM[[li, 5]]];
  L0b = ToExpression[testRKM[[li, 6]]];
  L1a = testRKM[[li, 7]];
  L1b = testRKM[[li, 8]];
  L2a = testRKM[[li, 9]];
  L2b = testRKM[[li, 10]];
```

```
L0 = L0a + L0b * T;
L1 = L1a + L1b * T;
L2 = L2a + L2b * T;
model = L0 * X * (1 - X) + L1 * X * (1 - X) * (X - (1 - X)) + L2 * X * (1 - X) * (X - (1 - X))^2;
model2 = model /. X → (1 - X);
If[testRKM[[li, 11]] === 0, RKM = model, RKM = model2];
full = RKM + R * T * (X * Log[X] + (1 - X) Log[1 - X]) /. R → 8.314;

If[L0 == 0, Goto[end]];

RKMtable0 = Table[{xi, RKM /. T → 0 /. X → xi}, {xi, 0, 1, 0.01}];
RKMtable300 = Table[{xi, RKM /. T → 300 /. X → xi}, {xi, 0, 1, 0.01}];
RKMtable500 = Table[{xi, RKM /. T → 500 /. X → xi}, {xi, 0, 1, 0.01}];
RKMtable1000 = Table[{xi, RKM /. T → 1000 /. X → xi}, {xi, 0, 1, 0.01}];
RKMtable1273 = Table[{xi, RKM /. T → 1273 /. X → xi}, {xi, 0, 1, 0.01}];
RKMfit0 = NonlinearModelFit[RKMtable0, a * x * (1 - x), {a}, x];
RKMfit300 = NonlinearModelFit[RKMtable300, a * x * (1 - x), {a}, x];
RKMfit500 = NonlinearModelFit[RKMtable500, a * x * (1 - x), {a}, x];
RKMfit1000 = NonlinearModelFit[RKMtable1000, a * x * (1 - x), {a}, x];
RKMfit1273 = NonlinearModelFit[RKMtable1273, a * x * (1 - x), {a}, x];

(*whether the fit is good to a symmetric regular solution model*)
Hmix[[li, 1]] = If[RKMfit0["RSquared"] > 0.8, RKMfit0["BestFit"] / ((1 - x) * x), 99];
Hmix[[li, 2]] = If[RKMfit300["RSquared"] > 0.8, RKMfit300["BestFit"] / ((1 - x) * x), 99];
Hmix[[li, 3]] = If[RKMfit500["RSquared"] > 0.8, RKMfit500["BestFit"] / ((1 - x) * x), 99];
Hmix[[li, 4]] = If[RKMfit1000["RSquared"] > 0.8, RKMfit1000["BestFit"] / ((1 - x) * x), 99];
Hmix[[li, 5]] = If[RKMfit1273["RSquared"] > 0.8, RKMfit1273["BestFit"] / ((1 - x) * x), 99];

Hmixtable[[solute, solvent]] = Hmix[[li, 4]];
```

(*finding ΔHint*)

```
Va = .; Vb = .; nwsA = .; nwsB = .; KA = .; KB = .; GA = .; GB = .; ψA = .; ψB = .; WA = .; WB = .;
(*elastic term*)
```

$$cAs = \frac{cA * Va^{2/3}}{cA * Va^{2/3} + cB * Vb^{2/3}}; \quad cBs = \frac{cB * Vb^{2/3}}{cA * Va^{2/3} + cB * Vb^{2/3}};$$

$$\Delta HelasticAinB = \frac{2 * KA * GB * (WA - WB)^2}{3 * KA * WB + 4 * GB * WA};$$

$$\Delta HelasticBinA = \frac{2 * KB * GA * (WA - WB)^2}{3 * KB * WA + 4 * GA * WB};$$

$$WA = \left(Va * 10^6 + \alpha * \frac{(\psi A - \psi B)}{nwsA}\right) * 10^{-6}; \quad WB = \left(Vb * 10^6 + \alpha * \frac{(\psi A - \psi B)}{nwsB}\right) * 10^{-6};$$

$$\alpha = 1.5 * \frac{(Va * 10^6)^{2/3}}{\frac{1}{nwsA^{1/3}} + \frac{1}{nwsB^{1/3}}};$$

```
KA = 10^10 * (ModulusArray[[solute, 1]]);
KB = 10^10 * (ModulusArray[[solvent, 1]]);
GA = 10^10 * (ModulusArray[[solute, 2]]);
GB = 10^10 * ModulusArray[[solvent, 2]];
Va = 10^-6 * (ParameterArray[[solute, 3]]);
Vb = 10^-6 * (ParameterArray[[solvent, 3]]);
```

```
nwsA = ParameterArray[[solute, 2]];
nwsB = ParameterArray[[solvent, 2]];
ψA = ParameterArray[[solute, 1]];
ψB = ParameterArray[[solvent, 1]];
cbarray = Range[0, 1, 0.01];
ΔHelasticSS = ConstantArray[0, Length[cbarray]];
ΔHchemSS = ConstantArray[0, Length[cbarray]];
For[cbi = 1, cbi ≤ Length[cbarray], cbi++,
 ΔHelasticSS[[cbi]] =
  cA * cB * (cB * ΔHelasticAinB + cA * ΔHelasticBinA) /. cB → 1 - cA /. cA → cbarray[[cbi]];
 ΔHchemSS[[cbi]] = 1000 * cA * cB * (cBs * ΔH + cAs * ΔH2) /. cB → 1 - cA /.
   cA → cbarray[[cbi]];] ;
(*A is solute ΔH is AinB, ΔH2 is BinA*)
dH1 = ConstantArray[0, 1000]; dH2 = ConstantArray[0, 1000];
For[ii = 2, ii ≤ 98, ii++,
  ij = 100 - ii;
  error =
   Check[solveans = Solve[{ΔHchemSS[[ii]] + ΔHelasticSS[[ii]] == RKM /. X → cbarray[[ii]],
       ΔHchemSS[[ij]] + ΔHelasticSS[[ij]] == RKM /. X → cbarray[[ij]]}, {ΔH, ΔH2}], 99];
  dH1[[ii]] = ΔH /. solveans[[1]];
  dH2[[ii]] = ΔH2 /. solveans[[1]];
  If[error == 99, dH1[[ii]] = 0; dH2[[ii]] = 0]]
 dH1 = DeleteCases[dH1, 0];
dH2 = DeleteCases[dH2, 0];
HintAinB = Mean[dH1] * 1.0;

(*Elastic contribution to segregation enthalpy*)
Eelast = 6.02 * 10^23 *
  (24 * π * K2 * G1 * r1 * r2 * (r1 - r2)^2 / (3 * K2 * r2 + 4 * G1 * r1)) /. K2 → KB /. G1 → GA /. r1 → RadiusArray[[solvent, 1]] *
      10^-10 /. r2 → RadiusArray[[solute, 1]] * 10^-10 ; (*1 is solvent*)
(*full segregation enthalpy*)
ΔHsegGB =
 Eelast - 1 * 0.71 * 1 / 6 (-HintAinB * 1000 - 4.5 * 10^8 * surfaceE[[solvent, 1]] ■ (Vb)^2/3 +
      4.5 * 10^8 * (surfaceE[[solute, 1]]) * (Va)^2/3) /.
   γB → (surfaceE[[solute, 1]]) /. γA → surfaceE[[solvent, 1]];

Hseg[[li, 1]] = If[Hmix[[li, 1]] ≠ 99, ΔHsegGB /. T → 0, ΔHsegGB = 99];
Hseg[[li, 2]] = If[Hmix[[li, 2]] ≠ 99, ΔHsegGB /. T → 300, ΔHsegGB = 99];
Hseg[[li, 3]] = If[Hmix[[li, 3]] ≠ 99, ΔHsegGB /. T → 500, ΔHsegGB = 99];
Hseg[[li, 4]] = If[Hmix[[li, 4]] ≠ 99, ΔHsegGB /. T → 1000, ΔHsegGB = 99];
Hseg[[li, 5]] = If[Hmix[[li, 5]] ≠ 99, ΔHsegGB /. T → 1273, ΔHsegGB = 99];

Hsegtable[[solute, solvent]] = Hseg[[li, 4]];

ΔHint[[li]] = HintAinB;
Label[end];] // Quiet
```

```
Export["C:\\Documents and Settings\\Heather\\My
    Documents\\My Dropbox\\Miedema paper\\hmixlist.txt", Hmix, "Table"];
Export["C:\\Documents and Settings\\Heather\\My Documents\\My
    Dropbox\\Miedema paper\\hseglist.txt", Hseg, "Table"];
Export["C:\\Documents and Settings\\Heather\\My Documents\\My
    Dropbox\\Miedema paper\\hintlist.txt", ΔHint, "Table"];
Export["C:\\Documents and Settings\\Heather\\My Documents\\My
    Dropbox\\Miedema paper\\hsegtable.txt", Hsegtable, "Table"];
Export["C:\\Documents and Settings\\Heather\\My Documents\\My
     Dropbox\\Miedema paper\\hmixtable.txt", Hmixtable, "Table"]; // Quiet

(*elements we are not including in table i.e. C, Hg, U, ...*)
nolist = {5, 9, 12, 17, 18, 19, 22, 25, 26, 32, 38, 44, 45, 47, 55, 59, 64, 65, 69};
totallist = {99};
For[ii = 1, ii ≤ Length[elementlist], ii++,
 For[jj = 1, jj ≤ Length[elementlist], jj++,
  listpt = elementlist[[ii]] <> "-" <> elementlist[[jj]];
  matchj = Cases[nolist, jj];
  If[matchj == {jj}, listpt = 99;];
  matchi = Cases[nolist, ii];
  If[matchi == {ii}, listpt = 99;];
  totallist = Append[totallist, listpt];
 ]]
totallist = DeleteCases[totallist, 99]
Export["C:\\Documents and Settings\\Heather\\My
    Documents\\My Dropbox\\inputfiles\\totallistname.txt", totallist];
ΔHmix = Import["C:\\Documents and Settings\\Heather\\My
     Documents\\My Dropbox\\inputfiles\\ΔHmixJ.txt", "Table"];
(*elements we are not including in table i.e. C, Hg, U, ...*)
nolist = {5, 9, 12, 17, 18, 19, 22, 25, 26, 32, 38, 44, 45, 47, 55, 59, 64, 65, 69};
totalmix = {99};
For[ii = 1, ii ≤ Length[elementlist], ii++,
 For[jj = 1, jj ≤ Length[elementlist], jj++,
  listpt = {ΔHmix[[jj, ii]]};
  matchj = Cases[nolist, jj];
  If[matchj == {jj}, listpt = 99;];
  matchi = Cases[nolist, ii];
  If[matchi == {ii}, listpt = 99;];
  totalmix = Join[totalmix, listpt];
 ]]
totalmix = DeleteCases[totalmix, 99];
Export["C:\\Documents and Settings\\Heather\\My
    Documents\\My Dropbox\\inputfiles\\totalmix.txt", totalmix];
segtable = Import["C:\\Documents and Settings\\Heather\\My
     Documents\\My Dropbox\\Miedema paper\\segregation table.txt", "TSV"];
Dimensions[segtable]
{52, 52}
```

```
totalseg = {99};
For[ii = 1, ii ≤ 52, ii++,
 For[jj = 1, jj ≤ 52, jj++,
  listpt = {segtable[[jj, ii]]};
  totalseg = Join[totalseg, listpt];
 ]]
totalseg = DeleteCases[totalseg, 99];
Export["C:\\Documents and Settings\\Heather\\My
    Documents\\My Dropbox\\inputfiles\\totalseg.txt", totalseg];
param =
  Import["C:\\Users\\Heather\\Documents\\My Dropbox\\inputfiles\\parameter table.txt",
   "Table"];
hint =
  Import["C:\\Users\\Heather\\Documents\\My Dropbox\\inputfiles\\deltaHint solute row
     - solvent column.txt", "Table"];
elements = Import[
   "C:\\Users\\Heather\\Documents\\My Dropbox\\inputfiles\\element list.txt", "Table"];
hintlist2 =
  Import["C:\\Documents and Settings\\Heather\\My Documents\\My Dropbox\\Miedema
     paper\\hintlist.txt", "TSV"];
hintlist3 = Table[ToExpression[hintlist2[[pi, 1]]], {pi, 1, Length[hintlist2]}];
hintlist4 = ConstantArray[0, Length[hintlist3]];
For[pi = 1, pi ≤ Length[hintlist3], pi++,
  hintlist4[[pi]] = ToString[NumberForm[hintlist3[[pi]] // Expand, {7, 4}]];];
Export["C:\\Documents and Settings\\Heather\\My Documents\\My
    Dropbox\\Miedema paper\\hintlistE.txt", hintlist4, "Table"];
```

```
z = 12; w_b = wbarray[[wi]]; w_ig = Heatherwig[[ww]]; ν = 1 / 2;
γ_A = Heather1[[3]]; γ_B = Heather1[[4]]; R = 0.00008617; dim = 3; t = 0.5;
```

APPENDIX B .3

```
SetOptions[SelectedNotebook[], InputAliases -> {"xig" → "x_ig"}]
```

```
wbarray = Join[Range[-0.01, -0.08, -0.01], Range[-0.015, -0.035, -0.01](*,{-0.0125}*)]
```

```
{-0.01, -0.02, -0.03, -0.04, -0.05, -0.06, -0.07, -0.08, -0.015, -0.025, -0.035, -0.0125}
```

```
wbarray
```

```
{-0.01, -0.015, -0.02, -0.025, -0.03, -0.035, -0.04,
 -0.045, -0.05, -0.055, -0.06, -0.065, -0.07, -0.075, -0.08}
```

```
stoich = {{0.25, -10000/eVtoJ}}
```

```
{{0.25, -103.68}}
```

```
-50000 / eVtoJ
```

```
-518.4
```

```
(*MIN IS NEVER ASSIGNED TO MINARRAY*)
```

```
stoich[[1, 2]] < dGnumPointsIN[[ct, 2]]
```

```
True
```

```
For[wbi = 1, wbi ≤ (Length[wbarray]), wbi++,
  fig = .; z = .; w_b = .; w_ig = .; γ_A = .; γ_B = .; X = .; R = .; T = .; xb = .; A = .; B = .; ν = .;
  Heather1 = {wbarray[[wbi]], (-1 / 2) * 0.05, 0.085, 0.085};
  (*Heather1Tcr=z*w_b/(2*R)/.w_b→Heather1[[1]]/.z→12/.R->0.00008617;*)
  temperature = 1000(*-0.35*Heather1Tcr*);
  Heatherwig = Table[(aaa * Heather1[[1]]), {aaa, 1, 7, 0.05}];
  X = .; T = .; dfit = .; dG = .; xigfit = .; hj = .; dyay = .; dyay2 = .;
  z = 12; w_b = Heather1[[1]]; w_ig = Heatherwig[[1]];
  ν = 1 / 2; γ_A = Heather1[[3]]; γ_B = Heather1[[4]]; R = 0.00008617;
  dim = 3; t = 0.5; d = .; γ = .; T = .; x = .; X = .; Ω = 1.095 * 10^-2;
  deltaGtwo = z * (1 - fig) * x_b * (1 - x_b) * w_b + fig * (1 - x_ig) * γ_A +
      fig * x_ig * γ_B + z * fig * x_ig * (1 - x_ig) * w_ig +
      z * ν * fig * ((x_ig * (x_ig - x_b) - (1 - x_ig) * (x_ig - x_b)) * w_ig - 1/z * (x_ig - x_b) * (γ_B - γ_A)) +
      R * T * ((1 - fig) * (x_b * Log[x_b] + (1 - x_b) * Log[1 - x_b]) +
          fig * (x_ig * Log[x_ig] + (1 - x_ig) * Log[1 - x_ig])) /.
    x_b -> (X - fig * x_ig) / (1 - fig) /. T → temperature;
  fig = 1 - ((d - t)/d)^dim;
  (*regular solution*)
  deltaGreg2 = Limit[deltaGtwo, d → ∞];
  wbstring = ToString[wbarray[[wbi]]];
  (*foldername=
    "C:\\Users\\Heather\\Documents\\My Dropbox\\negative wb\\z12 -0.35Tcr\\wb"<>
     wbstring;*)
  foldername = "C:\\Documents and Settings\\Heather\\My Documents\\My
      Dropbox\\negative wb\\z12 1000K\\wb" <> wbstring; (**)
  SetDirectory[foldername];
  (*set empty arrays for types of behavior expected*)
```

```
notNC = ConstantArray[0, Length[Heatherwig]];
metaNC = ConstantArray[0, Length[Heatherwig]];
bimodalNCR = ConstantArray[0, Length[Heatherwig]];
bimodalAR = ConstantArray[0, Length[Heatherwig]];
bimodalARwNC = ConstantArray[0, Length[Heatherwig]];
For[p = 1, p ≤ (Length[Heatherwig]), p++,
 (*Read in files*)
 error = 0; errorIN = 0;
 wbstring = ToString[Heather1[[1]]];
 wigstring = ToString[Heatherwig[[p]]];
 xigfilenameIN = "wb" <> wbstring <> "wig" <> wigstring <> "gba=gbbXIG.txt";
 xDTfilenameIN = "wb" <> wbstring <> "wig" <> wigstring <> "gba=gbbXDT.txt";
 segfilenameIN = "wb" <> wbstring <> "wig" <> wigstring <> "gba=gbbDHSeg.txt";
 dgptfilenameIN = "wb" <> wbstring <> "wig" <> wigstring <> "gba=gbbDGPTS.txt";
 dGnumPointsIN = Import[dgptfilenameIN, "TSV"];
 xDTarrayIN = Import[xDTfilenameIN, "TSV"];
 xigArrayIN = Import[xigfilenameIN, "TSV"];
 segregationIN = Import[segfilenameIN, "TSV"];
 dGnumPointsIN = ToExpression[dGnumPointsIN];
 xDTarrayIN = ToExpression[xDTarrayIN];
 xigArrayIN = ToExpression[xigArrayIN];
 segregationIN = ToExpression[segregationIN];
 X = .; T = .; dfit = .; dG = .; xigfit = .; hj = .; dyay = .; dyay2 = .;
 z = 12; w_b = Heather1[[1]]; w_ig = Heatherwig[[p]];
 v = 1 / 2; γ_A = Heather1[[3]]; γ_B = Heather1[[4]]; R = 0.00008617;
 dim = 3; t = 0.5; d = .; γ = .; T = .; x = .; X = .; Ω = 1.095 * 10^-2;
 deltaGtwo = z * (1 - fig) * x_b * (1 - x_b) * w_b + fig * (1 - x_ig) * γ_A +
     fig * x_ig * γ_B + z * fig * x_ig * (1 - x_ig) * w_ig +
     z * v * fig * ((x_ig * (x_ig - x_b) - (1 - x_ig) * (x_ig - x_b)) * w_ig - 1/z * (x_ig - x_b) * (γ_B - γ_A)) +
     R * T * ((1 - fig) * (x_b * Log[x_b] + (1 - x_b) * Log[1 - x_b]) +
         fig * (x_ig * Log[x_ig] + (1 - x_ig) * Log[1 - x_ig])) /.
    x_b -> (X - fig * x_ig) / (1 - fig) /. T → temperature;
 amorph2 = (1 - X) * γ_A + X * γ_B + z * X * (1 - X) * w_ig + R * T * (X * Log[X] + (1 - X) * Log[1 - X]) /.
   T → temperature;
 stable = 0; meta = 0; biARwNC = 0; biNCR = 0; amph = 0;
 xDTarray2 = ConstantArray[0, Length[xDTarrayIN]];
 metaarray = ConstantArray[0, Length[xDTarrayIN]];
 stablecounter = ConstantArray[0, Length[dGnumPointsIN]];
 starting = FindRoot[deltaGreg2 == amorph2, {X, 0.1}];
 startX = X /. starting;
 ending = FindRoot[deltaGreg2 == amorph2, {X, 0.9}];
 endX = X /. ending;
 If[(amorph2 /. X → 0.5) > (deltaGreg2 /. X → 0.5), startX = 0; endX = 1;, amph = 99];
 For[ct = 1, ct ≤ (Length[dGnumPointsIN]), ct++,
  If[Im[dGnumPointsIN[[ct, 2]]] == 0,
   dGnumPointsIN[[ct, 2]] = Re[dGnumPointsIN[[ct, 2]]]];
  If[Im[xDTarrayIN[[ct, 2]]] == 0, xDTarrayIN[[ct, 2]] = Re[xDTarrayIN[[ct, 2]]]];
  If[Re[xDTarrayIN[[ct, 2]]] > 1000, xDTarray2[[ct]] = 99];
  (*start the comparison of points where amorph and reg soln cross*)
  If[dGnumPointsIN[[ct, 1]] < startX,
```

```
      stablecounter[[ct]] = 99; metaarray[[ct]] = 99; Goto[nextpt]];
     If[dGnumPointsIN[[ct, 1]] > endX, stablecounter[[ct]] = 99;
      metaarray[[ct]] = 99; Goto[nextpt]];
     (*compare the dG point to the free energy of the regular solution,
     if higher than not stable*)
     If[dGnumPointsIN[[ct, 2]] > (deltaGreg2 /. X → dGnumPointsIN[[ct, 1]]) ||
       Abs[dGnumPointsIN[[ct, 2]] - (deltaGreg2 /. X → dGnumPointsIN[[ct, 1]])] < 10^-4,
      stablecounter[[ct]] = 1];
     If[stablecounter[[ct]] == 0 && (stoich[[1, 2]] < dGnumPointsIN[[ct, 2]]),
      metaarray[[ct]] = 1];
     (*if the dg point is lower than the common tangent but higher than the amorphous,
     amorph and reg have a common tangent*)
     If[dGnumPointsIN[[ct, 2]] > (amorph2 /. X -> dGnumPointsIN[[ct, 1]]) &&
       xDTarrayIN[[ct, 2]] < 1000, biARwNC = 99];
     (*If[dGnumPointsIN[[ct,2]]>(amorph2/.X->dGnumPointsIN[[ct,1]])&&
        xDTarrayIN[[ct,2]]>1000,biNCR=99];*)
     Label[nextpt]];
    xDTarray2 = DeleteCases[xDTarray2, 99];
    metaarray = DeleteCases[metaarray, 99];
    stablecounter = DeleteCases[stablecounter, 99];
    If[Mean[metaarray] > 0.5, meta = 99];
    If[Mean[stablecounter] > 0.2, stable = 99];
    (*assigns the wig/wb combindation
     to the appropriate array based on the if statements*)
    (*If[local==0,localmin[[p]]={(wig/wb),wb}];*)
    (*If[xDTarray2=={},notNC[[p]]={(wig/wb),wb};Goto[newp];];*)
    If[stable == 99(*&&meta==99*) || xDTarray2 == {}, notNC[[p]] = {(wig / wb), wb}];
    If[meta == 99, metaNC[[p]] = {(wig / wb), wb}];
    If[amph == 99 && (stable == 99 || xDTarray2 == {}), bimodalAR[[p]] = {(wig / wb), wb}];
    If[biARwNC == 99 && stable == 0, bimodalARwNC[[p]] = {(wig / wb), wb}];
    If[biNCR == 0 && stable == 0 && meta == 0, bimodalNCR[[p]] = {(wig / wb), wb}]; Label[newp];
   ];
   notNCplot = DeleteCases[notNC, 0];
   metaNCplot = DeleteCases[metaNC, 0];
   bimodalARplot = DeleteCases[bimodalAR, 0];
   bimodalARwNCplot = DeleteCases[bimodalARwNC, 0];
   bimodalNCRplot = DeleteCases[bimodalNCR, 0];
   Export["notNCpoints10kj.txt", notNCplot, "Table"];
   Export["metaNCpoints10kj.txt", metaNCplot, "Table"];
   Export["bimodalARpoints10kj.txt", bimodalARplot, "Table"];
   Export["bimodalARwNCpoints10kj.txt", bimodalARwNCplot, "Table"];
   Export["bimodalNCRpoints10kj.txt", bimodalNCRplot, "Table"];
   bimodal = 0; stable = 0; meta = 0; biNCR = 0;
minimumarray = ConstantArray[0, Length[Heatherwig]];
   (*Checking for bimodal nc*)
   (**)notNC = ConstantArray[0, Length[Heatherwig]];
   metaSSNC = ConstantArray[0, Length[Heatherwig]];
   bimodalNCR = ConstantArray[0, Length[Heatherwig]];
   bimodalAR = ConstantArray[0, Length[Heatherwig]];
   bimodalNCNC = ConstantArray[0, Length[Heatherwig]];
   bimodalRANC = ConstantArray[0, Length[Heatherwig]];
```

```
For[p = 1, p ≤ (Length[Heatherwig]), p++,
 wbstring = ToString[Heather1[[1]]];
 wigstring = ToString[Heatherwig[[p]]];
 bimodal = 0; stable = 0; meta = 0; biNCR = 0; biamorph = 0;
 X = .; T = .; dfit = .; dG = .; xigfit = .; hj = .; dyay = .; dyay2 = .;
 z = 12; wb = Heather1[[1]]; wig = Heatherwig[[p]];
 ν = 1 / 2; γA = Heather1[[3]]; γB = Heather1[[4]]; R = 0.00008617;
 dim = 3; t = 0.5; d = .; γ = .; T = .; x = .; X = .; Ω = 1.095 * 10^-2;
 deltaGtwo = z * (1 - fig) * xb * (1 - xb) * wb + fig * (1 - xig) * γA +
      fig * xig * γB + z * fig * xig * (1 - xig) * wig +
      z * ν * fig * ((xig * (xig - xb) - (1 - xig) * (xig - xb)) * wig - 1/z * (xig - xb) * (γB - γA)) +
      R * T * ((1 - fig) * (xb * Log[xb] + (1 - xb) * Log[1 - xb]) +
          fig * (xig * Log[xig] + (1 - xig) * Log[1 - xig])) /.
    xb -> (X - fig * xig) / (1 - fig) /. T → temperature;
 amorph2 = (1 - X) * γA + X * γB + z * X * (1 - X) * wig + R * T * (X * Log[X] + (1 - X) * Log[1 - X]) /.
   T → temperature;
 bimodalfilenameIN = "wb" <> wbstring <> "wig" <> wigstring <> "gba=gbbDGPTSbimodal.txt";
 dgptfilenameIN = "wb" <> wbstring <> "wig" <> wigstring <> "gba=gbbDGPTS.txt";
 bimodalptsIN = Import[bimodalfilenameIN, "TSV"];
 dGPointsIN = Import[dgptfilenameIN, "TSV"];
 dGnumPointsIN = Join[bimodalptsIN, dGPointsIN];
 xDTfilenameIN = "wb" <> wbstring <> "wig" <> wigstring <> "gba=gbbXDT.txt";
 XDTarrayIN = Import[xDTfilenameIN, "TSV"];
 tangentfilenameIN = "wb" <> wbstring <> "gba=gbbTANGENTS.txt";
 tangentsIN = ToExpression[Import[tangentfilenameIN, "TSV"]];
 (*Find lowest dGpt*)
 sortedarrayofpoints = Sort[dGnumPointsIN, #1[[2]] < #2[[2]] &];
 min = sortedarrayofpoints[[1]];
 minimumarray[[p]] = min;
 If[min == 0, minimumarray[[p]] = 0];
 (*Is this lowest dGpt lower than amorphous*)
 If[min[[2]] < (amorph2 /. X → min[[1]]), bimodal = 99];
 match = Cases[dGPointsIN, {min[[1]], _}];
 If[Abs[match[[1, 2]] - min[[2]]] < 1 * 10^-6, bimodal = 0;];
 (* Does this amorphous come down below the REG/Bimodal NC tangent line?*)
 tangentlinecheck = tangentsIN[[p, 1]];
 If[tangentlinecheck == 0, Goto[notneed];];
 birange = Range[startX, min[[1]], 0.01];
 For[bi = 1, bi ≤ Length[birange], bi++,
  If[(amorph2 /. X → birange[[bi]]) < (tangentlinecheck /. X → birange[[bi]]),
    biamorph = 99; Goto[notneed]];];
 (*Is nc point below reg soln common tangent*)
 Label[notneed];
 starting = FindRoot[deltaGreg2 == amorph2, {X, 0.1}];
 startX = X /. starting;
 ending = FindRoot[deltaGreg2 == amorph2, {X, 0.9}];
 endX = X /. ending;
 If[(amorph2 /. X → 0.5) > (deltaGreg2 /. X → 0.5), startX = 0; endX = 1;];
 metaarray = ConstantArray[0, Length[dGnumPointsIN]];
 stablecounter = ConstantArray[0, Length[dGnumPointsIN]];
```

```
  For[ct = 1, ct ≤ Length[dGnumPointsIN], ct++,
   If[Im[dGnumPointsIN[[ct, 2]]] == 0,
    dGnumPointsIN[[ct, 2]] = Re[dGnumPointsIN[[ct, 2]]]];
   If[Im[xDTarrayIN[[ct, 2]]] == 0, xDTarrayIN[[ct, 2]] = Re[xDTarrayIN[[ct, 2]]]];
   If[Re[xDTarrayIN[[ct, 2]]] > 1000, xDTarray2[[ct]] = 99];
   (*start the comparison of points where amorph and reg soln cross*)
   If[dGnumPointsIN[[ct, 1]] < startX, Goto[nextpt]];
   If[dGnumPointsIN[[ct, 1]] > endX, Goto[nextpt]];
   (*compare the dG point to the free energy of the regular solution,
   if higher than not stable*)
   If[dGnumPointsIN[[ct, 2]] > (deltaGreg2 /. X → dGnumPointsIN[[ct, 1]]) ||
     Abs[dGnumPointsIN[[ct, 2]] - (deltaGreg2 /. X → dGnumPointsIN[[ct, 1]])] < 10^-4,
    stablecounter[[ct]] = 1];
   If[stablecounter[[ct]] == 1 && (Limit[deltaGreg2 /. X → dGnumPointsIN[[ct, 1]] /.
         x_ig → xigArrayIN[[ct, 2]], d → ∞] < dGnumPointsIN[[ct, 2]]), metaarray[[ct]] = 1];
   (*if the dg point is lower than the common tangent but higher than the amorphous,
   amorph and reg have a common tangent*)
   If[dGnumPointsIN[[ct, 2]] > (amorph2 /. X -> dGnumPointsIN[[ct, 1]]) &&
     xDTarrayIN[[ct, 2]] < 1000, biNCR = 99];
   Label[nextpt]];
  xDTarray2 = DeleteCases[xDTarray2, 99];
  If[Mean[stablecounter] > 0.25, stable = 99];
  If[Mean[metaarray] < 0.02, metaSS = 99];
  If[stable == 99 && metaSS == 99, notNC[[p]] = {(w_ig / w_b), w_b}];
  If[stable == 99 && metaSS == 0, metaSSNC[[p]] = {(w_ig / w_b), w_b}];
  (*If[biNCR==99&&stable==0,bimodalAR[[p]]={(w_ig/w_b),w_b}];*)
  If[biNCR == 0 && stable == 0
   (*&&meta==0*), bimodalNCR[[p]] = {(w_ig / w_b), w_b}]; Label[newp];
  If[bimodal == 99 && stable == 0(*&&meta==0*), bimodalNCNC[[p]] = {(w_ig / w_b), w_b}];
  If[biamorph == 99 && bimodal == 99, bimodalRANC[[p]] = {(w_ig / w_b), w_b}];
  graphfilename = "wb" <> wbstring <> "wig" <> wigstring <> "gba=gbbGRAPH.gif";
  Export[graphfilename, Show[ListPlot[dGnumPointsIN, PlotRange → All],
    Plot[{deltaGreg2, amorph2, tangentlinecheck}, {X, 0, 1}]]];]
 metaSSNCplot = DeleteCases[metaSSNC, 0];
 Export["metaSSNCpoints.txt", metaSSNCplot, "Table"];
 bimodalNCNCplot = DeleteCases[bimodalNCNC, 0];
 bimodalRANCplot = DeleteCases[bimodalRANC, 0];
 Export["bimodalNCNCpoints.txt", bimodalNCNCplot, "Table"];
 Export["bimodalRANCpoints.txt", bimodalRANCplot, "Table"];
 (**)
 (*Export["minimumarray.txt",minimumarray,"Table"]*)] // Quiet
```

```
$Aborted
```

APPENDIX B .4

```
eVtoJ = 1.60217 * 10^-19 * 6.02 * 10^23;

wbarray = Range[-0.01, -0.08, -0.005];

stoich = {{0.25, -20000 / eVtoJ}};
stoichname = ToString[(IntegerPart[stoich[[1, 2]] * eVtoJ / 1000])] <> "kJ.txt";

notNC = ConstantArray[0, Length[wbarray]];
stableNC = ConstantArray[0, Length[wbarray]];
bimodalNCNC = ConstantArray[0, Length[wbarray]];
metastableNC = ConstantArray[0, Length[wbarray]];
metastablebimodalNCNC = ConstantArray[0, Length[wbarray]];
amorph = ConstantArray[0, Length[wbarray]];
metaamorph = ConstantArray[0, Length[wbarray]];

For[hh = 1, hh ≤ Length[wbarray], hh++,
 wbfolder = ToString[wbarray[[hh]]];
 foldername =
  "C:\\Documents and Settings\\Heather\\My Documents\\My Dropbox\\negative wb\\z12
     1000K\\wb" <> wbfolder;
 SetDirectory[foldername];
 notNC[[hh]] = Import["notNCpoints" <> stoichname, "Table"];
 stableNC[[hh]] = Import["stableNCpoints" <> stoichname, "Table"];
 bimodalNCNC[[hh]] = Import["bimodalNCNCpoints" <> stoichname, "Table"];
 metastableNC[[hh]] = Import["metastableNCpoints" <> stoichname, "Table"];
 metastablebimodalNCNC[[hh]] =
  Import["metastablebimodalNCpoints" <> stoichname, "Table"];
 metaamorph[[hh]] = Import["metastableamorphpoints" <> stoichname, "Table"];
 amorph[[hh]] = Import["amorphpoints" <> stoichname, "Table"];]

notNClistAll = {{0, 0}};
stableNClistAll = {{0, 0}};
bimodalNCNClistAll = {{0, 0}};
metastableNClistAll = {{0, 0}};
metastablebimodalNCNClistAll = {{0, 0}};
metaamorphlistAll = {{0, 0}};
amorphlistAll = {{0, 0}};

For[hhh = 1, hhh ≤ Length[wbarray], hhh++,
  notNClistAll = Join[notNClistAll, notNC[[hhh]]];
  stableNClistAll = Join[stableNClistAll, stableNC[[hhh]]];
  bimodalNCNClistAll = Join[bimodalNCNClistAll, bimodalNCNC[[hhh]]];
  metastableNClistAll = Join[metastableNClistAll, metastableNC[[hhh]]];
  metastablebimodalNCNClistAll =
   Join[metastablebimodalNCNClistAll, metastablebimodalNCNC[[hhh]]];
  metaamorphlistAll = Join[metaamorphlistAll, metaamorph[[hhh]]];
  amorphlistAll = Join[amorphlistAll, amorph[[hhh]]];
 ];

Show[ListPlot[{notNClistAll, metastableNClistAll,
   metastablebimodalNCNClistAll, stableNClistAll, bimodalNCNClistAll},
  AspectRatio → 1, Frame → True, PlotStyle → {Red, Yellow, Orange, Green, Purple}]
  (*,ListPlot[metaamorphlist,PlotStyle→Blue,PlotMarkers→"O"]*)]

(*reverse & convert*)
```

```
fig =.; z =.; wb =.; wig =.; γA =.; γB =.; X =.; R =.; T =.;
 xb =.; A =.; B =.; v =.; deltaHnot = z * (wb - wig/2 - (γB - γA)/(2 * z)); // Quiet
dH0 = deltaHnot /. z → 12 /. γB → 0.085 /. γA → 0.085; // Simplify
deltaHnot
```

$$z\left(w_b - \frac{w_{ig}}{2} - \frac{-\gamma_A + \gamma_B}{2\,z}\right)$$

```
eVtoJ * dH0 /. wb → -0.01 /. wig → -0.2
```

104 167.

```
notNClist =
  Table[{eVtoJ * 12 * notNClistAll[[ww, 2]], eVtoJ * (dH0 /. wb → notNClistAll[[ww, 2]] /. wig →
        notNClistAll[[ww, 1]] * notNClistAll[[ww, 2]])}, {ww, 1, Length[notNClistAll]}];
stableNClist = Table[{eVtoJ * 12 * stableNClistAll[[ww, 2]],
    eVtoJ * (dH0 /. wb → stableNClistAll[[ww, 2]] /. wig → stableNClistAll[[ww, 1]] *
         stableNClistAll[[ww, 2]])}, {ww, 1, Length[stableNClistAll]}];
metastableNClist = Table[{eVtoJ * 12 * metastableNClistAll[[ww, 2]],
    eVtoJ * (dH0 /. wb → metastableNClistAll[[ww, 2]] /.
       wig → metastableNClistAll[[ww, 1]] * metastableNClistAll[[ww, 2]])},
   {ww, 1, Length[metastableNClistAll]}];
bimodalNCNClist = Table[{eVtoJ * 12 * bimodalNCNClistAll[[ww, 2]],
    eVtoJ * (dH0 /. wb → bimodalNCNClistAll[[ww, 2]] /. wig → bimodalNCNClistAll[[ww, 1]] *
         bimodalNCNClistAll[[ww, 2]])}, {ww, 1, Length[bimodalNCNClistAll]}];
metastablebimodalNCNClist = Table[{eVtoJ * 12 * metastablebimodalNCNClistAll[[ww, 2]],
    eVtoJ * (dH0 /. wb → metastablebimodalNCNClistAll[[ww, 2]] /. wig →
        metastablebimodalNCNClistAll[[ww, 1]] * metastablebimodalNCNClistAll[[ww, 2]])},
   {ww, 1, Length[metastablebimodalNCNClistAll]}];
metaamorphlist = Table[{eVtoJ * 12 * metaamorphlistAll[[ww, 2]],
    eVtoJ * (dH0 /. wb → metaamorphlistAll[[ww, 2]] /. wig → metaamorphlistAll[[ww, 1]] *
         metaamorphlistAll[[ww, 2]])}, {ww, 1, Length[metaamorphlistAll]}];
Show[ListPlot[
  {notNClist, metastableNClist, metastablebimodalNCNClist, stableNClist, bimodalNCNClist},
  AspectRatio → 1, Frame → True, PlotStyle → {Red, Yellow, Orange, Green, Purple}]
  (*,ListPlot[metaamorphlist,PlotStyle→Blue,PlotMarkers→"O"]*)]
-0.03 * 12 * eVtoJ
```

-34 722.2

```
notNCedge = ConstantArray[0, (Length[notNClist] + 1)];
For[i = 1, i ≤ Length[notNClist], i++,
  If[(notNClist[[i, 1]] ≠ notNClist[[i - 1, 1]]),
   notNCedge[[i + 1]] = {notNClist[[i - 1, 1]], notNClist[[i - 1, 2]]}]];
notNCedge = DeleteCases[notNCedge, 0]; notNCedge = DeleteCases[notNCedge, {0., 0.}]
```

Part::partd: Part specification {{0., 0.}, {-11574.1, 30381.9}, {-11574.1, 33275.5}, {-11574.1, 36169.}, {-11574.1, 39062.5}, {-11574.1, 41956.}, {-11574.1, 44849.5}, {-17361.1, -8680.56}, {-17361.1, -8246.53}, {-17361.1, -7812.5}, ≪31≫, {-23148.2, -8680.56}, {-23148.2, -8101.85}, {-23148.2, -7523.15}, {-23148.2, -6944.45}, {-23148.2, -6365.74}, {-23148.2, -5787.04}, {-23148.2, -5208.33}, {-23148.2, -4629.63}, {-23148.2, -4050.93}, ≪101≫}[[0, 1]] is longer than depth of object. ≫

```
{{-11574.1, 44849.5}, {-17361.1, 3472.22}, {-23148.2, 0.}, {-28935.2, -3616.9},
 {-34722.2, -6076.39}, {-40509.3, -10127.3}, {-46296.3, -12731.5}, {-52083.3, -16927.1},
 {-57870.4, -20254.6}, {-63657.4, -23871.5}, {-69444.5, -26041.7},
 {-75231.5, -30092.6}, {-81018.5, -34432.9}, {-86805.6, -36892.4}}
```

```
notNCedgefit
```

$$72578.9 + \frac{4.1261 \times 10^{8}}{x} + 1.34808\,x$$

```
notNCedgefit = Fit[notNCedge, {1, 1 / x, x}, x];
Show[ListPlot[{notNClist, notNCedge}, PlotMarkers → {".", {"O"}}, PlotRange → All],
 Plot[notNCedgefit, {x, -1, -100000}]]
```

```
notNCedgefit50 = notNCedgefit
```

$$13906.2 + \frac{3.31489 \times 10^{6}}{x} + 0.586658\,x$$

```
metaNCNCedge = ConstantArray[0, (Length[metastablebimodalNCNClist] + 1)];
For[i = 1, i ≤ Length[metastablebimodalNCNClist], i++,
  If[(metastablebimodalNCNClist[[i, 1]] ≠ metastablebimodalNCNClist[[i - 1, 1]]),
   metaNCNCedge[[i + 1]] =
    {metastablebimodalNCNClist[[i - 1, 1]], metastablebimodalNCNClist[[i - 1, 2]]}]];
metaNCNCedge = DeleteCases[metaNCNCedge, 0]; metaNCNCedge =
 DeleteCases[metaNCNCedge, {0., 0.}]
```

Part::partd: Part specification {{0., 0.}, {-17361.1, 3906.25}, {-17361.1, 4340.28}, {-17361.1, 4774.31}, {-17361.1, 5208.33}, {-17361.1, 5642.36}, {-17361.1, 6076.39}, {-17361.1, 6510.42}, {-17361.1, 6944.45}, {-17361.1, 7378.47}, {-17361.1, 7812.5}, ≪30≫, {-28935.2, -2893.52}, {-28935.2, -2170.14}, {-28935.2, -1446.76}, {-28935.2, -723.38}, {-28935.2, 0.}, {-28935.2, 723.38}, {-28935.2, 1446.76}, {-28935.2, 2170.14}, {-28935.2, 2893.52}, ≪15≫}[[0, 1]] is longer than depth of object. ≫

```
{{-17361.1, 14322.9}, {-23148.2, 8680.56}, {-28935.2, 3616.9},
 {-34722.2, -1736.11}, {-40509.3, -7089.12}, {-46296.3, 11574.1},
 {-52083.3, -15625.}, {-81018.5, -30381.9}, {-86805.6, 34722.2}}
```

```
metaNCNCedgefit50 = metaNCNCedgefit;
metaNCNCedgefit30 = metaNCNCedgefit;
metaNCNCedgefit20 = metaNCNCedgefit;
```

```
metaNCNCedgefit
```

$$6761.62 - \frac{3.03107 \times 10^{8}}{x} + 0.51646\, x$$

```
metaNCNCedgefit50
```

$$68\,494.4 - \frac{1.97145 \times 10^{7}}{x} + 0.961062\, x$$

```
metaNCNCedgefit = Fit[metaNCNCedge, {1, 1 / x, x}, x];
Show[ListPlot[{metastablebimodalNCNClist, metaNCNCedge},
  PlotMarkers → {".", {"O"}}, PlotRange → All], Plot[metaNCNCedgefit, {x, -1, -100 000}]]
Plot[{metaNCNCedgefit20, metaNCNCedgefit30, metaNCNCedgefit50},
 {x, -100, -100 000}, PlotRange → {-50 000, 150 000}, AspectRatio → 1, Frame → True]
```